Jordan Journal of Mechanical and Industrial Engineering (JJMIE)

JJMIE is a high-quality scientific journal devoted to fields of Mechanical and Industrial Engineering. It is published by Hashemite University in cooperation with the Jordanian Scientific Research and Innovation Support Fund, Ministry of Higher Education and Scientific Research.

SUBMISSION ADDRESS:

Prof. Moh'd Sami Ashhab, Editor-in-Chief
Jordan Journal of Mechanical & Industrial Engineering,
Hashemite University,
PO Box 330127, Zarqa, 13133 , Jordan
E-mail: jjmie@hu.edu.jo

Hashemite Kingdom of Jordan

Hashemite University

Jordan Journal of Mechanical and Industrial Engineering

JJMIE

An International Peer-Reviewed Scientific Journal

Financed by Scientific Research Support Fund

Volume 15, Number 1, March 2021

Special Issue: Instrumentation & Measurements in Engineering

http://jjmie.hu.edu.jo/

ISSN 1995-6665

Jordan Journal of Mechanical and Industrial Engineering (JJMIE)

JJMIE is a high-quality scientific journal devoted to fields of Mechanical and Industrial Engineering. It is published by Hashemite University in cooperation with the Jordanian Scientific Research and Innovation Support Fund, Ministry of Higher Education and Scientific Research.

Introduction: The Editorial Board is very committed to build the Journal as one of the leading international journals in mechanical and industrial engineering sciences in the next few years. With the support of the Ministry of Higher Education and Scientific Research and Jordanian Universities, it is expected that a heavy resource to be channeled into the Journal to establish its international reputation. The Journal's reputation will be enhanced from arrangements with several organizers of international conferences in publishing selected best papers of the conference proceedings.

Aims and Scope: *Jordan Journal of Mechanical and Industrial Engineering* (JJMIE) is a refereed international journal to be of interest and use to all those concerned with research in various fields of, or closely related to, mechanical and industrial engineering disciplines. *Jordan Journal of Mechanical and Industrial Engineering* aims to provide a highly readable and valuable addition to the literature which will serve as an indispensable reference tool for years to come. The coverage of the journal includes all new theoretical and experimental findings in the fields of mechanical and industrial engineering or any closely related fields (Materials, Manufacturing, Management, Design, Thermal, Fluid, Energy, Control, Mechatronics, and Biomedical). The journal also encourages the submission of critical review articles covering advances in recent research of such fields as well as technical notes.

Guide for Authors

Manuscript Submission:
High-quality submissions to this new journal are welcome now and manuscripts may be either submitted online or email.

Online: For online and email submission upload one copy of the full paper including graphics and all figures at the online, submission site, accessed via http://jjmie.hu.edu.jo. The manuscript must be written in MS Word Format. All correspondence including notification of the Editor's decision and requests for revision, takes place by e-mail and via the Author's homepage, removing the need for a hard-copy paper trail

Submission address and contact :
Prof. Moh'd Sami Ashhab
Editor-in-Chief
Jordan Journal of Mechanical & Industrial Engineering, Hashemite University
PO Box 330127, Zarqa, 13115, Jordan
E-mail: jjmie@hu.edu.jo

Types of contributions*:* Original research papers and Technical reports

Corresponding author: Clearly indicate who is responsible for correspondence at all stages of refereeing and publication, including post-publication. Ensure that telephone and fax numbers (with country and area code) are provided in addition to the e-mail address and the complete postal address. Full postal addresses must be given for all co-authors.

Original material: Submission of an article implies that the work described has not been published previously (except in the form of itstan abstract or as part of a published lecture or academic thesis), that it is not under consideration for publication elsewhere, tha publication is approved by all authors and that, if accepted, it will not be published elsewhere in the same form, in English or in any other language, without the written consent of the Publisher. Authors found to be deliberately contravening the submission guidelines on originality and exclusivity shall not be considered for future publication in this journal.

Withdrawing: If the author chooses to withdraw his article after it has been assessed, he shall reimburse JJMIE with the cost of reviewing the paper.

Manuscript Preparation:

General: Editors reserve the right to adjust style to certain standards of uniformity. Original manuscripts are discarded after .publication unless the Publisher is asked to return original material after use. Please use MS Word for the text of your manuscript

Structure: Follow this order when typing manuscripts: Title, Authors, Authors title, Affiliations, Abstract, Keywords, Introduction, Main text, Conclusions, Acknowledgements, Appendix, References, Figure Captions, Figures and then Tables. Please supply figures imported into the text AND also separately as original graphics files. Collate acknowledgements in a separate section at the end of the article and do not include them on the title page, as a footnote to the title or otherwise.

Text Layout: Use 1.5 line spacing and wide (3 cm) margins. Ensure that each new paragraph is clearly indicated. Present tables and figure legends on separate pages at the end of the manuscript. If possible, consult a recent issue of the journal to become familiar with layout and conventions. All footnotes (except for table and corresponding author footnotes) should be identified with superscript Arabic numbers. To conserve space, authors are requested to mark the less important parts of the paper (such as records of experimental results) for printing in smaller type. For long papers (more than 4000 words) sections which could be deleted without destroying either the sense or the continuity of the paper should be indicated as a guide for the editor. Nomenclature should conform to that most frequently used in the scientific field concerned. Number all pages consecutively; use 12 or 10 pt font size and standard fonts.

Corresponding author: Clearly indicate who is responsible for correspondence at all stages of refereeing and publication, including post-publication. The corresponding author should be identified with an asterisk and footnote. Ensure that telephone and fax numbers (with country and area code) are provided in addition to the e-mail address and the complete postal address. Full postal addresses must be given for all co-authors. Please consult a recent journal paper for style if possible.

Abstract: A self-contained abstract outlining in a single paragraph the aims, scope and conclusions of the paper must be supplied.

Keywords: Immediately after the abstract, provide a maximum of six keywords (avoid, for example, 'and', 'of'). Be sparing with abbreviations: only abbreviations firmly established in the field may be eligible.

Symbols: All Greek letters and unusual symbols should be identified by name in the margin, the first time they are used.

Units: Follow internationally accepted rules and conventions: use the international system of units (SI). If other quantities are mentioned, give their equivalent quantities in SI

Maths: Number consecutively any equations that have to be displayed separately from the text (if referred to explicitly in the text).

References: All publications cited in the text should be presented in a list of references following the text of the manuscript.

Text: Indicate references by number(s) in square brackets in line with the text. The actual authors can be referred to, but the reference number(s) must always be given.

List: Number the references (numbers in square brackets) in the list in the order in which they appear in the text.

Examples:

Reference to a journal publication:

[1] M.S. Mohsen, B.A. Akash, "Evaluation of domestic solar water heating system in Jordan using analytic hierarchy process". Energy Conversion & Management, Vol. 38 (1997) No. 9, 1815-1822.

Reference to a book:

[2] Strunk Jr W, White EB. The elements of style. 3rd ed. New York: Macmillan; 1979.

Reference to a conference proceeding:

[3] B. Akash, S. Odeh, S. Nijmeh, "Modeling of solar-assisted double-tube evaporator heat pump system under local climate conditions". 5th Jordanian International Mechanical Engineering Conference, Amman, Jordan, 2004.

Reference to a chapter in an edited book:

[4] Mettam GR, Adams LB. How to prepare an electronic version of your article. In: Jones BS, Smith RZ, editors. Introduction to the electronic age, New York: E-Publishing Inc; 1999, p. 281-304

Free Online Color : If, together with your accepted article, you submit usable color and black/white figures then the journal will ensure that these figures will appear in color on the journal website electronic version.

Tables: Tables should be numbered consecutively and given suitable captions and each table should begin on a new page. No vertical rules should be used. Tables should not unnecessarily duplicate results presented elsewhere in the manuscript (for example, in graphs). Footnotes to tables should be typed below the table and should be referred to by superscript lowercase letters.

Notification: Authors will be notified of the acceptance of their paper by the editor. The Publisher will also send a notification of receipt of the paper in production.

Copyright: All authors must sign the Transfer of Copyright agreement before the article can be published. This transfer agreement enables Jordan Journal of Mechanical and Industrial Engineering to protect the copyrighted material for the authors, but does not relinquish the authors' proprietary rights. The copyright transfer covers the exclusive rights to reproduce and distribute the article, including reprints, photographic reproductions, microfilm or any other reproductions of similar nature and translations.

Proof Reading: One set of page proofs in MS Word format will be sent by e-mail to the corresponding author, to be checked for typesetting/editing. The corrections should be returned within 48 hours. No changes in, or additions to, the accepted (and subsequently edited) manuscript will be allowed at this stage. Proofreading is solely the author's responsibility. Any queries should be answered in full. Please correct factual errors only, or errors introduced by typesetting. Please note that once your paper has been proofed we publish the identical paper online as in print.

JJMIE

Volume 15, Number 1, March. 2021
ISSN 1995-6665

Jordan Journal of Mechanical and Industrial Engineering

JJMIE

Volume 15, Number 1, March. 2021
ISSN 1995-6665

Jordan Journal of Mechanical and Industrial Engineering

JJMIE

Volume 15, Number 1, March. 2021
ISSN 1995-6665
Pages 1 - 6

Jordan Journal of Mechanical and Industrial Engineering

Experimental Study on Formaldehyde Emission from Environmental Protection and Energy-Saving Alcohol Fuel for Vehicles

Dandan Liu, Shigang Li*, Hui Liu

College of Robotics, Beijing Union University, Beijing 100020 China

Received July 18 2020 *Accepted Feb 20 2021*

Abstract

With the further increase of domestic oil demand, the diversification strategy of energy supply represented by alternative energy sources, such as alcohol fuel which has become a direction of China's energy policy. Alcohol fuel can reduce conventional engine emissions by replacing conventional gasoline and diesel, but their unconventional emissions -- formaldehyde -- tend to have higher concentrations than conventional engines. Based on this, this paper analyzed the physical and chemical properties of mixture of methanol and gasoline and its feasibility as an energy fuel, and conducted experiments on formaldehyde emission of gasoline and methanol gasoline respectively, and then obtained a large number of experimental data that studied and analyzed the experimental results and methods, and drew relevant research conclusions. The results show that the high ratio of alcohol fuel can replace the use of chemical fuel and has good energy saving and environmental protection characteristics. When the same fuel is tested, the formaldehyde emission increases first and then decreases with the increase of power. In this paper, a large amount of formaldehyde emission data from alcohol fuel engines are obtained through bench experiments, which provides a scientific basis for the future development of alcohol fuel vehicle combustion system and the formulation of environmental emission standards.

Keywords: engine, alcohol fuel, methanol, unconventional emission, formaldehyde;

1. Introduction

With the rapid development of the global economy, China's automobile industry has also developed rapidly. However, the rapid increase of transportation and automobile ownership has brought great pressure to China's energy supply and environmental pollution. Air pollution caused by automobile emissions is becoming more and more serious. In large and medium cities in various countries, automobile exhaust emissions have become the most important source of air pollution [1].

To alleviate the pressure of oil resources shortage, and to improve the atmospheric environment, and promote the human society and the sustainable development of the auto industry, alcohol fuel (methanol, ethanol) as a new alternative fuel can be completely or partly replacing the traditional gasoline, diesel oil. Clean combustion, not only can greatly reduce the conventional emissions of harmful substances, specifically hydrocarbons (HC), nitrogen oxides (NO_X), carbon monoxide (CO), emissions of carbon dioxide (CO_2), but also particulate matter concentrations can significantly decrease, with good environmental properties [2]; Moreover, alcohol fuels are abundant in sources and are an ideal alternative to petroleum. Therefore, under the dual pressure of environmental protection and energy, alcohol fuel engine as a new type of vehicle power will present a broad development prospect [3].

Although the substitution of clean alcohol fuel for traditional fuel can reduce the content of conventional pollutants discharged by traditional engines and improve the quality of the environment, it also brings new problems.

When the engine uses alcohol fuel, the emission concentration of unconventional emissions—formaldehyde is often higher than that of traditional engine [4]. Formaldehyde emissions are very harmful to the environment and human health. Animal experiments have confirmed that it can cause nasal squamous cell carcinoma in rats, and its impact on human health is mainly manifested in abnormal smell, irritation, allergies, abnormal lung function, abnormal liver function and abnormal immune function [5]. When the concentration of formaldehyde in the air reaches 30mg/m3, it will cause death immediately. At present, people's understanding of the test methods, test standards and emission value of formaldehyde in automobile emissions is far from a deep understanding of the hazards of formaldehyde, and some people even predict the development prospects of alcohol fuels based on this. Therefore, it is very necessary to carry out research on the detection and analysis methods of formaldehyde in the exhaust of alcohol fuel engines.

* Corresponding author e-mail: lishigang2523@163.com.

Based on this, the paper analyzes the formaldehyde emission in engine exhaust under different working conditions and different fuels and obtains a large amount of regular test data. This method does not require any pre-treatment of engine exhaust and can be directly sampled and analyzed. The operation is simple and fast, which has laid an important foundation for further improvement of alcohol fuel engines and further study of the main unconventional emissions-formaldehyde under different catalytic conditions.

2. Feasibility Analysis of Methanol as a Fuel for Automobiles

Methanol is a colorless, transparent, volatile, and flammable liquid. Methanol is toxic, with low calorific value, high latent heat of evaporation, good anti-knock performance, and high oxygen content. In addition, methanol is prone to phase separation in the presence of a small amount of water [6]. The physical and chemical properties of methanol and gasoline are compared in Table 1.

Methanol can be directly used as the fuel of internal combustion engine with the following good characteristics [7-11]:

1. Methanol has small molecular weight and simple molecular structure. Methanol fuel contains oxygen, which is 50% oxygen in terms of mass, which is conducive to complete combustion. Small C/H is conducive to more water and less CO_2 during combustion.
2. The boiling point and freezing point of methanol are both low, the former is conducive to the formation of fuel-air mixture, while the latter can ensure the engine to work at a low temperature.
3. Compared with gasoline, the calorific value of methanol is relatively low, while the latent heat of vaporization is 3.6 times that of gasoline. Therefore, with the same thermal efficiency, the effective mass fuel consumption rate of methanol is high, and the high latent heat of vaporization can improve the internal cooling of the engine after combustion, improve the engine's power performance, and reduce the exhaust temperature.
4. Methanol has a higher-octane number and a higher anti-knock performance, and a wider ignition limit than gasoline. It can appropriately improve the compression ratio to improve the thermal efficiency, and it can also burn in a thinner mixture state, which is very beneficial to exhaust purification and fuel consumption reduction.
5. Methanol has a higher ignition point than gasoline, which is less prone to fire accidents and safer than gasoline.
6. Methanol gasoline is liquid under normal temperature and pressure, which is easy to operate and convenient to store.

Table1. Physical and chemical properties of alcohol fuel

Name		Methanol	gasoline
Chemical formula		CH_3OH	C_4～C_{12} hydrocarbon compounds
Molecular weight		32	95～120
Quality ingredients	Carbon content (mass ratio %)	37.5	85～88
	Hydrogen content (mass ratio %)	12.5	12～15
	Oxygen content (mass ratio %)	50.0	0
20℃ density (kg/L)		0.791	0.72～0.75
Theoretical air-fuel ratio (mass ratio)		6.47	14.7
Reid vapor pressure (37.8℃) (MPa)		0.037	0.05～0.09
Boiling point (℃)		64.5	30～190
Freezing point (℃)		-97.8	-57
Flash point (℃)		11	43
Auto-ignition temperature (℃)		470	260～370
Solubility in water (mg/L)		mutually soluble	100～200
Latent heat of vaporization (kJ /kg)		1109	310
Fuel low heating value (MJ/kg)		19.92	44.52
Octane number	Research Method (RON)	112	84～96
	Motor Method (MON)	92	70～84

After methanol is mixed with gasoline in a certain proportion and a certain additive is added to form the blended fuel, low-proportion methanol gasoline, such as M3 and M5, can be used like gasoline without any changes to the engine. In Europe and other places, a large number of methanol gasoline has been sold, but it is generally necessary to add auxiliary solvents to prevent fuel stratification; Medium proportion methanol gasoline, such as M15, M25, the engine only needs to be slightly adjusted, the technical problem is relatively simple, as it has been demonstrated in some international teams in Europe, but solvent must be added; high proportion methanol gasoline, such as M85 and M90, needs to modify and optimize the engine, and its power, emission and thermal efficiency are better than the original gasoline engine [12]. At present, methanol production technology, special methanol fuel vehicle technology with high combustion ratio and pure methanol fuel are relatively mature, and the market supply is relatively sufficient. Moreover, high proportion methanol fuel has been commercialized abroad [13]. However, methanol gasoline still has serious problems in toxicity, metal corrosion and other aspects. It is necessary to organize a comprehensive, systematic and scientific feasibility demonstration on methanol gasoline for vehicle use.

3. Unconventional Emission -- Formaldehyde Emission Test

In the process of this paper, the test data are mainly measured under partial load characteristic test of engine. Start from small load, gradually increase the throttle, appropriate distribution of more than 6 measurement points [14-16]. At each measurement point, the output torque, power, exhaust temperature and so on of the engine are recorded after the engine is running steadily for 1min.During engine operation or data recording, the difference between the engine speed and the selected speed should be no more than ± 1% or ±10 r/min, and the larger value should be taken. At the same time, data such as torque and power are recorded, and the average value of two consecutive stable values is taken. The difference between the two measured values of torque should be less than 2% [17, 18].

3.1. Test instruments and equipment

1. Formaldehyde collection device

The method of collecting formaldehyde in this test is to use the property of formaldehyde to be miscible with water at will and let the engine exhaust pass through a specific absorption device and mixing device to collect the formaldehyde in the exhaust gas.

2. Formaldehyde analyzer

The formaldehyde analyzer used in the test is GDYK-201S indoor air formaldehyde analyzer developed by Changchun Jida Cygnet Instrument Co., Ltd. The instrument consists of a silicon light source, a colorimetric bottle, an integrated photoelectric sensor and a microprocessor, which can directly display the content of formaldehyde in the measured sample on the LCD screen (mg/L), substitute the sampling volume, temperature and pressure, etc., to get the final formaldehyde emission (mg/m^3).

3.2. Experimental fuel

The main fuels used in this test are: RON93 gasoline currently sold on the market in Northwest China,RON93 gasoline refers to gasoline with an octane number of 93; Methanol, pure analysis, purity above 99.5%, Xi 'an Chemical Reagent Factory production; Ethanol, pure analysis, purity 99.7% above, Xi 'an chemical reagent factory production.

In the test, M15, M25, M85, E10, E25 and ED10 were prepared by volume percentage.

3.3. Formaldehyde-emission detection of bench test

The test gasoline engine is the Flyer M-TCE engine, gasoline injection closed-loop control, 0.8L, four-stroke water cooling. The test was conducted for formaldehyde test at engine speed of 2600r/min and different power [19]. The test results are shown in Table 2 to Table 5.

Table2. Bench test results of formaldehyde emission from RON93 gasoline

Serial number	Throttle opening	Torque	Power	Formaldehyde test value	Formaldehyde emission
	%	N•m	kW	mg/L	mg/m^3
1	20	10.7	2.9	0.47	6.542
2	25	20.3	5.5	0.52	7.245
3	30	33.6	9.1	0.51	7.111
4	35	42.2	11.6	0.48	6.699
5	40	48.7	13.2	0.46	6.424
6	50	55.4	15.0	0.45	6.293

Table 3. Bench test results of formaldehyde emissions from M15 methanol gasoline

Serial number	Throttle opening	Torque	Power	Formaldehyde test value	Formaldehyde emission
	%	N•m	kW	mg/L	mg/m^3
1	20	19.2	5.2	0.52	7.225
2	25	27.5	7.5	0.54	7.503
3	30	37.3	10.2	0.56	7.781
4	35	43.3	11.8	0.52	7.225
5	40	49.3	13.4	0.49	6.809
6	50	55.4	15.1	0.48	6.670

Table 4. Bench test results of formaldehyde emissions from M25 methanol gasoline

Serial number	Throttle opening	Torque	Power	Formaldehyde test value	Formaldehyde emission
	%	N•m	kW	mg/L	mg/m^3
1	20	12.0	3.8	0.58	8.100
2	25	28.0	7.6	0.73	10.212
3	30	36.0	9.8	0.75	10.503
4	35	43.9	12.0	0.56	7.847
5	40	48.8	13.3	0.53	7.439
6	50	54.0	14.7	0.51	7.166

Table 5. Bench test results of formaldehyde emissions from M85 methanol gasoline

Serial number	Throttle opening	Torque	Power	Formaldehyde test value	Formaldehyde emission
	%	N•m	kW	mg/L	mg/m^3
1	20	14.0	3.6	0.67	9.373
2	25	27.6	7.7	0.90	12.603
3	30	37.4	10.2	0.83	11.631
4	35	43.5	11.8	0.68	9.545
5	40	48.5	13.2	0.64	8.992
6	50	53.7	14.6	0.52	7.311

3.4. Formaldehyde emission detection in vehicle test

The vehicle used in the test was Chang'an star SC6360H, and its main technical parameters are shown in Table 6.

Table 6. Main technical parameters of Chang'an star SC6360H

Length/width/height	3600/1475/1925 mm	Wheelbase	2350 mm
Track front/back	1280/1290 mm	Seat number	5-8
Full Vehicle Readiness Quality	990 kg	Full load total mass	1575kg
Engine Model	JL465Q5	Displacement	1012 mL
Rated power	39 kW	Maximum torque	78 N·m
Maximum speed	≥105 km/h	100 km fuel consumption	≤6.4 L/100 km
Maximum gradient	≥30 %	Type of transmission	5 speed synchronization
Driving Type	Rear wheel drive	Braking mode	Front disc, rear drum, double circuit hydraulic pressure
Front suspension	McPherson independent suspension	Rear suspension	5 leaf springs
Tyre type	155E13LT	-----	-----

The main instruments and equipment used in the test are shown in Table 7.

Table 7. Instruments and equipment used in vehicle test

Device name	Model	Manufacturer
Chassis dynamo meter	1Axle48-inline	AVL, Austria
In-situ formaldehyde analyzer for indoor air	GDYK-201S	Changchun Ji Swan Instrument Co., Ltd.
Formaldehyde meter sampling system	-----	Self developed

The test is the detection of formaldehyde emissions of several fuels at different speeds and different gears. The test data are shown in Table 8 to Table 10.

Table 8. Vehicle test RON93 gasoline formaldehyde emission results

Serial number	Speed	Gear position	Formaldehyde test value	Formaldehyde emission
	Km/h		mg/L	mg/m^3
1	30	3	0.68	9.689
2	40	3	0.70	9.991
3	50	4	0.79	11.290
4	55	4	0.85	12.172
5	65	5	0.77	11.052
6	75	5	0.80	11.509
7	85	5	0.80	11.535

Table9. Vehicle test M15 methanol gasoline formaldehyde emission results

Serial number	Speed	Gear position	Formaldehyde test value	Formaldehyde emission
	Km/h		mg/L	mg/m^3
1	30	3	0.72	10.361
2	40	3	0.95	13.680
3	50	4	1.07	15.438
4	55	4	0.98	16.507
5	65	5	0.94	15.859
6	75	5	0.91	15.378
7	85	5	0.92	15.572

Table 10. Vehicle test M85 methanol gasoline formaldehyde emission results

Serial number	Speed	Gear position	Formaldehyde test value	Formaldehyde emission
	Km/h		mg/L	mg/m^3
1	30	3	0.80	13.519
2	40	3	0.92	15.547
3	50	4	0.95	16.054
4	55	4	1.00	16.916
5	65	5	0.98	16.588
6	75	5	0.80	13.550
7	85	5	0.76	12.885

4. Experimental Results and Comparative Analysis

The emission levels of formaldehyde when the engine burns different fuels are shown in Figure 1 to Figure 4.

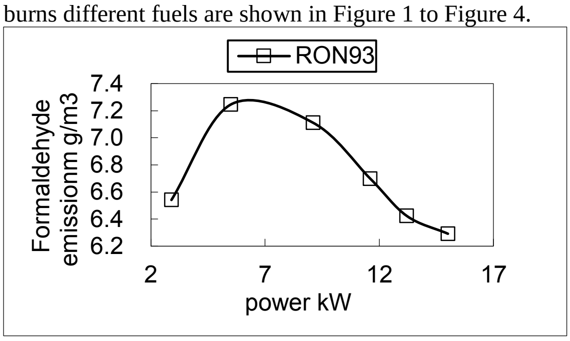

Figure 1. RON93 gasoline formaldehyde emission

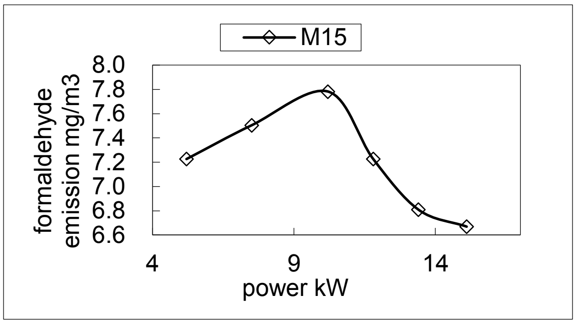

Figure 2. M15 methanol gasoline formaldehyde emission

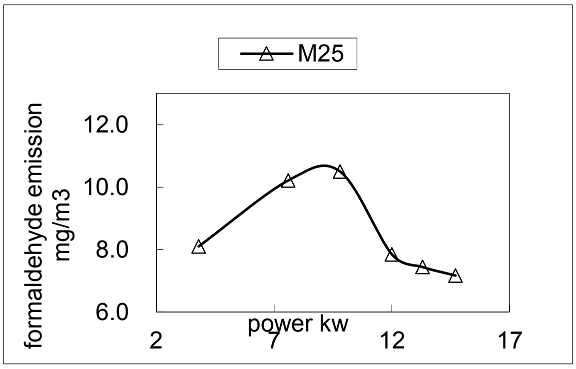

Figure 3. M25 methanol gasoline formaldehyde emission

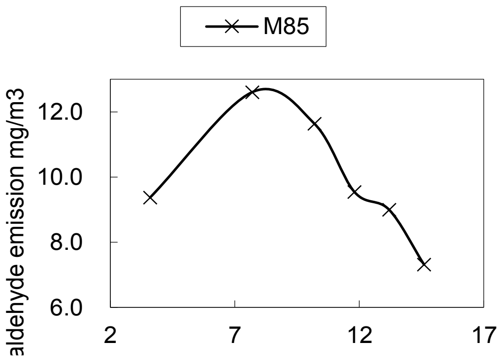

Figure 4. M25 methanol gasoline formaldehyde emission

4.1. Influence of methanol content on results

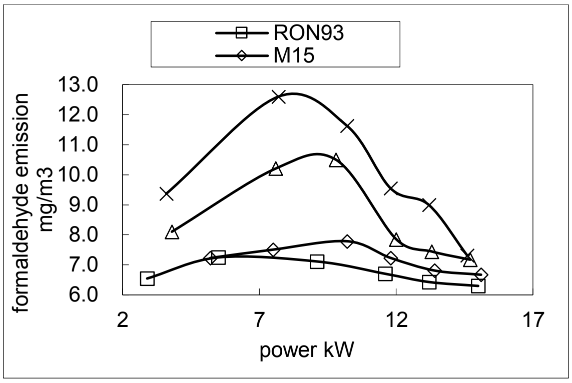

Figure 5. Comparison of Methanol Gasoline and RON93 Formaldehyde Emissions

As can be seen from Figure 5, with the increase of methanol content in the fuel, the emission of formaldehyde is generally increasing. Moreover, at the same speed, with the increase of throttle opening, the formaldehyde emission generally shows a trend of first rising and then falling, and the formaldehyde emission is the largest near the throttle opening of 30%. The reason is that in the case of small load, the amount of mixture filled in the engine cylinder is less, the combustion is more complete, and the emission of formaldehyde is less. The decrease of formaldehyde emission under heavy load is mainly due to the rise of temperature, and high temperature is not conducive to the formation of formaldehyde. This is also verified by analyzing formaldehyde emission concentration at different sampling points in the exhaust system.

Table 11 shows the comparison of the maximum, minimum and average formaldehyde emission of the selected fuels within the range of engine test conditions. It can also be seen that the emission of formaldehyde shows a gradual rising trend with the increase of methanol or ethanol in the fuel.

Table 11. Comparison of formaldehyde emission averages of several fuels

Fuel	Maximum value	minimum value	average value
RON93	7.11	6.29	6.72
M15	7.78	6.67	7.20
M25	9.80	7.12	8.31
M85	11.07	7.31	9.49

5. Conclusion

Through the experimental study, the following conclusions are drawn:

1. When the engine uses gasoline and alcohol fuel, formaldehyde pollutants are present in the exhaust gas.
2. When the engine uses a mixed fuel of alcohol and gasoline, as the alcohol content in the mixed fuel increases, the amount of formaldehyde emissions in the exhaust also increases.

3. When the engine uses gasoline and alcohol fuels, formaldehyde emissions first increase and then decrease with the increase of load.
4. The combustion characteristics and combustion speed of M85 methanol gasoline are similar to that of RON93 gasoline, which can be used as fuel for ignition engine, and has good energy-saving and environmental protection characteristics.
5. M85 methanol gasoline has a very strong anti-knock performance, and its octane number is about 103. When M85 methanol gasoline is used as fuel, the engine runs smoothly with extremely low noise.
6. Due to the limitation of adjustment of the oxygen sensor of the engine, the adaptability of the engine is poor when using methanol gasoline above M50, or even the engine may not work. In order to ensure the good combustion of the engine, it is very necessary to develop the flexible fuel controller, which is beyond the scope of this article.

The analysis of formaldehyde emissions from alcohol fuel vehicle engines is a multi-disciplinary technology. In the actual test process, few successful experiences can be used for reference. Each step is done in trial and exploration. Although a complete measurement and analysis system has been established in the end, there are still many shortcomings, which need to be improved in some areas.

References

[1] Han, J.X, "Research on the prevention and control policies of automobile exhaust pollution in Beijing". North China Electric Power University, 2016.

[2] H.R. Chao, T.C. Lin, "Effect of methanol-containing additive on the emission of carbonyl compounds from a heavy-duty diesel engine". Hazardous Materials, 2000, 39-54.

[3] M.F. Othman, A. Adam, G. Najafi, R. Mamat, "Green fuel as alternative fuel for diesel engine: A review". Renewable and Sustainable Energy Reviews, Vol. 80, 2017, 694-709.

[4] V.A. Likhanov, O.P. Lopatin, "Study on toxicity of biodiesel engine running on alcohol". No. 25, 2019, 92-100.

[5] J.F. Wang, C.J. Shi, "Aldehydes and ketones in vehicle engine emissions". Shanghai Automobile, 1999, 31-33.

[6] X. Wang, Y.J. Guo, J.J. Zhang, "Comparison of properties of methanol, gasoline and methanol gasoline as internal combustion engine fuel". Chemical Industry Times, No. 3, 2005, 46-49.

[7] F. Yüksel, B. Yüksel, "The use of ethanol-gasoline blend as a fuel in an SI engine". Renewable Energy, No. 29, 2004, 1181-1191.

[8] O.M. Ali, R. Mamat, N.R. Abdullah, A.A. Abdullah, "Analysis of blended fuel properties and engine performance with palm biodiesel-diesel blended fuel". Renewable Energy, Vol. 86, 2016, 59-67.

[9] A.K. Agarwal, H. Karare, A. Dhar, "combustion, performance, emissions and particulate characterization of a methanol-gasoline blend (gasohol) fuelled medium duty spark ignition transportation engine". Fuel Processing Technology, Vol. 121, 2013, 16-24.

[10] X.M. Zhang, "Feasibility and prospect of methanol automobile industrialization in China under the constraint of energy environment". China University of Geosciences, 2017.

[11] X. Wang, Y.G. Guo, J.J. Zhang, "Comparison of properties of methanol, gasoline and methanol gasoline as internal combustion engine fuel". Chemical Industry Times, No. 3, 2005, 46-49.

[12] K.R. Pan, "The development and evaluation of methanol fuel vehicles". Commercial Automobile, No. 6, 1999, 6-10.

[13] L.Q. Dou, L.H. Zhang, "The situation of methanol and alternative fuel engine vehicles in Japan and Germany". No. 2, 2002, 7-9.

[14] M.F. Aly, I.H. Afefy, R.K. Abdel-Magied, E.K.A. Elhalim, "A comprehensive model of reliability, availability, and maintainability (RAM) for industrial systems evaluations". Jordan Journal of Mechanical and Industrial Engineering, Vol. 12, No. 1, 2018, 59-67.

[15] E. Rezaei, M. Poursina, M. Rezaei, A. Ariaei, "A new analytical approach for crack modeling in spur gears". Jordan Journal of Mechanical and Industrial Engineering, Vol. 13, No. 2, 2019, 69-74.

[16] GB/T 18297-2001, Performance test code for road vehicle engines. Beijing: State Administration of Machinery Industry, 2001.

[17] GB/T 17692-1999, Measurement methods of net power for automotive engines. Beijing: State Administration for Market Regulation, 1999.

[18] R.K. Maurya, A.K. Agarwal, "Experimental investigations of performance, combustion and emission characteristics of ethanol and methanol fueled HCCI engine". Fuel Processing Technology, Vol. 126, 2014, 30-48.

[19] Liu, D.D, "Study on measurement method of methanol content and formaldehyde emission in alcohol fuel". Chang'an University, 2008.

JJMIE

Volume 15, Number 1, March. 2021
ISSN 1995-6665
Pages 7 - 14

Jordan Journal of Mechanical and Industrial Engineering

Design of the Lower Control Arm of an Electric SUV Front Suspension Based on Multi-Disciplinary Optimization Technology

Zhenqi Yu[1,2], Huifang Jia[2], and Xingyuan Huang[3*]

[1]Nanchang Institute of Technology, Nanchang 330044, China
[2]Product Development & Technical Center, Jiangling Motors Co., Ltd, Nanchang 330001, China
[3]School of Mechatronics Engineering, Nanchang University, Nanchang 330031, China

Received July 18 2020 Accepted Feb 20 2021

Abstract

An electric SUV is designed and developed based on the original traditional fuel vehicle model. The design scheme of the front suspension lower control arm of prototype vehicle is referred to save the development cycle and cost of the design. The original design scheme is optimized to meet the performance and lightweight requirements. In this paper, the analysis model of lower control arm is firstly established based on the finite element technology to conduct free modal analysis. The results show that the first two modes appear as bending and torsion. The modal frequency is higher than excitation frequency, which satisfies the requirement of vibration characteristics. Then free modal test on lower control arm is carried out based on hammer method, and the test results show that the accuracy of the analysis value is high. Then, the front suspension dynamics model of electric SUV model is established to extract the load of lower control arm. The inertial release method is applied to analyze its limit strength, the results show that its maximum stress is lower than its used stress which meets the requirements of strength design. Finally, the multidisciplinary optimal design of lower control arm is carried out to obtain the best design scheme. After optimization, both modal characteristics and strength characteristics meet the design requirements, and its mass is reduced by 16.7%. And its optimization scheme has passed the bench test and road test certificate successfully, so it has high accuracy and feasibility, providing a new idea for the design and development of the lower control arm, the front suspension of electric SUV.

Keywords: lower control arm; modal; inertia release; strength; optimization; bench test;

1. Introduction

The suspension structure of electric vehicle is an important system which guarantees the stability and comfort of the vehicle. As the guiding and force transmission component of the former Macphersan suspension, lower control arm is connected with the wheels and subframes by ball hinges and bushings to withstand forces and torques from both vertical and horizontal directions when the vehicle is moving, which may make abnormal noise and failure risk occur. Its vibration characteristics and strength characteristics directly affect the safety and reliability of the vehicle, while lightweight affects the endurance mileage and manufacturing cost of the vehicle. Therefore, the design of lower control arm needs to consider various performance requirements and lightweight requirements. In order to save development cycle and cost, the optimization is carried out according to the front suspension lower control arm of original traditional fuel SUV models, which makes the structure of lower control arm meet the performance requirements required by electric SUV.

Fuchs Hannes et al. [1] discuss the results of a study to develop lightweight steel proof-of-concept front lower control arm (FLCA) designs that are less expensive and achieve equivalent structural performance relative to a baseline forged aluminum FLCA assembly. Yoo, Sang Hyuk et al. [2] show topology optimization of lower control arm (LCA), made of carbon fiber reinforced plastic (CFRP), that was originally composed of aluminum alloy, and authors propose the new design of CFRP LCA with 30% weight reduction compared to Al alloy LCA. Heo, S.J. et al. [3] presents shape optimization of lower control arm considering multi-disciplinary (stiffness, strength and durability) constraint conditions, and the optimal model meets all the design constraint conditions and reduces the weight by about 200 grams comparing with that of the initial model. Huang He [4] conducts stiffness performance analysis, strength performance analysis and modal performance analysis on a certain lower control arm and optimizes its structure and obtained its lightweight scheme. Its weight is significantly reduced after optimization, which also meets the requirements of fatigue life.

The following is the method to analyze whether the static and dynamic performance of the front suspension lower

* Corresponding author e-mail: huangxingyuan001@126.com.

control arm of an electric SUV can meet the design requirements. Firstly, the free modal analysis is carried out based on finite element method; secondly, the modal test is carried out to verify the accuracy of the model; thirdly, the dynamic simulation analysis of the front suspension is carried out to obtain the load of its typical working condition, and then the strength analysis is carried out; fourthly, the lightweight design is carried out on the basis of multiple disciplines and multiple objectives; finally, bench test and road test are carried out.

2. Dynamic characteristics analysis of lower control arm

2.1. Build finite element model

This type of electric SUV front suspension lower control arm follows the design scheme of the prototype fuel car. It is mainly composed of upper plate, lower plate and reinforcing shaft tube, its front point and back point are connected with the sub-frame, and its external point is connected with the steering knuckle. The 3d model of lower control arm is established using Catia software and imported into Hypermesh software [5,6]. The middle surface of upper plate, lower plate and reinforced shaft tube is extracted, and processed by grid division using 4mm mixed unit (CTRIA3 unit and CQUAD4 unit). It should be ensured that it is quadrilateral elements, and triangular elements should be reduced. Weld joint between each other is replaced by aligned quadrilateral shell elements. The thickness of upper plate of lower control arm is 4.0 mm, the thickness of lower plate is 4.0 mm, the thickness of reinforced shaft tube is 4.5 mm, and the mass of lower control arm is 4.2 kg. The material of each part of lower control arm is QSTE420TM, its yield strength is 420 MPa, the tensile strength is 480 MPa, the fracture strain is 21%. The material properties are shown in Table 1. The materials and their attributes of the same property are established to create a lower control arm finite element model, as shown in Fig. 1.

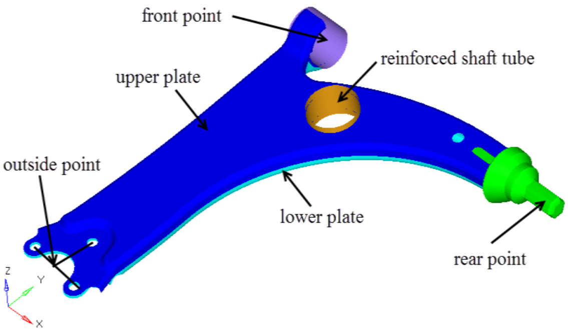

Figure 1. Finite element model of lower control arm

Table 1. material properties of QSTE420TM

Name	Elastic Modulus	Poisson's ratio	Density
QSTE420TM	210GPa	0.3	7.9E3 kg/m^3

2.2. Analysis of modal results

Based on general theory of modal analysis as well-known [7,8], free modal analysis is conducted on the lower control arm using Nastran software [9,10] to obtain the result that the first two natural frequencies are 610.8 Hz and 693.5 Hz, and their mode shapes are shown as bending and torsion respectively. What is shown in Fig. 2 and Fig. 3 are the torsional and bending modal shapes of the front suspension lower control arm respectively. The excitation frequency of the tire cavity was 180.5 Hz, and the excitation frequencies range of the motor were 16.7 Hz-200 Hz. Through modal analysis, it can be known that the lower control arm belongs to high-order frequency structure, which is far higher than the excitation frequency of its motor and the frequency of tire cavity, so it can meet the requirements of modal characteristics.

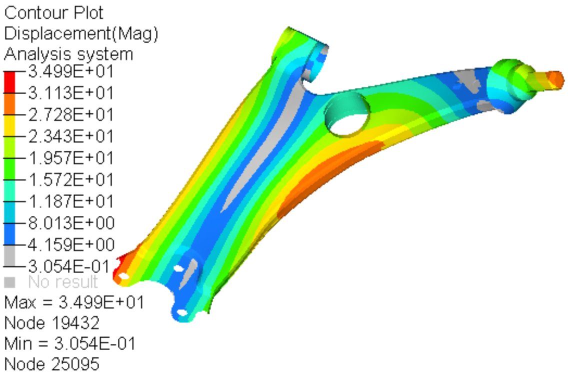

Figure 2. Bending modal shape of lower control arm

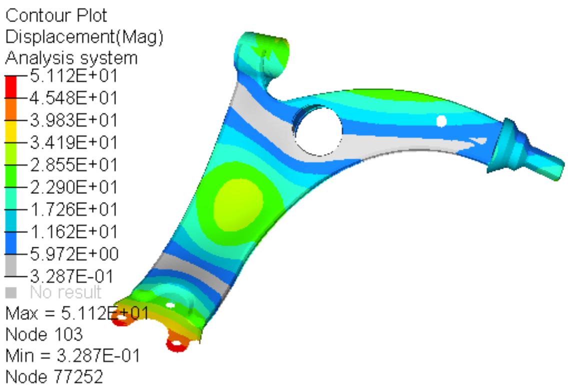

Figure 3. torsional modal shape of lower control arm

3. Modal test of lower control arm

In order to verify the accuracy of modal analysis of lower control arm, elastic rope is adopted to suspend the lower control arm on the platform, and free-modal tests are conducted on the basis of hammer method [11,12] and LMS Test.Lab platform, The experimental equipment includes LMSTest.Lab13.0 test software, LMS data collector, DELL laptop, 4 pcs of 356A16 modal vibration sensor from PCB company, ICP hammer, network cable and BNC cable, as shown in Fig. 4.

Since the lower control arm free-modal test needs to be placed in a free state, an elastic rubber cable is used to suspend the lower control arm in the test to make it in a balanced and free state. Six acceleration sensors are arranged on the arm, which should be placed as far as possible in obvious vibration. The channel of the hammer input is defined as the reference channel using the LMS Test.Lab test software. The direction of the excitation point should be consistent with the reference direction. Multi-point input free modal test method for multi-point output response of excitation. Try to keep the magnitude of the excitation force consistent during each excitation during the experiment. Each measurement point is unidirectionally excited five times. At the same time, the relationship between the excitation and response is checked to ensure that the coherence coefficient is close to 1. To ensure that the stimulus signal is valid. The excitation signal measured by the acceleration sensor is converted into a frequency response function by using LMS Test.Lab software. The resulting frequency response graph is shown in Figure 5.

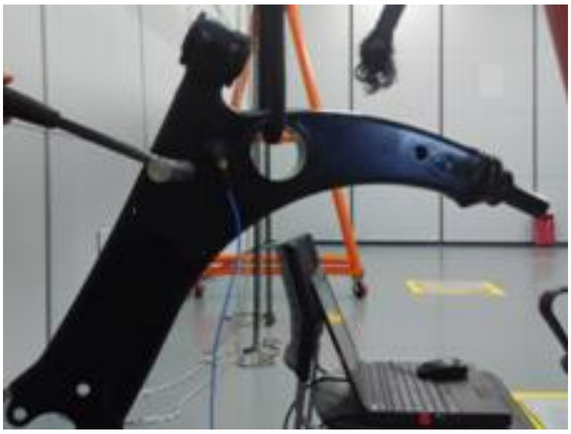

Figure 4. Modal test of lower control arm

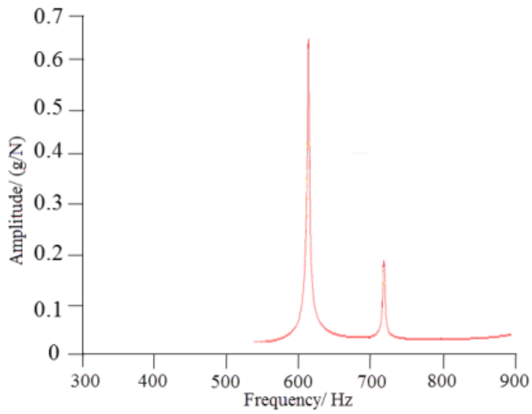

Figure 5. Frequency response graph

The modal shapes of the lower control arm obtained through experiments are shown in Figures 6 and 7. The modal shapes are consistent with those of the previous analysis.

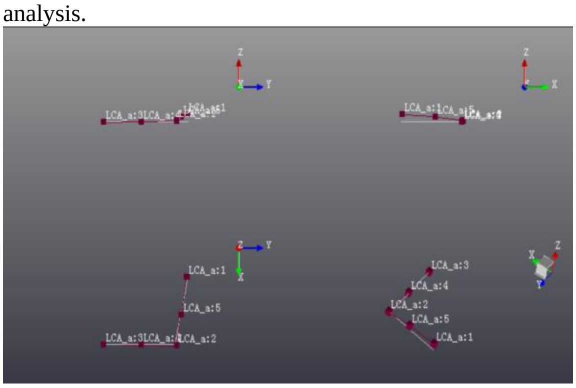

Figure 6. Bending modal shape of lower control arm

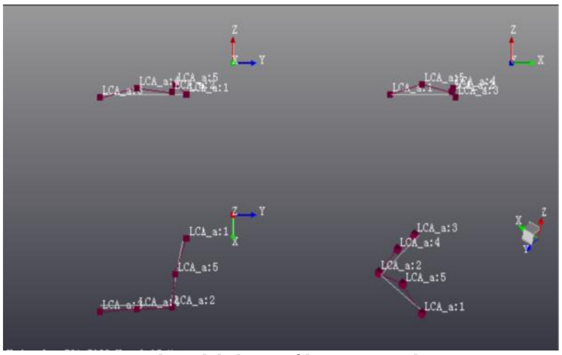

Figure 7. torsional modal shape of lower control arm

What is shown in Table 2 is comparison of analysis value and test value of lower control arm modal frequency. As shown in Table 1, the analysis value of the lower control arm's modal frequency is basically the same as the test value, and the relative errors of the first two orders are 1.5% and 3.3% respectively, which proves the accuracy of finite element modeling and analysis.

Table 2. lower control arm modal frequency comparison

	Test value/Hz	Analysis value/Hz	Relative error
First-order modal frequency	620.3	610.8	1.5%
Second-order modal frequency	717.2	693.5	3.3%

4. Static strength analysis of lower control arm

4.1. Force analysis of typical working conditions

The typical working conditions of vehicles in the process of driving are divided into brake vertical impact and turning. The stress states of tyre junction under each working condition are calculated according to vehicle parameters. The relevant vehicle parameters of this electric vehicle are shown in Table 3 with obvious changes compared with the raw fuel vehicle. The structural optimization of the front suspension lower control arm should be carried out according to the whole vehicle parameters of electric vehicle.

Table 3. Vehicle Parameters

Parameter	Value
Mass on front axle	850 kg
Mass on rear axle	950 kg
Height of center of gravity	0.65 m
Axle distance	2.6 m
Wheelbase	1.6 m

The braking conditions is taken as an example:

$$F_Z = \frac{1}{2} M_F \times g + \left(M_F + M_R\right) \times a \ \times \frac{H}{2L} \tag{1}$$

$$F_X = F_Z \times \mu \tag{2}$$

where: F_Z is the vertical load on the tire junction of this type of electric SUV; F_{X1} is the longitudinal load on the tire landing place of this type of electric SUV; M_F is mass on the front axle; M_R is mass on the rear axle; g is the acceleration of gravity; H is the center of gravity height of ; L is the wheelbase ; a_1 is the braking acceleration of type, which is 1.0 g; μ is ground adhesion coefficient, which is 1.0 [13-15]. The stress at the tire junction can be obtained by the above vehicle parameters and the corresponding calculation formula, and the stress state at the tire junction in other working conditions can be obtained by analogy.

4.2. Dynamic simulation analysis of front suspension

The front suspension model is established based on the coordinate information, vehicle parameters and performance curve of the connection points of the electric vehicle front suspension system by using Adams/Car Platform [16], which is as shown in Fig. 8. The force states of the tire ground points under the above operating conditions are input into its front suspension model, so that dynamic simulation analysis can be performed to extract the load at the front and rear points and the outside points of the lower control arm respectively under braking vertical impact and turning conditions.

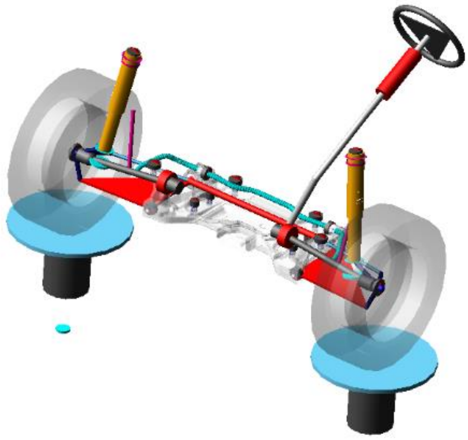

Figure 8. Adams/Car model of front suspension

4.3. Strength result analysis

Based on Nastran software and using the inertial release method [17] to load the loads extracted from the multi-body dynamics model, as shown in Table 4. The forces in the table are the forces that the connector reacts on the lower control arm. The inertia release method is based on loading inertial force to balance the external load, make it balance, and then solve the stress distribution. The force balance equation of the inertial release method can be expressed as:

$$\{F\}+M\{\ddot{\sigma}\}=0 \tag{3}$$

$\{F\}$ is the external load matrix of the finite element element node, $\{\ddot{\sigma}\}$ is the acceleration matrix of the finite element element node, and *M* is the mass matrix. By solving equation (3), the node acceleration and inertial force required to maintain balance at each node can be obtained, and then the inertial force of the node is loaded on the node as an external load, thereby constructing a self-balancing force system. Since the external load is balanced by the acceleration load of each node, the restraining force of the restraint point is zero, which can reduce the influence of restraint points on the stress results, improve the calculation accuracy, and obtain more reasonable stress results. If the inertial load is regarded as an external load, then the system will have the same external load and the inertial load under the constant acceleration state, that is, the static equilibrium state will be reached.

the ultimate strength analysis was performed without any constraints. The strength analysis of the electric vehicle lower control arm is carried out to obtain its stress distribution under various working conditions. The inertial release method refers to solving the acceleration required by each node in order to maintain balance, and then obtaining the inertial force of each node, and then loading the inertial force of the node as an external force on the node of the finite element, then a self-balanced force system can be constructed. That is, the inertia force of the structure is used to balance with the external force.

Table 4. Loads extracted from the multi-body dynamics model

	X (N)			Y (N)			Z (N)		
	braking	impact	turning	braking	impact	turning	braking	impact	turning
Outside point	9317	-1938	266	-1840	-5000	-1124	306	-109	-54
Front point	-7573	1653	-219	12888	2762	1442	169	46	93
Rear point	-1744	285	47	-11048	2238	-318	-465	63	-39

What is shown in Fig. 9, Von Mises Equivalent stress contour plot of lower control arm braking condition. According to Fig. 9, the maximum stress of lower control arm during braking is 301.2 MPa, which is located at the front bend of lower control arm. This is because the whole axle load of the vehicle transfers to the front-end during braking, resulting in relatively large longitudinal stress. What is shown in Fig. 10, is the Von Mises Equivalent stress contour plot of lower control arm under the vertical impact condition. According to Fig. 10, the maximum stress value of the lower control arm during vertical impact is 98.7 MPa, which is located near the connection between the outer point of the lower control arm and the steering knuckle. Because the phenomenon of stress concentration at the outer point of the vehicle due to the vertical impact force acting vertically downward. As shown in Fig. 11, is the Von Mises Equivalent stress contour plot under lower control arm's turning condition. It can be known from Fig. 11 that the maximum stress value of lower control arm during turning is 31.9 MPa. In practical engineering, the safety factor of the component is generally 1.2, and the yield strength of lower control arm material is 420 MPa. Allowable stress as the maximum stress value that the structure can withstand is equal to the yield strength of the material divided by the safety factor. that is the allowable stress is 350 MPa. Therefore, the maximum stress of the lower control arm under three typical working conditions is lower than its allowable stress, which conforms to the design requirements of ultimate strength characteristics.

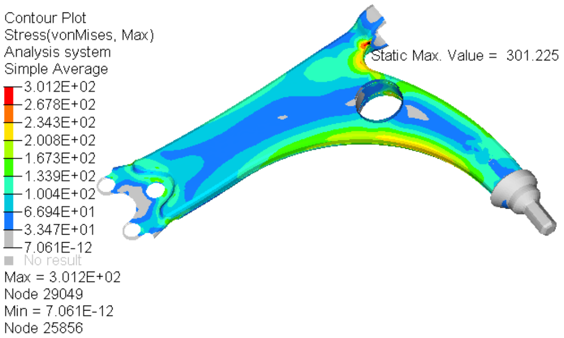

Figure 9. Von Mises Equivalent stress contour plot of lower control arm (braking condition)

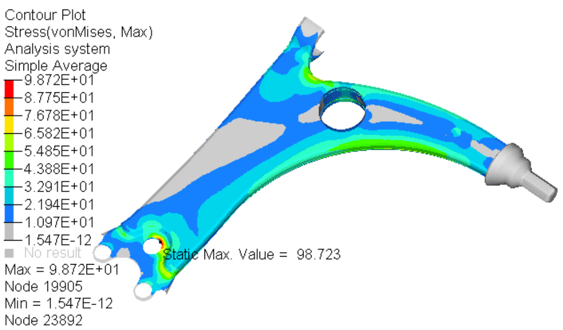

Figure 10. Von Mises Equivalent stress contour plot of lower control arm (vertical impact condition)

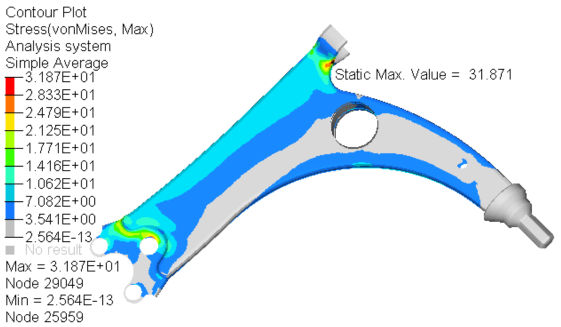

Figure 11. Von Mises Equivalent stress contour plot of lower control arm (turning condition)

5. Multi-disciplinary optimization analysis

5.1. Establishment of optimization model

In order to carry out lightweight design on the lower control arm and ensure its modal characteristics and strength performance, the thickness values of the upper and lower board and strengthened shaft tube of the lower control arm are taken as design variables, and the minimum mass of the lower control arm is taken as the target response function. Due to lower stress level of lower control arm in the vertical impact condition and turning condition, in order to improve optimization efficiency, that only the maximum stress under braking condition is lower than the allowable stress (350 MPa) and the first-order natural frequency is not lower than 95% (580.3 Hz) of the initial frequency is taken as constraint conditions to establish the optimization model.

Minimize Weight (a,b,c)

$$\text{Subject to} \quad \begin{cases} Weight < 4.2 \\ Stress < 350 \\ Modal > 580.3 \end{cases} \tag{3}$$

where: *Weight* is total mass of lower control arm; *Stress* is the maximum stress of lower control arm under braking condition; *Modal* is the first inherent frequency of lower control arm; *a* is the thickness of lower control arm upper plate; *b* is the thickness of lower control arm lower plate; *c* is the thickness of strengthen shaft tube of lower control arm:

5.2. Optimization results analysis

Its finite element model, modal analysis, and strength analysis are integrated based on the optimization mathematical model and the Isight platform [18], as shown in Fig. 12. The lower control arm finite element model source file are imported into the HyperMesh assembly, the upper plate thickness, the lower plate thickness and the reinforced shaft tube thickness are processed by the input parameters analysis (parametric processing), and set as the design variable; its static strength analysis source file and its result file are imported into the Strength component, and the maximum stress in braking conditions is processed by output parameter analysis; its modal analysis source file and its result file are imported into the Mode component to analyze the output parameters of its first-order frequency; the neighborhood cultivation genetic algorithm, regards each target as equally important. The method of adjacent breeding is achieved by sorting and grouping to cross, so that the probability of cross breeding of solutions close to the Pareto front is increased, and the calculation convergence process is accelerated. Improved efficiency is selected in the optimization component, and the target response function and design variable range are set to perform multidisciplinary optimization analysis of lower control arm. What is shown in Fig. 13 is the optimal iteration curve for the mass of lower control arm. After 99 iterations of Iisght platform, the optimal design variables of lower control arm are finally obtained. Table 5 shows the comparison of parameters before and after optimization. According to Table 4, after optimization, the upper board thickness of lower control arm is 3.6 mm, the lower board thickness of lower control arm is 3.2 mm, and the strengthened shaft tube thickness of lower control arm is 3.5 mm.

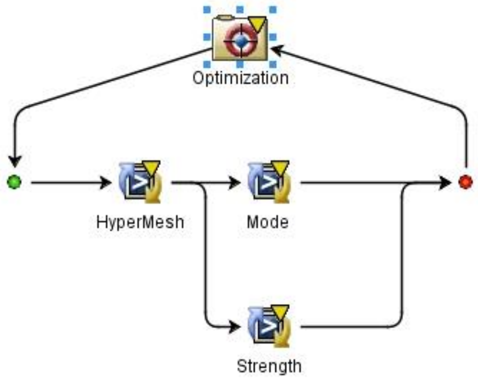

Figure 12. Isight platform

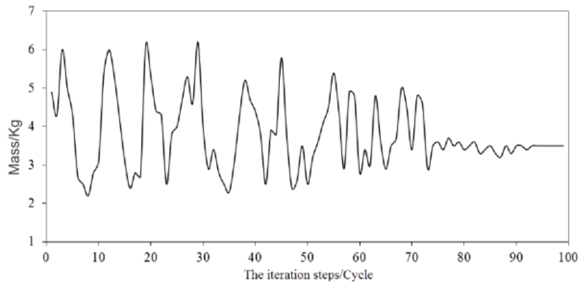

Figure 13. Mass optimization iteration curve of lower control arm

Table 5. Comparison of Parameters before and after Optimization

Parameters	Before optimization	After optimization
Upper plate thickness/mm	4.0	3.6
Lower plate thickness/mm	4.0	3.2
Reinforced shaft tube thickness/mm	4.5	3.5
Lower arm weight/*kg*	4.2	3.5
Maximum stress in braking conditions/MPa	301.2	346.4
Maximum stress in vertical impact conditions/MPa	98.7	163.2
Maximum stress in turning conditions /MPa	62.5	135.3
First-order frequency/Hz	610.8	585.7
Second-order frequency/Hz	693.5	661.2

Based on the optimal design variables, modal check analysis and strength check analysis are carried out on lower control arm. As shown in Table 3, the first two modal frequencies of lower control arm after optimization are 585.7 Hz and 661.2 Hz, both of which are higher than 95% of the initial frequency. Their modal performances are approximately the same, and all meet the requirements of modal characteristics. The reduction of the thickness of the lower control arm plate will lead to a reduction in its stiffness, but to a certain extent, it has a small impact on the dynamic performance of the suspension.

What is shown in Fig. 14 is the stress distribution cloud diagram which lower control arm's braking condition after optimization is used. As can be seen from Fig. 12, after optimization, the maximum stress of lower control arm in braking is 346.4 MPa and lower than its permitted stress, which meets the strength design requirements. As can be seen from Table 4, the maximum stress of lower control arm under vertical impact and turning conditions is 163.2 MPa and 135.3 MPa respectively, and its strength safety coefficient is 2.6 and 3.1 respectively, both are lower than its allowable stress. After optimization, the mass of lower control arm is reduced to 3.5 kg, and 16.7% of the mass is successfully reduced, with relatively obvious overall optimization effect.

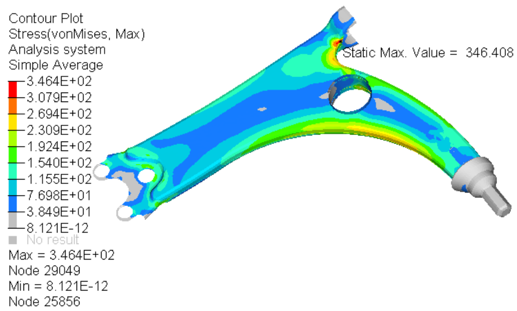

Figure 14. Von Mises Equivalent stress contour plot of lower control arm optimization scheme (braking condition)

6. Test and Analysis

In order to verify and check the feasibility and accuracy of the lower control arm optimization scheme, the bench test platform of lower control arm is built, as shown in Fig. 13. The lower control arm is under the most stress during braking conditions. In order to verify the strength performance of the arm optimization scheme, the front and rear points of the arm are fixed, and a longitudinal load of 9,500 N is applied to its outer point (based on the Adams model to extract the brake condition load), the schematic representation as shown in Fig. 14. After the test completed, the lower control arm does not crack and deform, so its strength analysis has high reliability.

And tested for durability is necessary, the outer point and the front point of lower control arm are fixed, longitudinal force of 3,000 N in a sinusoidal manner is applied on the latter point with a frequency of 1 Hz, the schematic representation as shown in Fig. 15. And no cracking is found after the test is conducted for 300,000 cycles. Referring to Figure 15, a similar approach is taken to fix the front and rear points of lower control arm, and longitudinal force of 15,000 N in a sinusoidal manner is applied on its external points with a frequency of 1 Hz, And no cracking is found after the test is conducted for 300,000 cycles.

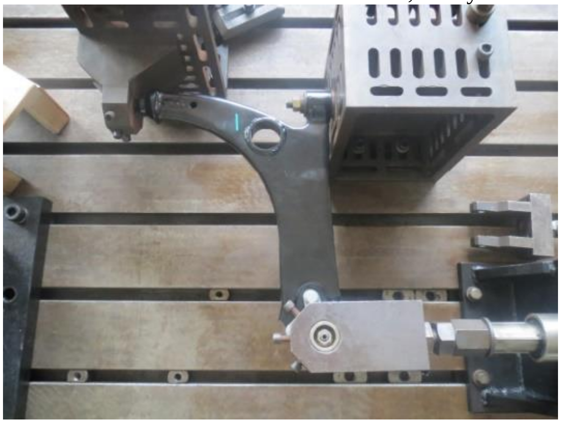

Figure 13. The bench test platform of lower control arm

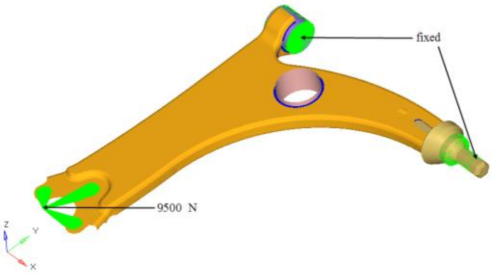

Figure 14. The schematic representation of Strength test

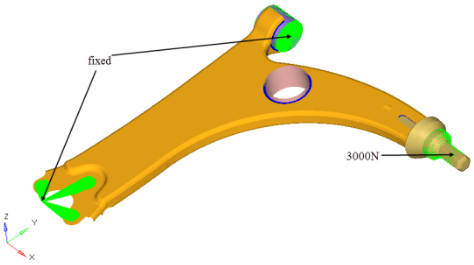

Figure 15. The schematic representation of Durability test

In order to further verify the reliability of lower control arm under the complete vehicle state, complete vehicle road reliability test is carried out according to design standards and specifications. The test roads are divided into expressway, twisted road, convex block road, long wave road, short wave road and washboard road. The test mileage is 50,000 km in total, and no abnormal vibration and cracking fault occur during the test. In conclusion, the entire finite element modeling, modal analysis, strength analysis and optimization design method have high accuracy and stability, which can provide reliable analysis methods and references for other similar structures.

7. Conclusion

1. The electric SUV lower control arm model is established by using finite element method on the Hypermesh software; the free modal analysis is carried out using Nastran software; the first and second order natural frequencies are 610.8 Hz and 693.5 Hz respectively. Free modal Test on lower control arm is conducted based on hammer method and LMS test. Lab platform, and the relative error between the Test value and the analysis value is within a reasonable range.
2. On the basis of the lower control arm load extracted from the dynamics model of front suspension Adams/Car, the intensity analysis of the typical operating conditions is carried out to obtain that the maximum stresses in acceleration, turning and vertical conditions are 301.2 MPa, 98.7 MPa and 62.5 MPa, which are all lower than its permitted stress.
3. The multi-discipline and multi-objective optimization design are carried out on structure parameters of lower control arm using Isight platform to obtain the optimal value of its structural parameters. Namely: the thickness of lower control arm upper board is 3.6 mm, the thickness of lower board thickness is 3.2 mm, and the thickness of reinforced shaft tube is 3.5 mm. After optimization, the first and second order modal frequencies of lower control arm are 585.7 Hz and 661.2 Hz respectively, which meets the requirements of modal characteristics; the maximum stress of lower control arm is 346.4 MPa, and its strength safety coefficient meets the actual engineering requirements; the mass of lower control arm is successfully reduced by 16.7%, with a significant lightweighting effect.
4. The optimization scheme of lower control arm is analyzed using bench test and vehicle road test, which has successfully passed the test verification, so it has high accuracy and feasibility.

References

[1] Fuchs, H.; Salmon, R. Lightweight MacPherson strut suspension front lower control arm design development. SAE 2011 World Congress and Exhibition 2011.

[2] Yoo, S.H.; Doh, J.; Lim, J.H., et al. Topologically optimized shape of CFRP front lower control ARM. International Journal of Automotive Technology 2017, 18(4), 625-630.

[3] Heo, S.J.; Kang, D.O., Lee, J.H., et al. Shape optimization of lower control arm considering multi-disciplinary constraint condition by using progress meta-model method. International Journal of Automotive Technology 2013, 14(3), 499-505.

[4] Huang, H. Lightweight optimal design and fatigue performance analysis of control arm under the suspension. Changchun, China: Jilin University, Master's thesis, 2016.

[5] Hou, K.; Sun, H.W. Static characteristics and modal analysis of carframe of a new semi-trailer. Mechanical Design and Manufacturing 2017, (8), 172-174.

[6] Xu, G.Q. Optimal design of dimensions of front spline shaft for automobile drive shaft based on Isight. Chinese Science and Technology Paper 2017, 12(4), 408-411.

[7] Soria, L.; Peeters, B.; Anthonis, J., et al. Operational modal analysis and the performance assessment of vehicle suspension systems. Shock and Vibration 2012, 19(5), 1099-1113.

[8] Kronast, M., Theory and application of modal analysis in vehicle noise and vibration refinement. Vehicle Noise and Vibration Refinement 2010, 117-141.

[9] Liu, J.B. NVH analysis and optimization research on body structure of a certain light truck based on FEA. Taiyuan, China: North University of China, Master's thesis, 2018.

[10] Yin, H.J.; Liu, Y.; Wang, Y., et al. Modal analysis of a certain metal fuel tank and improvement of its partition structure. Machine Design 2017, 34(11), 94-97.

[11] Huang, C.F.; Wang, P.; He, M.C., et al. Free vibration analysis of large composite truss structure section using hammer

method. Journal of National University of Defense Technology 2018, 40(1), 37-41.

[12] Bao, J.; Jing, J.P.; Zhou, H.W. Research on influence of bolt connection on combustion chamber structure mode of gas turbine. Noise and Vibration Control 2018, 38(5), 134-138.

[13] Afefy, I.H.; Mohib, A.; El-kamash, A.M., et al. A new framework of reliability centered maintenance. Jordan Journal of Mechanical and Industrial Engineering 2019, 13(3), 175-190.

[14] Gong, J. Acceleration sensor abnormality detection method for axle box of unmanned vehicle. Jordan Journal of Mechanical and Industrial Engineering 2020, 14(1), 149-158.

[15] Chen, M. Design and optimization of car sub-frame. Hefei, China: Hefei University of Technology, 2010.

[16] Zhou, J.C.; Yuan, J.; Liao, Y.H., et al. Optimization of Macphersan suspension based on D-optimal test design. Chinese Journal of Construction Machinery 2018, 16(5), 443-447.

[17] Zhang, Z.F.; Chen, R.; Xu, Z.M., et al. Research on topology optimization of multi-objective vehicle suspension control arm. Journal of Mechanical Engineering 2017, 53(4), 114-121.

[18] Li, M.; Liu, B.; Zhang, L. Optimization design of key structural parameters of high-speed train head type aerodynamic shape. Journal of Mechanical Engineering 2016, 52(20), 120-125.

JJMIE

Volume 15, Number 1, March. 2021
ISSN 1995-6665
Pages 15 - 21

Jordan Journal of Mechanical and Industrial Engineering

Accurate Modeling and Numerical Control Machining for Spiral Rotor of Double Rotor Flowmeter

Chunyan Tian, Hai Jiang*, Chaochao Chen

School of Advanced Manufacturing Engineering, Hefei University, Hefei 230601, China

Received July 18 2020 *Accepted Feb 20 2021*

Abstract

Aiming at the design and manufacturing problems of the spiral rotor of dual-rotor flowmeter, the profile characteristics and forming principles of the spiral rotor are analyzed, and the function equation of its cross-section profile curve is derived. Based on the analysis, a mathematical model for machining screw rotor with spherical milling cutter is established and the accurate three-dimensional modeling of spiral rotor parts is realized by using UG software. The simulation of the two rotors proves that the modeling method is reasonable and effective. Then using automatic programming and manual programming methods, a multi-axis NC machining program for the parts is written. The macro variable is introduced for the main program to call many times, which greatly simplifies the program structure, reduces the amount of program, and is easy to modify. The NC machining experiment of the spiral rotor with a standard ball-end milling cutter on a four-axis milling machining center is conducted. The results show that the screw rotor machined by the mathematical model has good quality. This programming and manufacturing method is very suitable for processing spiral rotors in multi-variety small batch production, and thus a high machining accuracy can be achieved.

Keywords: spiral rotor; functional equation; digital modeling; NC programming; multi-axis simultaneous machining;

1. Introduction

The dual-rotor flowmeter is an advanced volumetric flowmeter with the advantages of accurate measurement, no pulsation, low noise, and strong viscosity adaptability [1, 2]. The key functional part of the flowmeter is a pair of meshing spiral rotors. The spiral rotor is a special helical surface gear with a complex end profile, and its structural parameters directly affect the working performance of the flowmeter [3, 4]. Based on the gearing theory, many researches relate to the geometry design, machining methods and machining tools of a screw rotor have been presented in references [5-7]. Su et al. proposed the contact lines on rotor surfaces as design indices for rotor profile optimization [8]. Zhihuang Shen et al. put forward a digital graphic scanning (DGS) method based on computer graphics to generate the grinding profile of the rotor or the forming tool [9]. But these rotor profile design methods still have their technical limitations and the further research on geometric profile generation of the rotor should be carried out. Manufacturing of screw rotors is a complex process that can be achieved by using a special helical grinding machines and form tools [10-13]. Wu and Hsu proposed a general mathematical model to continuously machine screw rotors using worm-shaped tools [14]. However, such approaches are very expensive because the machine and the tools are designed specifically for the rotors. So, in general it is used for small varieties and large manufacturing batches.

* Corresponding author e-mail: 2814884634@qq.com.

Due to the reasons such as actual production conditions and manufacturing costs, forming tools are generally not used to process spiral rotors in multi-variety small batch production in China. Unlike the form cutter which is necessary to redesign and manufacture for new type parts, a standard ball-end milling cutter can manufacture different types of screw rotors. Therefor the standard ball-end milling cutter is a great substitute for CNC milling [15-17]. So, cooperating with the related companies, we carry out the research on the digital accurate modeling of spiral rotors and multi-axis NC machining programming methods.

2. Working principle and contour analysis of spiral rotor

The working principle of the dual-rotor flowmeter is shown in Figure 1. The two helical rotors mesh with each other without active or passive distinction, which have the same tooth shape parameters and structural dimensions as well as opposite rotation directions. Under the action of fluid pressure, they rotate smoothly and uniformly in the direction shown by the arrow, and the fluid flows from the space between the cogging and the housing to the right pipe at the same time. The fluid flow rate is proportional to the number of rotor revolutions. To make the two rotors rotate smoothly without interference, the working tooth surfaces of the two rotors should be a pair of conjugate surfaces which can meet the basic law of tooth profile meshing. In order to meet the sealing requirements between the two rotors of the volumetric flowmeter, the teeth of the two rotors should be meshed with no backlash and no root clearance [18-21].

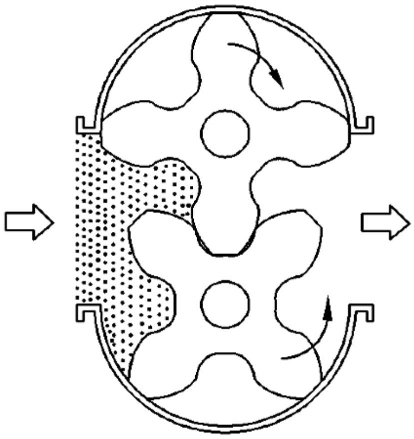

Figure 1. Working principle of the dual-rotor flowmeter

There are many tooth shapes that can meet the above requirements according to the principle of meshing. Considering such factors as ease of manufacture and maximum volume space of the flowmeter, a composite tooth profile composed of involute curve and transition curve is designed and analyzed. The cross-sectional shape of the tooth profile is composed of a tooth top arc, involute curve, transition curve, and tooth root arc, as shown in Fig. 2. So, the spiral rotor can be described as a helical gear with a large modulus and a small number of teeth. In order to meet the sealing requirements of the two rotors during meshing rotation, the double-sided tooth profile, tooth top circle and root circle of the rotor must participate in the meshing which is different from general helical gears. Due to the small number of teeth (e.g. only 4 teeth), the undercut phenomenon of the gear teeth will occur during the meshing transmission and the transition curve in the profile is formed. The spiral surface of the rotor is formed by the spiral movement of the end face tooth because of the plane meshing of the two rotors. Therefore, the core problem to be solved in the design and manufacture of the rotor is to accurately obtain the cross-sectional profile curve.

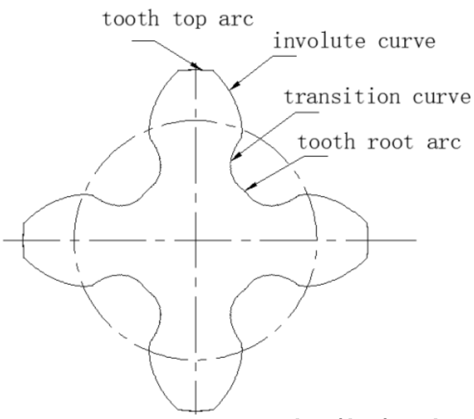

Figure 2. Cross-sectional profile of spiral rotor

3. Digital accurate modeling of spiral rotor

According to the above analysis of the spiral rotor contour, a function equation expression can be established for each curve segment to obtain the profile curve of the spiral rotor section. The rectangular coordinate parameter equation is used for UG software modeling.

3.1. Establishment of involute equation of sectional profile

In the spiral rotor cross-sectional profile, the section adjacent to the tooth top arc is an involute curve. As shown in Fig. 3, the involute is a locus EPS formed by any point P on a straight line CP when the straight line makes a pure rolling along a base circle O with a radius r_b.

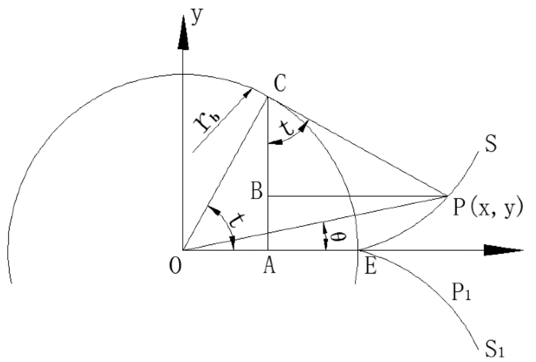

Figure 3. Establishment of involute equation of sectional profile

In the figure, θ is the spread angle of the involute and t is the angle between the occurrence line and the y-axis. When the involute starts from the base circle and the X-axis intersection E, the values of t and θ both increase from 0. It can be seen from the figure that the X coordinate of any point P on the involute EPS is as follows:

$$x = OA + BP = r_b \cos t + CP \sin t \tag{1}$$

Because the occurrence line cp makes a pure rolling along the basis circle o, the line CP is equal to the arc segment CE, that is:

$$CP = r_b \times t$$

Substituting the value of line CP into equation (1), the follow equation (2) can be obtained.

$$x = r_b \cos t + r_b t \sin t \tag{2}$$

Similarly, the y coordinate of any point P on the involute line is as follows:

$$y = AC - BC = r_b \sin t - CP \cos t = r_b \sin t - r_b t \cos t \tag{3}$$

Therefore, the rectangular coordinate parameter equation of the involute EPS is as follows:

$$\begin{cases} x = r_b(\cos t + t \sin t) \\ y = r_b(\sin t - t \cos t) \end{cases} \tag{4}$$

Correspondingly, the rectangular coordinate parameter equation of the involute EP_1S_1 in another direction symmetrical to the y-axis is:

$$\begin{cases} x = r_b(\cos t + t \sin t) \\ y = r_b(t \cos t - \sin t) \end{cases} \tag{5}$$

The parameter of the above curve function equation is t, $t \in [t_1, t_2]$.

3.2. Establishment of the cross-sectional profile transition curve equation

In the cross-sectional profile of the spiral rotor, the section adjacent to the tooth root circle is a transition curve, which is formed by undercutting of the gear teeth when the helical gear with a small number of teeth meshes. As shown in Figure 2 above, according to the principle of processing conjugate tooth profiles using Generating method, two pitch circles of equal diameter on the rotor are tangent and roll without sliding when the two rotors are engaged for transmission. It can be regarded that one rotor is fixed, and the pitch circle of the other rotor makes pure rolling along the pitch circle of the fixed rotor. Since both the rotor tooth top circle and the tooth root circle participate in meshing in this process, the trajectory generated by rolling the tooth tip edge point B of the rotor tooth is the transition curve formed by undercutting of the two rotors.

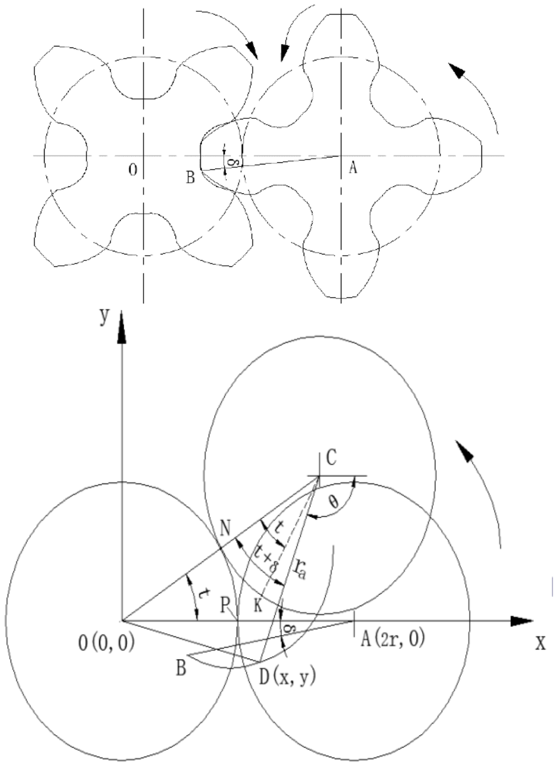

Figure 4. Establishment of the cross-sectional profile transition curve equation

The coordinate system is now established with the fixed rotor section center O as the origin, as shown in Fig. 4. The initial tangent point of the two rotor pitch circles on the rolling rotor is point P. Line AB is the connection between the center A of the rolling rotor and the edge point B of the tooth top, and line AO is the connection of the two-rotor center. The initial angle between line AB and line AO is δ which is half of the circumferential angle of the tooth top circle tooth thickness corresponding to the circumferential angle. When the rolling rotor pitch circle rotates through the angle t by pure rolling along the fixed rotor pitch circle, the original rolling rotor center point reaches point C, the original tangent point P reaches point K, the original tooth tip edge point B reaches point D, and the tangent point of the two rotor pitch circles becomes point N.

Because the two rotors have the same section shape, the base circle radius of both rotors can be set to r_b, the radius of the tip circle of both rotors is r_a, and the pitch radius of the two rotors is the average radius of the dividing circle r, therefor line AB and line CD are both equal to r_a. It can be seen from Figure 5 that arc segment NK is equal to arc segment NP, so angle NCK and angle NOP are both t. Correspondingly:

$$\theta = -(\pi - t - t - \delta) = -(\pi - (2t + \delta)) \tag{6}$$

Let the coordinates of the edge point D of the rolling rotor tooth tip be (x, y), and the geometric vector relationship in the figure is shown as follows:

$$\overrightarrow{OD} = \overrightarrow{OC} + \overrightarrow{CD} \tag{7}$$

$$\overrightarrow{OD} = \{x, y\} \tag{8}$$

$$\overrightarrow{OC} = \{2r\cos t, \quad 2r\sin t\} \tag{9}$$

$$\overrightarrow{CD} = \{r_a\cos\theta, \ r_a\sin\theta\} \tag{10}$$

Substituting equation (6) into equation (10), the equation (11) can be obtained:

$$\overrightarrow{CD} = \{-r_a\cos(2t+\delta), \ -r_a\sin(2t+\delta)\} \tag{11}$$

Substituting equations (8), (9) and (11) into equation (7), the follow equations can be obtained:

$$\{x, y\} = \{2r\cos t - r_a\cos(2t+\delta), \ 2r\sin t - r_a\sin(2t+\delta)\} \tag{12}$$

$$\begin{cases} x = 2r\cos t - r_a\cos(2t+\delta) \\ y = 2r\sin t - r_a\sin(2t+\delta) \end{cases} \tag{13}$$

$$t \in [t_1, t_2]$$

The equation (13) is the rectangular coordinate parameter equation of the spiral rotor section profile transition curve, and the parameter of the function equation is t.

In addition, during the pure rolling process of the two rotor pitch circles, the tooth top arc segment of the rolling rotor forms the tooth root arc segment of the other rotor, which is tangent to the transition curve segment. At this point, the form of each curve segment of the rotor section profile has been determined.

3.3. *Examples of spiral rotor modeling*

Given a pair of intermeshing spiral rotors, the known basic parameters are as follows:

Table 1. Basic parameters of spiral rotors

number of rotor teeth	end modulus	normal pressure angle (°)	center distance between two rotors	lead	Length of rotor
4	13.5	20	54	269	134.5

According to the above basic parameters, it is easy to obtain other parameters required for modeling and designing the spiral rotor, such as the indexing circle radius r, the base circle radius r_b, the tooth tip circle radius r_a, the tooth root circle radius r_f, the tooth tip circle tooth thickness S_a, and the tooth tip circle tooth thickness corresponding to the semicircle angle δ. Then, follow the basic steps to complete modeling by using UG software.

1. The parametric equation (5) of the rotor cross-section profile involute and the parametric equation (13) of transition curve are both input through the “Expression” function of UG software, and an appropriate parameter value range is selected. Then high-precision function equation curves are generated by using the “law Curve” function.

2. The corresponding tooth top circle, tooth root circle and necessary auxiliary lines are drawn; then a single tooth profile curve is obtained by trimming and rotating to a suitable position of the corresponding curve and arc segments etc.
3. And the complete rotor cross-section profile is obtained through the operations of arraying and trimming.
4. On this basis, a corresponding space spiral is constructed as a guide line, and a three-dimensional digital model of a complete spiral rotor is generated after the sweep operation, as shown in Fig. 5.

In the same way, another spiral rotor with opposite rotation can be modeled.

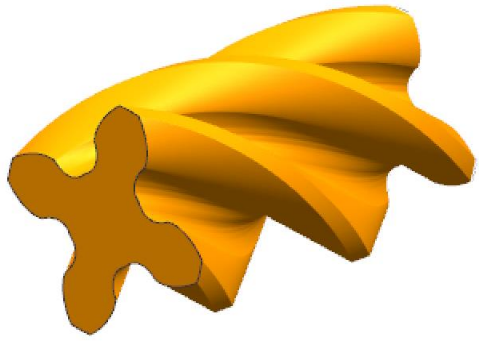

Figure 5. Three-dimensional digital model of spiral rotor

In order to verify the rationality of the above-mentioned modeling design method and results, the helical rotor digital model is simulated through UG software, as shown in Fig. 6. Using the interference analysis function of UG software, it can be confirmed firstly that there is no interference between the working tooth surfaces that mesh with each other during the movement of the dual rotors. Then the rotating effects of the dual rotors under the pressure difference are simulated. Simulation results show that the meshing operation of the two rotors can be performed tightly and smoothly without interference.

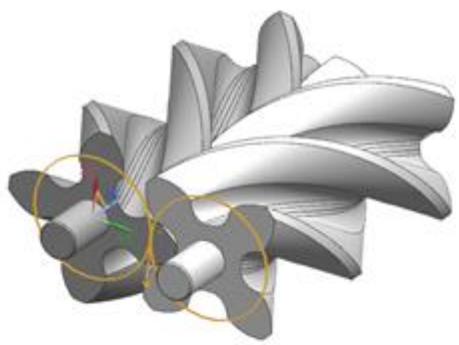

Figure 6. Meshing movement simulation of spiral rotor

4. CNC machining of spiral rotor part

4.1. CNC machining principle

The final finish machining of the spiral rotor is processed by using a standard ball-end milling cutter in a four-axis milling machining center according to its structural characteristics. Before finish machining, the blank of rotor has to go through the processes such as rough turning, finish turning and rough milling, so as to get the semi-finished product with finishing allowance which is approximately consistent with the final contour shape. Then the semi-finished product is processed by NC finish milling, and finally the four grooves at the end face of the rotor are milled to complete the part. The basic principle of NC finish milling of the semi-finished product is shown in Fig. 7, in which the rotary table on the machine tool drives the workpiece to rotate around the X axis to realize the A axis movement.

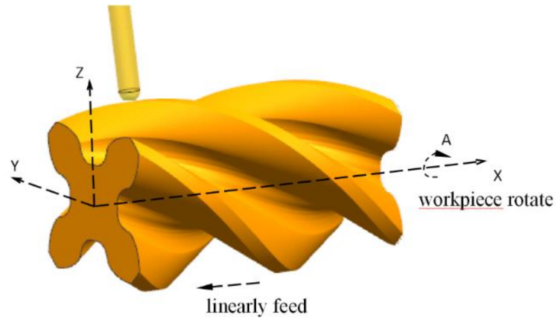

Figure 7. NC milling principle by using a standard ball-end milling cutter

During machining, the workpiece is linearly fed at a constant speed relative to the tool along the X axis, rotating at an average speed along the A axis, and the corresponding proportional relationship between the linear movement distance and the rotation angle is maintained. In this way, the tool will process a space spiral. Then the workpiece quickly reset, and the tool quickly moves to the starting point of the next spiral through linkage in the YOZ plane to processes the next spiral in turn until the milling of the entire spiral surface is completed. The milling technology parameters selected in NC finish milling are shown in Table 2:

Table 2. Milling machining technology parameters

Cutter Diameter (mm)	Cutter teeth	Feed rate (mm/min)	Spindle speed (rpm)	Maximum allowable roughness Ra (μm)
10	3	300	1200	3.2

4.2. Compiling of CNC machining programs

The essence of the NC program generated by computer-aided automatic programming is using a series of small straight-line segments to approximate the spatial profile along each processing path. And there is a certain difference from the formation mechanism of the rotor spiral surface which is not conducive to accuracy improvement. Therefore, manual programming combined with automatic programming is used to compile CNC programming. First, according to the previously generated digital model of the spiral rotor, tool point data of the tool at the starting spiral point when milling each spiral are calculated by using the CAM module of UG software. Then according to the above-mentioned principle of X and A axis linkage processing of spirals, manual programming is used to introduce macro variables. The tool point data at the starting cutting point of the spiral is used as values of macro variables to write the subroutine processing of the space spiral which can be called multiple times by the main program. This greatly simplifies the program structure, reduces the program volume, and is easily modified.

The planning of the machining path during programming can be based on the shape of the cogging and follows the principle of symmetry from the outside to the inside as much as possible. That is, the outermost profile spiral of the left and right sides of a cogging of the rotor is processed first separately, then the tool feeds a cutting row width along the Y and Z directions and processes the adjacent left and right profile spirals in sequence until a cogging cutting is completed. Then the same method is used to process the next cogging after rotating axis A for 90 degrees. On this basis, the corresponding CNC machining program is obtained. According to the program, the simulation operation is carried out by Yulong's multi-axis CNC machining simulation software. Then, the actual cutting experiment is carried out on the 4-axis machining center equipped with FANUC series 0i-MC CNC system. It takes about 180 minutes to complete the CNC finish milling of a rotor part. The accuracy and surface roughness of the finial part obtained can meet the requirements. The machined part is shown in Fig. 8. The machined cross-sectional profile of the rotor is consistent with the designed one, as shown in Fig. 9. Experiments show that the programming method is simple, efficient and effective.

Figure 8. Machined part

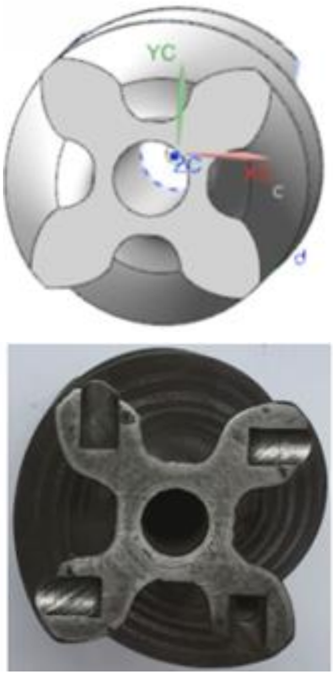

Figure 9. machined cross-sectional profile of the rotor in comparison with the designed one.

5. Conclusions

In this paper, the principle of forming the profile of the spiral rotor part is analyzed. The function equation of its cross-sectional profile curve is derived based on gear meshing theory and the three-dimensional accurate numerical model is constructed by using UG software. The automatic programming combined with the manual programming is used to write NC machining program for spiral rotors. A machining method with standard ball-end milling cuter is used in NC machining according to the characteristic of the helical surface, and the results show that the method fully meets the accuracy requirements of screw rotor. The simulation and actual numerical control machining experiments proves the correctness and efficiency of the mathematical model. The method provided in this paper can better solve the technical problems of processing the spiral rotor with standard tools under the existing production conditions, and has a certain application prospect.

Compared with the previous rotor profile design and machining methods, the method provided in this paper has the following advantages:

1. A three-dimensional accurate numerical model of new type rotor can be conveniently generated by changing the basic parameters of the rotor in the software using the parametric model constructed in this paper.
2. The macro variable is introduced for the main program to call many times, which greatly simplifies the program structure, reduces the amount of program, and is easy to modify.
3. The multi-variety small batch screw rotors can be manufactured with low cost by using standard milling cutters whose manufacturability and exchangeability are better.
4. According to the surface measurement results of the trial product, the machining technology parameters can be easily adjusted through the cutter length and radius compensation.

But the cutting efficiency of this method is lower than that of other methods such as grinding or machining with forming cutter, which is its technical limitation.

6. Acknowledgement

This work was financially supported by the natural science foundation project and quality engineering projects provided by Anhui provincial education department, and the project numbers are KJ2017A359, 2018sjjd030 and 2019hfjxtd08.

Appendix

The part code of NC machining program for spiral rotor parts is shown below:

```
O5002
G0G54Z100G90
X-5.Y0
M3S3500
G10L2P1X-396.Y-236.05Z-365.98
N1
G10L2P1A0
#101=24.633
#102=37.234
M98P502
#101=24.633
#102=36.634
M98P502
#101=24.633
#102=36.034
M98P502
#101=24.633
#102=34.943
M98P502
#101=23.650
#102=34.906
M98P502
#101=23.022
#102=34.869
M98P502
………
………
```

References

[1] Gu KJ. Application test of dual-rotor flowmeter in the measurement of crude oil transportation. Petrochemical Automation, 2008, 2: 59-61.

[2] Gao S, Wang L, Feng W, Chen YG, Xu L, Gong HW, Yang YW. Application analysis and discussion of double spiral flowmeter in crude oil measurement. Petroleum and Petrochemical Energy Saving, 2016, 6(07): 38-39.

[3] Yu G, Li F, Yu YM, Zai SX. Active profiling and polishing model and validation based on rotor spiral groove. Chinese Journal of Mechanical Engineering, 2018, 31(28): 1-10.

[4] Hayamizu Y, Yamamoto K, Yanase S, Hyakutake T, Morita S, Ohtsuka S. Experimental study of the viscous pump with a helical channel rotor: Torsion effect of the channel. Journal of Thermal Science, 2010, 19(2): 154−159.

[5] Stosic N. A geometric approach to calculating tool wear in screw rotor machining. International Journal of Machine Tools & Manufacture, 2006, 46: 1961–1965.

[6] Zheng F, Hua L, Han X, Li B, Chen D. Linkage model and manufacturing process of shaping non-circular gears. Mechanism & Machine Theory, 2016, 96: 192–212.

[7] Wang J, Cui F, Wei SH, Sha RD, Liu HJ. Study on a novel screw rotor with variable cross- section profiles for twin-screw vacuum pumps. Vacuum, 2017, 145: 299–307.

[8] Su SH, Tseng CH. Synthesis and optimization for rotor profiles in twin rotor screw compressors. Journal of Mechanical Design, 2000, 122(4): 543–552.

[9] Shen ZH, Yao B, Teng WB, Feng W, Sun WF. Generating Grinding Profile between Screw Rotor and Forming Tool by Digital Graphic Scanning (DGS) Method. International Journal of Precision Engineering and Manufacturing, 2016, 17(1): 35-41.

[10] Zhang ZX, Fong ZH. A novel tilt form grinding method for the rotor of dry vacuum pump. Mechanism and Machine Theory, 2015, 90: 47–58.

[11] Wang A, Liang J, Liu Y. Application of improved particle swarm optimization in gear fault diagnosis of automobile transmission. Jordan Journal of Mechanical and Industrial Engineering, 2020, 14(1): 175-182.

[12] Shakoor M, Qureshi MR, Jaber S. Applying management principles of lean manufacturing for enhancing efficiency and effectiveness of emergency department rooms. Jordan Journal of Mechanical and Industrial Engineering, 2019, 13(4): 291-299.

[13] Wei J, Zhang GH. A precision grinding method for screw rotors using CBN grinding wheel. The International Journal of Advanced Manufacturing Technology, 2010, 48: 495–503.

[14] Wu YR, Hsu WH. A general mathematical model for continuous generating machining of screw rotors with worm-shaped tools. Applied Mathematical Modelling, 2014, 38: 28–37.

[15] Stosic N, Smith IK, Kovacevic A, Mujic E. Geometry of screw compressor rotors and their tools. Applied Physics & Engineering, 2011, 12(4): 310-326.

[16] Stosic N. A geometric approach to calculating tool wear in screw rotor machining. International Journal of Machine Tools & Manufacture, 2006, 46: 1961–1965.

[17] Wei J, Zhang GH. A precision grinding method for screw rotors using CBN grinding wheel. The International Journal of Advanced Manufacturing Technology, 2010, 48: 495–503.

[18] He X, Pan C, Wu M, Ji X, Zhang R. A twin-screw rotor profile design and computational fluid dynamic simulation method. Materials Research Innovations, 2015, 19(8): 721-726.

[19] Liu ZM, Tang Q, Liu N, Song J. A profile error compensation method in precision grinding of screw rotors. The International Journal of Advanced Manufacturing Technology, 2019, 100: 2557-2567.

[20] Ilie K, Subic A. Parametric modelling of helical rotors for efficient design of twin-screw superchargers. Mechanical Engineering Science, 2007, 221: 267-272.

[21] Yu DY, Ding Z. Geometric characteristics analysis and parametric modeling for screw rotor precision machining. The International Journal of Advanced Manufacturing Technology, 2020, 107: 3615–3623.

JJMIE

Volume 15, Number 1, March. 2021
ISSN 1995-6665
Pages 23 - 27

Jordan Journal of Mechanical and Industrial Engineering

Simulation Analysis of the Effects of EGR Rate on HCCI Combustion of Free-piston Diesel Engine Generator

Chunhui Liu*, Kechuan Yi

College of Mechanical Engineering, Anhui Science and Technology University, Fengyang, Anhui 233100, China

Received July 18 2020 *Accepted Feb 20 2021*

Abstract

The effects of exhaust gas recirculation (EGR) rate on homogeneous charge compression ignition (HCCI) combustion and emission of free-piston diesel engine generator (FPDEG) was investigated by using a three-dimensional (3-D) computational fluid dynamics (CFD) model of FPDEG. In the 3-D CFD model of FPDEG, the diesel mechanism with 109 species and 543 reactions was incorporated into the combustion model, and the soot and NOx production were calculated by Hiroyasu-NSC model and 12 steps NOx model. The simulation results showed that the EGR rate had great influence on the HCCI combustion and emission performance of FPDEG. As the EGR rate was changed from 0 to 10%, the HCCI combustion phase of FPDEG slightly lagged, the peak value of heat release, the maximum in-cylinder temperature and pressure and the NOx content significantly decreased, but SOOT content increased. When the EGR rate was 20%, the HCCI combustion of FPDEG was incomplete, and the UCH, SOOT and CO content all obviously increased.

Keywords: Free-piston diesel engine generator, Homogeneous charge compression ignition, diesel mechanism, exhaust gas recirculation;

1. Introduction

The innovation of energy utilization technology has become an urgent issue due to the growing fossil fuel consumption and environmental pollution. Homogenous charge compression ignition (HCCI) combustion, one of new combustion modes, has been widely investigated owing to its high efficiencies and low emissions [1].

Onishi et al. first introduced HCCI in the experiments of two-stroke gasoline engines [2]. Najt et al. extended HCCI to four-stroke gasoline engines and found that HCCI mainly controlled by chemical kinetics [3]. Ryan et al. conducted the early HCCI combustion research work of diesel fuel and discovered that the operation of diesel HCCI engine mainly relied on EGR rate, compression ratio and air-fuel ratio [4]. Christensen et al. also carried out the research of diesel fuel HCCI combustion and obtained the acceptable ranges of compression ratios and mixture intake temperature [5].

In the recent decades, in addition to conventional internal combustion engines, HCCI is also operated on the free-piston engine generator (FPEG). FPEG has simple structures and high conversion efficiency and can give full play to the advantages of HCCI combustion [6, 7]. Bergman and Fredriksson integrated one-dimensional gas dynamics, SENKIN chemical kinetics, and KIVA-3V CFD simulation platform to compare the HCCI combustion of FPEC and combustion of conventional diesel engines and found the optimal working conditions [8]. Chiang et al. [9] presented the simulation research of a spark ignition (SI)/HCCI FPEG with electric mechanical valves.

Exhaust gas recirculation (EGR) is one of the most effective means to control the ignition time and combustion progress of HCCI. Tsolakis et al. [10] conducted the experiments of EGR system in a diesel engine, and found that EGR can effectively reduce smoke and NOx emissions. Jamal et al. came to the same conclusion as Tsolakis [11]. Yap et al. [12] found that EGR can affect the HCCI combustion characteristics of fuel and then control the ignition time.

It is necessary to choose the precise chemical reactions to study the HCCI combustion of diesel fuel. Nowadays, there exists a lot of chemical models of diesel surrogates. Previously, n-heptane, a single-component surrogate, has been proposed to represent diesel fuel [13]. However, the drawbacks of single-component surrogate are obvious. Currently, multi-component surrogate models, including the aromatic components, have been proposed for diesel fuel [14].

In this paper, the 3-D CFD FPDEG model coupling the 109 species detailed diesel mechanism was created to investigate the effects of EGR rate on HCCI combustion and emission performance.

2. 3D CFD modeling and verification

The key to modeling is to obtain the piston motion law of FPDEG. The method of zero-dimensional models to calculate the piston motion law of FPEG can be found in literature [15].

* Corresponding author e-mail: lch994211@163.com.

The main simulation parameters of CFD model are as follows: the bore is 60 mm, the maximum effective stroke is 61.5 mm, the maximum total stroke is 98 mm and the moving mass of the piston assembly is 6 kg. **Figure 1** displays the moving mesh model of FPDEG combustion chamber. The number range of the structural cartesian grid of the moving mesh model was 14620-1340888. The boundary condition of temperature defined of cylinder wall, cylinder head and position was 450 K, 500 K and 550 K separately.

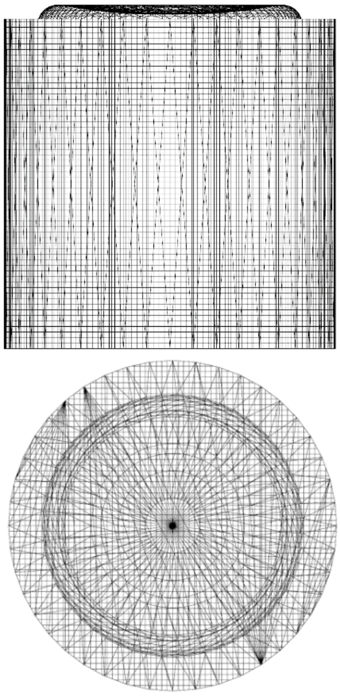

Figure 1. The moving mesh model of FPDEG combustion chamber

The 109 species and 543 elementary reactions mechanism of diesel developed by Wang was adopted in the combustion model of FPDEG [14]. The soot and NOx formation were calculated using the Hiroyasu-NSC model and the 12 steps NOx model separately.

The main parts of FPDEG experiment prototype include: two opposed-piston two-stroke FPEGs, high-pressure common rail system of diesel fuel, exhaust system, linear motor, motor control system, load system and test system. The experiment results of FPDEG experiment prototype can be found in literature [15-17]. **Figure 2** showed the calculation and experiment results of the in-cylinder pressure of the FPDEG. It was seen that the calculation results from the 3-D CFD FPDEG model were close to the experiment results, which proved the validity of the 3-D CFD FPDEG model.

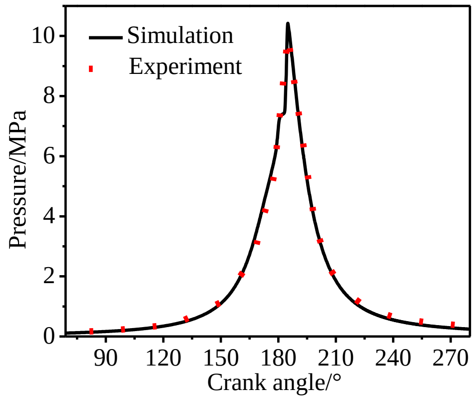

Figure 2. The calculation and experiment results of in-cylinder pressure

3. The effects of EGR rate on the combustion and emissions of FPDEG

Figure 3 and **Figure 4** showed the effects of EGR rate on the combustion and emissions of the FPDEG with the initial intake temperature of 345 K, equivalence ratio of 0.335, initial in-cylinder pressure of 0.114 MPa, and compression ratio of 20.2, separately. From the Figure 3, we can see that as the EGR rate increased (from 0 to 10%), the combustion phase lagged (the crank angle position of the first peak value was from 177° to 178°), peak value of heat release (from 312 J/° to 124 J/°), maximum in-cylinder temperature (from 2006 K to 1863 K) and in-cylinder pressure (from 13.8 MPa to 12.4 MPa) significantly decreased, and as the EGR rate was 20%, the HCCI combustion of FPDEG is an incomplete combustion, which was due to the increase of exhaust gas in the mixture. From the Figure 4, we can see that while the EGR rate increased (from 0 to 10%), the NOx content significantly decreased (from 1.08 g/kg fuel to 0.1 g/kg fuel), but SOOT content increased (from 0.004 g/kg fuel to 0.03 g/kg fuel), and as the EGR rate was 20%, due to the incomplete HCCI combustion, the UCH, CO and SOOT content were all high.

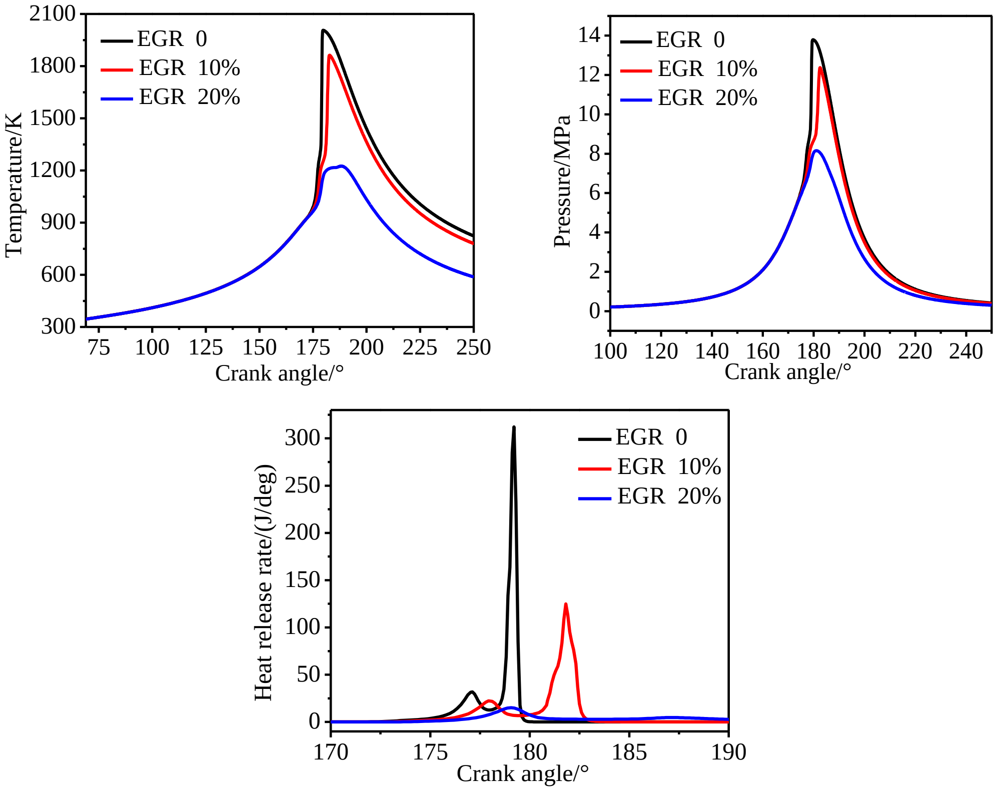

Figure 3. The effect of EGR rate on combustion

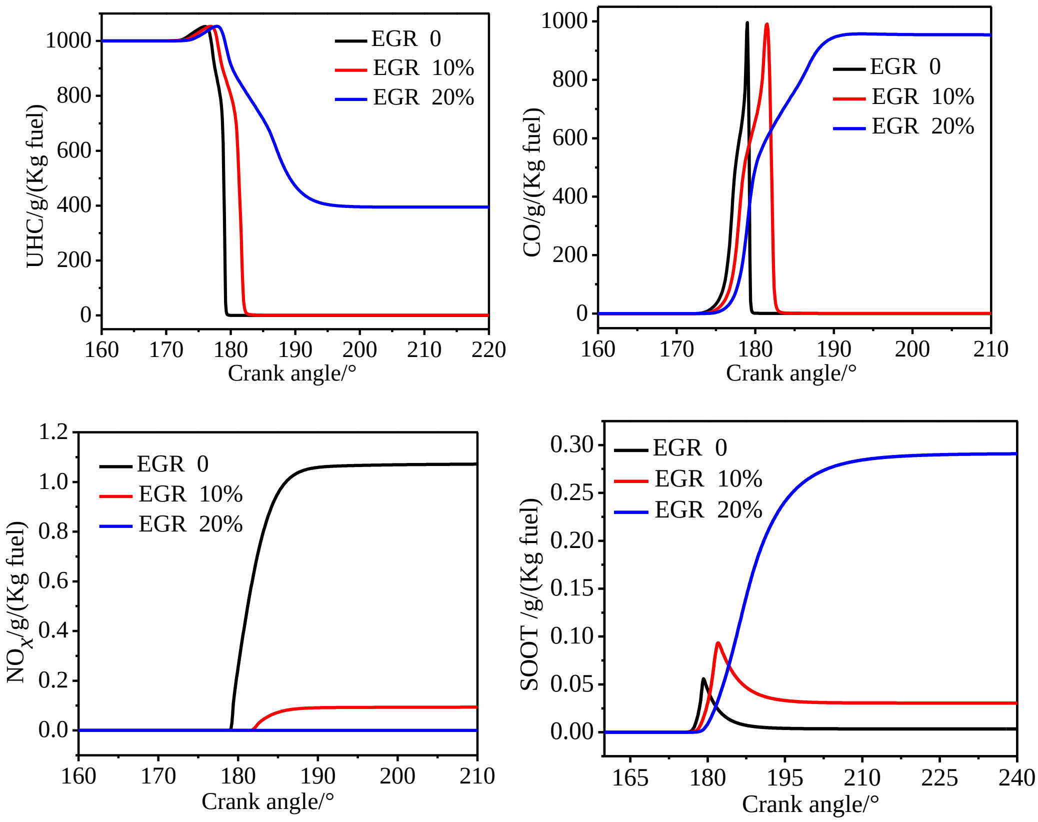

Figure 4. The effect of EGR rate on emissions

4. The effects of EGR rate on temperature and species concentration field distribution

Table 1-Table 4 demonstrated the calculated concentration field distribution in the cylinder of C7H8, C7H16, NO and CO respectively. **Table 5** showed the temperature field distribution in the cylinder. The CA10, the 10% cumulative heat release crank angle position, indicates the beginning of combustion. The CA50, the 50% cumulative heat release crank angle position, indicates the combustion phase. The CA90, the 90% cumulative heat release crank angle position, indicates the end of combustion.

Table 1. C7H8 concentration field distribution in the cylinder of FPDEG

EGR rate	CA10	CA50	CA90
0	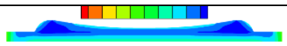	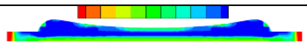	
10%	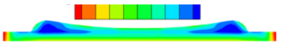	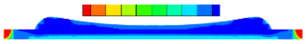	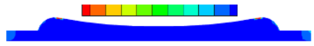
20%	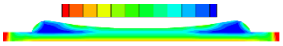	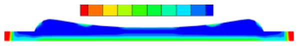	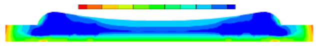

Table 2. C7H16 concentration field distribution in the cylinder of FPDEG

EGR rate	CA10	CA50	CA90
0	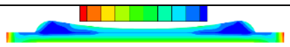		
10%	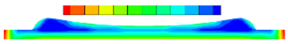	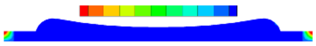	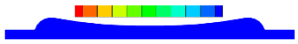
20%	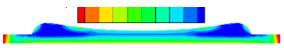	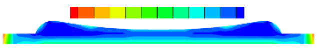	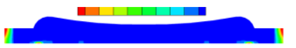

Table 3. CO concentration field distribution in the cylinder of FPDEG

EGR rate	CA10	CA50	CA90
0	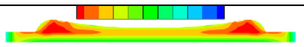	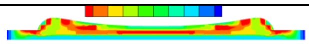	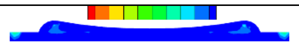
10%	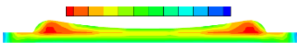	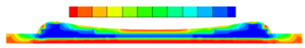	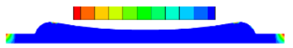
20%	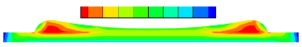	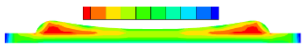	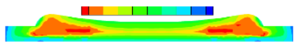

Table 4. NO concentration field distribution in the cylinder of FPDEG

EGR rate	CA10	CA50	CA90
0	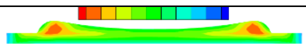	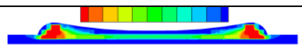	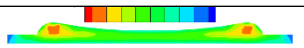
10%	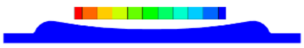	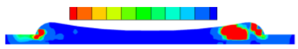	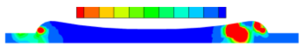
20%	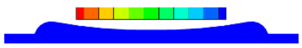		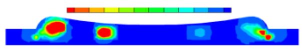

Table 5. The temperature field distribution in the cylinder of FPDEG

EGR rate	CA10	CA50	CA90
0	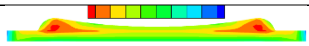	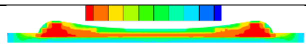	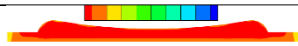
10%	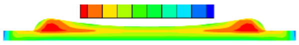	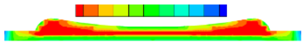	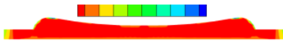
20%	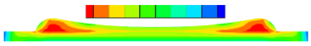	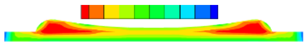	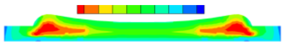

From **Table 1** to **Table 5**, we can see that, with the EGR rate of 0 and 10%, at the process of HCCI combustion, the temperature of the piston bowl was the maximum (about 1070 K), where the fuel (C7H8 and NC7H16) was first oxidized, while NO and CO were first produced; At the end of the HCCI combustion, the temperature, NO and CO concentration distribution were relatively uniform, and the fuel was completely consumed. However, with the EGR rate of 20%, the fuel (C7H8 and NC7H16) was not completely consumed, the temperature and CO concentration nearby piston bowl were the highest, and NO basically did not produce.

5. Conclusions

The simulation results of the 3-D CFD FPDEG showed that as the EGR rate increased (from 0 to 10%), the HCCI combustion phase of FPDEG slightly lagged, the peak value of heat release**,** the maximum in-cylinder temperature and pressure and the NOx content significantly decreased, but SOOT content increased. However, when the EGR rate was 20%, the HCCI combustion of FPDEG will be an incomplete combustion, and the UCH, SOOT and CO content all obviously increased. In addition, for the EGR rate of 0 and 10%, the temperature of the piston bowl was the maximum, where the fuel (C7H8 and NC7H16) was first oxidized, while the pollutants of NO and CO were first produced; at the end of the HCCI combustion, i.e. the CA90, the temperature (about 2000 K and 1850 K), NO and CO concentration distribution in the cylinder were relatively uniform, and the fuel (C7H8 and NC7H16) in the cylinder was completely consumed.

Acknowledgements

This work was supported by the Talent introduction Project of Anhui Science and Technology University (RCYJ201902) and the Key Excellent Young Teachers Program of Universities of Anhui Province (gxyqZD2019059).

References

[1] R.H. Thring, "Homogeneous-Charge Compression Ignition (HCCI) Engines", SAE Paper 892068, 1989.

[2] S. Onishi, S.H. Jo, K. Shoda, P.D. Jo, S. Kato, "Active Thermo-Atmosphere Combustion: A New Combustion Progress for Internal Combustion Engines", SAE Paper 790501, 1979.

[3] P.M. Najt, D.E. Foster, "Compression Ignited Homogeneous Charge Combustion", SAE Paper 830264, 1983.

[4] T.W. Ryan, T.J. Callahan, "Homogeneous Charge Compression Ignition of Diesel Fuel", SAE Paper 961160, 1996.

[5] M. Christensen, A. Hultqvist, B. Johansson, "Demonstrating the Multi-Fuel Capacity of a Homogeneous Charge Compression Ignition Engine with Variable Compression Ratio", SAE Paper, 1999-01-3679, 1999.

[6] Z.W. Zhang, H.H. Feng, Z.X. Zuo, "Numerical investigation of a free-piston hydrogen-gasoline engine linear generator", Energies, Vol. 13, No. 18, 2020, 4685, DOI: 10.3390/en13184685.

[7] C.Q. Li, Y.D. Wang, B.R. Jia, A.P. Roskilly, "Application of Miller cycle with turbocharger and ethanol to reduce NOx and particulates emissions from diesel engine - A numerical approach with model validations", Applied Thermal Engineering, Vol. 150, 2019, 904–911.

[8] M. Bergman, J. Fredriksson, V.I. Golovitchev, "CFD-based optimization of diesel-fueled free piston engine prototype for conventional and HCCI combustion", SAE Paper, 2008-01-2423, 2008.

[9] C.J. Chiang, J.L. Yang, S.Y. Lan, T.W. Shei, W.S. Chiang, B.L. Chen, "Dynamic modeling of a SI/HCCI free-piston engine generator with electric mechanical valves", Applied Energy, Vol. 102, 2013, 336-346.

[10] Tsolakis, A. Megaritis, M.L. Wyszynski, "Low temperature exhaust gas fuel reforming of hydrogen combustion engines", Fuel, Vol. 83, No. 13, 2004, 1837-1845.

[11] Y. Jamal, T. Wagner, M.L. Wyszynski, "Exhaust gas reforming of gasoline at moderate temperatures", International Journal of Hydrogen Energy, Vol. 21, No. 6, 507-519.

[12] D. Yap, S.M. Peucheret, A. Megaritis, M.L. Wyszynski, H.M. Xu, "Natural gas HCCI engine operation with exhaust gas fuel reforming", International Journal of Hydrogen Energy, Vol. 31, No. 5, 587-95, 2006.

[13] H.J. Curran, P. Gaffuri, W.J. Pitz, et al. "A comprehensive modeling study of n-heptane oxidation", Combustion and Flame, Vol. 114, No. 1-2, 1998, 149-177.

[14] H. Wang, M. Yao, Z. Yue, et al. "A reduced toluene reference fuel chemical kinetic mechanism for combustion and polycyclic-aromatic hydrocarbon predictions", Combustion and Flame, Vol. 162, No. 6, 2015, 2390-2404.

[15] Q. Zhang, Y. Wang, W. Lin, et al. "Contact mechanics analysis and optimization of shape modification of electric vehicle gearbox", Jordan Journal of Mechanical and Industrial Engineering, Vol. 14, No. 1, 2020, 15-24.

[16] H. Feng, C. Guo, C. Yuan, Y. Guo, Z. Zuo, A.P. Roskilly, B. Jia, "Research on combustion process of a free piston diesel linear generator", Applied Energy, Vol. 161, 2016, 395-403.

[17] M.B. Shongwe, O.O. Ajibola, M.E. Masonyaneng, et al. "Characterization and heat diffusion characteristics of spark plasma sintered Ni-50%Fe sintered alloy", Jordan Journal of Mechanical and Industrial Engineering, Vol. 13, No. 1, 2019, 61-67.

JJMIE

Volume 15, Number 1, March. 2021
ISSN 1995-6665
Pages 29 - 38

Jordan Journal of Mechanical and Industrial Engineering

Space Trajectory Planning of Electric Robot Based on Unscented Kalman Filter

Chang Kuang*, Xiaoyi Zheng

Department of Automation Engineering, Guangdong Polytechnic of Water Resources and Electric Engineering, Guangzhou 510635, China

Received July 18 2020 *Accepted Feb 20 2021*

Abstract

Because the motion state of electric robot cannot be determined, the result of planning has the phenomenon of moving collision in many environments. Therefore, a space trajectory planning method of electric robot based on Unscented Kalman filter is proposed. Through the working environment of electric robot, the kinematics and dynamics of electric robot are analyzed from the aspects of position, attitude and pose. According to the analysis results, the space trajectory constraint of electric robot is set, and the real-time motion state of electric robot is detected by using Unscented Kalman filter technology. The space trajectory planning of electric robot is completed by smoothing the space trajectory Stroke. The experimental results show that the collision times of the robot are reduced in both fault free and multi fault environments, which improves the accuracy of space trajectory planning and shortens the moving time of the robot.

Keywords: Kalman filter; Electric robot; Space track; Mobile trajectory planning;

1. Introduction

Robot is a kind of machine which can automatically perform work, including all the machines that simulate human behavior or thoughts and other creatures. In modern industry, robot is a kind of man-made machine that can automatically run tasks, which is used to replace or assist human work. Generally, it is an electromechanical device controlled by computer programs or electronic circuits. Based on the application environment, Chinese roboticists divide robots into two categories: industrial robots and special robots. The so-called industrial robot is a multi-joint manipulator or multi degree of freedom robot facing the industrial field. In addition to industrial robots, special robots are all kinds of advanced robots that are used in non-manufacturing industries and serve human beings [1]. International roboticists divide robots into two categories based on application environment: industrial robots in manufacturing environment and service and humanoid robots in non-manufacturing environment, which is consistent with China's classification. Electric robot is a kind of industrial robot, which is mainly responsible for the inspection of power equipment in substations or other power systems. The working process of the robot is to perform specific motion to meet the specific work needs, and trajectory planning is an important part of the robot's work, which is based on the task needs and the robot's own motion ability. The path planning method can be divided into two aspects: for the mobile robot, the path planning which means to move is preferred, for example, what kind of path the mobile robot will follow when the robot has a map or does not have a map; for the industrial robot, it means two directions, the curve path of the end of the mechanical arm, or the position of the operating arm in the movement process; the curve outline of displacement, velocity and acceleration. For the same task, its motion track may not be unique, different tracks have different operation indexes, such as running time, running energy consumption, running stability [2]. Based on realizing the requirements of motion function, trajectory planning can optimize these indexes to obtain a motion scheme with shorter time, lower energy consumption and less impact.

Researchers at home and abroad have done a lot of research work on the path planning methods of robots. The related researchers abroad have proposed the random landmark method and the flexible polyhedron search algorithm, which are very effective in solving the path planning problems of multi DOF robots. Chinese scholars have also proposed a sub group optimization algorithm, which regards a single robot as a particle to achieve optimal search. This method is used for multi robot collaborative path planning [3]. However, the obstacle avoidance problem of robot movement is not considered in the existing robot space trajectory planning methods, so the robot will encounter collision phenomenon when it moves according to the planned path, and the number of collisions is more, which will not only affect the working efficiency and results of the electric robot, but also shorten the service life of the electric robot.

After a long time of research and analysis, it is found that the problem of high collision rate in the traditional space trajectory planning of electric robot is mainly due to the fact that the real-time motion state of the robot is not considered in the planning process, so the Unscented Kalman filter technology is applied to the space trajectory planning of the

* Corresponding author e-mail: mynameiskc11@163.com.

robot, and the optimal trajectory planning method is obtained. Kalman filter is an algorithm that uses the linear system state equation to estimate the system state optimally through the system input and output observation data. Since the observation data includes the influence of noise and interference in the system, the optimal estimation can also be regarded as the filtering process [4]. The unscented Kalman filter is different from the extended Kalman filter, as it is an approximation of the probability density distribution. Because the higher-order terms are not ignored, the accuracy is higher when solving the nonlinearity. The core idea of Unscented Kalman filter Transformation: approximate a probability distribution ratio to approximate any nonlinear function or nonlinear transformation. Through the reference of Unscented Kalman filter technology, the collision free path planning in three-dimensional space is completed to ensure that the robot can better complete the work of the power operation production line.

2. Space trajectory planning of electric robot based on Unscented Kalman filter

The purpose of spatial trajectory planning of electric robot is to realize the non-collision inspection of electric robot. Therefore, in this spatial trajectory planning, it is necessary to optimize the trajectory from two aspects, namely, the inspection movement of robot and the spatial movement change of robot arm and joint [5].

2.1. Establish working environment of electric robot

The three-dimensional position parameters of the target are obtained by the trigonometry and parallax. On the premise of knowing the relative position relationship between the two cameras and the internal parameters of the camera, only the parallax of the features of the object needs to be known to obtain the spatial coordinates or dimensions of the object [6]. The environment image coordinate system is shown in Figure 1:

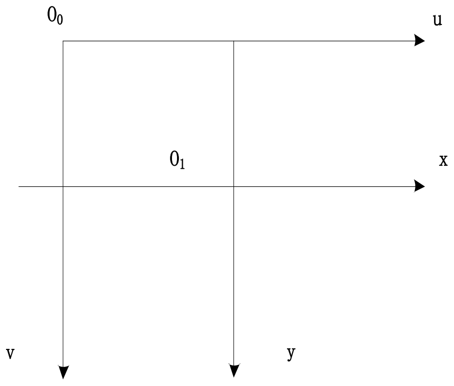

Figure 1. Environment image coordinate system

According to Fig. 1, $u-v-o$ rectangular coordinate system is defined in the obtained picture, and the coordinates of its pixel points refer to the rows and columns in the sequence, so (u,v) is the coordinates of the image coordinate system in pixels.

Since (u,v) only represents the number of columns and rows in which the pixel is located, to describe the pixel position in the image, a coordinate system with physical equivalent meaning needs to be established. Therefore, a coordinate system parallel to the (u,v) -axis is established, and the x-axis corresponds to the u -axis, and the y-axis corresponds to the v -axis [7]. Where (u,v) is the coordinate in pixels and (x,y) is the image coordinate in millimeters under the image coordinate system. Then the position of any pixel of the image has the following corresponding relationship in the two coordinate systems:

$$\begin{cases} u = \dfrac{x}{dx} + u_0 \\ v = \dfrac{y}{dy} + v_0 \end{cases} \tag{1}$$

where (u_0, v_0) represents the position of the coincidence point between the optical axis of the camera and the image plane in the xy coordinate system. By transforming the above formula into the form of homogeneous coordinates and matrix, it can be concluded that:

$$\begin{bmatrix} u \\ v \\ 1 \end{bmatrix} = \begin{bmatrix} \dfrac{1}{dx} & 0 & u_0 \\ 0 & \dfrac{1}{dy} & v_0 \\ z & 0 & 1 \end{bmatrix} \tag{2}$$

In the formula, z represents the state vector of the matrix.

The inversion is as follows:

$$\begin{bmatrix} x \\ y \\ 1 \end{bmatrix} = \begin{bmatrix} dx & 0 & -u_0 dx \\ 0 & dy & -v_0 dy \\ 0 & 0 & 1 \end{bmatrix} \begin{bmatrix} u \\ v \\ 1 \end{bmatrix} \tag{3}$$

When the camera is shooting an object, the real coordinates of the object and the image coordinates obtained by shooting have a unique projection relationship [8]. On the premise of knowing the geometric structure parameters of the camera, it can be obtained by the similar triangle principle:

$$\begin{cases} u = \dfrac{f}{-z_e} x_e \\ v = \dfrac{f}{-z_e} y_e \end{cases} \tag{4}$$

where $-z_e$ is the depth and $\dfrac{f}{-z_e}$ is the scale ratio. Perspective projection can only ensure the correspondence between image points one by one and projection lines, that is, the same point on the image corresponds to a series of points on the projection line. It is obvious that the depth information of spatial points is lost in this process, which just shows that the determination of 3D objects requires two or more cameras [9].

The position of 3D space point in camera coordinate system can be obtained by image coordinate calculation, namely:

$$\begin{cases} x_e = \dfrac{f}{f+w}u \\ y_e = \dfrac{f}{f+w}v \\ z_e = \dfrac{f^2}{f+w} \end{cases} \Rightarrow \begin{cases} x_e = \dfrac{-z_e}{f}u \\ y_e = \dfrac{-z_e}{f}v \\ z_e = z_e \end{cases} \quad (5)$$

where z_e is the parameter related to the true distance between the subject and the camera. Thus, the mapping transformation from 3D environment image to 2D image is realized.

2.2. Kinematic analysis of robot

The robot is generally composed of actuator, driving device, detection device, control system and complex machinery, among which the actuator is the robot body, the motion pairs are often called joints, and the number of joints is usually the number of degrees of freedom of the robot. The relevant parts of the robot body are often called base, waist, arm, wrist, hand and walking part [10]. The driving device is the mechanism that drives the actuator to move. According to the command signal sent by the control system, the robot moves with the help of power components. It inputs electrical signal and outputs line and angle displacement. The detection device is a real-time detection of the robot's movement and working conditions. It feeds back to the control system according to the needs. After comparing with the set information, the actuator is adjusted to ensure that the robot's action meets the predetermined requirements [11]. The control system is centralized control, that is, all the control of the robot is completed by a microcomputer. Based on the establishment of the working environment of the electric robot, the kinematics analysis of the robot is realized from the position, posture and pose of the robot.

2.2.1. Robot position

The position description of a point P in the space is shown in Figure 2. Set the point P in the built rectangular reference coordinate system a.

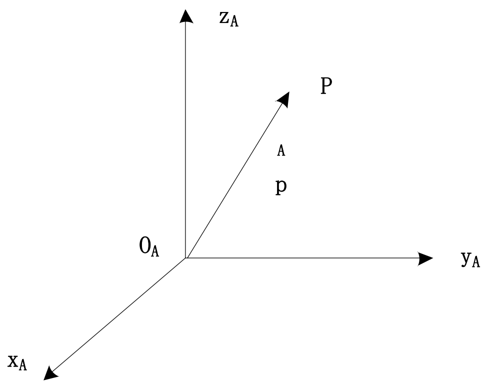

Figure 2. Location description

Its coordinates can be expressed as a matrix of 3 x 1:

$$^{A}P = \begin{bmatrix} p_x & p_y & p_z \end{bmatrix}^T \quad (6)$$

2.2.2. Robot posture

Determine the pose of the robot in the three-dimensional space, establish the rectangular coordinate system B, and place it on the object, where $^{A}R_B$ represents the rotation matrix, and the elements in the matrix represent the direction cosine of each unit vector in the coordinate system B and the unit vector corresponding to the reference coordinate system a:

$$^{A}R_B = \begin{bmatrix} ^{A}x_B & ^{A}y_B & ^{A}z_B \end{bmatrix} = \begin{bmatrix} r_{11} & r_{21} & r_{31} \\ r_{21} & r_{22} & r_{32} \\ r_{31} & r_{23} & r_{33} \end{bmatrix} \quad (7)$$

The result of formula (7) is the attitude of electric robot B in coordinate system a.

2.2.3. Posture of robot

By synthesizing the position matrix in coordinate system, a described in equation 6 and the attitude transformation matrix described in equation 7, the position and attitude of a rigid body in the coordinate system can be described. The transformation formula is as follows:

$$\{B\} = \{ ^{A}_{B}R \quad ^{A}p_{Bo} \} \quad (8)$$

where $^{A}p_{Bo}$ represents the position matrix of the origin of coordinate system B in reference coordinate system [12].

2.2.4. Forward kinematics of robot

When the angular velocity of the two driving wheels is known, set the left and right angular velocities of the electric robot as $\dot{q}_r$ and $\dot{q}_l$ respectively, so as to find out the moving track of the electric mobile robot:

$$\begin{bmatrix} x_R \\ y_R \\ \theta \end{bmatrix} = \begin{bmatrix} r\cos(\theta+\alpha) \\ r\sin(\theta+\alpha) \\ \dfrac{r}{L} \end{bmatrix} \begin{bmatrix} q_r \\ q_l \end{bmatrix} \quad (9)$$

where, θ is the angle of rotation of the robot after time t, and α is the initial attitude of the robot.

2.3. Robot dynamics analysis

The electric robot system is a multivariable and nonlinear kinematic coupling system. In order to further study the dynamics related problems, it is necessary to establish the dynamics model of KUKA robot [13]. The definition of Lagrangian function L is the difference between the kinetic energy k and potential energy P of the system, namely:

$$L = K - P \quad (10)$$

where the difference between K and P is independent of the coordinate system position. The dynamic state equation of electric robot can be expressed by Lagrangian function L as follows:

$$F_i = \frac{d}{dt}\left(\frac{\partial L}{\partial \dot{q}_i}\right) - \frac{\partial L}{\partial q_i} \quad (11)$$

where, q_i is the generalized coordinate selected by the robot, $\dot{q}_i$ is the generalized speed, F_i is the force or moment applied on the ith coordinate, and n is the number of connecting rods. The kinetic energy of connecting rod i is:

$$K_i = \int_i dK_i = \frac{1}{2} tr\left[\sum_{j=1}^{i}\sum_{k=1}^{i} \frac{\partial T_i}{\partial q_i} I_i \frac{\partial T^T{}_i}{\partial q_j} \dot{q}_j \dot{q}_k\right] \quad (12)$$

where I_i is the pseudo inertia matrix [14]. The total kinetic energy of the robot system can be expressed as:

$$K_i = K + K_a = \int_i dK_i = \frac{1}{2}\sum_{i=1}^{n}\sum_{j=1}^{i}\sum_{k=1}^{i}\left(\frac{\partial T_i}{\partial q_i} I_i \frac{\partial T^T{}_i}{\partial q_i}\right)\dot{q}_j \dot{q}_k + \frac{1}{2}\sum_{i=1}^{n} I_i \dot{q}_i^2 \quad (13)$$

According to the potential energy of particle DM at any position on the connecting rod, the dynamic equation of n-joint electric robot system is obtained as follows:

$$dP_i = -dmg^{T0} r = -g^T T_i^i r dm \quad (14)$$

2.4. Set the space trajectory constraint of electric robot

In order to study the working space of the manipulator, it is necessary to determine the range of rotation of each joint of the manipulator. For UR5 manipulator, although the range of the motor to allow the joint angle to rotate is - 360 ° - + 360 ° at each joint of the manipulator, due to the design of the mechanical structure of the manipulator itself, there are conflicts (overlaps, intersections, etc.) between the links of the manipulator at some joint angle positions, so not all joints of the manipulator can be - 360 ° - + 360 ° in any case Turn in range [15]. It is an essential step to determine the motion range of each joint of the manipulator or find out the constraints of the motion range of each joint angle.

The conflicts between the connecting rods of the manipulator are mainly intersection and overlap. The study of the possibility of such conflicts between the connecting rods is equivalent to the study of the collision avoidance between the connecting rods [16]. The connecting rod of the mechanical arm can be regarded as different line segments. In order to prevent the collision between the connecting rods of the mechanical arm, and as long as the distance between these lines in space is skillfully proved to be greater than the sum of the radius of the corresponding two connecting rods, its mathematical expression can be expressed as follows:

$$d\left(l_i, l_j\right) > r_i + r_j \quad (15)$$

where, l_i represents the segment corresponding to the manipulator link I, $d\left(l_i, l_j\right)$ represents the shortest distance between segment l_i and l_j, r_i represents the radius of the manipulator link corresponding to segment l_i, and r_j is the known parameter of the manipulator [17]. Let the coordinates of the two endpoints of segment l_i be $\left(x_1, y_1, z_1\right)$ and $\left(x_2, y_2, z_2\right)$, and the coordinates of the two endpoints corresponding to segment l_j be $\left(x_3, y_3, z_3\right)$ and $\left(x_4, y_4, z_4\right)$. Let Q be any point on the connecting rod l_i of the mechanical arm of the electric robot, then the coordinate $\left(Q_x, Q_y, Q_z\right)$ of Q can be expressed as:

$$\begin{cases} Q_x = x_1 + s\left(x_2 - x_1\right) \\ Q_y = y_1 + s\left(y_2 - y_1\right) \\ Q_z = z_1 + s\left(z_2 - z_1\right) \end{cases} \quad (16)$$

where s is the parameter. If W is any point on the connecting rod l_j, the coordinate of W can be obtained, and the parameter in W coordinate is t [18]. If the values of the parameters s and t obtained from this system of equations do not satisfy the conditions in formula (17), then the shortest distances from points $\left(x_1, y_1, z_1\right)$ to, $\left(x_2, y_2, z_2\right)$ to l_j, $\left(x_3, y_3, z_3\right)$ to l_i, and $\left(x_4, y_4, z_4\right)$ to l_i can be obtained respectively.

$$\begin{cases} 0 \le s \le 1 \\ 0 \le t \le 1 \end{cases} \quad (17)$$

Then compare the four distances, the smallest of which is the shortest distance $d\left(l_i, l_j\right)$ between l_i and l_j. The length and radius parameters of the connecting rod of the mechanical arm of the electric robot are shown in Table 1.

Table 1. Length and radius of connecting rod of mechanical arm of electric robot

connecting rod i	length/mm	radius/mm
1	89.159	60
2	425	54
3	392.25	40
4	93	45
5	94.65	45
6	82.3	45

Similarly, the range of joint angular motion of electric robot can be calculated, as shown in Table 2.

Table 2. movement angle range of each joint of mechanical arm

Joint angle i	Minimum range of motion	Maximum angle of motion
1	-360°	360°
2	-360°	360°
3	-145°	145°
4	-180°	0°
5	-360°	360°
6	-360°	360°

In practical engineering application, in order to ensure that the tool end can rotate freely and as much as possible, that is to say, when the sixth joint rotates, the tools and instruments at the end will not touch the mechanical arm itself, it is necessary to further limit the rotation range of the fourth and fifth joints [19].

2.5. Real time motion detection of electric robot based on Unscented Kalman filter

In order to achieve the purpose of research, this paper uses MATLAB software to obtain the waveform of the electric robot, which lays the foundation for the follow-up research. Figure 3 shows the waveform of the Unscented Kalman filter installed on the electric robot.

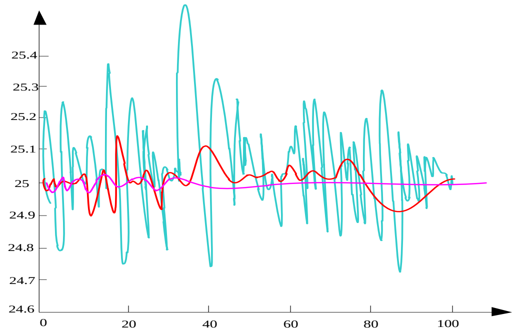

Figure 3. Waveform of Unscented Kalman filter

The initial state and variance are assumed to be:

$$\begin{cases} \hat{x}_0 = E(x_0) \\ P_0 = E\left[(x_0 - \hat{x}_0)(x_0 - \hat{x}_0)^T\right] \end{cases} \quad (18)$$

Then the initial state and variance of the whole dimension are respectively:

$$\begin{cases} \hat{x}_0^a = E(x_0^a) = \begin{bmatrix} \hat{x}_0^T & 0 & 0 \end{bmatrix}^T \\ P_0^a = E\left[(x_0^a - \hat{x}_0^a)(x_0^a - \hat{x}_0^a)^T\right] = \begin{bmatrix} P_0 & 0 & 0 \\ 0 & Q_0 & 0 \\ 0 & 0 & R_0 \end{bmatrix} \end{cases} \quad (19)$$

At k-1 moment, select x_{k-1}^a from sigma point, to select the corresponding mean and variance weights. Through the nonlinear state equation, the mean and variance of the state prediction of electric robot can be obtained, and the state update and prediction of electric robot can be realized [20].

2.6. Space trajectory planning of electric robot

In the working environment of electric robot, the space trajectory planning of electric robot is realized by generating path points from two aspects of joint and movement.

2.6.1. Joint trajectory planning of electric robot

In the process of electric robot motion, an interpolation function about the joint angle of the starting point and the ending point is used to describe the motion track, in which the joint angle of the starting point is known, and the joint angle of the ending point can be obtained through kinematic solution. There are many smoothing functions that can be used as joint interpolation functions. In order to realize the smooth movement of a single joint of the palletizing robot, the trajectory function must meet at least four constraints, namely the joint angle corresponding to the starting point and the ending point, the joint speed of the starting point and the ending point [21]. In the process of trajectory planning, the two adjacent path points are regarded as the starting point and the ending point respectively, then the interpolation function is determined, and finally the path points are smoothly connected [22-24].

2.6.2. Path planning of electric robot avoiding obstacles

Figure 4 is a schematic diagram of the path planning of the wheeled mobile robot with or without obstacles between two states, where r_{o1} and r_{o2} are the outer envelope radius of the obstacles, and r_{os1} and r_{os2} are the outer envelope radius after the safety dimension is increased.

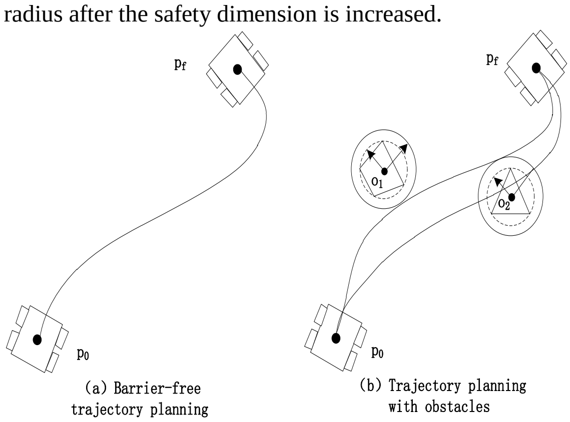

Figure 4. Path planning of electric robot with or without obstacles between two states

The solid line in Figure 4 (a) is the planning track between state p_0 and State p_f when there is no obstacle, but when there are obstacles o_1 and o_2, the original planning track (dotted line in Figure 4 (b)) can no longer meet the requirements and needs to be re planned to meet the requirements. The re planned track curve after considering the size of obstacles and safe obstacle avoidance is realized in Figure 4 (b) [25].

2.6.3. Planning track smoothing

Planning trajectory curve is a kind of controllable free curve, which has geometric invariance, convexity and symmetry. The direction of the curve is only related to the vertex and sequence of the feature polygon, not to the selection of the current coordinate system [26]. Using this kind of curve to smooth the path of electric robot, the path sequence of the algorithm can be taken as the feature vertex directly without additional interpolation. At the same time, the smooth path enables the omnidirectional robot to avoid the time loss at the turning point of the path, and ensures the consistency of the robot's motion [27]. The smoothing results of the spatial planning trajectory of electric robot are shown in Figure 5.

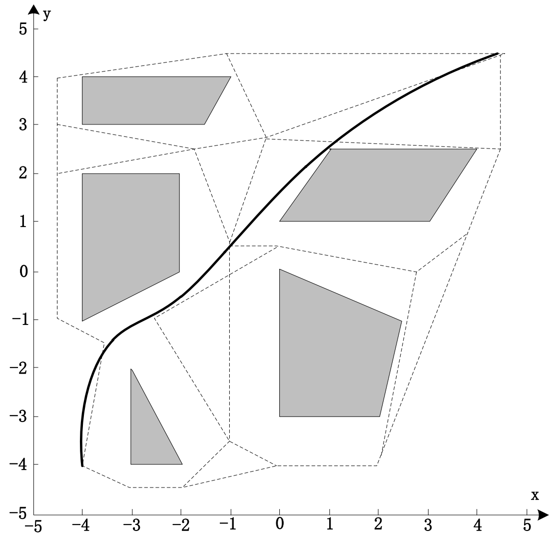

Figure 5. Smoothing results of spatial planning trajectory of electric robot

3. Experimental results and analysis

In order to prove the application performance of the designed space trajectory planning method of electric robot based on Unscented Kalman filter in actual electric power work, the space trajectory planning method of electric robot based on random landmark method, the space trajectory planning method of electric robot based on flexible polyhedron search algorithm and the space trajectory planning method of electric robot based on subgroup optimization algorithm are set up. As an experimental comparison method, under the same working environment, the corresponding planning results are obtained respectively, and the quantitative comparison results are obtained by counting the relevant parameters of the robot in the work.

3.1. Experimental platform

The control system software of electric robot takes Visual Stiudio 2018 integrated development environment as the experimental platform, combines Microsoft's Windows XP based operating system, uses C + + language to program, selects SCARA electric robot as the research object, and uses the above four methods to plan its space trajectory. The SCARA electric robot is shown in Figure 6.

Figure 6. SCARA electric robot

The GUI of MATLAB is used to write the simulation interface of electric robot to display the pose matrix and Euler angle of the robot end actuator. The simulation platform of electric robot is shown in Figure 7.

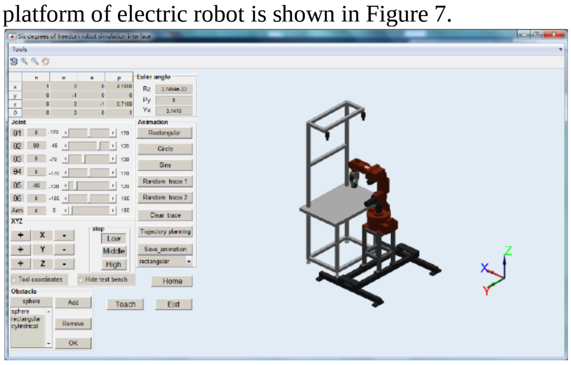

Figure 7. Simulation platform of electric robot

3.2. Parameter configuration

Through the simulation platform of electric robot, when the kinematic characteristics of the target electric robot are determined, the parameters that are useful for the kinematic transformation of electric robot are selected for configuration, which do not include the length and rotation of all connecting rods. The specific configuration parameters of the experimental objects are shown in Table 3.

Table 3. Parameter configuration of electric robot

Parameter exponent	Parameter value	Parameter representation
TRAFO6_KINCLASS	1	Type of kinematics used
TRAFO6_NUM_AXES	5	The joint axis / DOF of the target robot is 5
TRAFO6_MAIN_AXES	2	Type of basic joint sequence you need to use joint order
TRAFO6_AXIS_SEQ	6	Whether the fourth joint and the first hand joint are parallel or reverse parallel to the basic joint of the last rotation type
TRAFO6_A4PAR	1	Type of kinematics used
TRAFO6_AXES_TYPE	[3,1,3,3,3]	The type of each joint of the robot, is it a moving joint or a rotating joint
TRAFO6_AXES_DIR	[2,1,3,4,5]	Whether the positive direction of each joint of the target robot rotates and moves in accordance with the mathematically predefined positive direction in the module
TRAFO6_MAMES	[1,1,1,1,1]	Angular deviation of mechanical zero point and mathematical zero point on each joint
TRAFO6_MAIN_LENGTH_AB	[0.0,0.0,0.0,0.0,0.0]	Connecting rod length in basic joint
TRAFO6_TIRORO_POS	[0.0,500.0]	The frame shift of the front T_IRO_RO of electric robot
TRAFO6_TIRORO_RPY	[0.0,0.0,500.0]	The frame rotation of the frontT_IRO_RO of electric robot
TRAFO6_TX3P3_POS	[0.0,0.0,90.0]	T_X3_P3 frame deviation in the middle of electric robot
TRAFO6_TX3P3_RPY	[300.0,0.0,200.0]	Rotation of T_X3_P3 frame in the middle of electric robot
…	…	…

The controller with the same specification is installed on the configured electric robot. The purpose of installing the controller is to ensure that the electric robot can move according to the planned trajectory in the actual operation. Figure 8 shows the staff debugging the controller.

Figure 8. Schematic diagram of controller debugging

In this comparative experiment, the spatial trajectory and joint trajectory of electric robot are tested respectively, and the collision times, path length and movement time of different planning results are compared in different environments

where, P is the position matrix of the robot, and the three elements in the matrix are the coordinate components of P point in three directions.

3.3. Mobile planning function test

3.3.1. Accessible environment

Barrier free environment means that there are no other interference factors in the experimental environment except for electric robots and electric equipment. The space trajectory of electric robot is divided into six parts. The space trajectory planning method of electric robot based on random road sign method, the space trajectory planning method of electric robot based on flexible polyhedron search algorithm, the space trajectory planning method of electric robot based on sub group optimization algorithm and the space trajectory planning method of electric robot based on Unscented Kalman filter are used to make statistics The operation indexes of multiple robots are shown in Table 4 and Table 5.

From the data in Table 4 and Table 5, it can be seen that under the environment of no obstacle interference, the space trajectory planning method of electric robot based on the sub group optimization algorithm will have two collisions. The total space trajectory of the planned electric robot is 4.775 m, and the moving time of the robot is 39 s. There will be three collisions in the space trajectory planning method of electric robot based on the random landmark method. The total space trajectory of the planned electric robot is 5.054 m, and the moving time of the robot is 44.4 s. Based on the flexible polyhedron search algorithm, there will be four collisions in the space trajectory planning method of electric robot. The total space trajectory of the planned electric robot is 5.557 m, and the moving time of the robot is 50.4 s. However, no collision is found in the experiment by using the trajectory planning method designed in this paper. Compared with the space trajectory planning method of electric robot based on the sub group optimization algorithm, the planned trajectory is 0.407 m shorter and the moving time of the robot is saved by 1.8 s.

Table 4. Comparison between Subgroup Optimization Algorithm and Unscented Kalman Filter

Stage	Global planning time (s)	Spatial trajectory planning method of power robot based on sub-group optimization algorithm			Space trajectory planning of electric robot based on Unscented Kalman filter		
		Trajectory (m)	Time consuming (s)	Collision times (time)	Trajectory (m)	Time consuming (s)	Collision times (time)
1	1.239	0.711	6.3	1	0.700	6.1	0
2	0.535	0.909	7.8	0	0.906	7.3	0
3	0.212	0.828	6.9	0	0.823	6.5	0
4	0.123	0.973	8.1	1	0.796	7.9	0
5	0.114	0.739	4.8	0	0.568	4.6	0
6	0.265	0.615	5.1	0	0.575	4.8	0
合计	2.488	4.775	39	2	4.368	37.2	0

Table 5. Comparison Results Based on Random Path Method and Flexible Polyhedron Search Algorithm

Stage	Global planning time (s)	Spatial trajectory planning method of power robot based on stochastic routing method			Spatial trajectory planning method of power robot based on flexible polyhedron search algorithm		
		Trajectory (m)	Time consuming (s)	Collision times (time)	Trajectory (m)	Time consuming (s)	Collision times (time)
1	1.239	0.823	7.1	1	0.912	8.1	0
2	0.535	0.811	7.4	0	0.902	8.2	1
3	0.212	0.832	7.2	0	0.952	8.5	1
4	0.123	0.845	7.5	1	0.916	8.4	0
5	0.114	0.866	7.4	0	0.940	8.6	1
6	0.265	0.877	7.8	1	0.935	8.6	1
Total	2.488	5.054	44.4	3	5.557	50.4	4

3.3.2. Multi obstacle environment

Based on the barrier free environment, multiple obstacles are added to the experimental environment. The obstacles introduced in this experiment are divided into moving obstacles and fixed obstacles. The trajectory planning results obtained by using four spatial trajectory planning are shown in Figure 9.

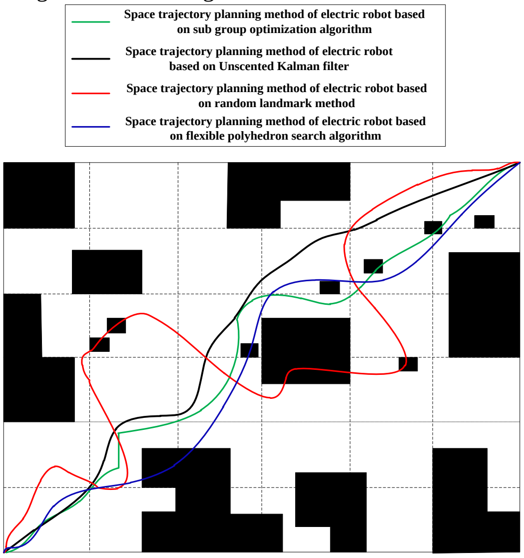

Figure 9. Comparison results of spatial trajectory planning in multi obstacle environment

It can be seen intuitively from the figure that in the first stage of trajectory planning, the trajectory results obtained by the design planning method in this paper do not coincide with the obstacles and their motion tracks, while the planning results of the spatial trajectory planning method of electric robot based on the sub group optimization algorithm overlap with the obstacles in two places, and the spatial trajectory planning method of electric robot based on the random landmark method. And the planning results of the space trajectory planning method of electric robot based on the flexible polyhedron search algorithm coincide with the obstacles many times. According to the statistics, there are 32 obstacles in the whole experiment. The number of collisions of the trajectory planning method based on the sub group optimization algorithm is 11, and the corresponding collision rate is 34.3%. However, the number of collisions of the trajectory planning method designed in this paper is 6, that is, the collision rate is 18.7%. In contrast, in the multi obstacle environment, the space trajectory planning of the robot is designed. The collision rate of the planning results is reduced by 15.6%.

3.4. Joint planning function test

The test of joint planning function is to plan the data reading track of electric robot when it performs patrol inspection task, carry out specific test for the track of multiple joints in electric robot, count the number of collisions between each joint and other electric equipment when it performs patrol inspection task, and the final statistical results are shown in Table 6.

Table 6. Comparison results of joint planning function test

Space trajectory planning method		Collision times			
		Joint 1	Joint 2	Joint 3	Joint 4
Spatial trajectory planning method of power robot based on sub-group optimization algorithm	1	2	3	1	3
	2	3	3	1	1
	3	1	2	4	3
	4	2	2	3	4
	5	3	3	2	3
	6	4	4	2	2
Space trajectory planning of electric robot based on Unscented Kalman filter	1	0	0	1	2
	2	1	1	0	0
	3	0	1	3	2
	4	3	1	2	2
	5	0	0	0	3
	6	2	2	1	1
Spatial trajectory planning method of power robot based on stochastic routing method	1	2	1	2	3
	2	2	2	1	1
	3	1	2	4	3
	4	2	2	3	3
	5	1	1	1	4
	6	1	3	2	2
Spatial trajectory planning method of power robot based on flexible polyhedron search algorithm	1	1	2	2	3
	2	3	2	1	1
	3	2	2	4	3
	4	2	2	3	3
	5	1	2	2	4
	6	3	3	3	3

By synthesizing the four joints of the electric robot, it can be found that the total number of joint collisions of the spatial trajectory planning method of the electric robot based on the sub group optimization algorithm is 61 times, the total number of joint collisions of the spatial trajectory planning method of the electric robot based on the random landmark method and the spatial trajectory planning method of the electric robot based on the flexible polyhedron search algorithm are 49 times and 57 times respectively In this paper, the total number of joint collisions is 28, which is 33 times lower than the total number of joint collisions based on the sub group optimization algorithm.

3.5. Trajectory planning error

In order to further verify the effectiveness of this method, the spatial trajectory planning method of electric robot based on random road sign method, the spatial trajectory planning method of electric robot based on flexible polyhedron search algorithm, the spatial trajectory planning method of electric robot based on subgroup optimization algorithm and the spatial trajectory planning method of electric robot based on Unscented Kalman filter are studied The results of human space trajectory planning are compared with the actual planning results, and the comparison results are shown in Figure 10.

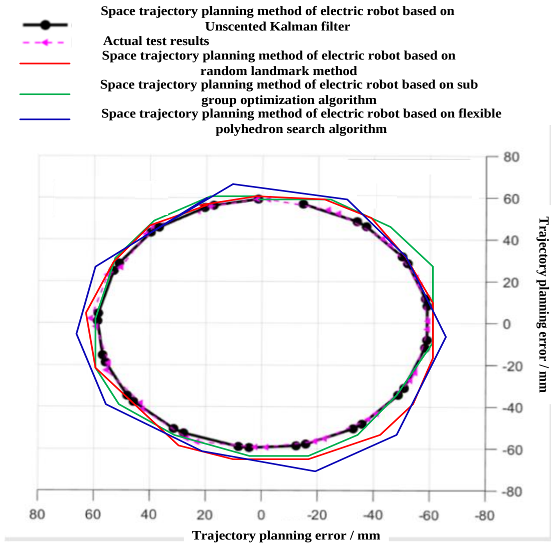

Figure 10. Comparison of trajectory planning errors

According to Figure 10, the spatial trajectory planning results of electric robot based on Unscented Kalman filter are basically consistent with the actual planning results, while the spatial trajectory planning methods of electric robot based on random road sign method, the spatial trajectory planning methods of electric robot based on flexible polyhedron search algorithm and the power robot based on subgroup optimization algorithm. The space trajectory planning results of electric robot based on robot space trajectory planning method are quite different from the actual planning results, which shows that this method can accurately plan the space trajectory of electric robot.

To sum up, applying the unscented Kalman filter technology to the space trajectory planning method of electric robot, the collision times of electric robot moving are reduced no matter in the barrier free or multi barrier environment, which realizes the design purpose of the space trajectory planning optimization method of electric robot.

4. Conclusion

China's electric robot market is the fastest growing and most dynamic electric robot market in the world, which brings great opportunities to the generation and development of electric robots in China. However, with the deepening of economic globalization, it is foreseeable that foreign large-scale robot companies will vigorously enter into the robot market. Due to the accumulation of technology and experience, Chinese robot companies still have a huge gap with foreign robot companies. Therefore, it is an urgent task to develop various functional modules of industrial robots with independent intellectual property rights as soon as possible. In view of the collision of traditional spatial trajectory planning methods for electric robots, which results in a long time and inaccurate trajectory planning, the optimal design of spatial trajectory planning method for electric robots is realized by using unscented Kalman filter. Firstly, the working environment of the electric robot is built. In this environment, the kinematics of the robot is analyzed, and the dynamics of the robot is analyzed. According to the analysis results of the kinematics and dynamics of the electric robot, the space trajectory constraint of the electric robot is set. Using unscented Kalman filter technology, the real-time motion state of the electric robot is detected, and then the spatial trajectory planning results of the electric robot are obtained by smoothing the spatial trajectory. Compared with the traditional space trajectory planning method, it is found that the collision times of the robot are reduced in the fault-free and multi fault environment.

Through the research of this paper, it can be concluded that using the trajectory planning method designed in this paper, no collision is found in the experiment. Compared with the space trajectory planning method based on sub group optimization algorithm, the planning trajectory is shorter by 0.407m and the robot motion time is saved by 1.8s. The number of collisions is 6, that is, the collision rate is 18.7%.

Acknowledgement

This research has been financed by The Young Talents Project of General Higher Education in Guangdong Province "Research on the Application of Graph State in Quantum Secure Direct Communication" (2018GkQNCX130).

References

[1] Zhang SG, Zhao J. Trajectory planning of packaging palletizing robot based on S-curve. Packaging Engineering, 2018, 39(1):136-140.

[2] Yang M, Jiang ZH, Li H, et al. A novel space target-tracking method based on generalized Gaussian distribution for on-orbit maintenance robot in Tiangong-2 space laboratory. Science China Technological Sciences, 2019, 62(6):1045-1054.

[3] Lim W, Lee S, Sunwoo M, et al. Hierarchical trajectory planning of an autonomous car based on the integration of a sampling and an optimization method. IEEE Transactions on Intelligent Transportation Systems, 2018, 19(2):1-14.

[4] Wang W, Huang XD. Virtual plate based controlling strategy of toy play for robot's communication development in JA space. International Journal of Automation and Computing, 2019, 16(1):93-101.

[5] Li YH, Huang T, Chetwynd DG. An approach for smooth trajectory planning of high-speed pick-and-place parallel robots using quintic B-splines. Mechanism & Machine Theory, 2018, 126:479-490.

[6] Liu Y, Shi L, Tian XC. Weld seam fitting and welding torch trajectory planning based on NURBS in intersecting curve welding. International Journal of Advanced Manufacturing Technology, 2018, 95(1-4):2457-2471.

[7] Nada D, Bousbia-Salah M, Bettayeb M. Multi-sensor data fusion for wheelchair position estimation with Unscented Kalman Filter. International Journal of Automation & Computing, 2017, 15(3):207-217.

[8] Ghorbani E, Cha YJ. An iterated cubature unscented Kalman filter for large-DoF systems identification with noisy data. Journal of Sound & Vibration, 2018, 2018(420):21-34.

[9] Lu N, Gao L, Shen XF. A doubly-selected channel estimation method based on an unscented Kalman filter. Journal of Shandong University (Engineering Science), 2019, 49(4):130-136.

[10] Li Y, Wang C, Gong J. A wavelet transform-adaptive unscented Kalman filter approach for state of charge estimation of LiFePo4 battery. International Journal of Energy Research, 2018, 42(2).

[11] Yan XL, Chen GG, Tian XL. Two-step fast reconfigurable unscented Kalman filter algorithm for measurement of missile rolling angle. Chinese Journal of Scientific Instrument, 2018, 39(6):140-147.

[12] Tang Q, He LM. Unscented Kalman filtering method with nonlinear equality constraint. Journal of Computer Applications, 2018, 28(5):1481-1487.

[13] Liu ZF, Xu JJ, Cheng Q, et al. Trajectory planning with minimum synthesis error for industrial robots using screw theory. International Journal of Precision Engineering & Manufacturing, 2018, 19(2):183-193.

[14] Jiao J, Chen J, Qiao Y, et al. Adaptive sliding mode control of trajectory tracking based on DC motor drive for agricultural tracked robot. Transactions of the Chinese Society of Agricultural Engineering, 2018, 34(4):64-70.

[15] Rahman MM, Ishii K, Noguchi N. Optimum harvesting area of convex and concave polygon field for path planning of robot combine harvester. Intelligent Service Robotics, 2019, 2019(4):1-13.

[16] He Z, Zhou F, Xia X, et al. Interaction between oil price and investor sentiment: Nonlinear causality, time-varying influence, and asymmetric effect. Emerging Markets Finance and Trade, 2019, 55(12): 2756-2773.

[17] Feng YC, Li XD, Wang S, et al. Study of Kinematic control of hexapod robot based on screw theory. Computer Simulation, 2019, 2019(8):298-304.

[18] Hwu T, Wang AY, Oros N, et al. Adaptive robot path planning using a spiking neuron algorithm with axonal delays. IEEE Transactions on Cognitive & Developmental Systems, 2018, 10(2):126-137.

[19] Sun QP, Li M, Wang ZH. Mobile robot path planning based on improved rapidly-exploring random tree algorithm. Journal of University of Jinan (Science and Technology), 2019, 33(5):431-438.

[20] Li J, You XM, Liu S, et al. Dynamic chaotic ant colony system and its application in robot path planning. Journal of Computer Applications, 2018, 38(1):1001-9081.

[21] Glorieux E, Franciosa P, Ceglarek D. End-effector design optimisation and multi-robot motion planning for handling compliant parts. Structural & Multidisciplinary Optimization, 2018, 57(3):1377-1390.

[22] Chiu SW, Kuo J, Chiu YP, et al. Production and distribution decisions for a multi-product system with component commonality, postponement strategy and quality assurance using a two-machine scheme. Jordan Journal of Mechanical and Industrial Engineering, 2019, 13(2):105-115.

[23] Zhang F, Li N, Yuan R, et al. Robot path planning algorithm based on reinforcement learning. Huazhong Keji Daxue Xuebao, 2018, 46(12):65-70.

[24] Zhu Y, Guo N. Unmanned vehicle route tracking method based on video image processing. Jordan Journal of Mechanical and Industrial Engineering, 2020, 14(1):139-147.

[25] Yan WJ, Fei SM. Path planning and software design based on dining robot on trains. Software Guide, 2019, 18(9):26-29.

[26] Kalani H, Akbarzadeh A, Nabavi SN, et al. Dynamic modeling and CPG-based trajectory generation for a masticatory rehab robot. Intelligent Service Robotics, 2018, 11(3):1-19.

[27] Wen F, Zhao Y, Zhang M, et al. Forecasting realized volatility of crude oil futures with equity market uncertainty. Applied Economics, 2019, 51(59):6411-6427.

JJMIE

Volume 15, Number 1, March. 2021
ISSN 1995-6665
Pages 39 - 49

Jordan Journal of Mechanical and Industrial Engineering

The Electric Vehicle Torque Adaptive Drive Anti-Skid Control Based on Objective Optimization

Yingqi He

Jiangsu Vocational College of Finance & Economics, Huai'an, 223003, China

School of Mechatronics and Information Engineering

Received July 18 2020 *Accepted Feb 20 2021*

Abstract

The vehicle is interfered by the lateral wind in the traditional anti-skid control method, which results in a bad anti-skid control effect of electric vehicle torque drive. For this reason, a method of torque adaptive drive anti-skid control for electric vehicle is proposed. In order to realize the driving force control of distributed driving electric vehicle, the driving motor is modeled and simplified. A battery model was established to analyze the influence of the bus voltage fluctuation on the motor torque response. The power system model is added to the existing vehicle model to complete the simulation model design of the distributed drive electric vehicle. According to the characteristics of the friction circle of the tire, the driving torque of the driving wheel is analyzed. In order to resist the influence of interference factors on vehicles during vehicle movement, through the concept of vehicle stability control, the left and right driving torque is dynamically adjusted by using the obtained ideal driving force distribution ratio of front and rear axles. The simulation results show that the proposed method can effectively increase the driving torque and improve the fitting coefficient of the driving anti-skid torque.

Keywords: Distributed drive; Drive skid control; Driving force distribution; Dynamical system modeling;

1. Introduction

Automobile is an important industry of national economy. As a big country of automobile production and sales, China is not a strong country, and the technology of independent products is still weak. We should grasp the opportunity of the development of electric vehicles, achieve the leap of automotive core technology, reach the international advanced level. With its unique advantages (more controllable degrees of freedom), high-performance distributed drive electric vehicles will occupy a place in the field of electric vehicles [1].

There are many types of electric vehicle drive motors, such as dc motor, ac induction motor, permanent magnet synchronous motor and so on. The following is a brief description of its characteristics. Distributed drive electric vehicle is an electric vehicle that is powered by one or more groups of vehicle-mounted power sources to provide power to the drive motor of the wheel, so as to distribute a single controllable drive system to each wheel [2]. The so-called distributed drive electric vehicle (dev) is an electric vehicle that is powered by one or more sets of on-board power sources for each wheel's drive motor. In this way, a separate controllable drive system is distributed to each wheel. Traditional distributed drive electric vehicles can better realize the power distribution and control by taking advantage of their own structural advantages [3]. For example, the increase and decrease of driving motor torque can be used to realize the drive anti-skid control. Driving force distribution is realized by using the advantages of independent control of driving motor and response speed. The driving anti-skid system controls the sliding rate of the driving wheel in the vicinity of the optimal sliding rate, so as to ensure that the driving wheel has the best longitudinal driving force and the ability to resist lateral interference. UOT Electric March II is an Electric car with two front wheels driven by an Electric motor [4]. The control algorithm of anti-skid drive and anti-lock braking is verified by controlling the wheel slip rate, and the concept of recognizing the wheel roll state by the driving force of the wheel is put forward. Some domestic scholars use the sliding mode control theory to achieve the drive anti-slip control. The control method of the synovial variable structure is to build the sliding mode surface by the slip rate error and the rate of error change. So it can achieve the purpose of controlling the roller slip rate. This method has good robustness, but its control principle leads to a high frequency switching of the slip rate on the synovial surface, which will cause the chattering of the drive motor and seriously affect the effect of the drive anti-slip control [5]. In order to solve the disturbance caused by side wind and buffeting of driving motor in the traditional anti-skid control method. An adaptive anti-skid control method for electric vehicle torque based on objective optimization is proposed. The effectiveness of the proposed method is verified by experiments.

* Corresponding author e-mail: yingqi_he@126.com.

2. Electric vehicle torque adaptive drive skid control

2.1. Objective optimization of power control algorithm

Based on the driving force control of distributed driving electric vehicles, the problem of the friction coefficient mismatch between the tire and the road caused by the torque of the driving motor and the slip of the driving wheel is studied. Under the condition of studying the driver's longitudinal intention, the car has the biggest problem of resisting lateral interference, that is, the problem of the driving force and ideal distribution between the front axle of the distributed drive electric vehicle [6]. In order to carry out research, firstly, an equivalent dynamic system model of distributed drive EV is established. Through this model, a model is sought to reflect the torque response characteristics of the motor. It can reflect the torque response caused by the battery bus voltage fluctuation problem. And the required model can meet the requirements of real-time simulation to prepare for the rapid prototyping of control algorithms in the future. In the distributed driving ev power system, the performance of the battery directly determines the performance of the vehicle [7]. Therefore, in the electric vehicle simulation, the battery model is an important link, it is very necessary to study the battery comprehensively and systematically. But the electrochemical reaction process of the battery is extremely complicated. It involves multidisciplinary fields, such as chemistry, electricity, heat, especially in the charging and discharging process, and all the performance parameters of the battery. For example, electromotive force and internal resistance, state of charge, Coulomb efficiency, self-discharge rate, and temperature, etc. can all affect each other, and there is a complicated relationship [8]. In this paper, the influence of bus voltage fluctuation on motor torque response is mainly concerned with distributed electric vehicle driving, so only a simplified internal resistance model is established. Although the internal resistance model is simple, it can reflect the basic characteristics of battery charging and discharging process, such as bus voltage fluctuation, the influence of temperature on the internal resistance, and the change of battery charge. This model is simple, universal, and convenient for simulation [9]. The following figure is the schematic diagram of the internal resistance model of the battery.

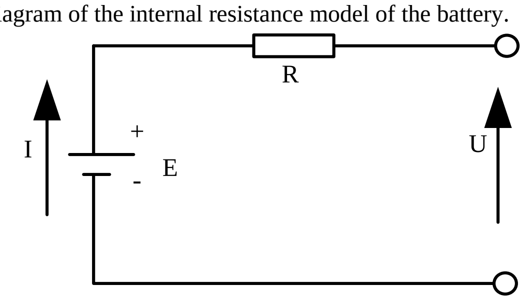

Figure 1. Internal resistance model of battery

In the vehicle model, the road adhesion coefficient is an important parameter to calculate the tire. The road adhesion coefficient where the wheels are located will change with the vehicle’s track. In order to adapt to the change of the road adhesion coefficient with the track. This paper also models the road input, the idea of which is to set the road adhesion and the coordinate range [10]. When the center of mass of the wheel moves to this coordinate, the road adhesion input model will output the adhesion coefficient under the current road surface as a parameter to calculate the current tire force. This paper illustrates how to use the road adhesion input model by taking the docking road as an example. The simplified internal resistance model simplifies the battery into the series of voltage source and internal resistance, and its basic voltage balance equation is as follows:

$$E=RI+U \tag{1}$$

where E is the electromotive force of the battery, R is the internal resistance of the battery, I is the current, and U is the bus voltage of the battery. Battery electromotive force E is determined by temperature Tess and battery charge Soc, and its functional expression is:

$$\Delta E=\sum E\,/\mathrm{f(Soc,Tess)}\times \mathrm{p} \tag{2}$$

The internal resistance R of the battery is determined by the battery temperature Tess, the battery charge Soc and the demand power p. The functional expression is as follows:

$$R=\prod \lim_{x\to\infty}\frac{\|\Delta E-E\|}{2f(soc,tess)} \tag{3}$$

where is the $f(p)$ lookup table function. Then the power balance equation of the battery can be further obtained:

$$I=\frac{R^2+EP_{\lim}}{2E} \tag{4}$$

where, $P_{\lim}$ is the charging and discharging power of the battery after power limitation. The charging and discharging current of the battery can be simplified as follows:

$$\Delta I=\iint\frac{0.5(UR^2+2EP_{\lim})}{2R+E} \tag{5}$$

As an emerging form of automobile, distributed drive electric vehicle has its unique advantages and many theoretical problems have not been solved. The state has carried out major basic project research (research on key basic issues of high-performance distributed drive electric vehicles) to provide theoretical support for the development of distributed drive electric vehicles. This research is not only of great significance to social environment and resource issues, but also a major strategic demand for national development [11]. The research is carried out from the two directions of driving anti-skid and driving force distribution. In the aspect of driving anti-skid control, firstly, the basic principle of driving anti-skid control and the estimation of reference speed are studied in detail, and finally, the driving anti-skid control logic for distributed driving electric vehicles is designed [12]. The distribution of driving force of distributed driving electric vehicles is divided into two parts: one is the ideal distribution of driving force in front and rear axle; the other is the dynamic adjustment of driving force from left to right. The distribution of driving force front and rear axle is a method to ensure the maximum lateral force allowance while ensuring the longitudinal acceleration of the vehicle. Dynamic adjustment of driving force from left to right is to dynamically adjust the driving torque from left to right based on the ideal distribution of driving force of front and rear axles to ensure the lateral stability of the vehicle [13]. Due to the minimum operating current limitation in the real battery system, when the battery charging current is recorded as a negative value, the minimum operating current of the battery is the maximum charging current. In order to prevent the charging current from being too large, the minimum current needs to be limited in the model. In the actual ev, due to the road condition or the driver, the power of the driving motor is often greater than the maximum power provided by the battery [14]. In order to be closer to the actual physical system, the model limits the external power demand. When the demand power of each driving wheel is greater than the maximum discharge power of the battery, the discharge power of the battery is limited.

2.2. Modeling of auto adaptive drive anti-skid control system

The longitudinal driving force of the vehicle is provided by the interaction between the tire and the ground. The adhesion coefficient of the road surface directly affects the longitudinal driving force, and the adhesion coefficient of the road surface has a nonlinear relationship with the slip rate of the vehicle. Through many experiments, the researchers proved that when the vehicle wheel slip rate is within a certain range, the maximum road use adhesion coefficient can be obtained. When the modified rotational slip rate becomes the optimal slip rate, the vehicle can obtain the maximum driving and braking force [15]. The larger driving force and braking force can guarantee the vehicle's handling stability and dynamic performance, so the optimal slip rate can be obtained and controlled in the optimal range, which can improve the vehicle performance. In order to make the magnetic flux density generated by PMSM close to sinusoidal distribution, the rotor magnetic steel is designed as a parabola [16]. In order to eliminate harmonic magnetomotive force, the stator windings are connected with a star. When the stator winding is connected with three-phase sinusoidal alternating current, the stator winding will generate a rotating magnetic field. The rotating magnetic field and the constant magnetic field generated by the permanent magnets of the rotor will influence each other to push the rotor to rotate. According to the above working principle of permanent magnet synchronous motor, it can be known that as long as the phase and frequency of three-phase sinusoidal ac power supply of stator winding are changed, the speed and position of the rotor can be controlled [17]. Fuzzy control is a control method based on fuzzy mathematical theory, which represents control variables by fuzzy sets. By refining human thinking and logical reasoning methods, human experience rules are transformed into reasoning rules of logical operations, and then the controller ACTS on the control object to achieve the control effect on the controlled object [18]. In the simulation control system, the most commonly used control method is PID control, its control system principle block diagram is shown in the figure.

PID control belongs to A linear control method [19], which constitutes the control deviation according to the given target value $r(t)$ and the actual output value $e(t)$, namely $e(t) = r(t) - y(t)$. Then carry out proportional, integral and differential calculation on the control deviation $e(t)$, and then add up the results of the three operations, and the control output $u(t)$ of the PID controller is obtained. In the continuous time domain, the expression of PID control algorithm is as follows:

$$\lambda = \iiint \frac{y(t)}{2e(t)+r(t)} - 1 \tag{6}$$

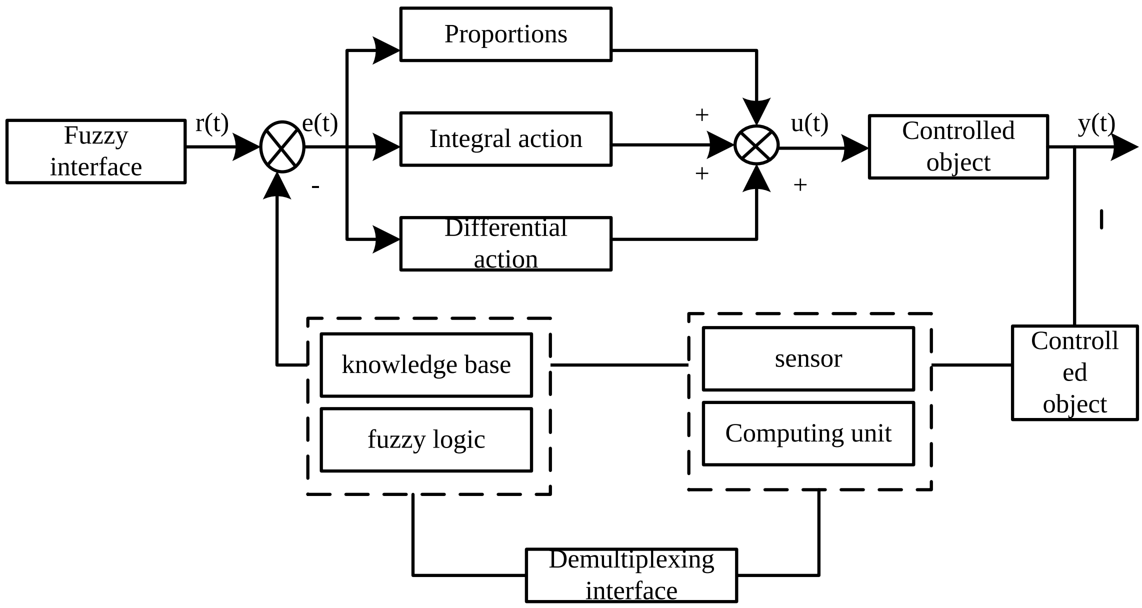

Figure 2. Schematic diagram of auto adaptive control system

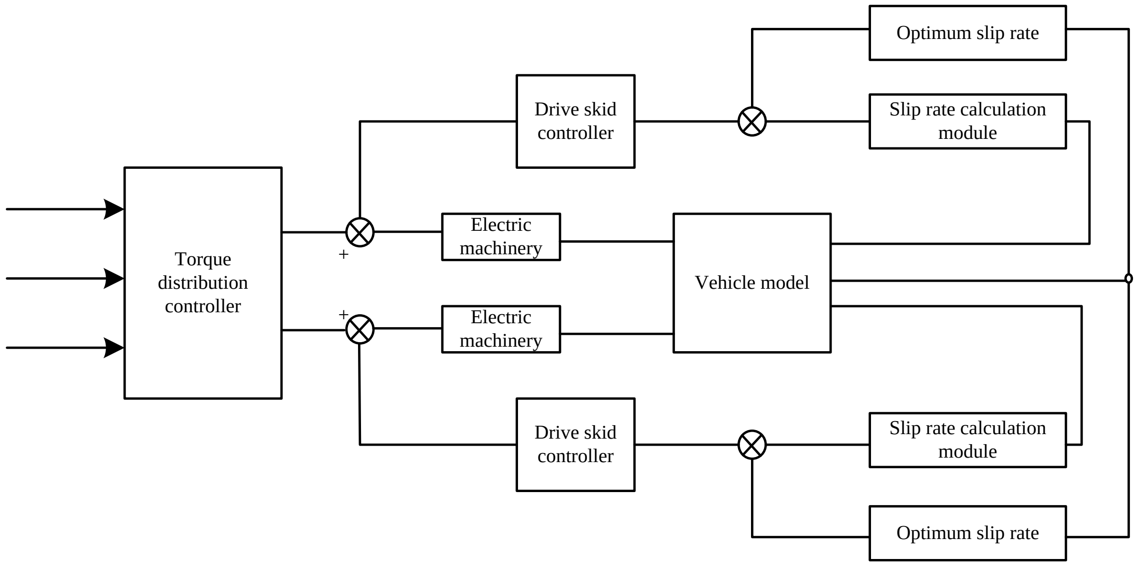

Figure 3. Skid control structure of electric vehicle

As the main controlled object of the electric vehicle, the driving motor's performance directly affects the performance of the vehicle. Therefore, we need to establish the mathematical model of the motor and analyze it [20]. The motor is a complex physical system. In order to facilitate the analysis, the following assumptions are made in the modeling process:

1. The inductance of the motor is constant.
2. Ignore rotor damping.
3. The permanent magnetic field is sinusoidal.
4. The stator winding magnetic field is sinusoidal.
5. The stator windings are symmetrically distributed, and the axes differ from each other by 120 electric angles.

Based on this, the control strategy can be divided into two layers according to the function. The upper layer is the torque distribution control layer, and the lower layer is the driving anti-skid control layer [21-23]. Based on the fuzzy self-tuning PID control, the lower controller adopts the optimal sliding rate control strategy to control the sliding rate of the left and right driving wheels respectively to keep them near the optimal sliding rate. The two layers of control complement each other, which not only guarantees the stability of the vehicle when turning, but also makes full use of the adhesion coefficient of the ground, and improves the dynamic performance of the vehicle. The control structure is shown in the figure.

According to the automobile theory, when the wheel enters the state of sliding rotation during the driving process, the angular acceleration of the wheel will increase rapidly, and the sliding rate of the wheel will also increase sharply. Therefore, the angular velocity of the wheel can reflect whether the vehicle is in a state of skidding to some extent. There is an important relationship between wheel slip rate and wheel angular acceleration. Therefore, an anti-slip control algorithm based on wheel angular acceleration and reference slip rate is proposed to combine the two as the input of the controller. The observation model of wheel angular acceleration and reference slip rate is derived. The drive anti-skid control method based on the optimal slip rate can solve the problem of excessive sliding of the drive wheel when the electric vehicle accelerates rapidly to a certain extent. However, there are also some defects, such as drive torque fluctuations, speed detection difficulties. In order to solve the above problems, a driving anti-skid control method based on wheel angular acceleration and reference slip rate is proposed. This control method can monitor the wheel angular acceleration in real time and predict the change of slip rate according to the positive and negative of the angular acceleration. The reference slip rate is used to estimate the speed. Therefore, it can effectively make up for the shortcomings of the control method based on the optimal slip rate.

2.3. Realization of anti-skid control of electric vehicle drive

Vehicle drive skid control system (ASR) belongs to vehicle traction control system (TCS), which is a kind of vehicle active safety control. Driving anti-skid control can control the wheel slip rate within a reasonable range, so that the wheels can obtain greater adhesion. It can prevent the vehicle from over-driving the wheels to slip during starting or accelerating, resulting in reduced longitudinal driving force and vehicle side adhesion. The drive skid control can effectively improve the stability and safety of the vehicle. With the development of pure electric vehicle (ev) has become a hot topic among researchers from all over the world, the research and development of anti-skid driving system has attracted more and more attention. One of the most important parts of the automobile drive anti-skid control system is the control method of the drive anti-skid system. At present, the logic threshold control method is used in most of the widely used drive anti-skid products. The logic threshold control method does not involve specific mathematical model, avoids complex theoretical calculation and analysis, and simplifies the controller design process. However, the controller threshold value can only be obtained through repeated tests, which is largely dependent on experience and has no sufficient theoretical basis. In addition, the vehicle's dynamic characteristics and road attachment conditions will change in real time during actual operations. Therefore, the robustness of logic limit control is not enough to satisfy the control effect of the vehicle under different conditions. The torque control of each wheel of distributed drive ev is independent of each other, so its driving force distribution scheme is varied. Also, since the driving force of each wheel is independently controllable, there is no need to add additional equipment for the driving force control of each driving wheel, and the driving anti-skid control system can be used at a lower cost. The purpose of this paper is to study a method of reasonably distributing the driving force of the front and rear axles to drive the wheels under the condition of ensuring the longitudinal force. So that the vehicle has the largest lateral force margin during driving. During driving, to resist lateral interference and ensure the lateral stability of the vehicle during driving. In actual electric vehicle systems, there are various forms of interference. For example, the drive motor drive torque expression error interference (the so-called drive motor drive torque expression error interference, such as a torque command of 100 N/m from the upper control system). And the actual output torque of the drive motor is 80 N/m, and yaw operation deviation is likely to occur. With the help of ESP, a driving force control algorithm for dynamic adjustment of left and right driving forces is designed to make the car more stable during driving. The relationship between slip rate and road adhesion coefficient can be seen that with the change of tire slip rate, both longitudinal and lateral road adhesion will change. In order to ensure a good longitudinal adhesion, lateral adhesion and not too much loss, it is necessary to control the tire slip rate in a certain range. The basic idea of logic threshold control is to control the tire slip rate between S (S is the specified slip rate range of vehicle tires). To ensure that the car tires have greater longitudinal adhesion during driving. In order to ensure the driving dynamic performance, there must be greater lateral adhesion to ensure the steering of the vehicle and prevent sideslip.

As can be seen from Fig. 4, the optimal adhesion characteristics of tires can be guaranteed as long as the control of wheel slip rate is maintained. Vehicle dynamics is mainly to study the vehicle motion under various working conditions, including longitudinal motion, lateral motion and vertical motion. Longitudinal dynamics mainly studies the dynamic response of vehicles in the longitudinal direction under driving and braking conditions. Lateral dynamics mainly studies the dynamic response of the vehicle in the lateral direction and the lateral characteristics of tires under the influence of steering wheel Angle input or crosswind. Vertical dynamics studies the dynamic response of vehicles in vertical direction, and mainly analyzes the vibration, pitch and other motion of vehicles under the excitation of road surface. An effective tool to study the dynamic characteristics of vehicles under various operating conditions is to establish mathematical models of vehicles. The mathematical model can express the motion state of the vehicle in the form of mathematical equation, and further study the vehicle dynamics. CarSim software was used to parameterize the vehicle model, including rolling resistance and air resistance characteristics of the vehicle, yaw moment of inertia, nonlinear tire sidetracking characteristics, steering gear ratio and other parameters [24]. The formula of longitudinal slip rate of wheels in the process of automobile driving is as follows:

$$\mathrm{S} = \frac{R-\lambda}{2\Delta E + \Delta I} \times 100\% \tag{7}$$

It can be seen from the formula that the wheel slip rate is determined by the vehicle speed and wheel speed. As long as the wheel speed is controlled, the purpose of controlling the wheel slip rate can be achieved. When a car is running, almost all external forces, except air resistance, act on the tires through the ground. The motion characteristics of the vehicle are closely related to the forces exerted on the tires, so the tire model has a great impact on the accuracy and reliability of the simulation results. Further calculate the anti-slip control program, and the iterative process is as follows:

1. Specify the population size, that is, how many individuals are in each generation. Using a large population scale, the genetic algorithm can search the space more thoroughly, but will make the genetic algorithm run slowly. Here, the initial population scale is set to 200. That is to seek the optimal solution of tire model parameters among 200 vectors.
2. The genetic algorithm iterates with the mechanism of superior and slight elimination to eliminate the individuals with small fitness and select the high-quality individuals with large fitness for reproduction. The best individual is selected through a sorting algorithm. This sorting algorithm measures the pros and cons of individuals based on the order of individual fitness values rather than the size of individual fitness. Thereby eliminating the influence of original fitness.
3. High quality individuals produce offspring through crossover and mutation. Crossover is when two good individuals swap genes at one point or more to produce a new individual. The probability of crossing is 0.85. Variation is to create variation children by changing individuals in a population with a small random number, so that the genetic algorithm can search a wider space and select uniform variation with a probability of 0.010.
4. Repeat 2 and 3 steps to carry out iterative calculation on the population, meet the cut-off condition, and get the optimal solution.

At present, the commonly used tire models are divided into empirical model, theoretical model and semi-empirical model. The semi-empirical model is based on theoretical research and combined with data. It has the advantages of other two models and is more accurate. The vehicle anti-skid (ASR) control system adjusts the torque of the driving wheels through appropriate control algorithms and control strategies. In this way, the slip ratio of the driving wheels is kept within the optimum range, thereby ensuring a vehicle with the best driving capability. In this paper, the anti-skid control algorithm and strategy of four-wheel drive vehicle are studied, as shown in Figure 5.

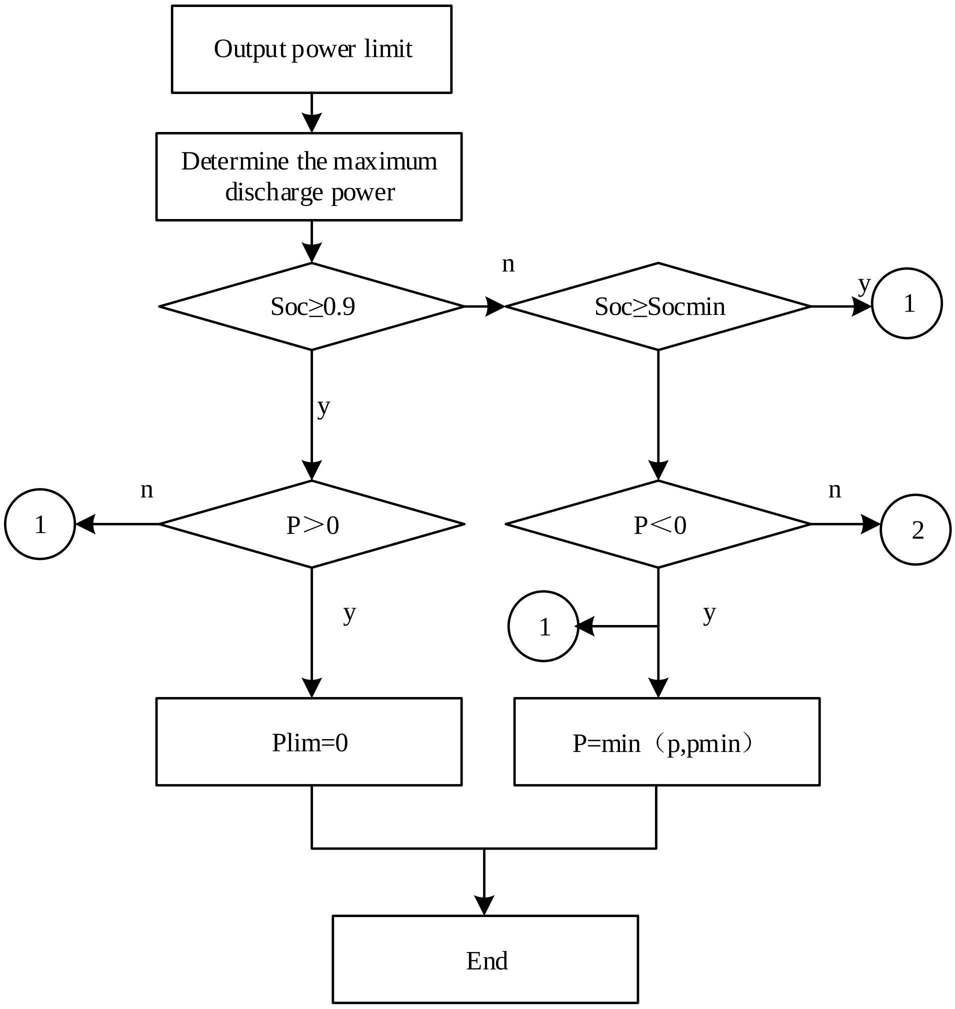

Figure 4. Anti-skid control flow of electric vehicle drive

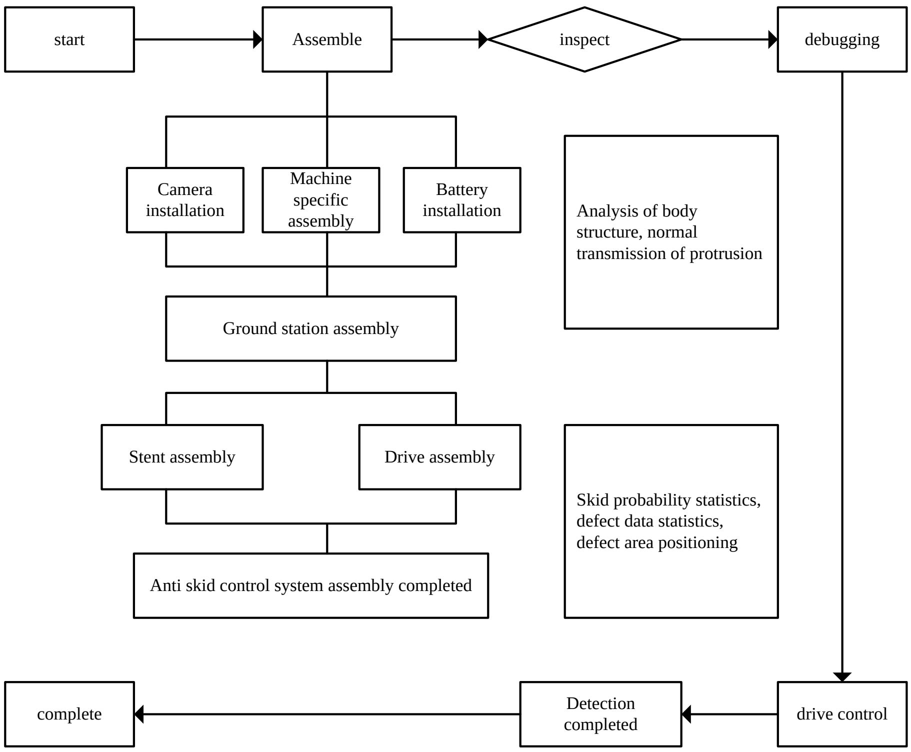

Figure 5. Anti-skid control mode of electric vehicle drive

Based on the sliding mode variable structure control algorithm, the optimal driving torque of the vehicle is determined in real time according to the speed of the vehicle and the sliding speed of the driving wheel. The torque allocation strategy is based on the fuzzy control algorithm, which comprehensively considers the driving speed, battery SOC and demand torque, and reasonably distributes the torque of engine, motor and wheel-yi motor on the principle of high engine efficiency and good economy. Both the sliding mode variable structure control and the fuzzy control have strong robustness. It does not need to establish an accurate mathematical model of the controlled system, and it has little dependence on the system.

3. Analysis of simulation results

3.1. Simulation design

Due to the real motion of the vehicle system there will be many unpredictable interference factors, such as lateral wind interference, driving motor, driving torque expression error interference. In order to resist the influence of interference factors on vehicles during vehicle movement, with the help of the concept of vehicle stability control, the left and right driving torque is dynamically adjusted by using the obtained ideal driving force distribution ratio of front and rear axles, and the theoretical algorithm is simulated and verified. Simulink was used to build ideal vehicle model. Simulink is a software package used to model, simulate and analyze dynamic systems. It supports linear and nonlinear systems, continuous and discrete time models, or a mixture of the two. In the vehicle simulation system, the ABS controller reads the wheel speed signal from the wheel speed sensor. According to the internal algorithm, it sends out the pressure increase, hold pressure and pressure reduction signals that make the brake actuate. This signal is input to the computer through the interface circuit and converted into a signal that can be recognized by the vehicle model. The vehicle model accepts inputted vehicle parameters such as vehicle mass, initial braking speed, etc., to simulate the operating state of the vehicle under ABS control. But the ideal model would ignore some degree of freedom, wind resistance, road surface and other factors. Therefore, this kind of simulation platform cannot well verify the control effect of the controller under the limit condition. A general electric vehicle co-simulation platform was established by using Simulink and Carsim software, and a simulation platform for pure electric vehicle drive control system was designed according to the requirements. Its structure is shown in the figure. The control strategy and motor model are built in Simulink software, and the vehicle dynamics model is built in CarSim software. The two can form a seamless connection. Based on this, the vehicle drive anti-skid control simulation platform based on Simulink is demonstrated as follows:

The vehicle test platform developed in this paper adopts the independent drive scheme of the rear wheel double motor. Considering cost, design difficulty, feasibility and other factors according to the actual requirements, the vehicle design mainly aims at the power and range. The vehicle design objectives are summarized as follows: Power: maximum speed >50 km/h; 100 km acceleration 5 s; Maximum climbing grade 10%;

Range: >30 km on a single charge;

Control system: it is a general configurable control platform which can quickly realize the modification of driving control strategy and realize the acquisition and processing of sensor signals.

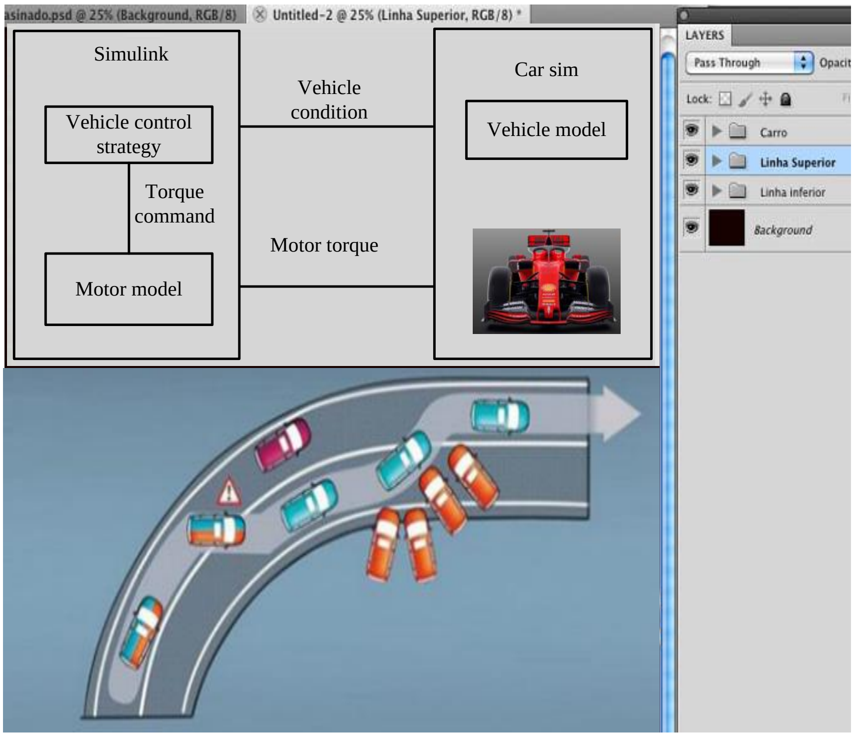

Figure 6. Simulation platform of vehicle drive anti-skid control based on Simulink

Table 1. Simulation parameters

Parameter	numerical value	Units
Vehicle quality	350	Kg
Length × width × height	160*120*180	mm
Wheelbase	1600	mm
Track width (front / rear)	1240/1260	Mm
Reduction ratio of reducer	4.2	-
Minimum ground clearance	80	mm
Centroid height	320	mm
Distance from center of mass to front / rear axle	860	mm
Yaw moment of inertia	221.62	Kg/m^2
Rated power	36	Kw
peak power	84	Kw
Torque setting	80	Nm
Peak torque	140-160	Nm
Maximum speed	300-320	Rpm
input voltage	300-330	v
Rated current	560-590	A
peak current	8000	A
Rated torque	5.4	Nm
Maximum torque	12000	Nm
Maximum input speed	3.6	Rpm
Quality	2.75	KG
Nominal capacity	4.6	mAH
Rated voltage	70	V
Discharge cut-off voltage	160	V
Charging cut-off voltage	280	V
Maximum continuous charging current	16	A
Maximum instantaneous charging current	≤0.6	A
Maximum continuous discharge current	264±0.2	A
Maximum continuous discharge rate	12-3600	C
internal resistance	3*360	m
Weight	3	kg
Operating temperature (charging and discharging)	0-35/-16-20	°C

Combined with the data in the above table, CRIO vehicle controller is further used for experiments. Its main functions include: collecting and processing the driver's driving intention, vehicle status and other signals, the calculation of vehicle drive control strategy, and sending the command signals such as torque output, mode and running state to the motor driver through the communication association. As the underlying controller, the main functions of the motor driver include: receiving the command signal of the vehicle controller, collecting the actual torque, speed, current, temperature and other signals of the drive motor, and feeding them back to the vehicle controller through the communication protocol. The sensor system is responsible for collecting the driver's driving intention and vehicle status signals, mainly including: accelerator pedal sensor, brake pedal sensor, steering wheel Angle sensor, triaxial acceleration sensor, wheel speed sensor, etc. CRIO vehicle controller input interface definition and each signal form are shown in Table 2.

Table 2. Output signal acquisition of vehicle controller

Input quantity	Function description	Signal source	Signal form
Accelerator pedal signal	Expected torque of the whole vehicle	Accelerator pedal sensor	0.5-4.5 v
Brake pedal signal	Brake control signal	Brake pedal sensor	0.5-4.5 v
Steering wheel angle signal	Check steering wheel angle	steering wheel angle sensor	Can communication protocol
Motor speed times	Detection of motor speed	Motor driver motor driver	Can communication protocol
Motor torque signal	Test motor torque	Motor driver motor driver	Can communication protocol
Yaw rate multiple	Obtain yaw rate	Triaxial acceleration sensor	0-5 V voltage
Longitudinal acceleration signal	Obtain longitudinal acceleration	Triaxial acceleration sensor	1.2 ~ 1.2 V
Lateral acceleration signal	Obtain lateral acceleration	Triaxial acceleration sensor	1.2~ 1.2 v
Wheel speed signal	Get wheel speed	Wheel speed sensor	0~5 V voltage
Reserved interface	Follow up signal supplement	-	-

3.2. The simulation results

3.2.1. Drive skid - proof buckle notification rule detection

According to practical experience and simulation results, in order to prevent the wheel from over-sliding, the wheel angular acceleration should be kept within the range of PM, and the slip rate should be kept within the range of PS. Therefore, the design of fuzzy inference rules is shown in the table, with a total of 28 fuzzy inference rules.

Table 3. detection results of the notification rules of the adaptive drive skid buckle

Rule	Input		Output
	Wheel angular acceleration	Slip ratio	Torque output
1	PS	NB	PS
2	ZE	NB	ZE
3	PM	NB	PM
4	PB	NB	PB
5	ZE	NM	PS
6	PS	NM	ZE
7	ZE	NM	PM
8	PB	NS	PB
9	PB	NS	PS
10	PS	NS	ZE
11	PM	NB	PM
12	PM	NM	PB

In Table 3, P is the initial value of actual acceleration, PB is the range of actual acceleration value, PM is the reasonable range of acceleration, PS is the predicted range of acceleration, N is the initial value of slip rate, and NB is the range of actual slip rate. NM is the reasonable range of slip rate, and NS is the predicted range of slip rate. ZE is the reasonable range of torque output. It is the key of the research to simulate the road running condition of the vehicle when the vehicle starts or accelerates rapidly, when the vehicle starts with the maximum output torque. In the simulation, the steering wheel angle was set to remain at zero. The road adhesion coefficient is 0.85. The driving torque of the vehicle within 15s under DRI reaches the maximum 70Nm dimension command. The vehicle continues to accelerate until the steering wheel is overloaded. The initial speed of the vehicle is set to 20 m/s, maintaining a uniform speed, the front wheel Angle reaches 60 at 0.5 s and remains unchanged, and the accelerator pedal opening remains unchanged. The road adhesion coefficient is set to 0.2. This condition is simulated when the driver suddenly encountered in front of the obstacle, there is no time to brake, to suddenly hit the direction of the operation.

3.2.2. Comparison of front and rear drive wheel slip rate

Based on the above, the simulation was conducted, and the test results were recorded. The specific results are shown in Figure 7:

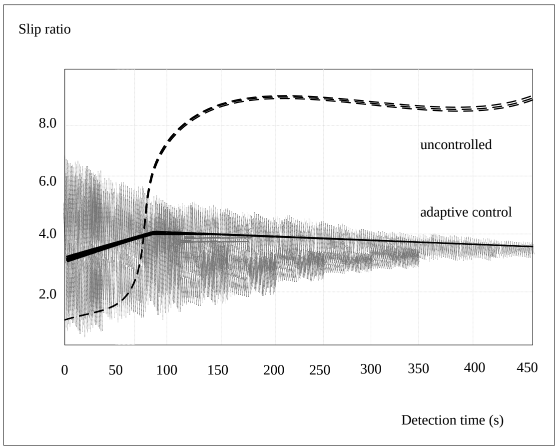

Figure 7. Detection of front and rear driving wheel slip rate of electric vehicle

As can be seen from Fig. 7, the dotted line is the slip rate of the driving wheel under the control of non-skid control. During acceleration, the slip rate of the driving wheel rapidly increases to 0.9, reaching the maximum value, and the wheel overrolls. The solid line is the curve of the sliding rate of the driving wheel after the driving anti-skid control. It can be seen from the figure that under the driving anti-skid control, the sliding rate of the driving wheel can be effectively controlled within the optimal sliding rate of 0.25 or so, and the maximum sliding rate does not exceed 0.3. Under the driving anti-slip control, the yaw velocity fluctuates greatly because of the additional yaw moment. Under the drive anti-slip control based on objective optimization, the yaw velocity is basically coincident with the ideal value, and the response is quick, and the overshoot is small. Under the drive anti-slip control, the maximum value of the center of mass side Angle is -0.16 rad, which fluctuates seriously and does not reach the steady-state value within 10 s. Under the drive anti-slip control based on the objective optimization control, the maximum value of the center of mass side Angle is -0.018 rad, and the response is rapid, and the steady-state value is reached at 0.5 s. It can be seen from the above analysis that the drive anti-skid control can control the slip rate of the drive wheel within the ideal range, and effectively control the excessive roll of the wheel. But it will produce extra yaw moment, increase the value of yaw angle, speed and center of mass yaw angle. And the fluctuation will become larger, which will damage the lateral stability of the vehicle. The anti-skid control based on objective optimization, by optimizing the left and right driving torque distribution and offsetting the additional yaw torque, ensures the lateral stability of the vehicle while controlling the driving wheel slip rate.

3.2.3. Comparison of fitting coefficient of driving anti-skid torque

In order to further verify the anti-skid control effect of the designed method for electric vehicle driving, the anti-skid torque fitting coefficient is detected, and the detection result is shown in Fig. 8.

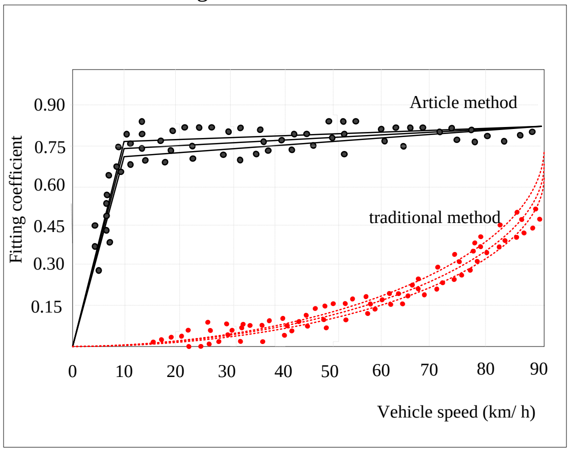

Figure 8. Test of torque fitting coefficient of driving skid resistance

The fitting coefficient of driving anti-skid torque determines the anti-skid control effect. The larger the coefficient is, the better the anti-skid control effect will be. Fig. 8 shows that the fitting coefficients of the driving anti-skid torque are different at different speeds. When the vehicle speed is low and the vehicle speed is 10 km/h, the fitting coefficient of the driving anti-skid torque of the traditional method is 0.01, while the fitting coefficient of the driving anti-skid torque of this method is 0.71. When the vehicle speed increases to 50 km/h, the fitting coefficient of the traditional method is 0.14, while the fitting coefficient of the driving anti-skid torque of this method is 0.75. The fitting coefficient of the driving anti-skid torque is always large, which indicates that the torque anti-skid control in this paper is effective.

3.2.4. Driving moment contrast

In order to verify the effect of driving torque control of the method in this paper, the anti-skid control method with energy consumption optimization and the anti-skid feedback control method with driving anti-skid control with target optimization are compared. The results are shown in Fig. 9.

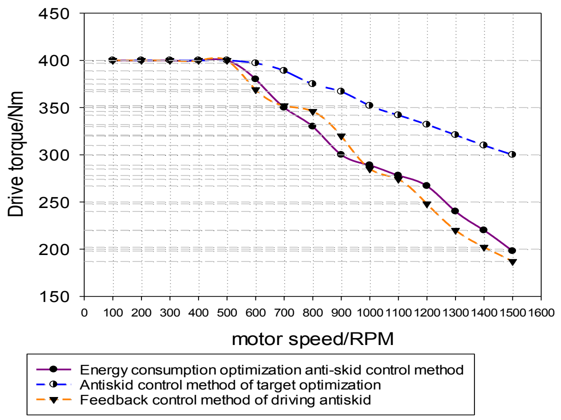

Figure 9. Driving torque control effect

Fig. 9 shows that when the motor speed of electric vehicles is within 0-500 RPM, the driving torque of the three methods is kept at 400 Nm. When the motor speed of the car exceeds 500 RPM and reaches 600 RPM, the driving torque of the energy consumption optimization anti-skid control method is 380 Nm. The driving torque of the anti-skid control method for driving is 369 Nm, and the torque of the target optimized anti-skid control method is 397 Nm. When the speed of the car motor reaches 1300 RPM, the energy consumption of the anti-skid control method with a driving torque of 240 Nm is optimized. The driving torque feedback control method is 220 Nm. The goal is to optimize the anti-skid control method of 321 Nm driving torque. This method can effectively increase the driving torque when the motor speed is too high and improve the anti-skid control effect.

4. Conclusion

In order to control the torque of electric vehicle, this paper designs a method of anti-skid control of vehicle torque based on objective optimization. The wheel angular acceleration and the reference slip rate are used as the two inputs of the fuzzy controller, and the torque of the driving motor is used as the output of the fuzzy controller. This controller can predict the change direction of tire slip rate according to the signal of wheel angular acceleration and prevent the fluctuation of driving torque caused by sudden change of motor torque. The wheel angular acceleration and reference slip rate were estimated by motor torque signal and wheel angular velocity signal. The following conclusions are drawn from the experiment:

1. The fitting coefficient of the driving anti-skid torque is always large, and the torque anti-skid control effect is better. When the vehicle speed increases to 50 km/h, the fitting coefficient of the traditional method is 0.14, while the fitting coefficient of the method in this paper is 0.75.
2. The method in this paper can effectively control the torque of electric vehicles against skid. When the motor speed reaches 1300 RPM, the driving torque of the method can still reach 321 Nm.

References

[1] Andersen KH, Bertelsen M, Zanini L, et al. Optimization of moderators and beam extraction at the ESS. Journal of Applied Crystallography, 2018, 51(2):264-281.

[2] Pinson RM, Lu P. Trajectory design employing convex optimization for landing on irregularly shaped asteroids. Journal of Guidance Control and Dynamics, 2018, 41(6):1-14.

[3] Ekanayake S, Dutta R, Rahman MF, et al. Direct torque and flux control of interior permanent magnet synchronous machine in deep flux-weakening region. Iet Electric Power Applications, 2018, 12(1):98-105.

[4] Otsuka T, Kuroiwa Y, Sato K, et al. Use of mixer torque rheometer to clarify the relationship between the kneading states of wet mass and the dissolution of final product in high shear granulation. Chemical & Pharmaceutical Bulletin, 2018, 66(5):554-561.

[5] Oene MMV, Ha S, Jager T, et al. Quantifying the precision of single-molecule torque and twist measurements using Allan variance. Biophysical Journal, 2018, 114(8):1970-1979.

[6] Janzen NR, Hight RE, Patel DS, et al. Estimation of critical end-test torque using neuromuscular electrical stimulation of the quadriceps in humans. European Journal of Applied Physiology, 2018, 118(2):1-8.

[7] Liang T, Wang XJ, Luo LQ. Torque adaptive allocation control of four wheel distributed drive electric vehicle. Computer Simulation, 2018, 035(012):111-116.

[8] Jiang T, Geng C, Xue QC, Zhang X. Torque distribution strategy of front and rear axle independent drive electric vehicle based on energy consumption optimization. Engineering of Surveying and Mapping, 2019, 43(05):102-109.

[9] Tang QD, Ge X, Liu YC, et al. An improved switching-table-based DTC strategy for the post-fault three-level NPC inverter-fed induction motor drives. Iet Electric Power Applications, 2018, 12(1):71-80.

[10] Siracusano G, Tomasello R, D'Aquino M, et al. Description of statistical switching in perpendicular STT-MRAM within an analytical and numerical micromagnetic framework. IEEE Transactions on Magnetics, 2018, 54(5):1-10.

[11] Ende MVD, Chen JY, Ampuero J, et al. A comparison between rate-and-state friction and microphysical models, based on numerical simulations of fault slip. Tectonophysics, 2018, 733:273-295.

[12] Zhou XP, Chen YD, Zhou, LM, et al. Power coordinated control method with frequency support capability for hybrid single/three-phase microgrid. Iet Generation Transmission & Distribution, 2018, 12(10):2397-2405.

[13] Xiao J, Hu C, Ouyang G, et al. Impacts of oil implied volatility shocks on stock implied volatility in China: Empirical evidence from a quantile regression approach. Energy Economics, 2019, 80(5):297-309.

[14] Wen F, Zhao Y, Zhang M, et al. Forecasting realized volatility of crude oil futures with equity market uncertainty. Applied Economics, 2019, 51(59):6411-6427.

[15] Jiang DS, Correa-Gallegos D, Christ S, et al. Two succeeding fibroblastic lineages drive dermal development and the transition from regeneration to scarring. Nature Cell Biology, 2018, 20(4):422-431.

[16] Linn, J, Wang, Z, Xie, L. The long-run effects of housing location on travel behavior: Evidence from China's housing reform. Canadian Journal of Chemistry, 2018, 49(6):695-702.

[17] Caldwell KB, Boyer RHW. Bicycle commuting in an automobile-dominated city: how individuals become and remain bike commuters in Charlotte, North Carolina. Transportation, 2018, 47(4):1-22.

[18] Othman RNFKR, Zuki NAM, Ahmad SRC, et al. Modelling of torque and speed characterisation of double stator slotted

rotor brushless DC motor. Iet Electric Power Applications, 2018, 12(1):106-113

[19] Hsu CH. Fractional Order PID Control for Reduction of Vibration and Noise on Induction Motor. IEEE Transactions on Magnetics, 2019, (99):1-7.

[20] Trancho E, Ibarra E, Arias A, et al. PM-assisted synchronous reluctance machine flux weakening control for EV and HEV applications. IEEE Transactions on Industrial Electronics, 2018, 65(4):2986-2995.

[21] Li J. Distributed multi-level inventory algorithms for automotive maintenance spare parts based on centralized control model. Jordan Journal of Mechanical and Industrial Engineering, 2020, 14(1):89-99.

[22] Rahimi M, Fazlollahtabar H. Optimization of a closed loop green supply chain using particle swarm and genetic algorithms. Jordan Journal of Mechanical and Industrial Engineering, 2018, 12(2):77-91.

[23] Gao H, Sun Z, Tao L, et al. Effect of fiber modulus on natural frequency of composite automobile drive shaft. Fiber Reinforced Plastics/Composites, 2018, (05):58-63.

[24] Li Y, Deng HF, Xu X, et al. Modelling and testing of in-wheel motor drive intelligent electric vehicles based on co-simulation with Carsim/Simulink. IET Intelligent Transport Systems, 2019, 13(1):115-123.

JJMIE

Volume 15, Number 1, March. 2021
ISSN 1995-6665
Pages 51 - 58

Jordan Journal of Mechanical and Industrial Engineering

The Role of Double-Cylinder Insulation Technology in Ensuring the Quality of Bored Pile Concrete under Negative Temperature Condition

Ziying Liu[a], Tianlai Yu[a,*], Ning Yan[a], Zhihai Piao[b], Hongxiang Zhang[a]

[a]*College of Civil Engineering, Northeast Forestry University, Harbin150040, China*

[b]*Research and Development Center, Longjian Road and Bridge Co., LTD,Harbin 150090, China*

Received July 18 2020 *Accepted Feb 20 2021*

Abstract

In this paper, the cement concrete with low heat of hydration was prepared by adding fly ash, and then used in the double-cylinder insulation technology. Based on heat dissipation test, thermal conductivity test and low temperature strength test of the prepared concrete, the growth law of concrete strength under negative temperature condition was studied. The strengths of three concrete test piles at the corresponding temperature were measured by ultrasonic method, and the influence law of double-cylinder insulation technology on the change of concrete strength was studied. The results show that the curing temperature dropped from 20□C to -3□C, -5□C and -7□C on the 28th day. Compared with the standard curing temperature, the strength loss was 29.7%, 31.7% and 42.8%, respectively. There were similar rules on the 60th day and 28th day. In the first 7 days, the temperature of low hydration heat concrete was 1. ~2.8°C lower than that of ordinary concrete. From the 7th day to the 28th day, the temperature of low hydration heat concrete was 0.5°C higher than that of ordinary concrete. After applying the double-cylinder insulation technology to the concrete, the temperature was increased by 7.9°C, 7.3°C and 4.8°C in 0~3rd day, 3rd~7th day and 7th~28th day, respectively. Compared with strength on the 28th day, the strength of low-hydration heat concrete was 2.15% higher than that of ordinary concrete. After applying polyurethane insulation layer, the strength of the low-hydration heat concrete increased by 18.6% compared with that of the low-hydration heat concrete without insulation layer.

Keywords: negative temperature, concrete, low heat of hydration, heat preservation, temperature of foundation pile, strength;

1. Introduction

Daxinganling belongs to the seasonal permafrost area, and bridges generally use bored pile foundations [1, 2]. The average ground temperature of frozen soil is basically 0 ~ -3.5°C [3, 4]. The cast-in-place pile concrete is in a low temperature environment for a long time, which will cause the hydration rate of the concrete to decrease obviously, and the hydration heat release is to be reduced significantly under the same period. Although the lower hydration heat release will reduce the disturbance of temperature rise to the frozen soil and shorten the frozen soil's refreezing time, it will cause a series of problems such as slow growth of the strength of the cast-in-place pile concrete itself, inadequate hydration and even insufficient strength [5]. Therefore, it is necessary to carry out experimental research on early mechanical properties of concrete under negative temperature conditions, and to grasp the law of concrete strength growth under negative temperature conditions, ~~which has practical significance for the~~ design and

* Corresponding author e-mail: tianlaiyu@126.com.

At present, the strength growth of concrete under negative temperature has been studied abroad. Michel Pigeon [6] and others believe that when the change of gas content could no longer improve the freezing resistance of high-strength concrete, the different types of cement, aggregates and curing periods have certain effects on the freezing resistance of small-water-binder ratio concrete. Through experiments, Nurse has found that the compressive strength of concrete increases as the product of temperature and time increases [7]. The research committee of natural environment concrete performance in Japan has studied the development law of concrete strength under natural cold and hot weather [8-12].

The research on the strength growth of concrete under negative temperature mainly focuses on the influence of antifreeze on concrete. Yang Yingzi and Ba Hengjing [13, 14] and others believe that after the completion of stirring, there are more water molecules around the coarse aggregate, after condensation hardening, it is loose porous, forming the interface transition zone, and they also think that the region is the weakest link, it has a significant impact on the mechanical properties and durability of concrete. The antifreeze is mainly to improve the microstructure of the

  - Volume 15, Number 1 (ISSN 1995-6665)

negative temperature interface, so that the frost heaving stress in the transition zone is reduced, thus reducing the internal structural damage. The addition of antifreeze has different effects on the negative temperature concrete. When the appropriate amount of antifreeze is added, it mainly reduces the freezing point of water in concrete and accelerates the formation of early structure effectively; when the antifreeze mixed is in excess, due to the large amount of salt in the antifreeze, it will cause different degrees of damage to the pore structure of the concrete. Tian Limei, Lu Weina[15] and others have studied the strength development of C35 concrete under naturally changing negative temperature. Li Fen and Yang Yongpeng [16] have studied the development law of compressive strength of concrete within C40 strength grade under negative temperature.

By summarizing the research contents of available literature, we can find that there are still some problems in the study of negative temperature concrete compressive strength, mainly including:

1. Under the condition of protecting permafrost, there are few studies on the strength variation rule of low heat of hydration mixed with fly ash under the condition of negative temperature.
2. In the ice rich area, there are few studies on the strength variation of concrete under the condition of negative temperature combined with actual engineering.
3. In the drilling pile construction, the double protective cylinder heat preservation plan is used, and the growth law of concrete strength is lack of study.

2. Study on low hydration heat concrete

In seasonal frozen soil areas, as the environmental temperature changes, liquid water and solid ice transform between each other and form complex physical and mechanical characteristics of frozen soil [17-20]. Therefore, how to reduce the thermal disturbance to the permafrost around the pile and ensure the concrete strength to meet the design requirements has become the main problem to be solved in the study of project construction in the frozen soil region. In order to solve this problem, this paper proposes to adopt low hydration heat concrete to replace conventional concrete and take necessary insulation measures.

2.1. The Selection of raw materials

In this paper, "Mengxi" P • O 42.5 ordinary silicate (low alkali) cement was selected, its properties are shown in Table 1; Coarse aggregate is composed of 10-20 mm and 16-31.5 mm single-grain grade gravelmixing in proportion, the former proportion accounts for 72% and the latter 28%. After mixing, it basically conforms to 5~31.5 mm continuous grading. River sand was adopted as the fine aggregate, which is smooth, hard, and well graded. It has fineness modulus of 2.51, which belongs to medium sand. Grade II fly ash from Qiqihar, KMSP water reducing agent, KMSP-14 antifreeze and drinking water were used in this work.

Table 1. The properties of cement

normal consistency	security /mm	setting time /min		compressive strength / MPa		flexural strength / MPa	
		Initial setting	Final setting	3d	28d	3d	28d
29.2	0.5	254	360	27.8	49.6	5.1	8.0

2.2. The influence law of fly ash on hydration heat

The hydration heat was measured by SHR-16S test instrument, and the measurement system of hydration heat of cement can be seen in Figure 1. According to the test method stipulated in GB/T 12959-2008, the hydration heat at different fly ash contents and different period were tested.

Figure 1. Hydration heat test instrument

In order to study the effect of fly ash on hydration heat, seven groups of experiments were carried out; group one was pure cement. In groups 2 to 7, the fly ash content was 20%, 22.5%, 24.8%, 27.0%, 29.0% and 31.1%, respectively. The experimental ages of hardening were 1d, 3 d, 7 d, 14 d and 28 d. The results of the experiment are shown in Figure 2.

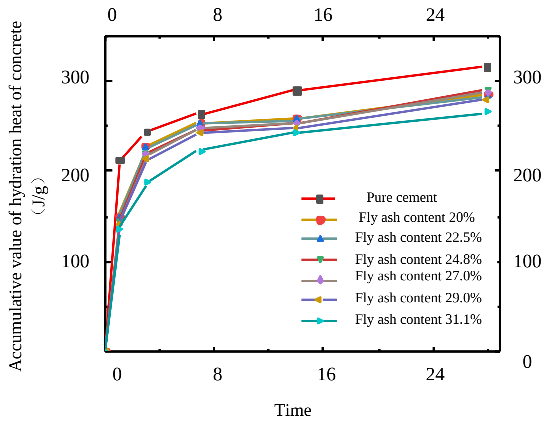

Figure 2. The curve of concrete hydration heat changing with time

Figure 2 shows that in the period of 0~3rd day, 3~14th day 14~28th day, pure cement in the hydration reaction of concrete released 243.2 J/g, 289.8 J/g, 315.8 J/g heat accumulatively. With the increase of fly ash content, the heat released by the concrete that falls into the fly ash gradually decreased. The amount of fly ash content increased from 20% to 31.1%, and the amount of heat released from hydration reduced from 228.4 J/g, 258.4 J/g, 285.7 J/g to 187.5 J/g, 243.2 J/g, 265 J/g, respectively.

It can be found that the hydration heat of pure cement in different ages of hardening is greater than that of different proportions of fly ash, and the greater the proportion of fly ash content, the smaller the hydration heat of cementing materials in each age of hardening was. Theoretically, the smaller the hydration heat of cementing material, the lower the temperature rise of the hydration heat of concrete will be, so the thermal disturbance to the soil around the pile foundation is much smaller. Combined with the relevant regulations in "Technical Specifications for Construction of Highway Bridges and Culverts" JTG / T F50-2011, in a freeze-thaw environment, the fly ash content should not exceed 30%, so 29% of cement material is selected.

2.3. The influence of cement content on hydration temperature

The concrete adiabatic temperature rise tester (HJW-3) was used to test the adiabatic temperature rise, and the influence of cement content on hydration temperature was studied. The instrument precision ≤±0.05°C, Temperature change of 50 L water at 72 hours ≤±0.05°C, as shown in Figure 3.

Figure 3. The laboratory concrete adiabatic temperature rise tester

The cement contents were 380 kg, 312 kg, 303 kg, 294 kg and 278 kg, respectively. The initial temperature was controlled at 20°C (error ± 0.5 °C). The content of admixture KSMP was 1.5%, and the antifreeze KM-14 was 5.0%, and the fly ash content was 29%. The shift test of adiabatic temperature rise is shown in Figure 4.

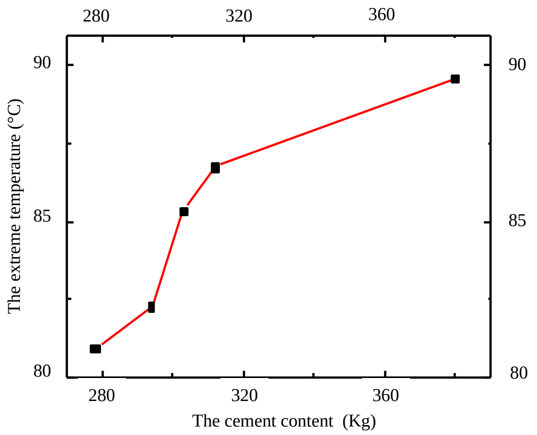

Figure 4. The influence of cement content on hydration temperature

As can be seen from Figure 2 to Figure 4, the adiabatic temperature increased continuously with the increase of concrete content. There was a nonlinear relationship between concrete content and adiabatic temperature rise. This was mainly due to that with the increase of cement content, the amount of water decreased, resulting in this uneven situation. Combined with the "Technical Specifications for Construction of Highway Bridges and Culverts" JTG / T F50-2011, the minimum concrete content of C30 concrete in severe cold areas cannot be less than 300 kg/m^3, so the final cement content was set to 303 kg/m^3.

2.4. Low hydration heat concrete mix ratio and slump test

According to section 2.3, 2.2, the mixing ratio of low hydration heat is, cement: fly ash: sand: gravel: water = (1:0.41:3.011:3.673:0.619). The mixing ratio of ordinary concrete is cement: fly ash: sand: gravel: water = (1:0.290:2.762:3.373:0.545). In order to meet the workability and water retention requirements of the construction process, slump test tests of cohesioness and water retention were added. In order to meet the workability and water retention required by the construction process, tests such as slump test, cohesion and water retention were conducted. The test results are shown in Table 2, which can meet the needs of the construction of bored pile project.

Table 2. The workability of low hydration hot concrete (mm)

Initial slump	Initial slump	slump after 60 min	cohesiveness	water retention
240	650×600	200	good	no bleeding

3. The influence of negative temperature on concrete strength

In order to study the strength growth law of bridge bored pile concrete in the frozen soil area under the low negative temperature curing environment, refer to literature [21-22], the proposed concrete mix ratio is seen in section 2.4. According to the method stipulated in*GB/T 50081—2002*, the curing temperature shall be conducted at 20°C (standard curing), -3°C, -5°C and -7°C, respectively. The compressive strengths of concrete specimen 150×150×150 mm at the 7th day, 14th day, the 28th day and the 60th day of hardening under different curing conditions were tested. The test data are shown in Figure 5.

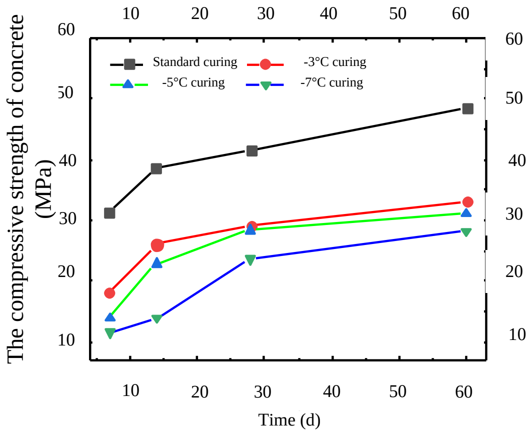

Figure 5. The summary chart of compressive strength of concrete

The data in Figure 5 show that at the same age of hardening, the strength of concrete decreased as the curing temperature decreased. When the age of hardening was 7 day, the concrete strength under -3°C curing only reached 43.4% of strength at the 28th day, under 20°C curing, and reached 75.8% under 20°C curing. When the age of hardening was 14 day, the concrete strength under -3°C curing only reached 62.8% of strength at the 28th day, under 20°C curing, and reached 93.0% under 20°C curing.

At the 28th day, the curing temperature was reduced from 20°C to -3°C, -5°C and -7°C, respectively. Compared with standard curing, the strength as reduced by 29.7%, 31.7% and 42.8%, respectively. The 60th day and 28th day of hardening showed similar rules, that is, the lower the curing temperature was, and the higher the strength loss was.

The higher the curing temperature was, the faster the strength of concrete developed in later period, that is, the 14th day- the 60th day strength. When the age of hardening was 60 d, the concrete under -3°C curing only reached 79.7% of the strength at the 28th day under 20°C curing and reached 117.4% under 20°C curing.

In order to ensure the strength of concrete under negative temperature, on the one hand, the temperature of the bored pile concrete must be increased, and on the other hand, the concrete strength level should be high. According to the research results of the temperature field of the concrete pile body, the curing temperature after concrete pouring was -2 ~ -3°C. Taking C30 concrete as an example, the strength loss under -3°C at the 28th day was 29.7%. At this point, it should be configured according to C43 to ensure that the concrete strength reaches C30.

4. Study on heat insulation effect of adding polyurethane between double-layer steel protective cylinders

4.1. The experimental site

The study was based on the bridge bored pile construction project of Jingmo highway. The site is located in an island-shaped permafrost area in the hilly and low mountains of Mohe County, Daxinganling area, Heilongjiang Province, with an average altitude of 550 m [23-24], the permafrost thickness in this area is 50-100 m [25], and the average annual ice age is 7 months [26]. Site I is located near pile 11 of K424+380 frozen soil bridge. Site II is located between Piers 15-16 of K425+290 frozen soil bridge. The depth of frozen soil on both sides of the piles is 11.5m. The soil layer on the pile side is shown in Table 3-a, Table 3-b.

4.2. Test pile materials and construction

1. Insulation scheme and materials

Polyurethane material was added between double cylinder for insulation. The polyurethane foam was used as insulation material, which has the advantages of low thermal conductivity and good insulation performance. The materials of protective cylinder is q235 steel, which has good plasticity and welding properties, and is convenient for construction.

2. Test pile construction

Three test piles were constructed by means of percussion drilling. Test pile 1# and 2# were located in site I, and the distance between them was 6m. Test pile 3# was located in site II. The concrete mix ratio is shown in section 2-4. Specific plans are shown in Table 4.

Table 3-a. Soil distribution of the site I

The serial number of soil layer	Name of the soil layer	The types of frozen soil	Soil thickness /m	Depth from the surface /m
1	Cumulosol	Ice layer containing soil	2.1	2.1
2	Ice layer	Pure ice	1.3	3.4
3	Cumulosol	Ice layer containing soil	1.6	5.0
4	Mucky soil	Ice layer containing soil	1.3	6.3
5	Roundstone	ice-rich permafrost	2.4	8.7
6	intense weathering tuff	Permafrost with much ice	2.8	11.5

Table 3-b: Soil distribution of the site II

The serial number of soil layer	Name of the soil layer	The types of frozen soil	soil thickness /m	Depth from the surface /m
1	Cumulosol	Ice layer containing soil	0.9	0.9
2	Silty clay	Permafrost with less ice	0.7	1.6
3	Silty clay	ice-rich permafrost	4.4	6.0
4	mucky soil	Permafrost with much ice	1.5	7.5
5	Roundstone	Permafrost full of ice	2.2	9.7
6	Pebble	Permafrost with much ice	1.8	11.5

4.3. The monitoring scheme of temperature field

In each test pile, a temperature measuring line was arranged at y of pile core and pile wall, and the numbers are A and B respectively. The lateral arrangement of thermometer hole is shown in Figure 6. In each thermometer hole, 13 to 14 measuring points were arranged along the depth of the rock and soil layer. The location of the measuring points should consider the boundary of the soil layer. The distance between the sensors in the same soil layer was 0.2-1.3 m, as shown in Figure 7.

The temperature sensor is resistive temperature sensing element DS18B2. Temperature collection range is -55 ~ +125°C, and the accuracy is ±0.2°C. JMWT-64RT system is adopted for automatic collection. The system is powered by batteries in winter and solar energy in summer.

The temperature of the concrete throughout the pouring process was monitored. The temperature before concrete pouring was studied; the temperature data every 4 hours after concrete pouring until 24 hours were collected; afterwards, temperature measurement data every 3 days, 7 days, 14 days and 28 days were collected; After 28 days of concrete curing, temperature data was collected every 15 days.

Table 4. Comparison table of test pile scheme (m)

Pile number	site	Pile diameter	pile length	Cement type	The type of protective cylinder	Pouring time
1#	I	1.4	11.5	C30ordinary cement concrete	Single layer steel protective cylinder	2017.10.31 11:20
2#	I	1.4	11.5	C30low hydration heat cement concrete	Double-layer steel protective cylinder, adding 10 cm polyurethane foam between layers	2017.11.04 11: 03
3#	II	1.4	11.5	C30low hydration heat cement concrete	Single laer steel protective cylinder	2017.10.22 14: 00

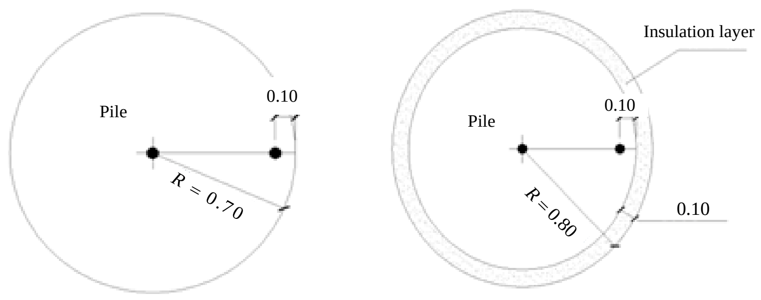

(a) 1# 3#test pile (b) 2#test pile

Figure 6: Horizontal layout of thermometer hole (m)

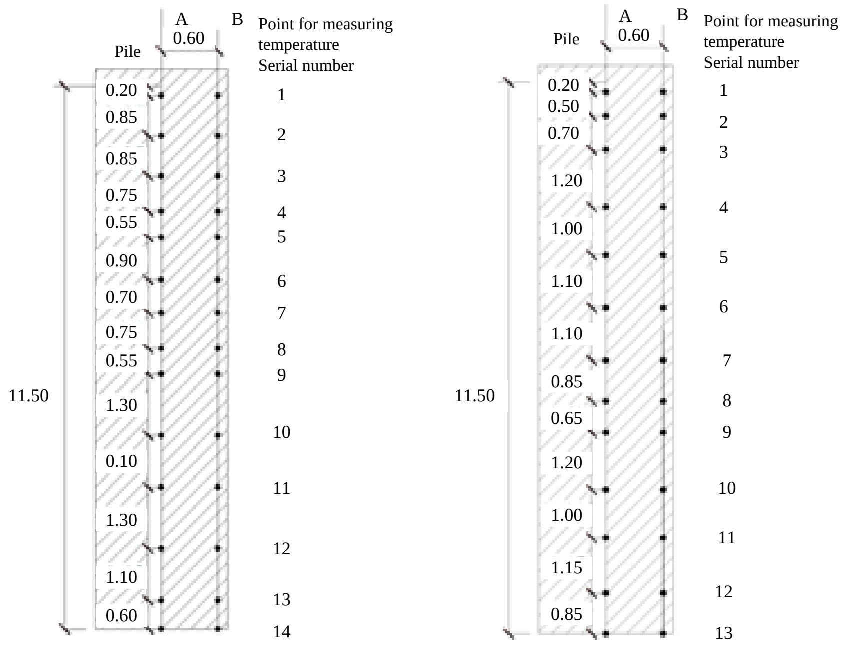

(a) 1# and 2# test pile (b) 3# test pile

Figure 7: Longitudinal layout of thermometer hole (m)

4.4. Study on temperature variation of pile foundation concrete

At the same age of hardening, the lower the curing temperature, the lower the compressive strength was. In the whole temperature field of pile foundation concrete, the temperature of pile wall was the lowest temperature. Therefore, the change law of pile wall temperature can better illustrate the effectiveness of low-hydration heat concrete integrating insulation layer. See the details in Figure 8-Figure 9 as below.

In Figure 8, the temperature field of the three test piles is unevenly distributed within a depth of 4.1 m from the surface, which was mainly due to the interference of external low temperature. In order to study the effect of low hydration heat concrete and the addition of insulation layer, only the temperature field below 4.1 m from the surface was considered in the analysis.

In the soil layer below 4.1 m, the temperature of the test pile 3 # was significantly lower than that of test piles 1# on the 1st day and 3rd day, which shows that the use of low hydration heat concrete reduced the early heat release of concrete and effectively reduced the thermal disturbance to the soil around the pile foundation. In the period of the 1st-28th day, the temperature of the test pile 2# was higher than that of the test pile 2#, indicating that the insulation effect of polyurethane material was better; The temperature of test pile 2# was obviously more uniform than that of test pile 3# and 1#, which indicates that the adding polyurethane between the two cylinders made the curing environment of pile foundation concrete more uniform. This provides a condition for the formation of the overall strength of pile foundation concrete and reduces the occurrence of too low local strength.

With the deepening of depth, the wall temperature gradually decreased, and the lowest temperature appeared at 11.5 m at the bottom of the pile. Based on Figure 9, the change of temperature with time was analyzed.

In the period of 0~3rd day, all the piles showed phenomenon of temperature rise, and in the 3th day, and test piles 1#, 3#and 2# had a maximum temperature of 11.2°C, 8.4°C and 16.3°C, respectively. In the 3rd~7th day, the temperature of each pile began to decrease, the average temperatures of test piles 1#, 3# and 2# were7.5°C, 6.3°C and 13.8°C, respectively. In the 7th-28th day, the average temperature of test piles 1#, 3# and 2# were 1.6°C, 2.1°C and 5.9°C, respectively. In the 28th~60th day, the temperature of all the piles reduced to -0.4 ~ -1.1°C.

In summary, the temperature of low hydration heat concrete was 1.2°C~2.8°C lower than that of ordinary concrete in the 0-7th day. In the 7th~28th day, the temperature of low hydration heat concrete was 0.5 C higher than that of ordinary concrete. This is because the low hydration heat concrete contained more fly ash content, which delayed the hydration process of the concrete. After adding the insulation layer in the same kind of concrete, the temperature of concrete improved by 7.9°C, 7.3°C and 4.8°C in the 0~3rd day, 3rd~7th day and 7th~28th day, respectively. The increase of curing temperature can directly enhance the strength of pile foundation concrete and reduce the loss of strength.

5. The quality verification of pile concrete

5.1. Monitoring scheme and data arrangement

In order to verify the quality of concrete, ultrasonic wave method was used to test the strength of three test piles at different ages of hardening. The sounding pipe was pre-buried in the concrete pile. Two sounding pipes were used to form a detection surface with a measuring point spacing of 100 mm. The cumulative height difference between the transmitting and receiving transducers of each measuring point did not exceed 2 cm. The test instrument is HC-U86 concrete ultrasonic detector. Figure 10 (a), (b) show the test principle, test instrument and test site for testing the concrete strength by ultrasonic method on site.

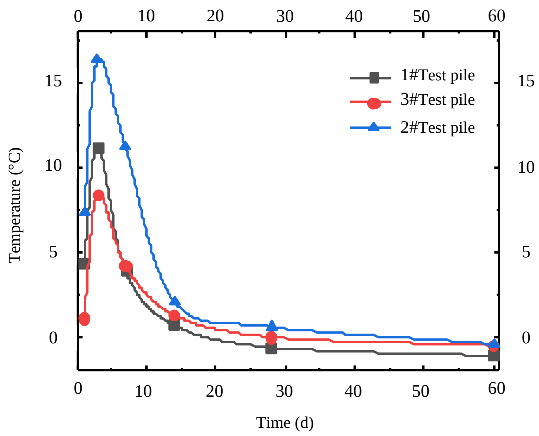

Figure 9. The change of pile bottom temperature with time (m)

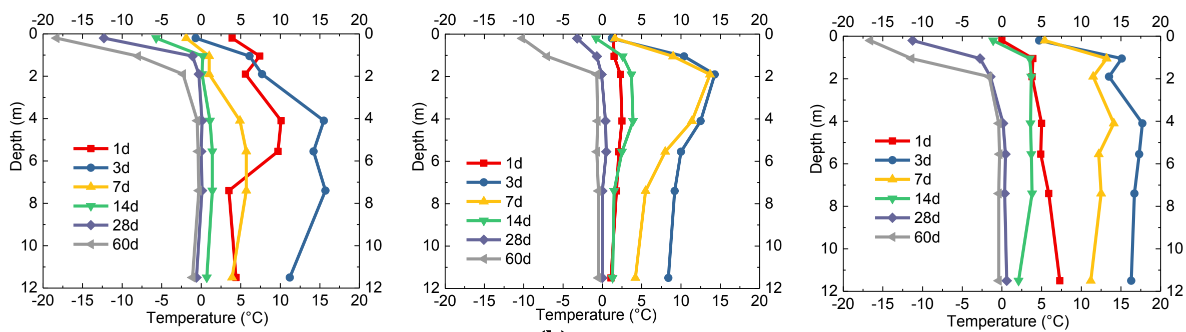

(a) Pile 1# **(b)** Pile 3# **(c)** Pile 2#

Figure 8. The curve of temperature changing with depth of test pile at each age of hardening (m)

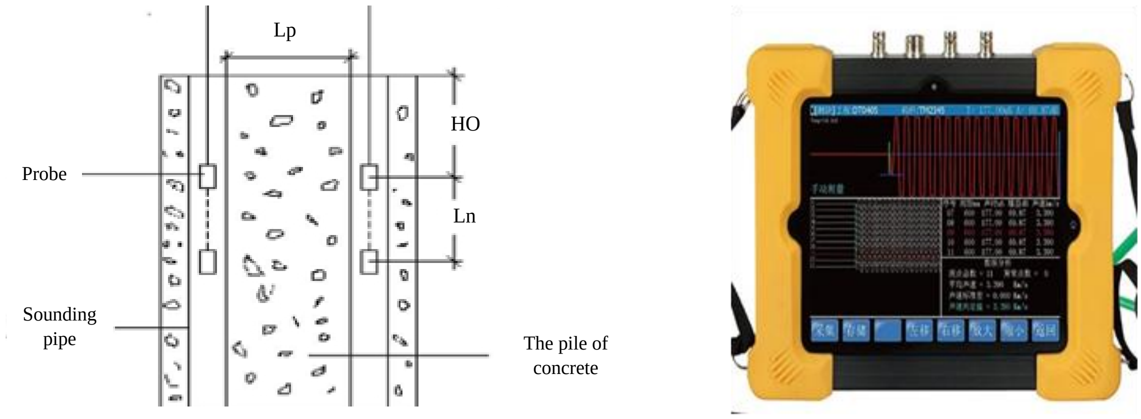

(a) Schematic diagram of field strength measurement

(b) HC-U86 concrete ultrasonic detector

Figure 10. Ultrasonic on-site measurement of concrete strength

The measured data of strength and sound velocity of concrete sample on the 28th day under negative temperature environment were fitted, and the results showed that the strength increased exponentially with the sound velocity, as shown in equation (1).

$$f_{cu} = 0.035 \cdot v^{4.437}, \quad R^2 = 0.989 \tag{1}$$

The correction coefficients of concrete strength for the 7th day and 14th day of curing are shown in equation (2) and equation (3) respectively.

$$\lambda_7 = 0.669 + 0.022 \cdot T - 0.001 \cdot T^2, \quad R^2 = 0.934 \tag{2}$$

$$\lambda_{14} = 1.087 + 0.049 \cdot T - 0.003 \cdot T^2, \quad R^2 = 0.969 \tag{3}$$

5.2. Pile quality analysis

In the study of pile quality, the law of compressive strength of concrete at a depth of 11.5 m changing with time was analyzed. In Section 4-4, the lowest temperature of each test pile appeared at a depth of 11.5 m. Through analysis of the compressive strength at this depth, the advantages of low hydration heat concrete with adding insulation layer can be reflected.

In Figure 11, the strength of test pile 2# at each age of hardening was greater than that of pile 1#and pile 3#. At the 28th day, there was not much difference in the strength of pile 1# and pile 3#, and the compressive strength of pile 2# was 18.2% higher than that of pile 3#. It shows that the method of adopting double cylinder insulation technology with addition of insulation layer can keep the pile in a relatively high curing temperature, which has an obvious effect on the growth of concrete strength.

6. Conclusions

1. In the indoor low temperature curing test, when the age of hardening was 28 day, the curing temperature dropped from 20°C to -3°C, -5°C and -7°C. Compared with the strength of standard curing, the strength was decreased by 29.7%, 31.7% and 42.8%, respectively. In order to ensure the strength of concrete under negative temperature, on the one hand, the temperature of bored pile concrete should be raised, on the other hand, the strength grade of concrete should be higher.
2. In the first 7 day, the temperature of low hydration heat concrete was 1.2°C~2.8°C lower than that of ordinary concrete. In the period of the 7th-28th day, the temperature of low hydration heat concrete was 0.5°C higher than that of ordinary concrete.
3. After applying double-cylinder insulation technology to the concrete, the temperature of concrete improved by 7.9°C, 7.3°C and 4.8°C in the 0~3rd day, the 3rd~7th day and the 7th ~28th day, respectively. Compared with the strength of concrete on the 28th day, the strength of concrete after adding polyurethane material between double cylinders was increased by 18.2% than that of low hydration heat concrete. This indicates that double cylinder insulation technology with addition of polyurethane material can increase the quality of concrete pile.

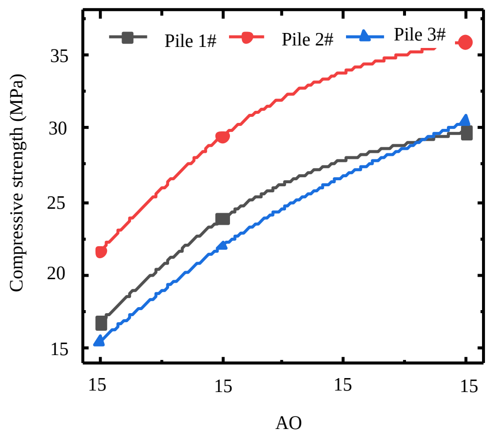

Figure 11. The curve of compressive strength of pile foundation concrete changing with time

Acknowledgements

The research was funded by National Natural Science Foundation of China (NSFC) (No. 51408258); Basic Scientific Research Operating Expenses of Central Universities (No. 2572015BB03).

References

[1] LX Zhang, ZW Xiong, LW Han. "Qinghai-Tibet Railway Permafrost Environment and Permafrost Project". Beijing: China Communications Press. Vol. 45, 2011.

[2] ZW Wu, YZ Liu. "Permafrost Foundation and Engineering Architecture". Beijing: Maritime Press, 2005, 26-31.

[3] H Ma, XP Liao, YM Lai. "Temperature control problem of concrete of pile foundation under construction in the permafrost regions of the Qinghai-Tibet Railway". Journal of Glaciology and Geocryology, Vol. 27, No. 2, 2005, 176-180.

[4] YW Zhou, DX Guo, GQ Qiu. "Permafrost in China". Beijing: Science Press, 2000. 89.

[5] ZG Liu, HJ Ba, HX Liu. "Development law of compressive strength of concrete cast-in-place pile in the permafrost region". Concrete, Vol. l. No. 6, 2005, 11-12+17.

[6] M Pigeon, R Gagné, PC Aïtcin et al. "Freezing and thawing tests of high-strength concretes". Cement and Concrete Research, Vol. 21, No. 5, 1991, 844- 852.

[7] L Quan, B Tian, DC Feng, et al. "Research on early strength prediction model of cement concrete based on maturity theory". Journal of Highway Communication Technology (Application Technology Edition), Vol. 02, 2012, 35-39.

[8] Katsura, E Kamada. "Strength Development of High Strength Concrete under Low Temperature". JCI- C32. Vol. 64. 1993.

[9] E Kamada, O Senbu. "A Study of Cold Weather Concreting of High Strength Considering Rising Temperature of Concrete Element". JCI- C32. 1993. 457.

[10] M Tabata. E Kamada. "A Long Term Exposure Test in Cold District on the Concrete Using Expansive Admixture". JCI-C32. 1993. 76-88.

[11] M Tabata, E Kamada. "A Study on Frost Resistance of the Concrete Exposed in Cold Districts". JCI- C32. 1993.66-68.

[12] Senbu, CG Han. "Investigation on Cumulative Temperature Equation of Concrete with Cold Weather Admixture". JCI-C32. 1993. 75-87.

[13] YZ Yang, HJ Ba. "Interface microstructure and mechanical properties of concrete with ant freezing admixture at subzero temperatures". Journal of the Chinese Ceramic Society, Vol. 08, 2007, 1125-1130.

[14] HW Deng, YZ Yang, SW Yang. "Influence of temperature regime on early damage degree of construction minus temperature concrete". Low Temperature Architecture Technology, Vol. 04, 2005, 19-21.

[15] LM Tian, WN Lu, HZ Zhu. "Test research on compressive strength of concrete under outdoor varied negative temperature curing and standard condition curing". Journal of Hebei Polytechnic College, Vol. 05, 2014, 68-69.

[16] F Li, YP Yang, HY Liu, et al. "Study on development law of concrete compressive strength under negative temperature". Railway Engineering, Vol. 02, 2016, 162-165.

[17] AV Sedelnikov, AS Filippov, TA Ivashova. "Earth's magnetic field measurements data accuracy evaluation on board of the small spacecraft "aist" flight model". Jordan Journal of Mechanical and Industrial Engineering, Vol. 12, No. 4, 2018, 253-260.

[18] R Wang, N Wu, XYu. "Design of digital aerial photography system for unmanned aerial vehicle based on wireless sensor network". Jordan Journal of Mechanical and Industrial Engineering, Vol. 14, No. 1, 2020, 25-36.

[19] EC Jekwu, AG Precious, AB Evans. "Evaluating the impact of unsteady viscous flow and presence of solid particles on pipeline surfaces during crude oil transport". Acta Mechanica Malaysia, Vol. 2, No. 2, 2019, 20-27, DOI: 10.26480/amm.02.2019.20.27

[20] SL Wang. "Temperature Field Change and Concrete Strength Growth Rule of Cast-in-Place Pile in Permafrost Environmental". Lanzhou Jiaotong University, Vol. 04, 2016, 1.

[21] JP Dai, QC Wang, ZG Xie. "Influence factors of strength growth of equal strength concrete under -3°C curing". Journal of Lanzhou Jiaotong University, Vol. 12, 2018, 1.

[22] Y Tian, Y Li. "Influence of admixture on strength development of low temperature concrete under different curing conditions". Concrete, Vol. 07, 2014, 1.

[23] Y Lu, WB Yu, M Guo, et al. "Spatiotemporal variation characteristics of land cover and land surface temperature in Mohe County, Heilongjiang Province". Journal of Glaciology and Geocryology, Vol. 39, No. 5, 2017, 1137-1149.

[24] B Zhao, Y Yu, J Guo, et al. "Using Wire Beam Electrode (WBE) to evaluate the corrosion behavior of Nd steel in acid medium". Materials & Corrosion Engineering Management, Vol. 1, No. 2, 2020, 23-26.

[25] HJ Jin, QH Yu, LZ Lv, et al. "Degradation of permafrost in the Xing'anling Mountains, Northeastern China". Permafrost and Periglacial Processes, Vol. 18, No. 3, 2007, 245 -258.

[26] L Chen, WB Yu, X Yi, et al. "Application of ground penetration radar to permafrost survey in MoheCounty, Heilongjiang Province". Journal of Glaciology and Eocryology, Vol. 37, No. 3, 2015, 723-730.

JJMIE

Volume 15, Number 1, March. 2021
ISSN 1995-6665
Pages 59 - 63

Jordan Journal of Mechanical and Industrial Engineering

Wear Properties of Aluminum Alloy 211z.1 Drilling Tool

Yong Liu[1], Lin He[2*], Sen Yuan[3]

[1]College of Mechanical Engineering, Guizhou University, Guiyang, 550025, China
[2]School of Minning and Civil Engineering, Liupanshui Normal College, Liupanshui 553004, China
[3]College of Mechanical Engineering, Guizhou Institute of Technology, Guiyang 550003, China

Received July 18 2020 Accepted Feb 20 2021

Abstract

In the application process of China's independently produced new aluminum alloy 211z.1 into high-end military and civilian industries, a great many holes are needed for fastening connection. However, the severe wear of the cutting edge of twist drill is an important factor that restricts the quality of hole processing and tool life. In this paper, the wear condition of the standard high-speed steel twist drill in drilling the new aluminum alloy 211z.1 is studied based on the drilling test, and the influence law of the drilling amount on the tool wear is revealed by designing a reasonable drilling test plan. The research results show that the cutting speed has a significant effect on the flank wear, and the drilling feed and the drilling height have relatively little influence on the flank wear of the tool.

Keywords: Aluminum Alloy 211z.1; High-speed Steel; Standard Twist Drill; Drilling Test; Flank Wear;

1. Introduction

Drilling is a commonly used processing method in production, it is one of the most important processes in metal cutting (accounting for about one-third of all metal cutting processes), and billions of drills are consumed every year in the world[1]. As early as in the 1960s, a large number of experimental studies on the processing of aluminum alloy, especially in the precision of hole making and surface integrity, were carried out from the aspects of tools, process methods, lubrication conditions, etc. As a widely used free-cutting material, especially with the emergence of various new aluminum alloy materials, the analysis of the drilling tool wear situation is still of great significance in the large-volume, continuous drilling process[2].

Aluminum alloy 211z.1 is one of the five registered grades of the 211z.x series independently developed by China, and it belongs to the new high-strength aluminum alloy materials of Al-Cu-Mn series. The main chemical composition is shown in Table 1[3]. At present, a lot of research has been done on thephase transformation[4-5], high temperature mechanical properties[6-7], fatigue properties[8] and microstructure properties[9-10] ofthe new aluminum alloy 211z.1. However, there are few studies on the cutting performance of the aluminum alloy, except for the processing methods of aluminum alloy such as turning[11] and milling[12], it is necessary to further expand the research scope and increase the research on the cutting performance of cast aluminum alloy, thus providing a theoretical basis for increasing the application of the aluminum alloy material in various high-end military and civilian industries and fields.

Based on theoretical analysis and drilling experiment results, the wear pattern of the tool during the processing of aluminum alloy 211z.1 is analyzed in this paper by using the standard high-speed steel twist drill,anda quadratic polynomial regression prediction model for the VB_{Bmax} wear value of the flankwas constructed by orthogonal test and linear regression analysis by taking the flank wear amount as the research object.

2. Drilling Test Plan

Aluminum alloy 211z.1 is produced by Guizhou Hualco Aluminum Co., Ltd., and its main mechanical properties are shown in Table 2[3]. The upper surface of the processed workpiece is flat, the size is 145 mm × 160 mm × 45 mm, and the V850A numerical control (vertical) machining center is adopted as the drilling experiment tool. The high-speed steel twist drill meets the technical standard of GB t 17984-2000. The tool diameter d = 8, 10 and 12mm for analyzing the drilling wear phenomenon of aluminum alloy 211z. 1, and the tool diameter d = 10mm for calculating the tool wear prediction model. Dry cutting and blindhole drilling are adopted in the experiment. Jerry DJCL Y92B detector and DMSZ7 video all-in-one machine are adopted as the tool wear detection device.

* Corresponding author e-mail: helin6568@163.com.

3. Breakage Form Analysis of Aluminum Alloy 211z.1 Drilling Tool

The twist drill is a complex-form double-edged boring tool that performs a semi-closed cutting pattern with cutting temperatures higher than the other cutting forms (such as turning, milling, etc.) under the same cutting conditions. Under the action of uneven high-field thermal coupling, the cutting load on the cutting edge is very uneven, and different areas of the cutting edge have different wear properties in different processing stages. In the continuous processing, with the parameter change of different processing objects , tool materials, pore sizes and processing, the form and characteristics of wear vary greatly, and the wear law is complex, often appear one wear pattern with many other forms of wear.

3.1. Chisel edge wear

In the drilling process of aluminum alloy 211z.1 and the pre-use of tool under the same working condition, the twist drill's chisel edge that plays the main function of positioning, centering and reducing the chattering effect during processing first contacts the material being processed. While rotating around the central shaft, the chisel edge crushes and scrapes the materials being cut, causing severe deformation, and the force of contact and thermal stress between the cutting edges of the tool are concentrated, and then a triangular-like smooth surface is quickly grinded out on both sides accompanied by bonding of aluminum alloy materials, forming a built-up edge, as shown in Figure 1. The hardness of the built-up edge is generally 2-3 times the hardness of the workpiece, and the built-up edge is stacked on the cutting edge to replace the cutting edge in cutting and protecting the cutting edge, and to increase the actual working front angle and reduce the cutting deformation[13-15]. The blunt circular cutting edge formed by stacking causes extrusion and overcutting, which reduces the processing accuracy, and the built-up edge is adhered to the processed surface after detaching, resulting in the surface roughness and unevenness.

Table 1. Chemical composition of aluminum alloy 211z.1[3]

Elemnt	Cu	Mn	Ti	Zr	B[a]	C[a]	Cd
%	4.0-7.5	0.20-0.6	0.05-0.40	0.05-0.50	0.005-0.07	0.003-0.005	0.05-0.50
Elemnt	RE	Be	Fe	Si	Other[b]		Al[c]
					single	total	
%	0.02-0.30	0.001-0.08	≤0.30	≤0.10	≤0.05	≤0.15	Rest

Table 2 Mechanical properties of aluminum alloy 211z.1[3]

Sample state	Tensile properties at room temperature		Tensile properties at high temperature (350°C)		Hardness (HBW)	Shock absorption energy (KU_2)/J
	Tensile strength R_m/MPa	Elongation after break A/%	Tensile strength R_m/MPa	Elongation after break A/%		
No less than						
T5	450	8	130	6	125	6.5

Processing parameters	$d=10mm$ $n=1000$r/min $f=0.13$mm/r $h=20mm$	$d=10mm$ $n=2750$r/min $f=0.13$mm/r $h=20mm$	$d=10mm$ $n=4500$r/min $f=0.13$mm/r $h=20mm$	$d=10mm$ $n=62500$r/min $f=0.13$mm/r $h=20mm$	$d=10mm$ $n=8000$r/min $f=0.13$mm/r $h=20mm$
Physical map	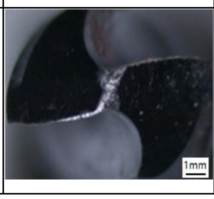	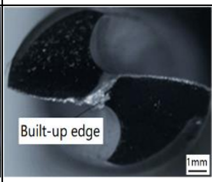	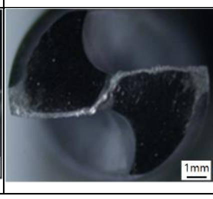	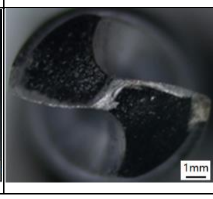	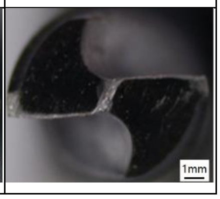

Figure 1. Physical map of chisel edge wear and built-up edge

3.2. Flank wear

In the drilling process of aluminum alloy 211z.1, the main flank of the twist drill is in continuous contact with the material being cut. Under the axial feed force and the rotational driving force, severe deformation and friction is caused between the tool and the material being cut, increasing the temperature and internal pressure in the contact zone and causing wear on the flank of the twist drill. The flank wear of the twist drill appears uneven wear distribution affected by the complex structure of the twist drill’s flank, and by the rotating and feeding composite spiral motion form. The flank wear of the main cutting edge is usually fanshaped with wear or a strip with an approximately uniform shape and a smaller width, as shown in Figure 2. The outermost edge of the main cutting edge has the largest rake angle, the highest cutting line speed, the heaviest cutting load and the highest cutting temperature, which is easy to form corner wear, as shown in Figure 3. The outer edge of the twist drill has the most serious wear, and the width of the wear band is the largest. When the rotational speed is high, the temperature and friction velocity of the outer edge increase, the thermal wear is intensified, and obvious “ablation” occurs, these observations are similar to that found by other researchers [16-17].

3.3. Rake wear

In the drilling process of aluminum alloy 211z.1, the contact surface between the tool and the chips has an inner friction zone and an outer friction zone, namely, a bonding zone and a sliding zone. The outer friction zone of sliding is away from the cutting edge, and the cutting temperature of which is lower than the temperature at the cutting edge, the heat dissipation is relatively fast, and sliding friction is formed between the chips and the tool, and thus the tool rake is less damaged; the inner friction zone of sliding is where the relative movement of the tool and the material occurs, high temperature and high pressure(2-3 GPa) are formed under the action of friction and extrusion. Under the affinity between the chips and the tool material, bonding (cold welding) of the material is formed, which is prone to bond and spread wear, causing craters on the rake area that is close to the main cutting edge. In addition, due to the semi-closed cutting form, the heat cannot be dissipated and discharged in time, causing the twist drill temperature to rise and chips to accumulate in the chip pocket and to adhere to the rake, aggravating the bonding and wear of the rake while making the craters more prominent, as shown in Figure 4.

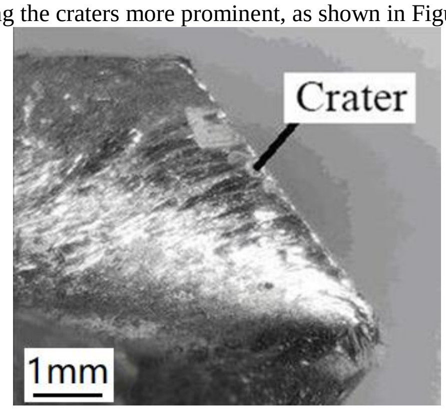

$d=8mm$, $n=1000\text{r/min}$, $f=0.13\text{mm/r}$, $h=15mm$

Drilling conditions: $d=8mm$, $n=1000\text{r/min}$, $f=0.13\text{mm/r}$, $h=15mm$

Figure 4. Physical map of the rake wear band of twist drill

Processing parameters	$d=8mm$ $n=4500\text{r/min}$ $f=0.1\text{mm/r}$ $h=10mm$	$d=8mm$ $n=4500\text{r/min}$ $f=0.2\text{mm/r}$ $h=10mm$	$d=10mm$ $n=4500\text{r/min}$ $f=0.2\text{mm/r}$ $h=15mm$	$d=12mm$ $n=8000\text{r/min}$ $f=0.2\text{mm/r}$ $h=10mm$	$d=12mm$ $n=8000\text{r/min}$ $f=0.2\text{mm/r}$ $h=20mm$
Physical map	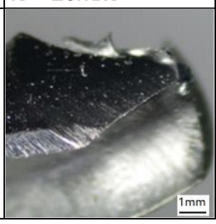	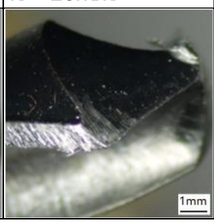	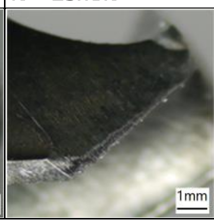	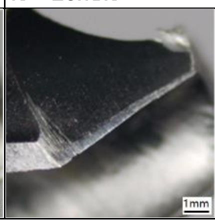	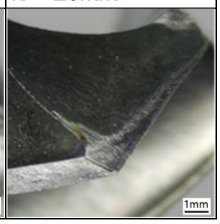

Figure 2. Physical map of the flank wear band after continuous drilling of 30 blind holes

Processing parameters	$d=12mm$ $n=2750\text{r/min}$ $f=0.25\text{mm/r}$ $h=20mm$	$d=12mm$ $n=4500\text{r/min}$ $f=0.25\text{mm/r}$ $h=20mm$	$d=12mm$ $n=6250\text{r/min}$ $f=0.25\text{mm/r}$ $h=20mm$	$d=12mm$ $n=4500\text{r/min}$ $f=0.05\text{mm/r}$ $h=20mm$	$d=12mm$ $n=4500\text{r/min}$ $f=0.15\text{mm/r}$ $h=20mm$
Physical map	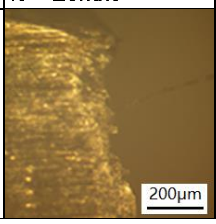	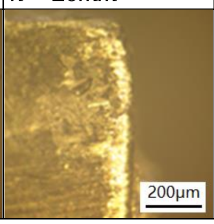	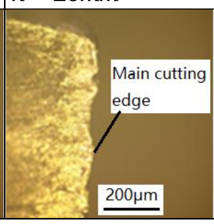	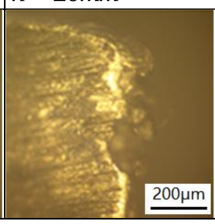	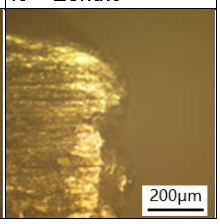

Figure 3. Physical map of the outer edge corner after continuous drilling of 30 blind holes

4. Prediction Model of Flank Wear

As shown in Figure 5, the cross cutting edge angle ψ between the cross cutting edge and the main cutting edge is taken as the measurement reference, and the wear value of flank VB_{Bmax} is taken as the research object, and the orthogonal drilling experiment is conducted, the VB_{Bmax} is measured according to different drilling processing parameters, and the flank wear prediction model is analyzed. Each group of experiments is repeated three times, and the average value is taken as the experimental result, as shown in Table 3.

Table 3. Parameters and flank wear values of the orthogonal drilling experiment

Plan	*v* (m/min)	*f* (mm/r)	*h* (mm)	VB_{Bmax} (mm)
1	250	0.13	10	0.4046
2	140	0.13	15	0.3217
3	250	0.2	15	0.8802
4	30	0.13	10	0.0932
5	140	0.13	15	0.3217
6	140	0.2	20	0.5522
7	140	0.05	10	0.2054
8	140	0.2	10	0.3387
9	250	0.05	15	0.3586
10	30	0.05	15	0.0439
11	140	0.05	20	0.3121
12	140	0.13	15	0.3217
13	140	0.13	15	0.3217
14	140	0.13	15	0.3217
15	30	0.2	15	0.1355
16	30	0.13	20	0.1744
17	250	0.13	20	0.9196

Note: *v*-cutting speed, *f*-feed, *h*-drilling height

The regression analysis on the experimental data of Table 3 is performed by using the Design Expert software, and the quadratic polynomial regression prediction model of the flank VB_{Bmax} wear value is obtained as follows:

$$\begin{cases} VB_{B\max} = 0.59101 - 3.13476\times10^{-3}\times v - 1.02093\times f - 0.057065\times h \\ +0.013194\times v\times f + 1.97182\times10^{-4}\times v\times h + 0.0712\times f\times h \\ +3.30785\times10^{-6}\times v^2 - 1.03556\times f^2 + 1.449\times10^{-3}\times h^2 \\ 30 \le v \le 250 \\ 0.05 \le f \le 0.2 \\ 10 \le h \le 20 \end{cases}$$

As shown in Table 4, a significance analysis of the regression model established is conducted, and the correction coefficient of the flank wear model is 0.982. The model can only reflect 98.2% of the relationship between the factor and the response value, and the influence of each factor on the flank wear is ranked as: cutting speed > feed > drilling height. The variable coefficient of the flank wear model response is 13.64%, and the experiment has a certain degree of reliability, thus the prediction model can be used for the analysis and prediction of flank wear of the aluminum alloy 211z.1 drilling tool.

The response surface diagram and contour map of the interaction of drilling parameters on flank wear are obtained by quadratic multiple regression fitting, as shown in Figure 6. The rise of the three response surfaces is obvious, and the curvature radius of the contour line is large, indicating that *f* and *v*, *h* and *v*, *h* and *f* have significant interaction effects on flank wear. As *v* increases, flank wear increases obviously; with the increase of *f* and *h*, the increase of flank wear is not obvious.

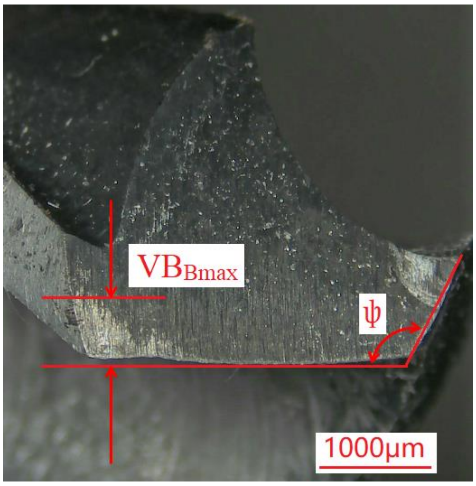

Figure 5. Measurement of wear band on flank of main cutting edge

5. Conclusion

1. The normal wear pattern of aluminum alloy 211z.1 drilling tool includes chisel edge wear, rake wear and flank wear, among which chisel edge wear appears first, accompanied by built-up edge; rake wear is usually accompanied by craters; and flank wear has a wide range, and the most worn parts are in the outer corner area. The aluminum alloy 211z.1 often occurs “sticking on tools” during the drilling process.
2. Based on the flank wear amount, a prediction model of aluminum alloy 211z.1 drilling flank wear is constructed, which ranks the influence of each factor on flank wear as follows: cutting speed > feed > drilling height.

Table 4. Checklist of the regression model

	Source of variance	Sum of squares	Degree of freedom	Mean square	F value	*P* value	Significance
VB_{Bmax}	Model	0.89	9	0.099	42.35	< 0.0001	Significant
	v	0.56	1	0.56	237.80	< 0.0001	
	f	0.12	1	0.12	51.40	0.0002	
	h	0.10	1	0.10	44.83	0.0003	
	Residual	0.016	7	2.342E-003			
	R^2 = 0.9820, R^2_{adj} = 0.9588, CV% = 13.64						

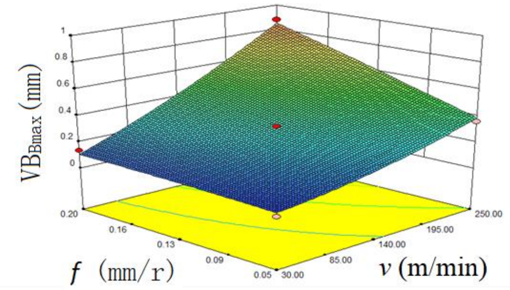

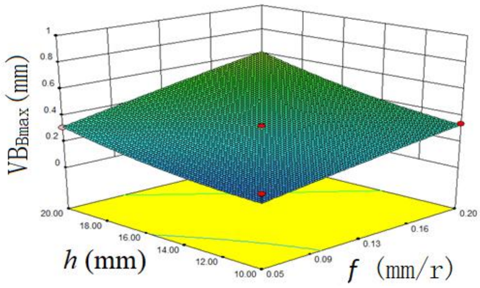

(a) Response surface of *f* and *v* to VB_{Bmax} (b) Response surfaces of *h* and *f* to VB_{Bmax}

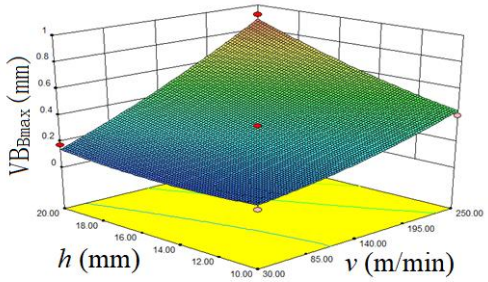

(c) Response surface of *h* and *v* to VB_{Bmax}

Figure 6. Multi-factor interactive response surface map

Acknowledgement

Supported by the projects of National Natural Science Foundation of China (51765009).

References

[1] Liu J.A. Discussion on the development trend of aluminum alloy materials and processing industry and technology (I). Aluminum Machining, 2012, 1(204): 13-18.

[2] Davim J.P., Sreejith P.S., Gomes R., and Peixoto C. Experimental studies on drilling of aluminium (AA1050) under dry, minimum quantity of lubricant, and flood-lubricated conditions. Proceedings of the Institution of Mechanical Engineers Part B Journal of Engineering Manufacture, 2006, 220(10): 1605-1611.

[3] Li R.H., Zeng P., and Li J.D. Interpretation of the national standard of aluminum alloy ingot for heat-resistant high-strength and toughness castings. Casting, 2013, 8(62): 811-813.

[4] Wu Y.F., Liu K.J., Zhang Z.K., Li Q., and Fu Y.Y. Thermal energy analysis: phase transformation of an Al-Cu alloy. Shanghai Metals, 2013, (3): 27-30.

[5] Zhang Z.K., Che Y., Men S.Q., and Chen X.M. Aging precipitates in Al-Cu-Mn high strength aluminum alloy. Special Casting and Nonferrous Alloy, 2014, 34(10): 1114-1116.

[6] Zhang Z.K., Che Y., Men S.Q., and Li X. High temperature mechanical properties of Al-Cu-Mn cast aluminum alloy. Hot Working Technology, 2012, 41(19): 8-10.

[7] Xu X., Yang M., Liang Y.L., Zhang S.W., and Gong Q.J. Research on hot compressive deformaion and processing map of 211Z.X heat-resisting high strength aluminium alloy. Materials guide B: Research, 2016, 30(9): 143-148.

[8] Zhang X.M., Mao J., Che Y., and Zhang Z.K. Inverstigations on the fatigue property of the high-strength and toughness 211Z casting aluminum aiioy. Appliced Mcchanics and Materials, 2013, 197-201.

[9] Wu X.Y., Mao J., Che Y., and Zhang Z.K. Effect of solution time on properties of 211Z hot extrusion deformed aluminum alloy. Hot Working Technology, 2014, 43(10): 191-193.

[10] Cheng X.H., Mao J., Che Y., and Zhang Z.K. Effect of extrusion-heat on intergranular corrosion of 211Z aluminum alloy. Transactions of Materials and Heat Treatment, 2015, 36(1): 63-66.

[11] Zhang R.R. Effect of turning process parameters on surface quality of aluminum alloy 211Z. Guiyang: Guizhou University, 2016, 143-148.

[12] Tang Q.Q., Zhao X.F., Wang D.D., and Huang Q. Experimental study on the influence of milling parameters on surface roughness of aluminum alloy. Machinery Design and Manufacture, 2016, 9(9): 134-136.

[13] Wang H. Deep drainage detection system for inland vessels based on machine vision. Jordan Journal of Mechanical and Industrial Engineering, 2020, 14(1): 119-128.

[14] Prasad, G., and Das, A. Design approach of shell and tube vaporizer for LNG regasification. Jordan Journal of Mechanical and Industrial Engineering, 2018, 12(2): 109-116.

[15] Xu X.W., and Wang Q.M. On the influence of chip accumulation on machining accuracy. Science & Technology Information, 2010, (17): 627-628.

[16] Zhang Y.Z. Metal cutting theory. Aviation Industry Press, 1988.

[17] Liu L.Y., Wang J.F., Tu Z.B., Qing Z.H., and Ye Z. Study on the roughness of the machined surface and wear mechanism of the cutter in dry cutting aluminum alloy with YG8 cemented carbide. Technology and Test, 2018, (6): 120-123.

JJMIE

Volume 15, Number 1, March. 2021
ISSN 1995-6665
Pages 65 - 71

Jordan Journal of Mechanical and Industrial Engineering

Calculation Method of Stiffness and Deflection of Corroded RC Beam Strengthened by Steel Plate

Qian Zhang[1], Huang Tang[2*], Shihui Guo[3]

[1] Civil Contruction Office, Nanyang Institute of Technology, Nanyang 473000, China
[2] School of Civil Engineering, Hunan City University, Yiyang 413000, China
[3] School of Civil Engineering, Nanyang Institute of Technology, Nanyang 473000, China

Received July 18 2020 Accepted Feb 20 2021

Abstract

Given that corrosion is not considered in calculating the stiffness of reinforced concrete structures under existing cord, this paper improves the calculation formula in cord, and proposes a method to calculate the stiffness of the corroded beam strengthened by steel plate, then the formula for calculating the deflection is proposed. Nine corroded beams are strengthened by steel plates, the static test results of which are used to verify the correctness of calculation method. The influence of corrosion rate and thickness of steel plate on the stiffness are analyzed through the deflection change. Both experimental and theoretical analysis results show that the corrosion rate has a limited impact on the reduction of stiffness. When the thickness of steel plate reaches 6 mm and the corrosion rate reaches 30%, the change in deflection will decrease. At the same time, the influence of corrosion rate on the stiffness is greater than that of steel plate thickness.

Keywords: Steel Plate, Corroded RC Beam, Strengthening, Stiffness, Deflection, Calculation Method.;

1. Introduction

Corrosion of steel bars caused by chloride ion erosion in concrete is the most important reason of structural performance degradation. Over the past few decades, scholars have focused on the structural performance of corroded RC beams. Zhang et al. [1] and Zhang [2] et al. proposed the calculation formula of the ultimate bearing capacity of corroded RC beams, and verified the correctness of models through a series of tests on corroded beams. Sun at al. [3], Maaddawy et al. [4] and Yang [5] et al. have also established models of stiffness degradation model caused by the degeneration of bond stress between corroded steel bar and concrete. Wu [6] et al. studied the deformation performance and failure model of corroded RC beam under fatigue loading. Li [7] and Vidal [8] et al. examined the relationship between corrosion rate and crack width and proposed a calculation model of crack with. Du [9] et al. and Malumbela [10-13] et al. studied the mechanical properties of bending stiffness, stress strain and residual bearing capacity of corroded beams under the stress state.

The strengthening technology of steel plate has been widely used in engineering because of its simple construction, low cost and good strengthening effect. Scholars mainly focuses on the structural behavior of non-corroded beam. Ren et al. [14] studied the influence of anchorage spacing and loading on the strengthening effect of concrete beams strengthened by bonded steel plates. Gao et al. [15] analyzed the influence of amount and position of bonded steel and the width-to-thickness ratio of steel plate on the deformation and bearing capacity of RC beam through test. Raoof [16] et al. proposed the failure model of steel plate and pointed out that the spacing of cracks is the main reason for failure. Altin [17] et al. proposed a method for improving the shear resistance of T-beams strengthened by different side-mounted steel plates. Experiment results show that different shapes and layouts of side-laying modes have different effects on the failure mode and shear capacity of T-beams. Su [18-20] et al. studied the nonlinear behavior of RC beams laterally anchored by steel plate, as well as the influence of anchor placement, and the shear transfer between steel plates and anchors.

The above-mentioned studies on corroded RC beams have not considered the strengthening measures after degradation of mechanical properties. The researches on the strengthened beam also have not considered the corrosion of steel bar. However, in practice, the strengthening strategy is often carried out after the properties of RC structure appears degraded caused by steel bar corrosion. There are few theoretical studies that focused on the deflection behavior of corroded RC beam strengthened by steel plate [21-23].

In this paper, the formulas for calculating the stiffness of RC beams are improved, the stiffness calculation formula of corroded beams strengthened by steel plates is deduced considering the geometric, physical and mechanical equilibrium. Nine corroded beams are strengthened by steel plates, the static test results of which are used to verify the correctness of calculation method. The influence of corrosion rate and thickness of steel plate on the stiffness are analyzed through the deflection change.

* Corresponding author e-mail: guoguo91@126.com.

2. Theoretical Calculation of Stiffness of Corroded Beams Strengthened by Steel Plates

2.1. Analysis of Corrosion Model

The pitting corrosion is more consistent with the actual corrosion pattern of steel bar. Therefore, the pitting corrosion model should be adopted in the calculation model. The model of corroded steel bar proposed by Val [24] is used in this paper, as shown in the follows:

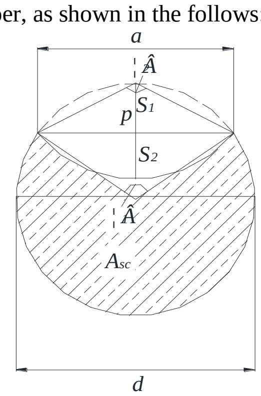

Figure 1. Model of steel bar with pitting corrosion.

The remaining cross-sectional area of steel bar in the model can be expressed as:

$$A_{sc}=\begin{cases}\dfrac{\pi d^2}{4}-S_1-S_2 & p\le\dfrac{\sqrt{2}}{2}d\\ S_1-S_2 & \dfrac{\sqrt{2}}{2}d<p\le d\\ 0 & p>d\end{cases} \tag{1}$$

In the above formula, S_1 and S_2 represent two semi-elliptical areas outside the shaded area, expressed as follows:

$$\begin{aligned} S_1&=\frac{1}{2}\left[\beta_1\left(\frac{d}{2}\right)^2-a\left|\frac{d}{2}-\frac{p^2}{d}\right|\right]\\ A_2&=\frac{1}{2}\left[\beta_2 p^2-a\frac{p^2}{d}\right]\\ a&=2p\sqrt{1-\left[\frac{p}{d}\right]^2}\\ \beta_1&=2\arcsin\left(\frac{2a}{d}\right);\beta_2=2\arcsin\left[\frac{a}{p(t)}\right]\end{aligned} \tag{2}$$

In reference [25], it is pointed out that the yield strength of steel bar with pitting erosion is linear:

$$f_{yc}=(1-\lambda\frac{A_s-A_{sc}}{A_s}\times 100)f_y \tag{3}$$

where f_{yc} is yield strength of steel bar with pitting corrosion, f_y is yield strength of steel bar without corrosion, A_s is cross-sectional area of steel bar without corrosion, λ is the experimental parameter. Through a large number of experiments results for plain steel bars and ribbed steel bars, Peng et al. [26] showed the value of λ is 0.0035.

2.2. Stiffness Analysis of Corroded Steel Bars

To analyze the stiffness of corroded RC beams strengthened by steel plates, the basic assumptions are:

1. The plane cross-section assumption is still applied to concrete strain;
2. Due to the influence of steel bar corrosion, the strain of tensile reinforcement is not compatible with the concrete strain at the same position, and the plane cross-section assumption is no longer applicable;
3. The tensile strength of concrete in the tension zone is no longer considered due to corrosion expansion.

The force of concrete beam strengthened by the steel plate is shown in Fig. 2:

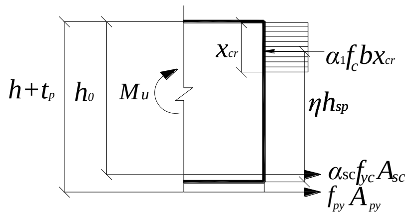

Figure 2. Forced section of the test beam after steel plate reinforcement.

It can be concluded from the equilibrium condition that:

$$\beta(\alpha_{sc}f_{yc}A_{sc}+f_{py}A_{py})=\alpha_1 f_c b x_{cr} \tag{4}$$

$$x_{cr}=\frac{\beta(\alpha_{sc}f_{yc}A_{sc}+f_{py}A_{py})}{b\alpha_1 f_c} \tag{5}$$

where α_{sc} is strength utilization factor of steel bar [1], b is depth of beam, β is coordinated working coefficient of steel plate and longitudinal steel bar, x_{cr} is depth of compressive zone, α_1 is the ratio of the stress value of equivalent rectangle stress diagram to the axial compressive strength, which is obtained according to the Code for Design of Concrete Structures (GB50010-2012).

Assuming that the h_{sp} is the distance from the joint action point of corroded tensile reinforcement and steel plate to the top of e beam, which is obtained from the centroid method [15] that:

$$h_{sp}=\frac{\alpha_{sc}f_{yc}A_{sc}(h-a_s)+f_{py}A_{py}(h+t_p/2)}{\alpha_{sc}f_{yc}A_{sc}+f_{py}A_{py}} \tag{6}$$

The key to calculating the deflection of an RC beam is to find its curvature and stiffness. The experimental results show that the failure process of corroded RC beams strengthened by steel plates is similar to that of corroded RC beams without strengthening. Due to the degradation of bond stress after corrosion, the strain of steel bar in the middle section lags that of concrete. Thus, the incompatibility between steel bar and concrete should be considered.

The stiffness and curvature of the section can be expressed as:

$$B=\frac{M}{\phi} \tag{7}$$

Where, B is flexural stiffness, M is external bending moment, φ is sectional curvature.

According to the stiffness theory in material mechanics, the sectional curvature can be deduced from the geometrical, physical, and equilibrium conditions of the section. Fig. 3 shows the stress distribution of simple bending section and mid-span section of corroded-strengthened beam:

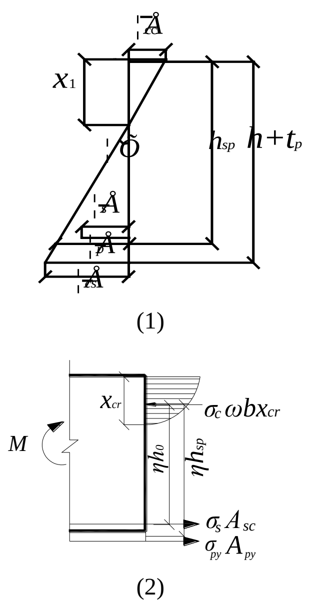

Figure 3. Stress distribution of simple bending section and mid-span section.

(1) Geometrical condition:

$$\phi=\frac{p(\eta_s)q(\eta_s)\psi(\varepsilon_s+\varepsilon_{cc}+\varepsilon_p)}{h_{sp}} \tag{8}$$

where ε_{cc} is concrete strain at the top of compression zone, ε_s is concrete strain near the tensile steel bar, ε_p is the average strain of bottom steel plate, h_{sp} is effective height of converted section, $p(\eta_s)$ is strain incompatibility coefficient of steel bars [27], $q(\eta_s)$ is cohesion degradation correction factor, ψ is obtained according to the Code for Design of Concrete Structures (GB50010—2012).

(2) Physical relationship between stress and strain

The stress distribution of crack section is shown in Fig. 3. The stress-strain relationship of the top concrete, tensile reinforcement and steel plate is expressed as:

$$\varepsilon_{cc}=\frac{\sigma_c}{E_c},\quad \varepsilon_s=\frac{\sigma_s}{E_s},\quad \varepsilon_p=\frac{\sigma_{py}}{E_p} \tag{9}$$

where, σ_c is concrete stress on top of beam, σ_s is stress of tensile steel bar, σ_{py} is steel plate stress, E_c is elasticity modulus of concrete, E_s is elasticity modulus of tensile steel bar, E_P is elasticity modulus of steel plate.

(3) Equilibrium condition of stress

Based on the stress distribution in Fig.s (2) and (3), the equilibrium equation can be obtained:

$$M=\omega\sigma_{\mathrm{c}}bx_{\mathrm{cr}}\eta h_{\mathrm{sp}} \tag{10-a}$$

$$M=\omega\sigma_{\mathrm{c}}bx_{\mathrm{cr}}\eta h_0+\sigma_{\mathrm{py}}A_{\mathrm{py}}(a_{\mathrm{s}}+\frac{d}{2}+\frac{t_{\mathrm{p}}}{2}) \tag{10-b}$$

$$\omega\sigma_{\mathrm{c}}bx_{\mathrm{cr}}=\sigma_{\mathrm{s}}A_{\mathrm{sc}}+\sigma_{\mathrm{py}}A_{\mathrm{py}} \tag{10-c}$$

where M is the bending moment of cross section, ω is the stress and shape integrity coefficient in the compressed zone, η is the coefficient of internal force arm on crack section, h_0 is the effective height of section.

Combining the above three conditions in formula (7) and (8), we conclude that the short-term stiffness of corroded-strengthened beam is:

$$B=\frac{E_{\mathrm{s}}A_{\mathrm{py}}h_{\mathrm{sp}}^{\;2}}{p(\eta_{\mathrm{s}})q(\eta_{\mathrm{s}})\psi A_{\mathrm{py}}\dfrac{2a_{\mathrm{s}}+d+t_{\mathrm{p}}-2\eta\left(h_{\mathrm{sp}}-h_0\right)}{\eta(2a_{\mathrm{s}}+d+t_{\mathrm{p}})\mathrm{A}_{\mathrm{sc}}}+\alpha_{\mathrm{s}}\dfrac{A_{\mathrm{py}}}{\omega bx_{\mathrm{cr}}\eta}+\dfrac{2\alpha_{\mathrm{s}}\left(h_{\mathrm{sp}}-h_0\right)}{a_{\mathrm{s}}+d+t_{\mathrm{p}}}} \tag{11}$$

After the bending stiffness is obtained, the following simplified formula can be used to calculate the deflection value of beam [15]:

$$\delta=S\frac{Ml_0^2}{B} \tag{12}$$

where S denotes the deflection calculation coefficient related to the load and the support condition, S is 13/216 for 4-point loading and S is 1/12 for mid-span concentrated load.

3. Experimental Investigation

3.1. Design of Tested Beam

There is a total of 9 tested beams. The reinforcement details of the specimens are shown in Fig. 4. Each specimen is 1,800 mm long, 150 mm wide, and 300 mm deep with a rectangular cross section and reinforced by two 22-mm-diameter (hot-rolled ribbed reinforcement steel bars) bottom longitudinal deformed reinforcing bars, two 16-mm-diameter top longitudinal deformed reinforcing bars, and 8-mm-diameter epoxy-coated deformed reinforcing stirrups spaced at 100 mm at the middle and 70 mm at the ends. A typical clear cover of 30 mm was used all around the stirrups.

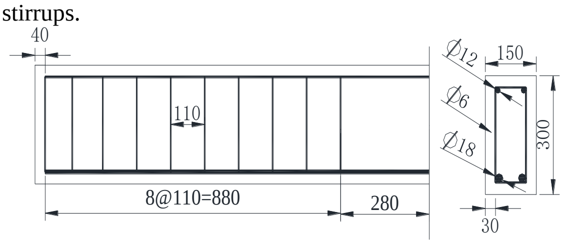

Figure 4. Test beam reinforcement drawing.

3.2. Test Material Properties

The average compressive strength of concrete measured by concrete strength test is 29.85 MPa. The yield strength of stirrups, compression and tensile reinforcement is respectively 338 MPa, 336 MPa and 340 MPa. All steel bars have a modulus of elasticity of 200 GPa. The yield strength of the reinforced steel plate is 238 MPa. The adhesive layer uses JN-S structural adhesive produced by Good Bond Company. The layer boasts a compressive strength of 89.5 MPa and a bonding strength with concrete of 4.0 MPa.

3.3. Corrosion of Tensile Steel bar and Installation of Steel Plate

As shown in Fig. 5, beams are immersed horizontally in a steel iron water tank, which has a size of 2,200 mm long, 700 mm wide, and 800 mm high, to a depth of about 200 mm in a 5% NaCl solution. Both ends of all specimens are placed above the concrete blocks and immersed up to one-third of their height in the solution. Distilled water is used to prepare the solution. A stainless-steel plate of 1.2 ×350 × 1,800 mm is immersed in the solution to be used as a counter electrode. The positive output is connected to the deformed bar, whereas the negative output is connected to the stainless-steel plate. The current supplied to each specimen is checked on a regular schedule and any shift is corrected by adjusting the ammeter, which monitored the cell current. The current intensity of the power supply and the corrosion period are selected for each beam in order to achieve the desired degree of corrosion of the submerged reinforcing bar. Therefore, a constant current of 1,760 mA was applied to each specimen for a period of 12 days to obtain theoretical mass loss of 10% in tension. The corrosion rate of 9 tested beams was divided into 3 grades, respectively of 10%, 20% and 30%. The thickness of steel plate is divided into 3 levels, 2 mm, 4 mm and 6 mm. The steel corrosion and steel plate layout are shown in Fig. 5 (1) and (2).

(1) Fast electrochemical corrosion

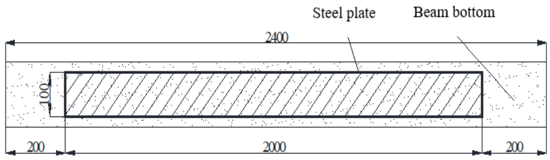

(2) Schematic diagram of bonded steel plate

Figure 5. Steel corrosion and bonded steel plate.

3.4. Loading Method

Following the corrosion period and strengthening work, all specimens were monotonically loaded in midpoint loading (Fig. 6). The load is applied using a 500 kN hydraulic jack through a bearing plate to the beam specimens. Per loading increment is 5 kN at the beginning of loading. The strain and deflection of steel plate across the middle and 1/4 span were recorded. The distribution of cracks on both sides of tested beam is also depicted.

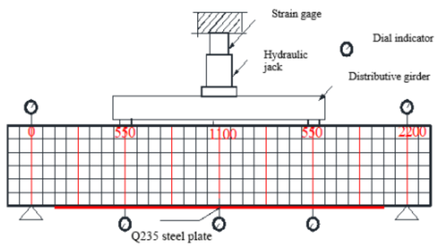

Figure 6. Test beam loading

4. Discussion of Tested Results

4.1. Corrosion of steel bar

Fig. 7 presents corrosion-induced cracks distribution of the beam specimens P1 and P2. It can be observed from Fig. 7 that the longitudinal corrosion-induced cracks are mainly on the side face along the longitudinal main reinforcements of beam specimens. This is resulted from the radial stress induced by the corrosion products exceeding concrete tensile strength. However, there is difference for the corrosion-induced crack distribution of each beam because of the non-uniform pitting corrosion. The factors such as impressed current density, the PH of NaCl solution and penetration rate of the Cl^- ions varies in the process of corrosion, which leads to the dispersion of corrosion pit on the surface of the steel bar, and then the corrosion-induced cracks distribution will be different. The corrosion conditions of tensile bars that are respectively located at 10 cm to 40 cm of beam specimen P1 and 40 cm to 80 cm of beam specimen P2 are also shown in Fig. 8. As can be observed in Fig. 7, the corrosion of tensile steel reinforcements has already reached the generalized corrosion stage defined by Zhang et al. [28]. In this stage, there is corrosion all along the bars, and there are also some zones where pit corrosion is significant.

4.1.1. Influence of steel plate thickness on the deformation of beam

Because there is a deviation between the measured corrosion rate and the design value in this test, beams with the similar corrosion rate are selected for comparison. Fig. 7 is the load-mid-span deflection curve of the test beam with the same protective layer and different thickness of steel plate. As can be seen from Fig.8, when the thickness of concrete protective layer is the same and the corrosion rate of steel bar is similar, the stiffness of the test beam is obviously lager as the thickness of steel plate increases from 2 to 4 mm. However, as the thickness of steel plate continues to increase, the steel degree of the test beam increases gradually. Under the same load, the mid-span deflection of the strengthened beam decreases with the increase of the reinforcement thickness of steel plate. The ductility of the stiffness of test beam decreases with the increase of the thickness of steel plate.

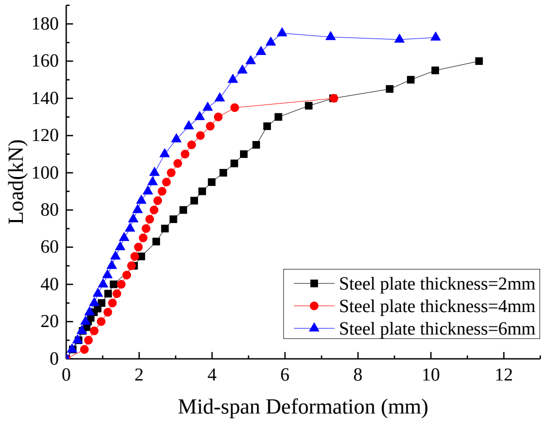

Figure 8. Load-mid-span deflection of beam with cover thickness=35mm

4.2. Influence of the thickness of protective layer on the deformation performance of the beam

Fig. 9 shows the load-mid-span deflection curve of test beam with different thickness of concrete cover with the same thickness of steel plate. As shown in Fig. 8, when the thickness of steel plate is 4 mm, the thickness of the concrete protective layer is changed, and the P–δ curves of each test beam are very close in the loading process. This indicates that when the corrosion rate of reinforcement is similar, the thickness of steel plate is the same when the corroded beam is strengthened, and the deformation performance of the beam is less affected by changing the thickness of the concrete protective layer.

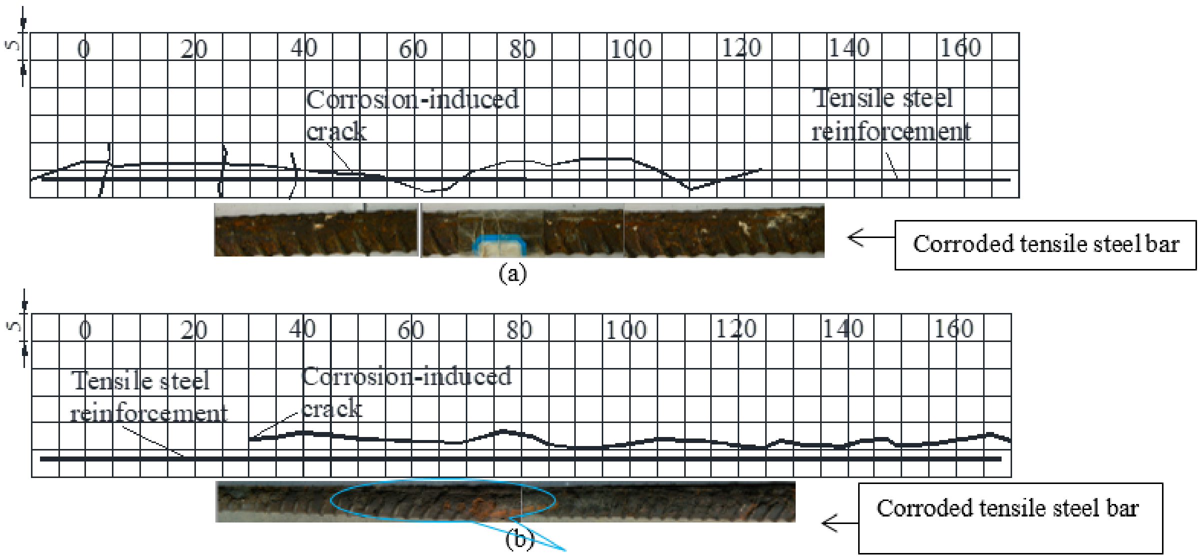

Figure 7. Corrosion-induced cracks distribution of the beam specimens and corrosion condition of tensile steel reinforcement: (a) P1; (b) P2

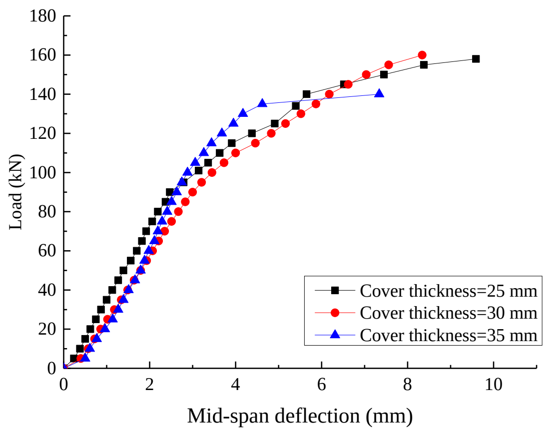

Figure 9. Load-mid-span deflection of beam with steel plate thickness=4mm

4.3. Comparison of Tested Values with Theoretical Values of Deflection

A comparison of theoretical and experimental values of mid-span ultimate deflection is given in Table 1, which shows that the theoretical value of ultimate deflection is close to the experimental value. The correlation between the tested value and theoretical value is listed in Fig. 10. The ratio of tested value to theoretical value ranges from 1.01 to 1.11, and the mean and coefficient of ratio variation are respectively 1.04 and 0.037. The results show that the theoretical formulas of stiffness and deflection presented in this paper can be used to predict the tested values.

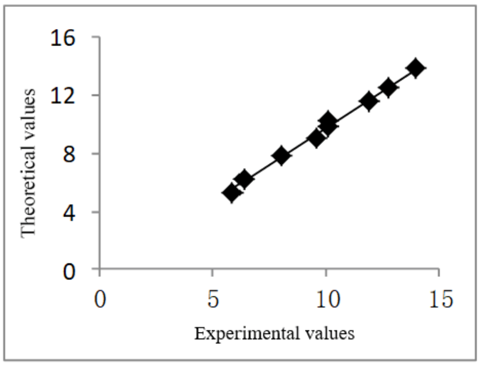

Figure 10. Correlation between theoretical values and tested values.

Theoretical and tested results show that when the steel plate increased by 2 mm and the corrosion rate is close, For example, beams P1 and P2, beams P4 and P5, the ultimate mid-span deflection of decreased by about 2.7 mm. Comparing beams P7, P8 and P9, it can be found that when the corrosion rate reaches about 30%, the mid-span deflection decreases as stiffness increases. It shows that the influence of thickness of steel plate on the increase of stiffness is not linearly. When the thickness of steel plate exceeds a certain value, the ultimate bearing capacity and stiffness no longer increase linearly [15, 29, 30].

Under the condition of same thickness of steel plate, when the corrosion rate is less than 20%, the deflection increases about 3 mm as the corrosion rate is increased by 10%. This shows that the influence of corrosion rate on the deflection of corroded-strengthened beams is greater than the thickness of the steel plate. When the corrosion rate reaches 30%, the increased deflection of beam compared with beam with 20% corrosion rate is lower than that between beams with 10% and 20% corrosion rate It is also stated that the corrosion rate has a limited effect on the reduction in stiffness.

Table 1. Comparison of calculated and tested values of deflection theory.

No.	*t* (mm)	*c* (mm)	f_c (MPa)	Average corrosion rate	δ (mm) theoretical value	δ (mm) experimental value
P1	2	25	30.4	9.60%	9.56	9.06
P 2	4	25	29.8	11.20%	6.38	6.28
P 3	6	25	29.5	11.60%	5.89	5.3
P 4	2	30	30.6	19.80%	12.8	12.5
P 5	4	30	29.9	20.50%	10.1	9.8
P 6	6	30	30	21.50%	8.03	7.8
P 7	2	35	28.5	31.5%	13.97	13.84
P 8	4	35	29.6	28.91%	11.95	11.60
P 9	6	35	30.4	29.8%	10.1	10.21

5. CONCLUSIONS

This paper revises the formula in cord and proposes the formula for calculating the stiffness and deflection of corroded beams strengthened by steel plate. The correctness of deflection formula is verified by the test study of nine corroded-strengthened beams. At the same time, the influence of the thickness of steel plate and corrosion rate on the stiffness of corroded-strengthened beam is analyzed. following conclusions can be drawn:

1. The theoretical results of mid-span deflection are close to the tested results. The theoretical calculation formula can better predict the stiffness and deflection values of corroded beams strengthened by steel plate.
2. The corrosion rate has a limited influence on the reduction of stiffness. When the thickness of steel plate reaches 6 mm and the corrosion rate reaches 30%, the change of deflection will decrease.
3. When the thickness of steel plate exceeds a certain value, the ultimate bearing capacity and stiffness no longer increase linearly.
4. Comparing the influence of both the thickness of the steel plate and corrosion rate on the deflection, it can be found that the effect of the corrosion rate on the stiffness is greater than that of steel plate thickness.

Acknowledgment

This work was supported by Fund Program: Henan provincial science and technology key project-international cooperation (182102410068), Natural Science Foundation of Hunan Province (Grants nos. 2019JJ50023), 2020 Yincheng Science and Technology Talents Supporting Project of Yiyang.

References

[1] Zhang, X., Wang, L., Zhang, J. and Liu, Y., **2016**. Model for flexural strength calculation of corroded RC beams considering bond–slip behavior. *Journal of Engineering Mechanics*, *142*(7): 04016038.

[2] Zhang, J.R., Zhang, K.B., Peng, H. and Gui, C., **2009**. Calculation method of normal section flexural capacity of corroded reinforced concrete rectangular beams. *China Journal of Highway and Transport*, *22*(3), pp.45-51.

[3] Sun, B., Niu, D.T. and Wang, Q.L., **2004**. Analysis and calculation of bending stiffness of corroded reinforced concrete beams. *Building Structure*, *10*, pp.42-45.

[4] Maaddawy, T.E., Soudki, K. and Topper, T., **2005**. Analytical model to predict nonlinear flexural behavior of corroded reinforced concrete beams. *ACI Structural Journal 102*(4), pp.550-559.

[5] Yang, S.Y., Liu, X.L. and Leng, Y.B., **2012**. Prediction of flexural deformation of a corroded RC beam with a polynomial tension-stiffening model. *Journal of Structural Engineering*, *139*(6), pp.940-948

[6] Wu, J., Wang, C.X., Xu, J., Xiao, Z. and Wu, F.H., **2012**. Study on flexural behavior of corroded reinforced concrete beams under fatigue loads. *China Civil Engineering Journal*, *10*, pp.118-124.

[7] Brandonisio, G., Lucibello, G., Mele, E. and Luca, A.D., **2013**. Damage and performance evaluation of masonry churches in the 2009 L'Aquila earthquake. *Engineering Failure Analysis*, *34*(0), pp.693-714.

[8] Harish, K.V., Dattatreya, J.K. and Neelamegam, M., **2013**. Experimental investigation and analytical modeling of the σ–ε characteristics in compression of heat-treated ultra-high strength mortars produced from conventional materials. *Construction and Building Materials*, *49*(0), pp.781-796.

[9] Du, Y.G., Cullen, M. and Li, C., **2012**. Structural performance of RC beams under simultaneous loading and reinforcement corrosion. *Construction and Building Materials*, *38*, pp.472-481.

[10] Malumbela, G., Alexander, M., and Moyo, P., **2009**. Steel corrosion on RC structures under sustained service loads-A critical review. *Engineering Structures*, *31*(11), pp.2518-2525.

[11] Malumbela, G., Alexander, M. and Moyo, P., **2010**. Lateral deformation of RC beams under simultaneous load and steel corrosion. *Construction and Building Materials*, *24*(1), pp.17-24.

[12] Malumbela, G., Alexander, M. and Moyo, P., **2010**. Variation of steel loss and its effect on the ultimate flexural capacity of RC beams corroded and repaired under load. *Construction and Building Materials*, *24*(6), pp.1051-1059.

[13] Malumbela, G., Moyo, P. and Alexander, M., **2012**. Longitudinal strains and stiffness of RC Beams under load as measures of corrosion levels. *Engineering Structures*, *35*, pp.215-227.

[14] Ren, W., He, S.H., Zhao, X.X. and Luan, H.F., **2008**. Model test on preloaded RC T-beam strengthened by bonded steel plates. *China Journal of Highway and Transport*, *03*, pp.64-68.

[15] Gao, X.N., Zhou, Q.Y. and Chen, M.H., **2006**. Theoretical and experimental research on bearing behavior of RC beams strengthened by bonded steel plates. *China Civil Engineering Journal*, *39*(8), pp.38-44.

[16] Raoof, M., El-Rimawi, J.A. and Hassanen, M.A.H., **2000**. Theoretical and experimental study on externally plated R.C. beams. *Engineering Structures*, *22*(1), pp.85-101.

[17] Altin, S., Anil, Ö. and Kara, M.E., **2005**. Improving shear capacity of existing RC beams using external bonding of steel plates. *Engineering Structures*, *27*(5), pp.781-791.

[18] Siu, W.H. and Su, R.K.L., **2010**. Effects of plastic hinges on partial interaction behaviour of bolted side-plated beams. *Journal of Constructional Steel Research*, *66*(5), pp.622-633.

[19] Su, R.K.L., Li, L.Z. and Lo, S.H. **2013**. Shear transfer in bolted side-plated reinforced concrete beams. *Engineering Structures*, *56*(0), pp.1372-1383.

[20] Su, R.K.L., Siu, W.H. and Smith, S.T., **2010**. Effects of bolt–plate arrangements on steel plate strengthened reinforced concrete beams. *Engineering Structures*, *32*(6), pp.1769-1778.

[21] Jiang, Z. and Jia, Z., **2018**. Effects of students basketball club participation motivation on club cohesion organizational commitment as the mediator. *Journal of Interdisciplinary Mathematics*, *21*(2), pp.519-528.

[22] Chen, D.Z., **2018**. Performance evaluation model for government-supportive urbanization. *Journal of Discrete Mathematical Sciences and Cryptography*, *221*(4), pp.859-868.

[23] Ekman, J., Hietaniemi, M., Kolari, M., Nelson, M. and Keegan, K., **2017**. Novel starch saving programme improves sustainability in board manufacturing through the reuse of recycled fibre starch. *Paper Asia*, *33*(6), pp.18-22.

[24] Val, D.V. and Melchers, R., **1997**. Reliability of deteriorating RC slab bridges. *Journal of Structural Engineering*, *123*(12), pp.1638-1644.

[25] Stewart, M.G., **2009**. Mechanical behaviour of pitting corrosion of flexural and shear reinforcement and its effect on structural reliability of corroding RC beams. *Structural Safety*, *31*(1), pp.19-30.

[26] Peng, J.X., Zhang, J.R., Zhang, K.B. and Peng, H., **2012**. Probabilistic Resistance Model and experimental investigation on for corroded RC bridges. *Engineering Mechanics*, *29*(6), pp.125-131.

[27] Sun, B., **2006**. Structural performance degrading and seismic evaluation of existing reinforced concrete structures. Xi'an: Xi'an University of Architecture and Technology.

[28] Li, J., **2020**. Distributed multi-level inventory algorithms for automotive maintenance spare parts based on centralized control model. *Jordan Journal of Mechanical and Industrial Engineering*, *14*(1), 89-99.

[29] Sedelnikov, A.V., Filippov, A.S. and Ivashova, T.A., **2018**. Earth's magnetic field measurements data accuracy evaluation on board of the small spacecraft "AIST" flight model. *Jordan Journal of Mechanical and Industrial Engineering*, *12*(4), 253-260.

[30] Zhang, R., Castel, A. and François, R., **2010**. Concrete cover cracking with reinforcement corrosion of RC beam during chloride-induced corrosion process. *Cement and Concrete Research*, *40*(3), 415–425.

JJMIE

Volume 15, Number 1, March. 2021
ISSN 1995-6665
Pages 73 - 82

Jordan Journal of Mechanical and Industrial Engineering

Electromechanical Coupling Model of AC Asynchronous Motor Drive System Based on Multiscale Method

Qiuping Pan*, Jiaxiang Zhang

College of Electrical Engineering, Zhengzhou Railway Vocational & Technical College, Zhengzhou 451460, China

Received July 18 2020 *Accepted March 13 2021*

Abstract

Due to the development of motor drive system towards high power, integration and high-power density, this model cannot control mechanical vibration caused by electromechanical coupling. A new electromechanical coupling model of alternating current (AC) induction motor drive system is proposed. The transient characteristics of the motor were studied by multi-scale method, and the electromechanical coupling dynamic characteristics of the drive system were extracted. According to the dynamometer, the impact load is applied to the drive system, which causes the load on the inertial flywheel to suddenly increase by 3.5 times from 2500 Nm. The service coefficient of the realization shaft is defined as the ratio of the measured post-impact torque to the average pre-impact torque. The experimental results show that when the AC asynchronous motor's influence is passed through the electromechanical coupling model, the difference between the input and output shafts of the gearbox is minimal, and when the AC asynchronous motor's influence is different, the input and output shafts of the gearbox are maximum. It can be seen that the electromechanical coupling model established in this paper can control the mechanical vibration caused by electromechanical coupling and convert the internal load threat to the external load threat.

Keywords: multiscale method; AC asynchronous motor; drive system; electromechanical coupling model;

1. Introduction

All kinds of electromechanical systems generally have the phenomenon of electromechanical coupling. The general electromechanical systems are composed of mechanical system, electrical system and coupling magnetic field. The mechanical coupling parameters include displacement, angle, force, moment, speed and acceleration; the electromagnetic coupling parameters include voltage, current, magnetic field strength and air gap permeability. In the electromechanical system, a variety of physical processes exist at the same time, integrating all the dynamic processes. Its essence is to connect the mechanical system with the electrical system by coupling the magnetic field, so as to achieve the purpose of energy transfer [1]. It can be said that "coupling" has become an important feature of electromechanical system. On the one hand, it determines the function generation of the system, and it is the form that the system relies on to achieve its functional objectives; on the other hand, it determines the operation performance of the system. Traditional methods study different electromechanical coupling models for AC asynchronous motor, which are used to control the use of AC asynchronous motor. However, after many tests, it is found that there are some disadvantages in this model. Therefore, aiming at this question, the electromechanical coupling model of AC asynchronous motor drive system based on multiscale method is studied.

In essence, almost all scientific and engineering problems are multiscale. At the atomic scale, matter is made up of nuclei and electrons. Meanwhile, atomic time is marked in femtoseconds (10-15 seconds). In everyday life, time scales are known to be much larger. Therefore, in the face of some special problems, scales that are easily perceived are generally called macroscopic scales, while very small scales are called microscopic scales. In many cases, multi-scale effects are not that important. The equivalent physical and mathematical models of microprocesses are considered and satisfactory results are obtained. Most real-life scientific models are based on this assumption [2]. For example, in the study of fluid motion, people pay more attention to the change of fluid density and the distribution of flow field. For the molecular scale microscopic processes, the equation of state and the constitutive model are used to describe. These equivalent models are generally built on the micro scale, based on a lot of theoretical derivation and work accumulation, and have achieved many successful applications, but also have obvious limitations. The most obvious limitation is its accuracy. For complex systems, when the modeling error greatly exceeds the solving error, the practicability of the model is problematic. In addition, for those who are interested in microscopic mechanisms, the equivalent model can only be ignored blindly; Finally, for some complex systems, the equivalent models are often based on empirical formulas without strict theoretical basis. Therefore, people are more inclined to use micro scale models with higher accuracy and more complete physical and theoretical models. However, this is not the best choice,

* Corresponding author e-mail: panqiuping19881020@126.com.

and the result will be huge preprocessing effort and redundant data. Therefore, the multi-scale method came into being. Multi-scale method is one of the main research directions in the development of science and technology. It is a science that studies the modeling and solving methods of coupling phenomena between important features of different spatial and temporal scales. Through the coupling of different scale models, [3] fully absorbed the advantages of simple and efficient macroscopic scale and more accurate microscopic scale. Literature [3] proposed a model reference adaptive control (MRAC) method for the intelligent control of permanent magnet AC servo system. The system can identify parameters online and modify the network teacher values, which has strong robustness. But the accuracy of this method is low. Literature [4] proposed a design method of sliding mode fuzzy controller based on Sugeno type fuzzy reasoning and applied this method to the design of position controller of AC servo system of permanent magnet synchronous motor, which has good dynamic following performance and strong robustness, and effectively weakens the jitter. But the control of this method is not stableherefore, the basic research task of electromechanical coupling of AC induction motor drive system by using the proposed method is to study reasonable equivalent methods and coupling methods between different scales according to the required computational accuracy, as to obtain the required information more efficiently and accurately.

2. Electromechanical coupling model of AC asynchronous motor drive system based on multiscale method

2.1. Study of motor transient characteristics based on multiscale method

There are many different schemes which can be used to discretize the equations of motion and to establish the step-by-step numerical integration formula. In the field of computational science, the central difference method is widely used. It is based on the central difference formula of acceleration and velocity. The simulation time $0 \le t \le t_1$ is divided into $n=1$ to n^* steps with time interval Δt_n. n^* is the number of time steps; t_1 is the end time of the simulation; l_n is the displacement vector of the n-th time step. It is known that during the working process of the AC asynchronous motor drive system, with the deformation of the element in the calculation process, the change of the element characteristic size and the change of the critical stability integration step length will be caused. Therefore, this paper takes the explicit integration method with variable time step as an example, and Figure 1 is the schematic diagram of the time-domain discrete effect of the central difference method [4].

The time increment relationship is defined as formula (1):

$$\begin{cases} \Delta t_{n+\frac{1}{2}} = t_{n=1} - t_1 \\ t_{1+\frac{1}{2}} = \frac{1}{2}\left(t_{n=1} + t_1\right) \\ \Delta t_n = t_{1+\frac{1}{2}} - t_{1-\frac{1}{2}} \end{cases} \tag{1}$$

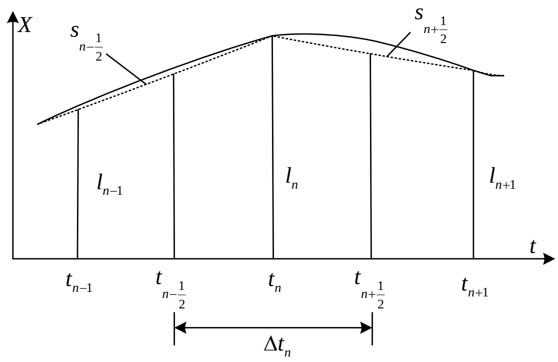

Figure 1. Time-domain discretization of central difference method

The central difference scheme of velocity is defined as follows:

$$l'_{n+\frac{1}{2}} = s_{n+\frac{1}{2}} = \frac{l_{n+1} - l_n}{t_{n+1} - t_1} = \frac{1}{\Delta t_{1+\frac{1}{2}}}\left(l_{n+1} - l_n\right) \tag{2}$$

Then the corresponding displacement recurrence formula is:

$$l_{n+1} = l_n + \Delta t_{n+\frac{1}{2}} \cdot s_{n+\frac{1}{2}} \tag{3}$$

The expression of acceleration is:

$$c_n = l''_n = \frac{1}{\Delta t_n}\left(l'_{n+\frac{1}{2}} - l'_{n-\frac{1}{2}}\right) \tag{4}$$

The corresponding speed expression is:

$$s_{n+\frac{1}{2}} = s_{n-\frac{1}{2}} + \Delta t_n \cdot c_n \tag{5}$$

In the above formula: s_n represents velocity; c_n represents acceleration. According to Figure 1 and the above derivation process, the central difference method in the multiscale method defines the speed at the midpoint of the time interval. The relationship between acceleration and displacement can be obtained by taking the above formula into formula (3):

$$c_n = l''_n = \frac{\Delta t_{n+\frac{1}{2}} \cdot \left(l_{n+1} - l_n\right) - \Delta t_{n-\frac{1}{2}} \cdot \left(l_n - l_{n-1}\right)}{\Delta t_{n+\frac{1}{2}} \cdot \Delta t_{n-\frac{1}{2}} \cdot \Delta t_n} \tag{6}$$

In the case of equal step size, the above formula is simplified as:

$$c_n = l''_n = \frac{1}{\Delta t^2}\left(l_{n+1} - 2l_n + l_{n-1}\right) \tag{7}$$

With the above discrete scheme, the integration of the motion equations in the time domain is discussed. Without considering the damping temporarily, the following formula is given in the n-th step:

$$Kc_n = \lambda_n = W_n^{(in)} - Ml_n = W_n^{(in)} - W_n^{(out)} \tag{8}$$

The above formula is a second-order ordinary differential equation for time, where $W_n^{(in)}$ and $W_n^{(out)}$ represent internal and external nodal forces, Ml_n and λ_n is a function of displacement and time [5]. The internal joint force is related to the displacement of the structure, while the external joint force is usually time-dependent but may also be related to the displacement of the joint. According to the constitutive equation of the AC asynchronous motor and the strain and strain rate of the element, the element stress is solved, and then the internal node force is obtained, while the strain and strain rate are directly determined by the displacement and its derivative. The update format of node speed is:

$$s_{n+\frac{1}{2}} = s_{n-\frac{1}{2}} + \Delta t K^{-1} \lambda_n \tag{9}$$

Given the time step n, the n ode force . l_n, the constitutive equation and the external force of the node, so that the $s_{n+\frac{1}{2}}$ can be solved by the above formula, and the l_{n+1} can be obtained by combining the formula (3). When the mass matrix K is simplified reasonably, it becomes a diagonal matrix, so that the updating of node velocity and displacement can be realized without solving any equation, which is conducive to saving memory and dealing with large-scale questions, which is the significant advantage and feature of the multiscale method. Using the multiscale method with central difference proposed above, the transient characteristics of the motor are studied [6].

2.2. Extraction of electromechanical coupling dynamic characteristics of drive system

The centralized parameter method is used to analyze the dynamic characteristics of the gear system. The following assumptions are adopted in the process:

1. Each gear and rotor component is simplified to a lumped mass (inertia);
2. (2) Each gear is an involute spur gear. The meshing force between gears always acts on the meshing surface and is perpendicular to the contact line of the tooth surface.
3. Gear pair, bearing and transmission shafting are simplified to be connected by concentrated stiffness and damping.
4. The friction between the teeth is ignored.
5. The mass, size and other structural parameters of the same planetary gear are the same.
6. The damping in the system is viscous damping.
7. Each gear only considers three degrees of freedom in its own plane, including translational vibration along the radial direction and torsional movement along the axial direction.
8. Assuming that the box body is a rigid body, the influence of its mass and stiffness on the drive system is ignored [7].

The translation and torsion mode of the AC asynchronous motor drive system is shown in Figure 2.

In the figure, r_i is the radius of the gear; g_{12} is the time-varying meshing stiffness of the gear pair; z_{12} is the meshing damping; b_{12} is the comprehensive meshing error; β_{12} is the meshing angle; g' is the radial support stiffness of the gear; g'' is the radial support damping of the gear; Z_i is the rotation moment of the motor drive system; α_i is the rotation angle of the gear $i\left(i=1,2\right)$, and its expression is:

$$\alpha_i\left(t\right) = \int \mu_i\left(t\right) dt + h_i\left(t\right) \tag{10}$$

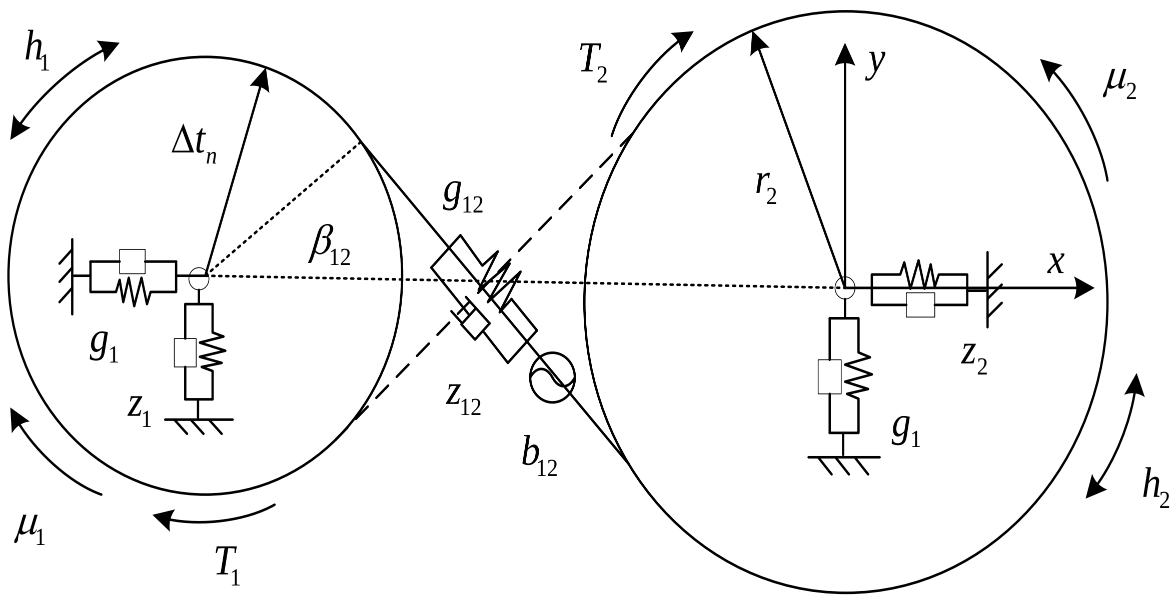

Figure 2. Translation and torsion diagram of AC asynchronous motor drive system

In the formula: μ_i is the rotational angular velocity of the rigid body of gear i, which is determined by the moment of prime mover and load in real time. This term has not been considered in the previous lumped parameter model of gear transmission; h_i is the angular displacement of elastic torsional vibration superimposed on the rigid body motion. In the past, researchers set the speed of gear as known, and reflect the law of speed change through the frequency of meshing stiffness. When running in the unsteady state, affected by the electric part of the motor and the external load of the system, the gear speed and meshing period are random and time-varying, so it is inconvenient to use time description. However, it is noted that no matter how the rotating speed changes, the active and passive gears rotate a pitch angle in each meshing cycle. Therefore, the gear angle can be used instead of time to represent the meshing cycle, that is:

$$\begin{cases} T = \dfrac{2\pi}{C_1\mu_1} \\ \alpha = \dfrac{2\pi}{C_1} \end{cases} \tag{11}$$

In the formula, T and α represent the meshing period of gear pair measured by time and angle respectively; C_1 represents the number of teeth of driving gear. Furthermore, the time-varying meshing stiffness and the comprehensive meshing error are fitted to a function that changes with the fixed period of the gear angle by the Fourier series method.

$$\begin{cases} g_{12}(\alpha_1) = \bar{g}_{12} + \sum\limits_{d=1}^{\infty} \eta_d \cos\left[d\left(C_1\alpha_1 + \theta_{12}\right)\right] \\ b_{12}(\alpha_1, \alpha_2) = Q_{12}\sin\left(C_1\alpha_1 + \varepsilon_{12}\right) + \\ \qquad Q_1 \sin\left(\alpha_1 + \kappa_1\right) + \\ \qquad Q_2 \sin\left(\alpha_2 + \kappa_2 + \beta_{12}\right) \end{cases} \tag{12}$$

In the formula, $\bar{g}_{12}$ represents the average value of meshing stiffness in a meshing period, which can be obtained by potential energy method; η_d represents the expansion coefficient of Fourier series, $\eta_d = \dfrac{-1.5g\sin\left[d\pi\left[2-e_\beta\right]\right]}{d\pi}$, where g represents the meshing stiffness in single tooth area, e_β represents the coincidence degree; d represents the harmonic number; θ_{12} represents the initial phase of meshing stiffness; Q_{12} represents the meshing frequency error; κ_1 represents the initial phase of error respectively [8]. The time-varying of meshing damping is ignored, so the meshing damping is expressed as a linear time invariant parameter

$$z_{12} = 2\varepsilon_{12}\sqrt{\bar{g}_{12} \cdot \frac{u_1 u_2}{u_1 + u_2}} \tag{13}$$

In the formula, ε_{12} represents the meshing damping ratio, generally within the range of $0.03 \sim 0.17$; u_1 and u_2 represent the mass of adjacent gears. Considering the three meshing states of gear tooth surface contact, separation and tooth back contact, the tooth surface meshing deformation $\zeta_{12}^{q'}$ and tooth back meshing deformation $\zeta_{12}^{q''}$ of the fixed shaft gear pair can be expressed as follows:

$$\begin{cases} \zeta_{12}^{q'} = \left(x_1 - x_2\right)\sin\beta_{12} - \left(y_1 - y_2\right) \\ \zeta_{12}^{q''} = \left(x_1 - x_2\right)\sin\beta_{12} - \left(y_1 - y_2\right) \end{cases} \tag{14}$$

In the formula, x and y are the translation vibration displacements in x and y directions of gear i respectively. Accordingly, the calculation expression of meshing force F_{12} of fixed shaft gear pair is as follows:

$$\begin{gathered} F_{12} = g_{12}^{q'} f_{12}^{q'} + z_{12} f_{12}'^{q'} - g_{12}^{q''} f_{12}^{q''} - z_{12} f_{12}'^{q''} \\ g_{12}^{q'} = g_{12}\left(\alpha_1\right), g_{12}^{q''} = g_{12}\left(-\alpha_1 + \frac{1}{\pi}\right) \\ f_{12}^{q'} = \begin{cases} \zeta_{12}^{q'} & \zeta_{12}^{q'} > 0 \\ 0 & \zeta_{12}^{q'} \le 0 \end{cases}, f_{12}^{q''} = \begin{cases} \zeta_{12}^{q''} - q_{12}'' & \zeta_{12}^{q''} > q_{12}'' \\ 0 & \zeta_{12}^{q''} \le 0 \end{cases} \end{gathered} \tag{15}$$

where: $g_{12}^{q'}$ and $g_{12}^{q''}$ respectively represent the meshing stiffness when the tooth surface and the tooth back contact; $f_{12}^{q'}$ and $f_{12}^{q''}$ are used to judge the contact state of the gear pair, where q_{12}'' represents the tooth side clearance, the value of which is $q_{12}'' = \dfrac{2}{3} \times \left(0.06 + 0.0005A_{12} + 0.03K_{12}\right)$, and A_{12} is the center distance of the gear pair. Considering the rigid body rotation and elastic vibration of each gear, the translation and torsion motion equation of AC asynchronous motor is established.

$$\begin{cases} u_i\ddot{x}_i = -a_i F_{12}\sin\beta_{12} - g_i x_i - z_i\dot{x}_i \\ u_i\ddot{y}_i = a_i F_{12}\sin\beta_{12} - g_i y_i - z_i\dot{y}_i \\ G_i\ddot{\alpha}_i = a_i T_i - a_i F_{12} r_i \end{cases} \tag{16}$$

In the formula: G_i represents the moment of inertia of gear i; $a_i = 1$ corresponds to the driving gear on the left side of Fig. 2, and $a_i = -1$ corresponds to the rotating gear on the right side of Fig. 2. According to the above process, the electromechanical coupling dynamics of the drive system is analyzed and extracted [9].

2.3. Extraction of operation characteristics of AC asynchronous motor

AC asynchronous motor is a high order, nonlinear, strong coupling multivariable system. Some basic assumptions are usually made in the research:

1. It is assumed that the three-phase winding is symmetrical and the difference between them is 120 ° in space. The generated magnetomotive force is sinusoidal along the air gap;
2. Ignoring the saturation of magnetic circuit, the self-inductance and mutual inductance of each winding are constant;
3. Core loss is ignored;
4. The influence of frequency change and temperature change on winding resistance is not considered.

A control test is a functional requirement that implements a requirement definition for a single logical function and determines whether the requirement really should be reflected in the requirement.The dynamic model of AC asynchronous motor includes voltage balance equation, Newton equation, flux equation and torque equation. Among them, the number of voltage balance equations is related to the number of winding sets. N set of winding includes N differential equations [10]. The stator-side's voltage balance equation of three-phase winding motor can be written as follows:

$$U = RI + \frac{d\Psi}{dt} \tag{17}$$

wherein

$$U = [U_A, U_B, U_C, U_a, U_b, U_c] \tag{18}$$

$$I = [I_A, I_B, I_C, I_a, I_b, I_c] \tag{19}$$

$$R = \begin{bmatrix} R_s & 0 & 0 & 0 & 0 & 0 \\ 0 & R_s & 0 & 0 & 0 & 0 \\ 0 & 0 & R_s & 0 & 0 & 0 \\ 0 & 0 & 0 & R_a & 0 & 0 \\ 0 & 0 & 0 & 0 & R_b & 0 \\ 0 & 0 & 0 & 0 & 0 & R_c \end{bmatrix} \tag{20}$$

The flux equation at the stator side can be written as follows:

$$\Psi = HI \tag{21}$$

Then the inductance matrix is:

$$H = \begin{bmatrix} L_{AA} & L_{AB} & L_{AC} & L_{Aa} & L_{Ab} & L_{Ac} \\ L_{BA} & L_{BB} & L_{BC} & L_{Ba} & L_{Bb} & L_{Bc} \\ L_{CA} & L_{CB} & L_{CC} & L_{Ca} & L_{Cb} & L_{Cc} \\ L_{aA} & L_{aA} & L_{aA} & L_{aa} & L_{ab} & L_{ab} \\ L_{bA} & L_{bA} & L_{bA} & L_{ba} & L_{bb} & L_{bc} \\ L_{cA} & L_{cA} & L_{cA} & L_{ca} & L_{cb} & L_{cc} \end{bmatrix} \tag{22}$$

where, the diagonal elements in the matrix are self-inductance of each winding, and the rest are mutual inductance between corresponding windings. It is known that the stator winding of AC asynchronous motor is three-phase, the spatial difference of winding is $\frac{2}{3}\pi$, and all phases have a non-zero mutual inductance, which will cause the voltage balance equation to be very complex in the modeling process, and the model can be simplified by equivalent transformation to two-phase coordinates [11]. The stator phase current is equal to the magnetomotive force divided by the number of turns of the stator phase winding. The two-phase equivalent motor is composed of two orthogonal windings. The vector j can be considered as the sum of two independent phase current vectors projected on the $\alpha-\beta$ orthogonal coordinate system, and the mutual inductance between the two orthogonal windings is zero. When the two-phase equivalent transformation is introduced, the same flux, magnetic energy and torque should be ensured as the initial three-phase motor. This requires that the amplitude and spatial direction of the magnetomotive force O of the stator remain unchanged.

$$\begin{bmatrix} j_\alpha \\ j_\beta \end{bmatrix} = \gamma_1 \begin{bmatrix} 1 & -\frac{1}{2} & -\frac{1}{2} \\ 0 & \frac{\sqrt{3}}{2} & -\frac{\sqrt{3}}{2} \end{bmatrix} \begin{bmatrix} j_a \\ j_b \\ j_c \end{bmatrix} \tag{23}$$

$$\begin{bmatrix} u_\alpha \\ u_\beta \end{bmatrix} = \gamma_2 \begin{bmatrix} 1 & -\frac{1}{2} & -\frac{1}{2} \\ 0 & \frac{\sqrt{3}}{2} & -\frac{\sqrt{3}}{2} \end{bmatrix} \begin{bmatrix} u_a \\ u_b \\ u_c \end{bmatrix} \tag{24}$$

$$\begin{bmatrix} \tau_\alpha \\ \tau_\beta \end{bmatrix} = \gamma_3 \begin{bmatrix} 1 & -\frac{1}{2} & -\frac{1}{2} \\ 0 & \frac{\sqrt{3}}{2} & -\frac{\sqrt{3}}{2} \end{bmatrix} \begin{bmatrix} \tau_a \\ \tau_b \\ \tau_c \end{bmatrix} \tag{25}$$

In the formula, γ_1, γ_2 and γ_3 represent the adjustment coefficients of different parameters. At this time, the number of winding turns of two-phase equivalent motor needs to be increased to 1.5 times of the previous one. After conversion, the voltage and current amplitude, impedance and inductance remain unchanged, and the power $P_{\alpha\beta} = \frac{2}{3} P_{abc}$ [12]. Then the flux equation is:

$$\begin{bmatrix} \tau_{s\alpha} \\ \tau_{s\beta} \\ \tau_{r\alpha} \\ \tau_{s\beta} \end{bmatrix} = \begin{bmatrix} H_s & 0 & H_m \cos\theta_m & -H_m \sin\theta_m \\ 0 & H_s & H_m \sin\theta_m & H_m \cos\theta_m \\ H_m \cos\theta_m & H_m \sin\theta_m & H_r & 0 \\ -H_m \sin\theta_m & H_m \cos\theta_m & 0 & H_r \end{bmatrix} \begin{bmatrix} j_{s\alpha} \\ j_{s\beta} \\ j_{r\alpha} \\ j_{s\beta} \end{bmatrix} \tag{26}$$

According to the above flux equation, the operation characteristics of AC asynchronous motor are extracted. Based on this, the electromechanical coupling model of AC asynchronous motor drive system based on multiscale method is constructed.

2.4. Establishment of electromechanical coupling model considering rotor eccentricity of asynchronous motor

As the energy source of the rolling mill drive system, the dynamic behavior of the motor directly affects the performance of the main drive system of the rolling mill. For example, motor current has harmonics, motor speed and electromagnetic torque fluctuations affect the load. The motor with eccentric stator produces cogging torque with harmonic and unbalanced magnetic pull, while the rotor with eccentric rotor produces harmonic and Uniform Magnatic Field (UMF) cogging torque, and the number of poles is ± 1st harmonic. Many researchers have studied the dynamic behavior of motor. The control equations of motor rotation and electromagnetic behavior are derived. The transient dynamic characteristics of the motor with dynamic rotor eccentricity and unbalanced electromagnetic excitation are studied by using multiscale method. The unbalanced magnetic torque of the motor is analyzed by using Fourier series to determine the electromagnetic force. The electromagnetic force is introduced into the motor translation motion equation, and it is considered that the electromagnetic behavior affects the mechanical behavior, but the mechanical behavior can not affect electromagnetic behavior. However, in a real motor, there is an interaction between mechanical and electromagnetic behaviors. Therefore, it is necessary to study the dynamic behavior of the motor by deriving the control equation considering the interaction between mechanical and electromagnetic behaviors. In this study, the dynamic behavior of the motor is studied when the mechanical and electromagnetic interaction of the motor changes and the air gap between the stator and rotor changes. Considering the translational and rotational motion of the rotor, the nonlinear equation based on Lagrangian equation is derived by using dynamics and energetics, and the dynamic characteristics and mechanical and electromagnetic interaction of the motor are analyzed [13-15]. The effects of motor eccentricity on stator current, electromagnetic torque and rotor speed are studied.

Rotor eccentricity is generally divided into static eccentricity, dynamic eccentricity and mixed eccentricity. Static eccentricity means that the geometric center of the rotor is the center of rotation, and the centers of the stator and the rotor are not coincident. That is, the fixed position of the rotor in a certain direction of the stator is eccentric and rotates. At this time, no matter how the rotor rotates, the minimum position M of the rotor air gap does not change, and the air gap length does not change in the spatial distribution of the motor. This situation is generally caused by installation error or inaccurate processing of parts. Rotor dynamic eccentricity refers to that the rotor takes the stator center as the rotation center, the position of air gap in space changes with time, the minimum position of air gap changes constantly, and the length of air gap changes with the rotor rotation. Dynamic eccentricity is easy to occur in the condition of bearing damage, main shaft bending and misalignment of rotor and stator center during installation. The geometry of the motor's rotor eccentricity is shown in Figure 3 below.

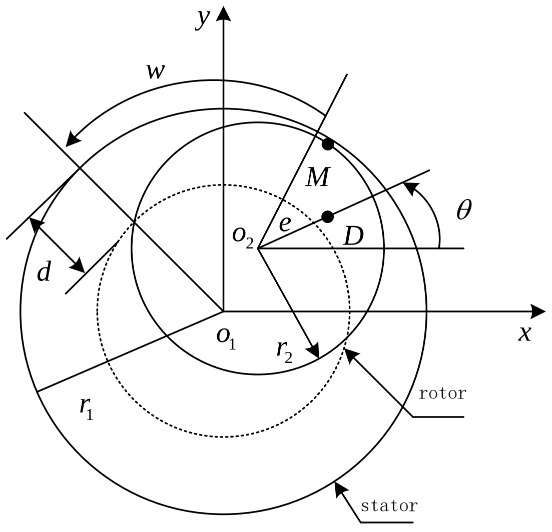

Figure 3. Geometry of rotor eccentricity

Mixed eccentricity refers to the situation that static eccentricity and dynamic eccentricity occur at the same time. Let the geometric center of the stator be o_1, the geometric center of the rotor be o_2; r_1 and r_2 are the stator radius and the rotor radius respectively. When the rotor appears eccentricity, the dotted line position of the rotor moves to the solid line position, the mass center D of the rotor rotates, and the rotation angle is expressed by θ. At this time, the air gap between the rotor and the stator at w will no longer be constant, that is, the air gap length d will change; the eccentric length between o_2 and D is expressed by e. Taking the point as the coordinate center, the $x-y$ coordinate system is established [16]. According to the coordinate system, the relative eccentricity is obtained. The kinetic energy of the drive system can be expressed as:

$$E = E_r + \frac{1}{2}\delta\theta_d^2 \tag{27}$$

In the formula, δ represents the moment of inertia of the rotor under relative eccentricity. The potential energy of the drive system is expressed as:

$$V = V_r + \frac{1}{2}\xi\left(\theta - \theta_d\right)^2 \tag{28}$$

where: ξ is the elasticity coefficient of rotor shaft. According to the Lagrange theorem, the equations are obtained.

$$\frac{d}{dt}\left[\frac{dE}{\partial\sigma}\right] + \frac{\partial F}{\partial\sigma} - \frac{\partial\left(E - V + U\right)}{\partial\sigma} = L \tag{29}$$

In the formula, σ is the generalized coordinate, which is the generalized moment of x, y and z. If $L_x = L_y = O$, $L_\theta = T_e$, then according to the above equation, the electromechanical coupling model with mechanical and electromagnetic interaction is obtained

$$\begin{cases} m\ddot{x} - me\ddot{\theta}\sin\theta - me\dot{\theta}^2\cos\theta + a_1\dot{x} + \xi x = F_x \\ m\ddot{y} - me\ddot{\theta}\cos\theta - me\dot{\theta}^2\sin\theta + a_1\dot{y} + \xi y = F_y \\ \left(\delta + me^2\right)\ddot{\theta} - me\ddot{x}\sin\theta + me\ddot{y}\cos\theta + a_2\dot{\theta} = T_e - T_s \\ T_s = \xi\left(\theta - \theta_d\right) \\ \delta_d\ddot{\theta}_d = T_s - T_d \end{cases} \tag{30}$$

In the formula: a_1 represents the equivalent damping coefficient of the rotor's translational motion; a_2 represents the equivalent damping coefficient of the rotor's rotational motion. So far, the electromechanical coupling model of AC asynchronous motor drive system based on multiscale method has been constructed [17].

3. Experimental study

In order to verify the reliability of the control effect of the electromechanical coupling model for the AC asynchronous motor drive system, the experimental platform of AC asynchronous motor drive system is built to carry out the experimental research on the dynamic characteristics of the system under the impact load condition, as more comprehensive and real dynamic characteristics of the motor gear drive system are obtained. The experimental results of the model established in this paper are compared with that of the traditional electromechanical coupling model, to provide the experimental basis for the dynamic design, condition monitoring and load shedding control of the drive system.

3.1. Experiment process

In order to maintain the similarity between the experimental system and the drive system, the main structural features of the drive system are preserved in the design of the experimental bench: between the driving motor and the drive system, a slender elastic shaft is set to simulate the AC asynchronous elastic torque shaft, and between the loading device and the drive system, an inertia flywheel is set to simulate the AC asynchronous large inertia roller. Because the motor drive system has many stages and high failure rate, in order to reduce the number of parts and improve the reliability of the system, the research plans to use the NGWN (planetary reducer) type of planetary gear transmission with large speed ratio instead of the multi-stage gear drive system of the AC asynchronous motor. Therefore, the NGWN type of planetary gear box with large speed ratio is developed and used in this experimental platform. In view of the difference between the experimental gearbox and the AC asynchronous motor drive system, when arranging the sensors, the dynamic characteristics of the area with similar structure to the drive system are mainly concerned, such as the dynamic load on the connecting shaft of the elastic shaft and the inertia flywheel and the dynamic response of the motor current. The common questions of the test-bed and the AC asynchronous motor drive system can be verified by experiments, including: the dynamic load response law of the drive system under variable speed and variable load conditions, the influence law of the torsional vibration of the drive system on the motor current, the effectiveness of the speed control strategy and the influence of different speed control strategies on the load state of the system. Figure 4 is the actual picture of the gear drive system test-bed.

The measurement and control system and software based on Disk Space Management Command (dSPACE) are designed and developed. The control system can realize the following functions: control the drive motor and the dynamometer on-line, control the start and stop of the drive motor and the dynamometer in the loading system through dSPACE, switch the speed/torque control mode and send the speed/torque target command value; monitor and collect the sensor speed, torque and current signals in real time through the QuantumX data acquisition system, and save the collected data to provide data support for the subsequent experimental analysis; the system has the ability to ensure the safe operation of the experimental platform and error command processing, to carry out safety limits on the key parameters of the system, and to have the function of emergency shutdown; the main subsystem of the measurement and control system is modularized to facilitate the subsequent improvement of the control system design. After the test platform and test system run without exception, the experiment is started.

3.2. Test and analysis

The speed of the drive motor is controlled at 600r / min by the frequency converter, and the impact load is applied to the drive system by the dynamometer, so that the load on the inertia flywheel suddenly increases by 3.5 times from 2500 Nm. The service coefficient of shaft is defined as the ratio of the measured value of torque after impact to the average value of torque before impact, and the dynamic load coefficient is the ratio of the measured value of torque during steady-state phase to the average value of torque. Taking the model constructed in this study as the test object of the experimental group, and the model constructed by two traditional methods as the test object of the control group, Figure 5 below is the comparison result of service factor of input and output shaft of gearbox at the moment of impact of AC asynchronous motor under the application of three models.

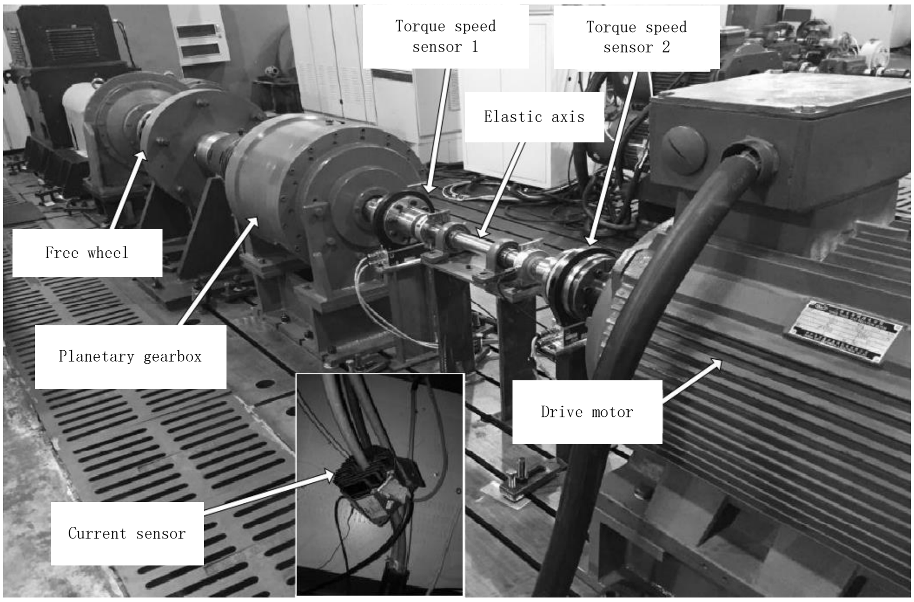

Figure 4. Actual picture of experimental platform

According to Figure 5 (a) above, there is no obvious difference between the maximum service coefficient of high-speed stage and low-speed stage in the experimental group, because the planetary transmission structure is relatively compact under the control of electromechanical coupling model. In the control group 1, the high-speed stage and low-speed stage use coefficient have a large difference, which shows that the control effect of electromechanical coupling model is poor, and the operation effect of planetary transmission structure is poor. The high-speed and low-speed use coefficients of control group 2 are also significantly different, which showed the same questions with control group 2. The experiment is carried out for two times in total, and the difference of service coefficient of high-speed stage and low-speed stage of the three test groups is shown in Table 1.

Table 1. Differences of service factor

Number of test	Experimental group	Control group 1	Control group 2
1st	0.78	0.472	0.545
2nd	0.71	0.495	0.520

According to Table 1, in the experimental group, the difference of service factor between high-speed stage and low-speed stage is very small, while the difference of service factor between the control groups is relatively large. The electromechanical coupling model in this study has better control effect on the planetary transmission structure. Under the application of the three models, Figure 6 below shows the dynamic load coefficient comparison results of the input and output shafts of the gearbox after the impact of the AC asynchronous motor.

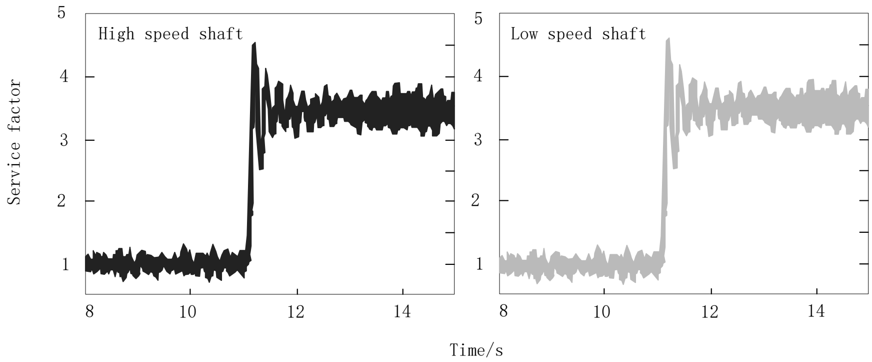

(a) Test results of experimental group

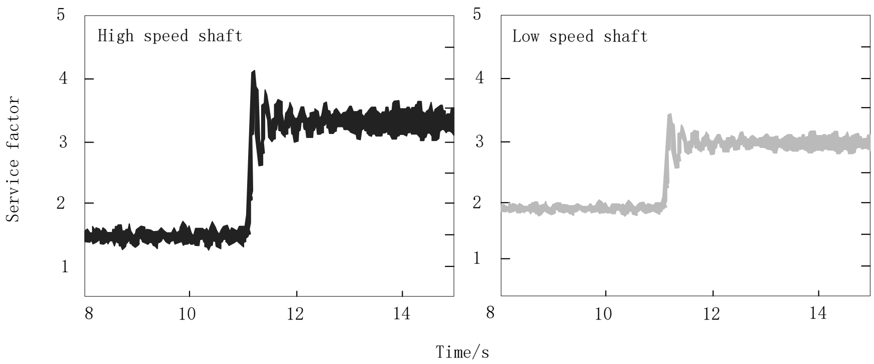

(b) Test results of control group 1

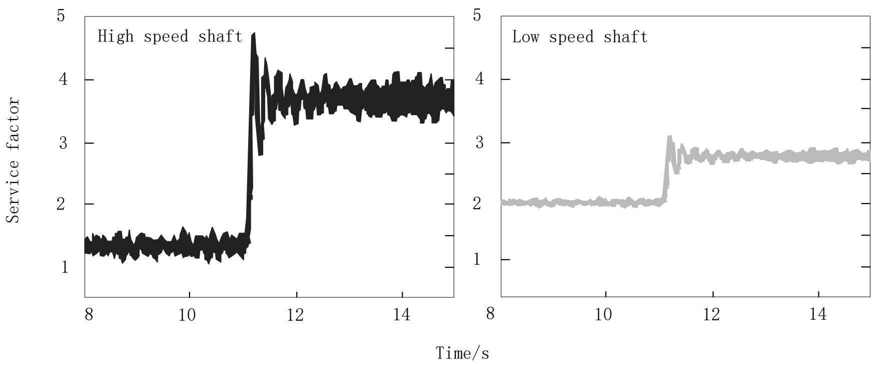

(c) Test results of control group 2

Figure 5. Test results of service factor at impact moment

According to Figure 6, the dynamic load coefficient of the experimental group decreases from the high-speed stage to the low-speed stage. After the load is increased, the service coefficient increases and the dynamic load coefficient decreases. It shows that under the control of the electromechanical coupling model, the dynamic load caused by the internal excitation such as load increase, meshing stiffness, meshing error and so on reduces the threat to the safe operation of the system, and the external load becomes the main threat. However, the dynamic load coefficient of the two control groups does not decrease due to the large difference of service coefficient, which shows that the dynamic load caused by internal excitation such as load aggravation, meshing stiffness and meshing error in the two control groups does not weaken the threat to the safe operation of the drive system, and the main threat to the motor is the internal load of the motor. In the same two tests, Table 2 below shows the test results of dynamic load coefficient in three test groups.

Table 2. Difference of dynamic load coefficient

Number of test	Experimental group	Control group 1	Control group 2
1st	0.887	0.65	0.142
2nd	0.864	0.59	0.107

According to the calculation results in Table 2, the dynamic load coefficient difference of the experimental group is the largest, while the dynamic load coefficient difference of the two control groups is very small, which shows that only the dynamic load coefficient of the experimental group is significantly reduced under the premise of increasing the service coefficient. According to the above experimental results, the electromechanical coupling model can control the normal operation of the AC asynchronous motor and the drive system, so that the AC asynchronous motor can work normally.

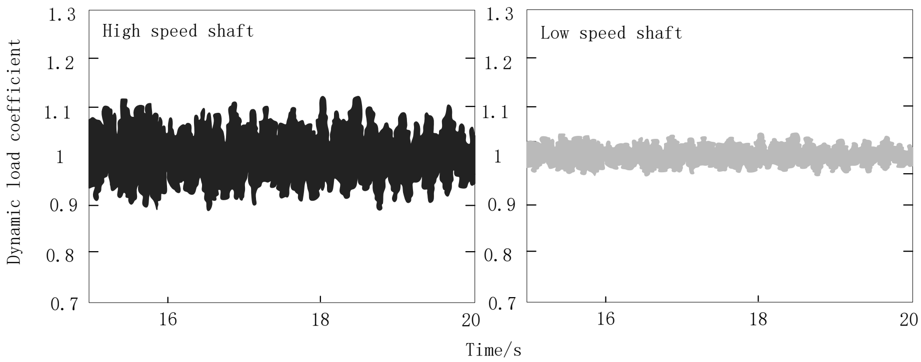

(a) Test results of experimental group

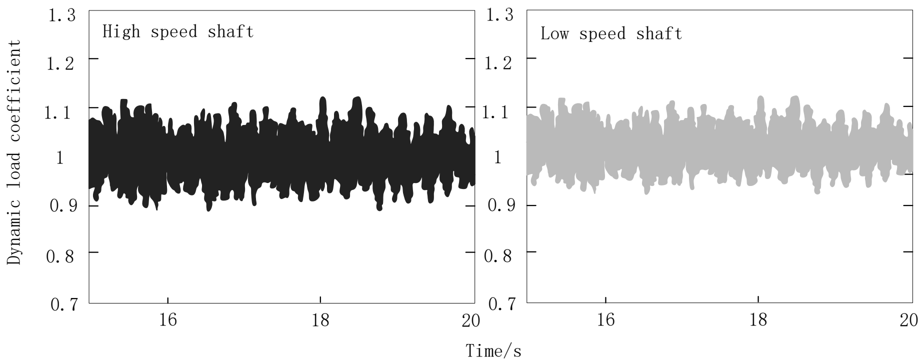

(b) Test results of control group 1

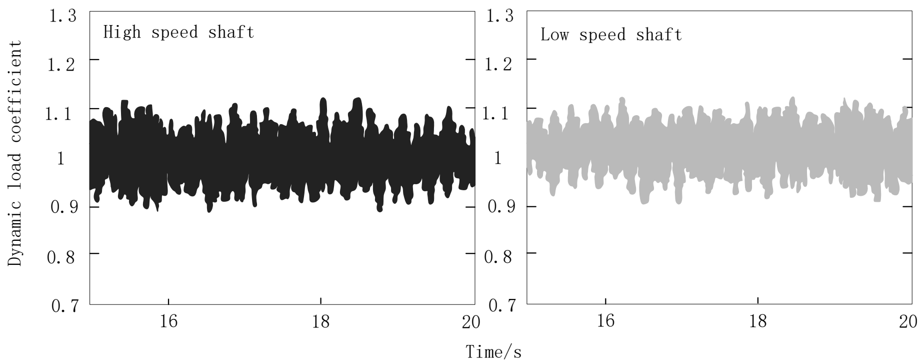

(b) Test results of control group 2

Figure 6. Dynamic load coefficient after impact

4. Conclusions

With the increase of load, the amplitude of gear meshing stiffness and bearing support stiffness increases, which leads to the increase of natural frequency in different degrees, and the increase speed slows down with the increase of load. Transient torsional vibration of the first mode is generated. In this paper, a new type of electromechanical coupling model of AC induction motor drive system is proposed. Under the control of electromechanical coupling model, the load caused by internal excitation increases. Dynamic loads such as meshing stiffness and meshing error reduce the threat to the safe operation of the system. At the moment of impact, the magnetic field of the motor can absorb part of the mechanical impact energy and play a role of buffer and protection to the driving system. It is concluded that the coupling vibration of motor gear reduces the load coefficient from high speed to low speed under stable load, and improves the internal vibration state of high speed gear safety gear train.

References

[1] Zanegin, S.; Ivanov, N.; Shishov, D.; et al. (2020) Manufacturing and testing of AC HTS-2 coil for small electrical motor. Journal of Superconductivity and Novel Magnetism, 33(2):355-359.

[2] Abboud, N.; Scovazzi, G. (2018) Elastoplasticity with linear tetrahedral elements: A variational multiscale method. International Journal for Numerical Methods in Engineering, 115(8):913-955.

[3] Vu, V.H.; Trouette, B.; TO, Q.D.; et al. (2018) Hybrid atomistic-continuum multiscale method for fluid flow with density variation in microchannels. International Journal of Numerical Methods for Heat & Fluid Flow, 28(1):3-30.

[4] Xing, Y.F.; Gao, Y.H. (2019) Multiscale eigenelement method for periodical composites: A review. Chinese Journal of Aeronautics, 32(01):104-113.

[5] Huang, Y.F.; Lu, J.F.; Ming, P.B. (2018) A concurrent global–local numerical method for multiscale PDEs. Journal of Scientific Computing, 76(2):1188-1215.

[6] Fang, Y.N.; Liang, X.H.; Zuo, M.J. (2018) Effects of friction and stochastic load on transient characteristics of a spur gear pair. Nonlinear Dynamics, 93(2):599-609.

[7] Kumar, P.; Kumar, N. Effect of EGR on performance and emission characteristics of a dual fuel engine fuelled with CNG and JOME. Biofuels, 2016.

[8] Tan, J.J.; Zhu, C.C.; Song, C.S.; et al. (2019) Effects of flexibility and suspension configuration of main shaft on dynamic characteristics of wind turbine drivetrain. Chinese Journal of Mechanical Engineering, 32(1):1-15.

[9] Fernández-Mariño, A.I.; Harpole, T.J.; Oelstrom, K.; et al. (2018) Gating interaction maps reveal a noncanonical electromechanical coupling mode in the Shaker K^+ channel. Nature Structural & Molecular Biology, 25(4):320-326.

[10] Vysotsky, V.F.; Gulyaev, I.V.; Nagirniak, A.A.; et al. (2019) Features of an asynchronous motor with a double-layer rotor in ship pumping equipment. Russian Electrical Engineering, 90(1):1-5.

[11] Zheng, J.C.; Wang, Y.; Lin, C.C.; et al. (2018) A fusion algorithm of target dynamic information for asynchronous multi-sensors. Microsystem Technologies, 24(10):3995-4005.

[12] Chuang, H.C.; Li, G.D.; Lee, C.T. (2019) The efficiency improvement of AC induction motor with constant frequency technology. Energy, 174:805-813.

[13] Li, J.; Sheng, P.; Shao, K. (2020) Optimization of clutchless AMT shift control strategy for electric vehicles. Jordan Journal of Mechanical and Industrial Engineering, 14(1):109-117.

[14] Zhang, Q.; Wang, Y.; Lin, W.; et al. (2020) Contact mechanics analysis and optimization of shape modification of electric vehicle gearbox. Jordan Journal of Mechanical and Industrial Engineering, 14(1):15-24.

[15] Vavilov, V.E. (2018) Influence of rotor eccentricity in ultrahigh-speed electrical machines on their characteristics. Russian Engineering Research, 38(8):617-622.

[16] Othmani, C.; Zhang, H.; Lü, C.F.; et al. (2019) Effects of initial stresses on the electromechanical coupling coefficient of SH wave propagation in multilayered PZT-5H structures. The European Physical Journal Plus, 134(11):1-18.

[17] Chu, L.L.; Li, Y.B.; Dui, G.S. (2019) Size-dependent electromechanical coupling in functionally graded flexoelectric nanocylinders. Acta Mechanica, 230(9):3071-3086.

JJMIE

Volume 15, Number 1, March. 2021
ISSN 1995-6665
Pages 83 - 91

Jordan Journal of Mechanical and Industrial Engineering

Impact Evaluation of Industrial Energy Consumption Based on Input-output Complex Network

Ren Zhou, Xinhua Wang*

College of Finance and Economics, College of Economics and Management, Shandong University of Science and Technology, Qingdao 266590, China

Received July 18 2020 *Accepted March 13 2021*

Abstract

Target control and industrial transfer are important methods to regulate energy conservation and emission reduction in the region, so measuring the influence of each industry to energy consumption is the basis of regional industrial structure adjustment. Firstly, an energy flow network model is constructed based on the theory of Industrial Complex Network. It describes the mutual input and consumption of material and energy among industrial sectors. Then, the index system is designed to evaluate the influence of each industry on energy consumption in the economic system. According to the evaluation, methods are searched for to regulate energy-saving and emission-reducing on the industrial level. Based on the data of Shandong Province, the strategies of energy saving and emission reduction are put forward: research and develop new technologies; Sort management, focusing on the control of “key industries”, and paying attention to the industries that consume less energy but relevant more with others appropriately; Rational layout industry, optimize industrial structure and so on.

Keywords: energy consumption; energy flow network; Shandong province; evaluation of industrial impact;

1. Introduction

Industrial transfer is an important method to realize the rational distribution of productive forces and the coordinated development of the region. With the influence of the pressure of energy conservation and emissions reduction, many economic developed areas limit the development of the industry with high energy consumption and high pollution, so more and more such industries were transferred to less developed area. How to adjust regional industrial structure? Domestic and foreign scholars have studied the influence of industrial structure on energy consumption.

Watanabe analyzed the impact of changes in industrial structure on energy consumption to 20% [1]. Ang [2], Hasanbeigi et al. [3], Choi and Ang [4] concluded that the change of the industrial structure in different periods contribute different to energy consumption by LMDI. Lu confirmed that the total amount of energy consumption is highly correlated with the industrial structure by regression analysis [5]; Zhang and Huang confirmed that economic structure dominated by second industries has an accelerating effect on energy consumption [6]. Yin et al. constructed VECM and found that the changes in energy consumption and industrial structure present a positive correlation in the long run, and the development of the second and tertiary industries has a significant impact on the increase of energy consumption [7]. Most of these studies are based on the three industry divisions, but in fact there are thousands of floor links between the sub sectors, and the energy consumption level varies greatly. It is very important to analyze the impact of changes in the structure of industry segments on energy consumption.

In the late twentieth century, complex networks were applied to the field of social science. More and more scholars combine input-output theory with complex network theory to study industrial association. In foreign countries, of professor Campbell [8], the professor of Washington University introduced graph theory into industrial association research firstly; Schnabl [9], Aroche [10], Morillas et al. used different quantitative methods to determine the threshold and extract strong correlation, and construct their respective industrial complex network models [11]. Mcnemey et al. built industrial networks based on input-output data from more than 20 countries and found that they have similar associations [12]. In China, Zhao et al. constructed a graph model of industry association structure using the WI index to study the industry supply chain and related structure of Shandong province [13]. Chen et al. used the industry complex network theory to study the side effect of industry [14]. Sun and Wang [15] and Wang and Sun [16] compared the industrial correlation of Beijing Tianjin and Hebei, and identified their key industry.

From the existing research results, the modeling and optimization of industrial related networks using input-output table has made great progress. However, using complex networks to analyze energy flow and evaluate the impact of energy consumption in subdivision industries is not deep enough. Therefore, this paper uses the input-output table and the industrial energy consumption data of Shandong province, constructs the energy consumption flow network model and the industrial energy consumption

* Corresponding author e-mail: zwhx741@sina.com.

influence evaluation system, and looks for the road of industrial development under the premise of energy saving and emission reduction.

2. Theoretical Model and Research Method

An energy flow network model is constructed based on the theory of Industrial Complex Network. It describes the mutual input and consumption of material and energy among industrial sectors. Then, the index system is designed to evaluate the influence of each industry on energy consumption in the economic system. After that, using entropy weight method to determine the index weight.

2.1. Construction of energy flow associated network model

With each industry sector as the node, the amount of energy invested and consumed by the industrial sector as a link, according to the input-output relation of energy consumption among industries, a complex network model with energy flow relationship is established. The point set V is used to represent the industrial sector set, and the edge set L represents the inter industry input-output relation. The weight set W represents the weights of each edge, that is, the relationship of input and output between the industries [17]. The network graph T = (V, L, W). The edge set L embodied energy flow relationship between the industry, if the industry i invest energy to industrial j, then there is an edge Lij from i to j; if no energy is invested from industry i to industry j, Lij does not exist. Because the energy input from industry i to industry j does not necessarily exist when the energy input from industry j to industry i exists, lij≠lji. The energy input weights from industry i to industry j is marked on each side in the figure as Wij. The inter industry input-output is different, so Wij ≠ Wji. Since most industry sectors have mutual input and mutual consumption, Lij and Lji may exist simultaneously. So, the complex network is asymmetrical, directed with multiple edges possibly.

2.2. The index to evaluate the influence of each industry to energy consumption

Based on the statistical index properties of the complex network, four types of indicators are set including breadth of node, depth of node, spread degree of node and dominant degree of node, to analyze the energy consumption influence of the node from forward, backward and integrated three angles.

1. Breadth index of node

It describes the ability of the target node to affect other nodes directly. 3 indexes including forward, backward and integrated breadth index are set to describe the node range directly pushed, pulled and related strongly. The forward breadth of nodes describes the number of strongly related nodes that are directly affected by the active supply or passive demand, and is expressed by in-degree centrality [18-20]. The backward breadth of nodes describes the number of backward strong connected nodes, which is directly affected by the passive supply or the active demand, and is expressed by out-degree centrality. The comprehensive breadth of nodes describes the number of forward or backward strongly connected nodes that are directly affected by the supply and demand relationship. It can be measured by the sum of in-degree centrality and out-degree centrality. The higher the 3 indexes, the stronger the width of the associated nodes. If $d_I(n_i)$ represents in-degree centrality, $d_O(n_i)$ represents out-degree centrality, then

$$d_I(n_i) = \sum_{j=1}^{g} x_{ji}, \quad d_O(n_i) = \sum_{j=1}^{g} x_{ij}.$$

x_{ij} represents the weight value of the effective connection between n_i and n_j, and g represents the number of sectors.

2. Depth of node

Depth of node describes how the target node transfers its affection directly and indirectly to other nodes via network association. 3 indexes including forward, backward and integrated depth index are set. The forward depth describes the degree to which nodes extend forward through the supply chain. It can be calculated by reciprocal of out closeness centrality. Out closeness centrality can be calculated by the reciprocal of the sum of the shortcuts from the destination node to all other nodes along the direction of the network edge.

The backward depth describes the degree to which nodes extend backward progressively through the demand chain. It can be calculated by reciprocal of in closeness centrality. In closeness centrality can be calculated by the reciprocal of the sum of the shortcuts from the destination node to all other nodes inverse the direction of the network edge. The integrated depth describes the degree to which the nodes extend forward or backward through the supply chain or demand chain, which is calculated by the sum of the forward depth and the backward depth. The higher the 3 indexes, the stronger the individual depth of nodes. If $C_c(n_i)$ represents closeness centrality, then $C_c(n_i) = \dfrac{g-1}{\sum_{j=1}^{g} d(n_i, n_j)}$.

$d(n_i, n_j)$ represents the shortest path from n_i to n_j.

3. Spread of node

Spread of node describes the potential level of the target nodes. 3 indexes are set up: forward spread, backward spread and complete spread. Forward spread is calculated by Katz horizontal influence, (the row sum of network adjacency matrix or flow matrix). Backward spread degree is calculated by Katz vertical influence, (the column sum of network adjacency matrix or flow matrix). Integrated spread degree describes the sum of Katz horizontal influence and Katz vertical influence. The higher the three indexes, the greater the spread of nodes.

4. Dominance of node

Dominance of node describes the degree to which nodes control other nodes. 2 indexes, node relation dominance and node flow dominance, are used to describe the degree of node control to other nodes and traffic flow. The dominance of node relation represents the relation control ability of nodes on the whole network. If a node is in many other nodes on the path through the interactive network, so it occupies an important position, can affect other nodes through energy transfer control, in the middle of the central node of the relation between dominant degree [21]. The node flow dominance describes the network path where the nodes interact with each other, and the degree of control of the energy transfer between other nodes is expressed by the center of the flow. The higher the 2 indexes, the stronger the dominance of nodes. If $C_B(n_i)$ represents betweenness centrality, then

$$C_B(n_i) = \frac{\sum_{j<k} g_{jk}(n_i) / g_{jk}}{(g-1)(g-2)/2}.$$

g_{jk} represents the number of shortest paths associated with energy flows between industries j and k, $g_{jk}(n_i)$ represents how many ni industry is contained in the shortest energy flow path connecting industries j and k.

2.3. Index weight determination

In order to understand the influence of each department more clearly, the index weight is determined by entropy weight method. The forward impetus, the backward pulling power and the comprehensive influence are evaluated respectively.

According to the variability of indexes, entropy weights determine the weights of indexes. The weighting steps are as follows:

First of all, data standardization processing.

Suppose there are n indicators $X_1, \ldots, X_n$, among $X_j = \{x_{1j}, x_{2j}, x_{3j}, \ldots x_{ij}\}$, x_{ij} Represents indicator j of industry I, then the standardized value of each index is $x_{ij}^* = \frac{x_{ij} - x_{\min j}}{x_{\max j} - x_{\min j}}$.

Then, calculate the information entropy of each index.

According to information theory, Information entropy is $E_j = \frac{-\sum_{i=1}^{n} P_{ij}\ln(P_{ij})}{\ln(n)}$, among which, if $P_{ij} = \frac{x_{ij}^*}{\sum_{i=1}^{n} x_{ij}^*}$, let $\lim_{P_{ij}\to 0} P_{ij}\ln(P_{ij}) = 0$.

Finally, the weight of each index is determined $W_j = \frac{1-E_j}{n-\sum_{i=1}^{n} E_j}$, $Score = \sum w_j x_{ij}^*$

3. Results

Based on the data of Shandong Province, the complex network model of energy flow is constructed, the sub-index of energy flow influence is calculated, and the energy flow influence of each industry is evaluated.

3.1. Data sources and processing

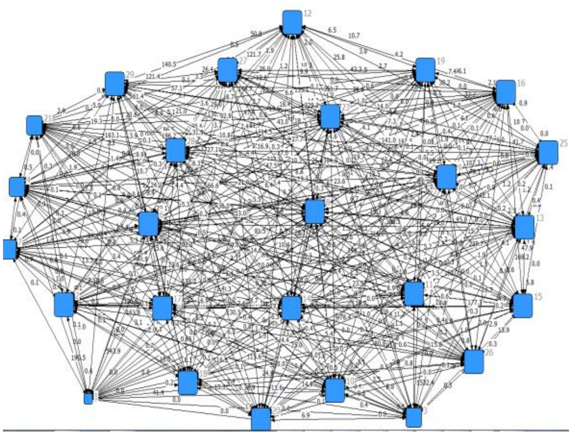

Figure 1. energy flow associated 2 mode network diagrams

The construction of the complex network model requires data of input-output table and energy consumption table. The design department of them are not unified, so in order to facilitate the analysis and comparison, based on the input-output table and the energy consumption table of Shandong in 2012, the energy consumption table and input-output table of 29 sectors are merged, and the energy input and output table of the department is calculated on this basis [22]. The energy consumption data of each industry sector in 2012 were obtained from the statistical yearbook in 2013, and the industrial energy consumption matrix was calculated according to the direct industrial consumption coefficient. To facilitate observation, a network diagram (**Fig. 1**) is constructed. In **Fig. 1**, the point set V consists of 29 industry sectors with input-output relationships. The size of the node represents the magnitude of the degree. The industry code is marked on the right side of the node. The energy flow between nodes is marked on the line. The industry code is shown in **Table 1**.

Table 1. Industry code

code	industry	code	industry
1	Agriculture, forestry, animal husbandry and fishery	16	General purpose equipment manufacturing
2	Coal mining and cleaning	17	Transportation equipment manufacturing
3	Oil and gas extraction	18	Electrical machinery and equipment manufacturing
4	Metal mining industry	19	Communications equipment, computers and other electronic equipment manufacturing
5	Non-metal mining and other mining industry	20	Instrument and culture office machinery manufacturing
6	Food manufacturing and tobacco processing industry	21	Crafts and other manufacturing industries
7	Textile industry	22	waste
8	Textile, clothing, shoes and caps, leather, down and its products	23	The production and supply of electricity and heat
9	Wood processing and furniture manufacturing	24	Gas production and supply
10	Paper making, printing and the manufacturing of stationery and sports goods	25	Water production and supply
11	Petroleum processing, coking and nuclear fuel processing	26	Construction industry
12	Chemical industry	27	Transportation, ware-housing and postal services
13	Non-metallic mineral manufacturing	28	Wholesale & retail, accommodation catering
14	Metal smelting and rolling industry	29	Other social services
15	Metal products		

3.2. Industry energy flow influence index calculation

According to the formula in 2.1 and industry energy flow matrix, using UCINET software, the indicators are calculated to analyze the impact of energy flow in each industry, as shown in Table 2.

To see the effect of each industry more clearly, a scatter plot is plotted, as shown in **Fig. 2**.

Table 2. comprehensive analysis index of node influence.

code	breadth			depth			spread			dominance	
	Forward breadth	Backward breadth	Comprehensive breadth	Forward depth	Backward depth	Comprehensive depth	Forward spread	Backward spread	Complete spread	Relational dominance	Flow dominance
1	1.43	0.38	1.81	0.029	0.026	0.055	0.022	0.006	0.028	0.231	10.785
2	1.79	0.667	2.457	0.032	0.034	0.067	0.029	0.011	0.04	2.078	3.294
3	1.896	0.423	2.319	0.030	0.028	0.058	0.030	0.007	0.037	0.203	3.459
4	1.631	0.153	1.784	0.034	0.021	0.055	0.027	0.002	0.029	0.382	0.477
5	0.438	0.075	0.513	0.034	0.029	0.063	0.007	0.001	0.008	2.409	0.704
6	0.862	1.307	2.169	0.034	0.025	0.059	0.014	0.020	0.034	1.479	7.128
7	0.725	1.043	1.768	0.033	0.033	0.067	0.011	0.016	0.027	2.257	3.484
8	0.446	0.139	0.585	0.034	0.036	0.070	0.007	0.002	0.009	4.416	2.024
9	0.244	0.223	0.467	0.032	0.034	0.067	0.004	0.003	0.007	3.189	1.477
10	0.919	1.062	1.981	0.034	0.036	0.070	0.014	0.017	0.031	4.416	3.460
11	1.866	2.381	4.247	0.031	0.036	0.067	0.030	0.037	0.067	1.473	2.975
12	4.836	6.208	11.044	0.036	0.036	0.071	0.079	0.102	0.181	6.933	20.788
13	1.11	2.729	3.839	0.034	0.034	0.069	0.018	0.043	0.061	5.505	9.365
14	3.85	8.146	11.996	0.033	0.036	0.069	0.062	0.133	0.195	5.336	10.719
15	0.518	0.652	1.17	0.033	0.036	0.069	0.008	0.011	0.019	5.336	3.046
16	1.304	0.565	1.869	0.036	0.036	0.071	0.021	0.009	0.03	6.933	5.429
17	0.644	0.33	0.974	0.033	0.036	0.069	0.010	0.005	0.015	5.336	1.901
18	0.874	0.595	1.469	0.036	0.036	0.071	0.014	0.010	0.024	6.933	3.095
19	0.206	0.093	0.299	0.033	0.036	0.069	0.003	0.001	0.004	4.831	1.662
20	0.22	0.017	0.237	0.029	0.036	0.065	0.004	0.000	0.004	0.74	1.258
21	0.118	0.065	0.183	0.032	0.036	0.068	0.002	0.001	0.003	2.685	1.543
22	0.231	0.018	0.249	0.026	0.023	0.050	0.004	0.000	0.004	0	0.786
23	1.919	1.745	3.664	0.029	0.036	0.065	0.031	0.027	0.058	0.617	5.761
24	0.046	0.056	0.102	0.032	0.030	0.063	0.001	0.001	0.002	1.465	0.901
25	0.063	0.087	0.15	0.030	0.036	0.066	0.001	0.001	0.002	1.088	1.283
26	0.093	0.442	0.535	0.031	0.033	0.065	0.001	0.007	0.008	1.15	1.984
27	1.376	1.613	2.989	0.032	0.036	0.068	0.022	0.026	0.048	2.6	12.668
28	0.813	0.579	1.392	0.032	0.036	0.068	0.013	0.009	0.022	2.685	10.188
29	1.955	0.63	2.585	0.030	0.036	0.066	0.031	0.010	0.041	2.294	14.210

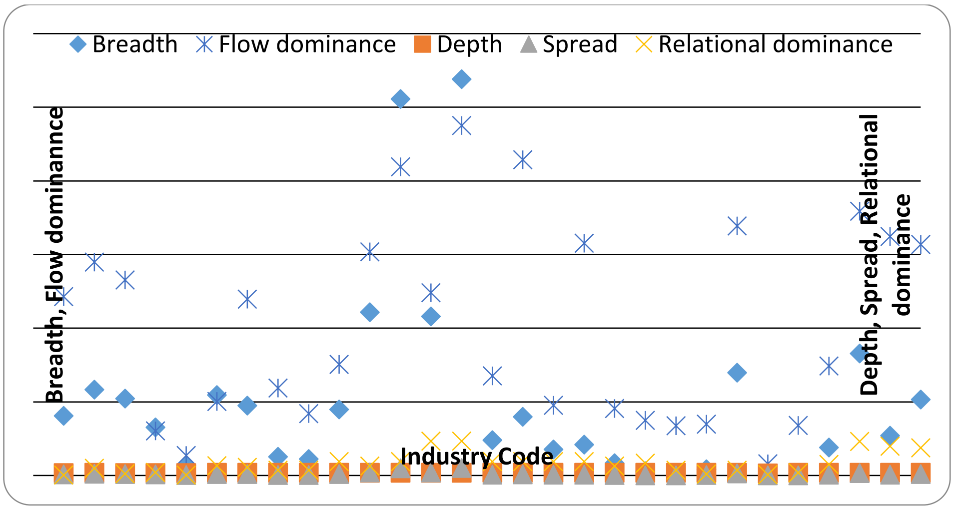

Figure 2. Index of node influence.

As can be seen from **Fig. 2**, among the chemical industry, metal smelting and rolling processing industry, non-metallic mineral products industry, transportation, warehousing, postal service, the indicators are in the top 10. While among waste, gas production and supply, water production and supply, instrument and culture office machinery manufacturing, non-metallic minerals and other mineral extraction and construction industry, the indicators are in the latter 10.

Most of the indexes in chemical industry, metallurgy and materials industry, transportation, machinery, production and supply of electronic equipment manufacturing industry and electric power are higher, especially the influence degree, and they have greater dominance, which is the main driving force of economic development in Shandong [23]. It shows that industry is the main industry of energy consumption and occupies a central position. The manufacturing industry is relatively mature, a relatively complete industrial chain, chemical industry, metallurgy, energy and raw materials have certain comparative advantages, but economic development is constrained by energy and resources.

The industries such as transportation, warehousing, postal services, other social services, wholesale and retail, accommodation, catering have strong impact, which means that traditional advantages of the third industry are flourishing, largely contributing to other industries and impacting the economy. But other social services are integrated data from multiple departments, and restricted by data acquisition, so they cannot fully analyze the specific circumstances of each department.

3.3. Comprehensive analysis of energy flow influence among industries

The comprehensive analysis of energy flow influence among industries is developed from three aspects: forward thrust force analysis, backward pull force analysis and comprehensive influence force analysis.

1. Forward thrust of energy flow

The weights of Forward breadth, Forward depth and Forward spread are 0.511621, 0.0748 and 0.413579 respectively by entropy weight method. The forward force of the energy flow obtained from the weighted sum of the normalized values of each index is shown in the last column of Table 3.

From the angle of forward force, all the indexes in chemical industry, metal smelting and rolling processing industry, electricity & heat production and supply industry, petroleum and natural gas exploitation industry, petroleum processing, coking and nuclear fuel processing, coal mining and cleaning industry are more than 0.9, far higher than 0.58 of the average. These industries are basic industries in the national economy, and the development of economy will drive the energy consumption of these industries to increase significantly. Take the chemical industry for example, if the final demand of each sector of the national economy grows by 1 unit, the energy consumption of the chemical industry will be increased by 2.5 times. Therefore, the industry should strengthen technological innovation and improve energy efficiency. Not only should they maintain a certain economic scale to meet the needs of the national economic development, but they also should not cause waste of energy.

Table 3. Calculation table of forward force

Code	Forward breadth (0.511621)	Forward depth (0.0748)	Forward spread (0.413579)	Forward force
1	0.731618	0.002169	0.009099	0.742886
2	0.915802	0.002394	0.011994	0.930189
3	0.970033	0.002244	0.012407	0.984685
4	0.834454	0.002543	0.011167	0.848164
5	0.22409	0.002543	0.002895	0.229528
6	0.441017	0.002543	0.00579	0.449351
7	0.370925	0.002468	0.004549	0.377943
8	0.228183	0.002543	0.002895	0.233621
9	0.124836	0.002394	0.001654	0.128883
10	0.47018	0.002543	0.00579	0.478513
11	0.954685	0.002319	0.012407	0.969411
12	2.474199	0.002693	0.032673	2.509564
13	0.567899	0.002543	0.007444	0.577887
14	1.969741	0.002468	0.025642	1.997851
15	0.26502	0.002468	0.003309	0.270797
16	0.667154	0.002693	0.008685	0.678532
17	0.329484	0.002468	0.004136	0.336088
18	0.447157	0.002693	0.00579	0.45564
19	0.105394	0.002468	0.001241	0.109103
20	0.112557	0.002169	0.001654	0.11638
21	0.060371	0.002394	0.000827	0.063592
22	0.118184	0.001945	0.001654	0.121784
23	0.981801	0.002169	0.012821	0.996791
24	0.023535	0.002394	0.000414	0.026342
25	0.032232	0.002244	0.000414	0.03489
26	0.047581	0.002319	0.000414	0.050313
27	0.70399	0.002394	0.009099	0.715483
28	0.415948	0.002394	0.005377	0.423718
29	1.000219	0.002244	0.012821	1.015284

2. Analysis of pulling force after flow

The weights of Backward breadth, Backward depth and Backward spread were determined by entropy weight method as 0.473245, 0.052171 and 0.474583 respectively. The backward pulling force of the energy flow obtained from the weighted sum of the normalized values of each index is shown in the last column of Table 4.

From the backward pulling power angle, all the indexes in metal smelting and rolling processing industry, chemical industry, non-metallic mineral products industry, petroleum processing, coking and nuclear fuel processing and manufacturing are more than 1, far higher than the average level, which means they have great influences on other industries. If the eventual use of each of these sectors grows by 1 unit, it will produce more the demand for other sectors of the national economy, resulting in a substantial increase in energy consumption. Take metal smelting and rolling processing industry as an example, a unit of final demand growth will promote the entire national economy energy consumption increased by 3.92 times.

Therefore, in order to save energy, the excessive growth of these industries should be appropriately controlled, and substantial increase in energy consumption also should be avoided so as not to have a great influence on the whole national economy. At the same time, these departments use policies incentives and technological advances to improve energy efficiency and reduce energy consumption per unit of output.

Table 4. calculation table of backward pulling force.

Industry	Backward breadth (0.473245)	Backward depth (0.052171)	Backward spread (0.474583)	Backward pulling force
&1	0.179833	0.001356	0.002848	0.184037
2	0.315655	0.001774	0.00522	0.322649
3	0.200183	0.001461	0.003322	0.204966
4	0.072407	0.001096	0.000949	0.074451
5	0.035493	0.001513	0.000475	0.037481
6	0.618532	0.001304	0.009492	0.629328
7	0.493595	0.001722	0.007593	0.50291
8	0.065781	0.001878	0.000949	0.068608
9	0.105534	0.001774	0.001424	0.108731
10	0.502586	0.001878	0.008068	0.512533
11	1.126797	0.001878	0.01756	1.146235
12	2.937907	0.001878	0.048408	2.988192
13	1.291486	0.001774	0.020407	1.313667
14	3.855056	0.001878	0.06312	3.920054
15	0.308556	0.001878	0.00522	0.315655
16	0.267384	0.001878	0.004271	0.273533
17	0.156171	0.001878	0.002373	0.160422
18	0.281581	0.001878	0.004746	0.288205
19	0.044012	0.001878	0.000475	0.046365
20	0.008045	0.001878	0	0.009923
21	0.030761	0.001878	0.000475	0.033114
22	0.008518	0.0012	0	0.009718
23	0.825813	0.001878	0.012814	0.840505
24	0.026502	0.001565	0.000475	0.028541
25	0.041172	0.001878	0.000475	0.043525
26	0.209174	0.001722	0.003322	0.214218
27	0.763345	0.001878	0.012339	0.777562
28	0.274009	0.001878	0.004271	0.280158
29	0.298145	0.001878	0.004746	0.304769

3. Comprehensive influence analysis of energy flow

Finally, the comprehensive influence of energy flow was analyzed, and the weights of Comprehensive Breadth, Comprehensive depth, Complete spread, Relational dominance, Flow dominance were 0.344592, 0.024065, 0.341423, 0.201428, 0.088492 respectively, the weighted summation of the normalized values of each index has a combined effect as shown in Table 5.Calculate the power flow impact as shown in the last column of Table 5.

From the angle of comprehensive influence, all the indexes in chemical industry, metal smelting and rolling processing industry, other social services, transportation and storage sector, non-metallic mineral products industry are much higher than the average level and have great influence on other industries.

As shown in **Fig. 3**, the dominance index makes the third industry and the first industry more influential, indicating that they are in the network path of the interaction between the nodes in the second industry and largely control energy transmission degree of the second industry nodes. The development of these industries will affect the development of the second industry; therefore, these industries should be developed moderately.

Table 5. Calculation chart of comprehensive influence

Industry	Comprehensive Breadth (0.285209)	Comprehensive depth (0.037602)	Complete spread (0.300492)	Relational dominance (0.138667)	Flow dominance (0.238029)	Comprehensive influence
1	0.516227	0.002068	0.008414	0.032032	2.567146	3.125888
2	0.700757	0.002519	0.01202	0.28815	0.784069	1.787515
3	0.661399	0.002181	0.011118	0.028149	0.823343	1.526191
4	0.508812	0.002068	0.008714	0.052971	0.11354	0.686105
5	0.146312	0.002369	0.002404	0.334049	0.167573	0.652706
6	0.618617	0.002219	0.010217	0.205088	1.696673	2.532814
7	0.504249	0.002519	0.008113	0.312971	0.829294	1.657147
8	0.166847	0.002632	0.002704	0.612353	0.481771	1.266308
9	0.133192	0.002519	0.002103	0.442209	0.351569	0.931594
10	0.564998	0.002632	0.009315	0.612353	0.823581	2.01288
11	1.211281	0.002519	0.020133	0.204256	0.708137	2.146327
12	3.149843	0.00267	0.054389	0.961378	4.948154	9.116434
13	1.094916	0.002595	0.01833	0.763362	2.229145	4.108347
14	3.421362	0.002595	0.058596	0.739927	2.551436	6.773916
15	0.333694	0.002595	0.005709	0.739927	0.725037	1.806962
16	0.533055	0.00267	0.009015	0.961378	1.292261	2.798379
17	0.277793	0.002595	0.004507	0.739927	0.452494	1.477316
18	0.418971	0.00267	0.007212	0.961378	0.736701	2.126932
19	0.085277	0.002595	0.001202	0.6699	0.395605	1.154579
20	0.067594	0.002444	0.001202	0.102614	0.299441	0.473295
21	0.052193	0.002557	0.000901	0.372321	0.367279	0.795252
22	0.071017	0.00188	0.001202	0	0.187091	0.26119
23	1.045004	0.002444	0.017429	0.085558	1.371287	2.521721
24	0.029091	0.002369	0.000601	0.203147	0.214464	0.449673
25	0.042781	0.002482	0.000601	0.15087	0.305392	0.502125
26	0.152587	0.002444	0.002404	0.159467	0.47225	0.789152
27	0.852488	0.002557	0.014424	0.360534	3.015355	4.245359
28	0.39701	0.002557	0.006611	0.372321	2.425043	3.203542
29	0.737264	0.002482	0.01232	0.318102	3.382397	4.452565

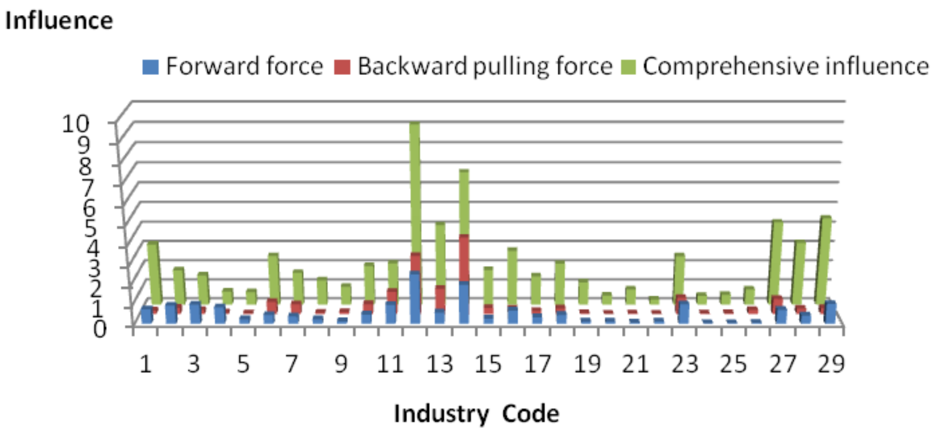

Figure 3. Energy flow influence of industry.

4. Conclusions and Policy Recommendations

Through the complex network analysis of energy input and output, we can see that the interaction between industries is frequent, the energy flow is active, and the network is closely linked, which provides the following inspiration for energy conservation and emission reduction policy formulation:

1. Rational distribution of industries and optimization of industrial structure

The optimization of industrial structure is the process of promoting the rationalization and development of industrial structure. The rational coordination of industrial structure requires not only the balance among industries, but also the strong complementarity and mutual transformation ability among industries. The high coordination among industries can improve the quality of industrial structure aggregation, curb the waste of energy, and improve the overall the effect of energy saving and emission reduction so as to realize the rationalization of industrial structure under certain economic conditions and ensure the coordination and sustainability of economic growth.

By studying the complex network of input and output flow we can see that industries are closely related with each other. The regional layout of any industry will affect other enterprises. Therefore, we should have a reasonable industrial layout, maximize the energy efficiency of the industry in the region energy flow, and make energy flow smoothly to reduce pollution emissions, assemble industries that can flow closely together, and optimize the overall allocation of resources.

2. classification management, focusing on controlling the key industries, and paying attention to the industries with less energy consumption but great relevance

By analyzing the influence of the nodes, the forward driving force and the backward pulling force are defined". Focus on control of the node with frequent and large energy flow. Prescribe the right medicine when making a policy.

The key sectors, such as chemical industry, metal smelting and rolling processing industry, petroleum processing, coking and nuclear fuel processing industry, which have both high "forward driving force" and "backward pulling power", not only made great contribution to the regional economic growth, but also caused a great deal of energy consumption. If these departments continue to develop at a high speed, they will drive the energy consumption of other departments to increase by a big margin, and the growth in the final demand for other sectors will also lead to an increase in energy consumption in such industries. So, in the process of adjusting industrial structure we should not only consider appropriate controls on the scale of these industries, optimize the internal structure of the industry through technological innovation and eliminating backward production capacity, but also protect proportion of these industries so as to avoid affecting economic development.

Some energy industries and basic industries, such as agriculture, forestry, animal husbandry and fishery; coal mining and cleaning industry; oil and natural gas extraction industry; metal mining industry, which have small "forward driving force" and "backward pulling force", are the energy output in the whole economy system. They transfer more energy consumption to maintain a certain economic scale to meet the needs of economic development. The eventual increase in demand from other sectors will lead to an increase in energy consumption in these sectors. But the expansion of these industries has a relatively small impact on the energy consumption of the entire economic system, we can strengthen technological innovation to ensure that energy waste is not caused by large-scale expansion

For other hi-tech industries and service industries, such as general purpose, special equipment manufacturing; instrument manufacturing; other manufacturing; metal products; electricity, thermal production and supply; construction; which have small "forward driving force" and big "backward pulling force", although the output of energy consumption is small, the demand for energy consumption is not small. Its energy consumption comes from the upstream sector of the industry chain, namely energy industry, basic industry and so on. This shows that in the economic chain, departments located upstream of the industry chain shift their energy consumption to the downstream sectors of the industry chain through intermediate inputs. Meanwhile, departments located downstream of the industry chain also meet their own end demand by net input from upstream sectors. Proper controls should be taken on the scale of such industries and we should optimize the industrial structure by eliminating backward production capacity and encouraging technological innovation to prevent a significant increase in energy consumption in other industries. The energy sector has undertaken a large amount of energy consumption for other sectors and is a key sector of the economic system. It is vital to improve energy efficiency and increase the use of low-carbon energy. The development of low-carbon energy is of great significance for achieving the goal of energy conservation and emission reduction.

In some departments, neither "forward driving force" nor "backward pulling force" is large, such as gas, water production and supply industry; accommodation and catering; whose energy consumption is not high. Their investment in energy consumption of other industries is not much, either. However, they relate to all sectors of the national economy and have more indirect energy consumption, and proper control is also necessary.

In conclusion, considering the transformation of industrial structure and energy saving and emission reduction, we should not simply consider the energy consumption and emission intensity of each industry, but comprehensively. Direct energy consumption and emission intensity in some industries may be low, but the total energy consumption and emission intensity are not low, so when the industrial structure was transformed into a low-powered industry, it is likely to reduce energy consumption per unit of GDP without reducing the energy consumption across the entire economy, because there is a problem of energy transfer within the industrial structure. Simply limiting the development of high-energy industries may reduce the energy consumption and emission intensity, but at the same time it may also pose a threat to other industries.

3. Actively develop new technologies

For those highly spreading and dominant industries, such as the chemical industry, metal smelting and rolling processing industry, non-metallic mineral products industry, we should increase technology investment, actively develop energy-saving and energy-reducing consumption and clean production technologies and improve energy efficiency.

4. Optimize the industrial cluster and enhance the competitiveness of the cluster

Regional industrial competitiveness, optimization of industrial structure and the development and policy induction of industrial clusters should be based on the internal division of labor. Through cluster analysis, we study the relationship between division of labor and cooperation in industry and then formulate industrial cluster policy, cultivate, optimize and even rebuild the industrial chain to form the optimal economic development path for the region.

Acknowledgements

This work was financially supported by project of National Social Science Fund (13BJY026) and National Natural Science Foundation of China (51574157).

References

[1] Watanabe, C. (1999): Systems option for sustainable development-effect and limit of the Ministry of International Trade and Industry’s efforts to substitute technology for energy. Research Policy (28): 719-749.

[2] Ang, B.W. (2005): The LMDI approach to decomposition analysis: a practical guide. Energy Policy 33 (7): 867-871.

[3] Hasanbeigi, A., Can, S.D.L.R.D., Sathaye, J. (2012): Analysis and decomposition of the energy intensity of California industries. Energy Policy 46 (7): 234-245.

[4] Choi, K.H., Ang, B.W. (2012): Attribution of changes in Divisia real energy intensity index-An extension to index decomposition analysis. Energy Economics 34 (1): 171-176.

[5] Lu, Z.N., (1999): An empirical analysis of the impact of industrial structure adjustment on China’s energy consumption. Quantitative and Technical Economics (12): 53-55.

[6] Zhang, L., Huang, Y.X. (2008): Energy saving potential analysis of China’s industrial structure. Chinese Soft Science 23 (5): 27-29, 32-34, 51.

[7] Yin, S., Zhang, Y.H., Yan, J. (2014): The dynamic relationship between China’s industrial structure, energy efficiency and energy consumption-Empirical research based on co integration and VECM. East China Economic Management (07): 53-56, 80.

[8] Campbell, J. (1970): The relevance of input-output analysis and digraph concepts to growth pole theory. University of Washington.

[9] Schnabl, H. (1995): The subsystem MFA: a qualitative method for analyzing national innovation systems: the case of Germany. - Economic Systems Research 7 (4): 383-396.

[10] Aroche, F. (1996): Important coefficients and structural change: a multi-layer approach. Economic Systems Research 8 (3): 235-246.

[11] Morillas, A., Robles, L., Diaz, B. (2008): Grading the I-O coefficients importance: a fuzzy approach. The Intermediate Input-output Meeting, Seville, Spain.

[12] Mcnerney, J., Fath, B.D., Silverberg, G. (2013): Network structure of inter-industry flows. Physica A Statistical Mechanics and Its Applications 392 (24): 6427-6441.

[13] Zhao, B.X., Yin, C., Zhang, J.H. (2011): Industrial complex network and its modeling-based on the case study of Shandong Province. Beijing: Economic Management (7).

[14] Chen, X.Z., Zhao, B.X., Xiao, W.W. (2014): Research on industrial association network side. Beijing: Management Science of China (11).

[15] Sun, Q.M., Wang, H.Y. (2016): Comparison of industry associations of Beijing, Tianjin and Hebei based on complex network. Economic Management (4): 24-35.

[16] Wang, H.Y., Sun, Q.M. (2016): Identification and comparative study of key industries in Beijing, Tianjin and Hebei Provinces-based on complex network model. East China Economic Management (12): 77-85.

[17] Kang, L., Du, H.L., Du, X., Wang, H.T., Ma, W.L., Wang, M.L., Zhang, F.B. (2018). Study on dye wastewater treatment of tunable conductivity solid-waste-based composite cementitious material catalyst. Desalination and Water Treatment 125: 296-301.

[18] Al-Widyan, M.I., Soliman, I.A., Alajlouni, A.A., Al Zu'Bi, O.I., Jaradat, A.I. (2018). Energy performance assessment of a non-domestic service building in jordan. Jordan Journal of Mechanical and Industrial Engineering, 12 (2): 69-75.

[19] Lange, J., Hilgedieck, J., Kaltschmitt, M. (2019). Renewable resources of energy for electricity generation-development trends and necessities within the overall energy system. Jordan Journal of Mechanical and Industrial Engineering, 13 (3): 207-220.

[20] Liu, Z., Peng, W., Motahari-Nezhad, M., Shahraki, S., Beheshti, M. (2016). Circulating fluidized bed gasification of biomass for flexible end-use of syngas: a micro and nano scale study for production of bio-methanol. Journal of Cleaner Production 129: 249-255.

[21] Liu, Z. 2018. Economic analysis of energy production from coal/biomass upgrading; Part 1: Hydrogen production. Energy Sources Part B-Economics Planning and Policy 13 (2): 132-136.

[22] Peng, W., Ge, S., Ebadi, A.G., Hisoriev, H., Esfahani, M.J. (2017). Syngas production by catalytic co-gasification of coal-biomass blends in a circulating fluidized bed gasifier. Journal of Cleaner Production 168: 1513-1517.

[23] Singh, K., Gupta, N., Dhingra, M. (2018). Effect of temperature regimes, seed priming and priming duration on germination and seedling growth on American cotton. Journal of Environmental Biology 39 (1): 83-91.

JJMIE

Volume 15, Number 1, March. 2021
ISSN 1995-6665
Pages 93 - 97

Jordan Journal of Mechanical and Industrial Engineering

A New Method to Analyze CNC Lathe Faults Based on Gutenberg–Richter Curve

Jie Yu[1], Zhiwei Zhu[2,*], Tiebin Wang[1], Yue Yao[3], Jiexiang Ding[3]

[1]School of Mechanical and Material Engineering, Wuzhou University, Guangxi, 543002, China
[2]Qianjiang College, Hangzhou Normal University, Hangzhou 310018, China
[3]Mechanical and Vehicular Engineering College, Changchun University, Changchun 130021, China

Received July 18 2020 Accepted March 13 2021

Abstract

This paper collects and sorts out a large amount of fault data of a series of CNC lathes, and analyzes the fault data to classify fault levels. The values of a and b are obtained by Gutenberg–Richter (G-R) curve fitting, and then the relationship between a and b is used. The b value under each division criterion is obtained. By analyzing and comparing these b values, the rationality of classifying the fault levels according to these three methods is verified. The b-value is towards 1.0 when the reliability level of CNC lathes was promoted through ten years' reliability promotion.

Keywords: Gutenberg–Richter (G-R) curve; b value; CNC machine tool; fault level; reliability;

1. Introduction

In 1944, Gutenberg and Richter proposed the famous earthquake magnitude relationship lgN = a-bM by studying the activity characteristics of the California earthquake. Since then, this relationship is one of the important properties of seismic activity research and has been widely used in the study of earthquake-related issues. In this relation, M is the magnitude, and N represents the number of earthquakes in the area with a magnitude greater than or equal to M in a certain period of time. The values of a and b are constants, a-values reflect the average level of seismic activity in the area, and b-values reflect the proportional relationship between large and small earthquakes [1, 2]. Yu Jie [3] proposed to use Gutenberg–Richter (G-R) curve analysis method to analyze the relationship between the failure level and the occurrence frequency of a series of CNC lathes. This is a useful attempt in the reliability analysis method research of CNC lathes, and some conclusions have been drawn. This paper continues to apply this relationship to the reliability analysis of CNC machine tools. In the curve, M is the failure grade of the CNC machine tool, and N is the number of failures when the failure grade is greater than or equal to M. In seismic research, the commonly used methods of b-value calculation include least square method, maximum likelihood method and moment method.

2. The Significance of Analyzing the Reliability Fault Data of CNC Machine Tools

Reliability data is defined as a general term for various data that can reflect its reliability level and reliability-related data in the reliability work at each stage of the product life cycle, mainly including various numbers, characters, graphics, tables, etc. [4]. The reliability data of CNC machine tools mainly include the design data, fault data and working environment of CNC machine tools. The reliability data collection, sorting, analysis and research of CNC machine tools have been carried out in foreign countries for a long time, and the reliability data management system has been established. In the application of CNC machine tool reliability data research, not only has achieved great economic benefits, but also saved a large amount of money. Compared with foreign countries, due to the lack of awareness of the reliability data collection, storage, analysis and application of CNC machine tools in China, a large amount of data is missing, leading to the failure of enterprises to implement reliability engineering.

The reliability data generated during the design of CNC machine tools can be used to obtain the initial reliability and failure modes of CNC machine tools. The reliability data of the production stage of CNC machine tools reflects the design and manufacturing level of CNC machine tools. The field data of the CNC machine tools in use truly reflects the reliability level of the machine tools in various environments. Therefore, it is necessary to collect, sort out and analyze the reliability data of NC machine tools, which is beneficial to the reliability engineering and machine tool maintenance and design.

2.1. Classification and b Value Calculation of a Certain Series of CNC Lathes

According to GJB431-88 “Product Level, Product Interchangeability, Prototype and Related Terms”, the vertical order of products from simple to complex is generally: parts, components, assemblies, unit parts, units,

* Corresponding author e-mail: zhuzw5901@126.com.

devices, subsystems and systems. In order to verify the rationality of CNC machine tool fault classification, this paper uses three classification methods: machine tool body, machine tool subsystem, and machine tool components. The division criteria are; fault downtime, subsystem fault frequency and component fault frequency [5].

From the previous research, we get that the failure interval of CNC machine tools submits to Weibull Distribution. We get the fitted curves of a series of CNC machine tools as given in Figure 1 and Figure 2.

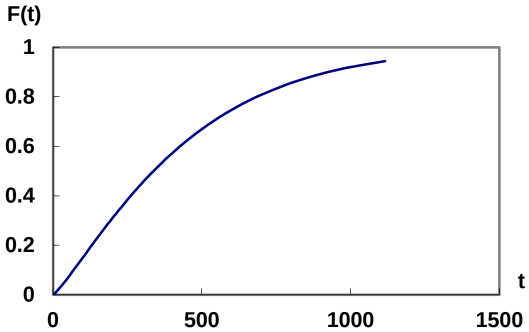

Figure 1. Fitting Diagram of Density Function Curve

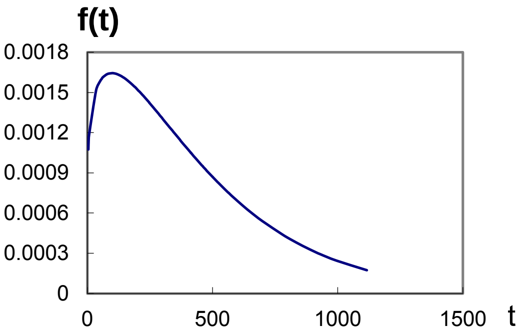

Figure 2. Fitting Diagram of Distribution Function Curve

At present, most reliability studies on CNC lathes are based on subsystems [6]. The subsystems of CNC lathes are divided according to the principles of functional independence, structural independence and convention. CNC lathe can be divided into 14 subsystems: basic components, spindle components, feed system, tool system, hydraulic system, lubrication system, cooling system, protection system, CNC system, electrical system, testing system, machine tool accessories, chip removal system and pneumatic system. In this paper, 11 subsystems with higher frequency of failures are selected for analysis.

The functional parts of CNC machine tools include: basic parts, NC rotary table, spindle parts, feed parts, CNC systems, automatic tool change parts, hydraulic system parts, cooling system parts, pneumatic system parts, lubrication system parts, chip removal system parts, and protection systems component. The accuracy, performance and stability of key components of CNC machine tools have the most direct impact on the reliability of CNC machine tools. Exploring the reliability of key functional components is of great significance to the reliability of CNC machine tool products [7-9]. Zhang Genbao [10] extracted the key functional components of CNC machine tools based on the four aspects of failure frequency, hazard, maintainability, and complexity, combined with experimental data and evaluation models, and provided theoretical basis and theoretical methods. Therefore, the analysis of functional components is conducive to the improvement of the reliability of the machine tool. In this paper, 11 fault components with high fault frequency are selected for analysis, most of which are key components. The specific division is shown in Table 1.

Table 1. Classification of fault levels

Failure grade	Downtime	Subsystem failure frequency	Component failure frequency
1	>0	Electrical system	Automatic tool changer
1.5	>0.5	Card attachment	Spindle component
2	>1	Chip removal system	Feeding component
2.5	>2	defensive equipment	CNC turntable
3	>5	servo system	Cooling system components
3.5	>8	Turret head	Hydraulic system components
4	>10	Hydraulic system	Pneumatic system components
4.5	>12	Spindle system	Protective system components
5	>20	Feed system	Chip removal system components
5.5	>24	Lubrication system	Lubrication system components
6	>30	cooling system	Basic component

In the table, the value of M represents the fault level. The fault level starts from 1 to 6, each 0.5 is a unit, and a total of 11 fault levels are divided. The unit of downtime is in hours.

The collected fault data is analyzed and sorted, and classified according to fault downtime, subsystem fault frequency, and component fault frequency. The number of fault occurrences at the corresponding fault level is obtained and the corresponding b value is calculated.

Table 2 to Table 8, where M represents the classification of fault levels, and N_1, N_2, and N_3 respectively represent the number of faults at the corresponding fault levels according to the breakdown time, number of subsystem faults, and number of component faults. $lgN=lg[(N_1+N_2+N_3)/3]$, a-value and b-value are calculated by fitting Gutenberg–Richter (G-R) curve with least square method. b_1, b_2 and b_3 can be obtained by substituting the value of a and the number of failures N_1, N_2 and N_3 under the corresponding fault level into the Gutenberg–Richter (G-R) relation.

Table 2. Failure data and b value of a series of CNC lathes from January 1998 to December 2000

M	N_1	N_2	N_3	lgN	a	b	b_1	b_2	b_3
1	2291	2399	2455	3.38	3.87	0.49	0.51	0.49	0.48
1.5	1303	1365	1396	3.13	3.87	0.49	0.50	0.49	0.48
2	741	776	794	2.89	3.87	0.49	0.50	0.49	0.49
2.5	422	442	452	2.64	3.87	0.49	0.50	0.49	0.49
3	240	251	257	2.40	3.87	0.49	0.50	0.49	0.49
3.5	136	143	146	2.15	3.87	0.49	0.50	0.49	0.49
4	78	81	83	1.91	3.87	0.49	0.50	0.49	0.49
4.5	44	46	47	1.66	3.87	0.49	0.49	0.49	0.49
5	25	26	27	1.42	3.87	0.49	0.49	0.49	0.49
5.5	14	15	15	1.17	3.87	0.49	0.49	0.49	0.49
6	8	9	9	0.93	3.87	0.49	0.49	0.49	0.49

Table 3. Failure data and b value of a series of CNC lathes from January 2001 to December 2003

M	N_1	N_2	N_3	lgN	a	b	b_1	b_2	b_3
1	1905	1995	1949	3.29	3.81	0.52	0.53	0.51	0.52
1.5	1059	1109	1083	3.03	3.81	0.52	0.52	0.51	0.52
2	588	616	602	2.78	3.81	0.52	0.52	0.51	0.52
2.5	327	342	334	2.52	3.81	0.52	0.52	0.51	0.51
3	181	190	186	2.27	3.81	0.52	0.52	0.51	0.51
3.5	101	105	103	2.01	3.81	0.52	0.52	0.51	0.51
4	56	58	57	1.76	3.81	0.52	0.52	0.51	0.51
4.5	31	32	31	1.50	3.81	0.52	0.52	0.51	0.52
5	17	18	17	1.24	3.81	0.52	0.52	0.51	0.52
5.5	9	10	9	0.97	3.81	0.52	0.52	0.51	0.52
6	5	5	5	0.70	3.81	0.52	0.52	0.52	0.52

Table 4. Failure data and b value of a series of CNC lathes from January 2004 to December 2006

M	N_1	N_2	N_3	lgN	a	b	b_1	b_2	b_3
1	1380	1318	1349	3.13	3.78	0.65	0.64	0.66	0.65
1.5	653	624	638	2.81	3.78	0.65	0.64	0.66	0.65
2	309	295	302	2.48	3.78	0.65	0.65	0.66	0.65
2.5	146	140	143	2.16	3.78	0.65	0.65	0.65	0.65
3	69	66	68	1.83	3.78	0.65	0.65	0.65	0.65
3.5	33	31	32	1.51	3.78	0.65	0.65	0.65	0.65
4	15	15	15	1.18	3.78	0.65	0.65	0.65	0.65
4.5	7	7	7	0.86	3.78	0.65	0.65	0.65	0.65
5	3	3	3	0.53	3.78	0.65	0.65	0.65	0.65
5.5	2	2	2	0.21	3.78	0.65	0.65	0.65	0.65

Table 5. Failure data and b value of a series of CNC lathes from January 2007 to December 2009

M	N_1	N_2	N_3	lgN	a	b	b_1	b_2	b_3
1	776	724	676	2.86	3.69	0.83	0.80	0.83	0.86
1.5	299	279	260	2.45	3.69	0.83	0.81	0.83	0.85
2	115	107	100	2.03	3.69	0.83	0.82	0.83	0.85
2.5	44	41	38	1.62	3.69	0.83	0.82	0.83	0.84
3	17	16	15	1.20	3.69	0.83	0.82	0.83	0.84
3.5	7	6	6	0.79	3.69	0.83	0.82	0.83	0.84
4	3	2	2	0.37	3.69	0.83	0.82	0.83	0.84

Table 6. Failure data and b value of a series of CNC lathes from January 2010 to December 2012

M	N_1	N_2	N_3	lgN	a	b	b_1	b_2	b_3
1	479	457	490	2.68	3.65	0.9	0.97	0.99	0.96
1.5	313	160	172	2.33	3.65	0.9	0.77	0.96	0.94
2	110	56	60	1.88	3.65	0.9	0.80	0.95	0.94
2.5	38	20	21	1.42	3.65	0.9	0.83	0.94	0.93
3	13	7	7	0.97	3.65	0.9	0.84	0.94	0.93
3.5	5	2	3	0.51	3.65	0.9	0.85	0.93	0.92
4	2	1	1	0.06	3.65	0.9	0.86	0.93	0.92

Table 7. Failure data and b value of a series of CNC lathes from January 2013 to December 2015

M	N_1	N_2	N_3	lgN	a	b	b_1	b_2	b_3
1	363	380	417	2.59	3.56	0.97	1.00	0.98	0.94
1.5	119	124	136	2.10	3.56	0.97	0.99	0.98	0.95
2	39	41	45	1.62	3.56	0.97	0.99	0.98	0.96
2.5	13	13	15	1.13	3.56	0.97	0.98	0.97	0.96
3	4	4	5	0.65	3.56	0.97	0.98	0.97	0.96
3.5	1	1	2	0.16	3.56	0.97	0.98	0.97	0.96

Table 8. Failure data and b value of a series of CNC lathes from January 2015 to December 2017

M	N1	N2	N3	lgN	a	b	b1	b2	b3
1	380	417	398	2.60	3.67	1.07	1.09	1.05	1.07
1.5	111	122	116	2.07	3.67	1.07	1.08	1.06	1.07
2	32	35	34	1.53	3.67	1.07	1.08	1.06	1.07
2.5	9	10	10	1.00	3.67	1.07	1.08	1.06	1.07
3	3	3	3	0.46	3.67	1.07	1.08	1.06	1.07

3. Gutenberg–Richter (G-R) Curve Analysis

Taking the fault data of this series of CNC lathes from January 1998 to December 2000 as an example, analysis and Gutenberg–Richter (G-R) curve fitting are performed to obtain the fitted a and b values, and b value of corresponding fault level is calculated by fitting a-value.

In this paper, the least square method is used to fit the Gutenberg–Richter (G-R) curve. The fitting result is shown in Figure 3.

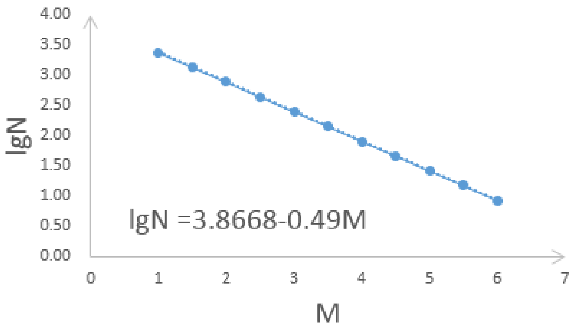

Figure 3. Gutenberg–Richter (G-R) fitting curve from January 1998 to December 2000

From the fitting relation in the figure, it can be concluded that fitting a=3.8668 and b=0.49. By substituting the fitting value of a and the corresponding failure times into the relational formula lgN= a-bM, the b-value of the corresponding fault level under the corresponding classification method can be calculated. The detailed calculation results are shown in table 2. The calculation methods for other years are the same and are not listed here one by one. The detailed fitting results are shown in Figure 4.

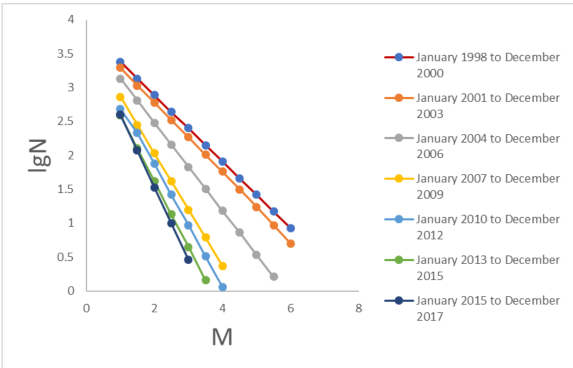

Figure 4. Gutenberg–Richter (G-R) fitting curve at each stage

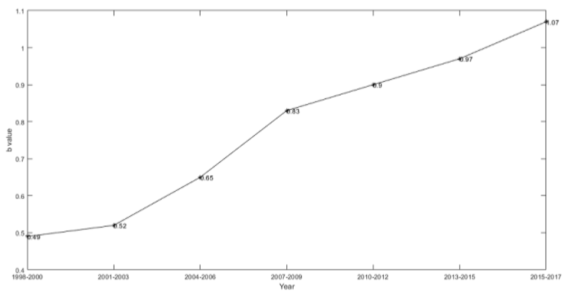

Figure 5. Variation curves of b-value at each stage

Notes: The abscissa values in Figure 5 correspond to the year of data collection in Tables 2 to 8 of the paper.

Through the analysis and comparison in Figure 4, it is known that the slope of the fitting curve increases with the increase of the year, that is, the greater the value of b. The corresponding b value of the fitted curve relation was extracted to make the change curve of b value, as shown in Figure 3. The curve showed an upward trend. In seismic research, many studies show that the decrease of b-value means the increase of large earthquake proportion, and vice versa [11-14]. Mean time between failures (MTBF) is the mean value of working time between two adjacent failures of CNC machine tools, which is the key index to measure the reliability of CNC machine tools.

The MTBF value of domestic CNC machine tools is more than 200 hours from the end of the "eighth five-year plan", more than 400 hours from the "ninth five-year plan", more than 600 hours from the" tenth five-year plan", and now more than 1000 hours. The reliability of CNC machine tools in China is constantly improving, which is also consistent with the gradual increase of b value. The rationality of the Gutenberg–Richter (G-R) curve relationship applied to the reliability of CNC machine tools is explained, which further proves the rationality of the fault classification method in this paper.

B-value is an important index in seismic research and is often used in seismic analysis and consultation system at all levels. If the b value is small, it means that the proportion of the number of large earthquakes is large. On the contrary, if the b value is large, it means that the proportion of the number of large earthquakes is small.

According to the dynamic change of B value, we can predict earthquakes; according to the G-R law, we can calculate the average recurrence period or average annual occurrence rate of earthquakes at all levels, we can infer the risk of earthquakes at all levels in a certain period of time in the future; according to the intercept a of Gutenberg–Richter (G-R) curves on the horizontal axis, we can predict the magnitude of strong aftershocks.

From Figure 4 and Figure 5, we can get that in the failure frequency period of CNC machine tool, b value is small, with the advance of reliability improvement measures, b value gradually increases, and finally in the stable period, b value tends to 1.0. This conclusion is very similar to that of seismology, so we can study parameter a again in order to predict the risk of CNC machine failure level.

4. Conclusion

The fault data analyses from 1998 to 2017 shows that b-values in frequent failure time are lower than in stable time. The b-value is towards 1.0 when the reliability level of CNC lathes was promoted through ten years' reliability promotion.

This article further collected a large amount of fault data, extended the time for collecting fault data, and further proved the rationality of using Gutenberg–Richter (G-R) curves to analyze fault data. Through the comparative analysis of the data collected in Table 2 to Table 8, corresponding values of b_1, b_2 and b_3 at each stage fluctuated up and down in the fitted b value, with a small difference. Thus, the rationality of fault classification in this paper is verified, and the application scope of Gutenberg–Richter (G-R) curve is further expanded, which is not only applicable to the whole machine, but also applicable to subsystems and components.

The result of this paper is very close to the conclusion of seismology, which verifies that the model hypothesis is correct and feasible.

Acknowledgement

This work was sponsored by Research on the Noise Characteristics of Automobile Multi-wedge Belt and the Optimization (2018JBA01L01).

References

[1] Wang YX, Zhang H, Liu SQ, Cao JQ, Li H, Chen S, Gao Y. Spatial and temporal variations of b-value in the Hebei plain seismic belt. China Earthquake Engineering Journal. 2015, 37(01):188-195.

[2] Zhang LL, Tang LL. Temporal and spatial variations of b-value in Tianshan, Xinjiang. Earthquake. 2015, 35(03):93-101.

[3] Yu J. Shi YL. Failure rate evaluation of CNC machine tools based on G-R curves analysis. Machine Tool & Hydraulics. 2009, 37(10):257-258+251.

[4] Zhao Y. Reliability Data Analysis. Beijing: National Defence Industry Press, 2011.

[5] Commission of Science Technology and Industry for National Defense. GJB 431-88. Product Hierarchy. Product Interchangeability. Prototype and Related terms.

[6] Wang H. Research on Preventive Maintenance Strategy of CNC Machine Tools Based on RCM. Changchun, China: Jilin University, 2012.

[7] Qi XD. Reliability Comprehensive Evaluation of Manufacturing Process for Key Components of CNC Machine Tools. Chongqing, China: Chongqing University, 2017.

[8] Wang A, Liang J, Liu Y. Application of improved particle swarm optimization in gear fault diagnosis of automobile transmission. Jordan Journal of Mechanical and Industrial Engineering, 2020, 14(1):175-182.

[9] Tao J, Jia Y, Gao Y. Intelligent remote monitoring system for minor faults of intelligent unmanned vehicle. Jordan Journal of Mechanical and Industrial Engineering, 2020, 14(1):61-70.

[10] Zhang GB, She L, Ran Y, Luo DM. Study on Extraction of Key Functional Components in CNC machine tools' reliability tests. China Mechanical Engineering. 2016, 27(17):2372-2378.

[11] Bian QK. Li SZ. Mao ZW. Li SL. Wang QC. A study of the seismic activity anomaly before the ZhangBei MS 6.2 Earthquake and the characeristics of its sequence. North China Earthquake Sciences. 1999(03):35-42.

[12] Xue JN. Li X, Zhang B, Wang YW. Statistical Analysis of B-values in Shandong Area. North China Earthquake Sciences. 2011, 29(01):1-5.

[13] Mishra M, Abhishek, Yadav RBS, Sandhu M. Probabilistic assessment of earthquake hazard in the Andaman–Nicobar–Sumatra region. Natural Hazards, 2020, 105(01):313-338.

[14] Tiwari VM. CSIR-national geophysical research institute — 60 years of enduring scientific contributions. Journal of the Geological Society of India, 2020, 96(4):319-324.

JJMIE

Volume 15, Number 1, March. 2021
ISSN 1995-6665
Pages 99 - 103

Jordan Journal of Mechanical and Industrial Engineering

Analysis of Activity Parameters of CNC Machine Tools Failures Based on Gutenberg–Richter Curve

Jie Yu[1], Zhiwei Zhu[2,*], Tiebin Wang[1], Yue Yao[3], Jiexiang Ding[3]

[1]School of Mechanical and Material Engineering, Wuzhou University, Guangxi, 543002, China
[2]Qianjiang College, Hangzhou Normal University, Hangzhou 310018, China
[3]Mechanical and Vehicular Engineering College, Changchun University, Changchun 130021, China

Received July 18 2020 *Accepted March 13 2021*

Abstract

Gutenberg–Richter (G-R) scaling relations are commonly used on seism prediction. The variance of b-values can reflect the seism active degree of the area. B value in frequent failure time is lower than in stable failure time. We use the curve to calculate the values of parameters a and b in the Gutenberg–Richter (G-R) relation, draw a graph of the b-value and the ratio of the number of failures over time, and find that the trend is reversed, which prove that the b-value can reflect the ratio of the number of failures. Draw the trend curve of a-value and lgN. By comparing and finding the same trend, it is proved that the a-value can reflect the overall level of failure data. The relationship between a and b-value is analyzed and the influencing factors on activity parameters are discussed.

Keywords: CNC machine tool, Gutenberg–Richter (G-R) curve, a-value, b-value, Gutenberg–Richter (G-R) scaling relation;

1. Introduction

In the manufacturing industry, CNC machine tools are the most fundamental processing equipment and a symbol of comprehensive national strength. With the modern advancements and the improvement of national demand, the requirements for CNC machine tools are constantly changing. In order to meet the market demand, CNC machine tools are developing towards high speed, multi-function, high reliability, intelligence, high precision and other directions [1]. With the increasing demand for CNC machine tools in the market, the reliability of China's machine tools is also constantly improving, but it is still insufficient compared with some advanced foreign machine tools. Therefore, the research on the reliability of CNC machine tools has not stopped. The research on the reliability of machine tools mainly improves the production efficiency by reducing the failure rate of machine tools as to reduce the number of failures and the impact of failures.

From the previous research, we get that the failure interval of CNC machine tools submits to Weibull Distribution. We get the fitted curves of a series of CNC machine tools as given in Figure 1 and Figure 2.

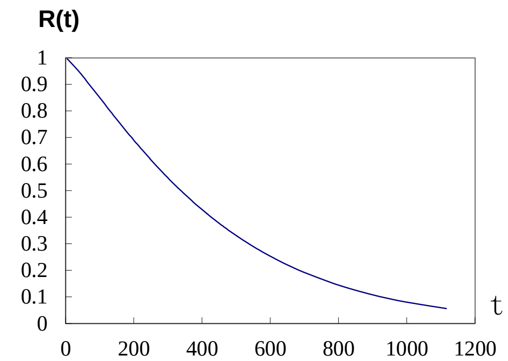

Figure 1. Fitting Diagram of Reliability Curve

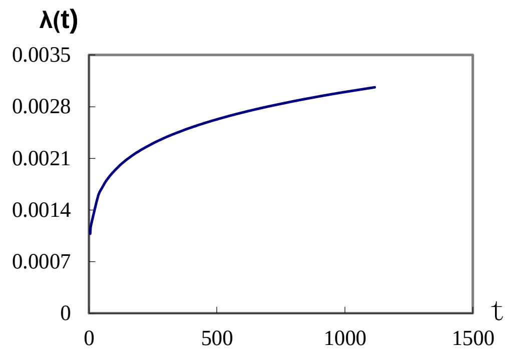

Figure 2. Fitting Diagram of Failure Rate Curve

* Corresponding author e-mail: zhuzw5901@126.com

The Gutenberg-Richter relation (G-R curve: $\lg N = a - bM$), which reflects the relationship between magnitude and frequency, is usually used to study the seismicity characteristics of various regions of the world [2-4]. In the Gutenberg–Richter (G-R) curve, the parameter a is the intercept of the straight line and the vertical axis, indicating the overall activity level of the earthquake, and the parameter b is the slope of the straight line, indicating the proportional relationship of the large and small earthquakes [5, 6]. When the b-value is low, it indicates that the large earthquake accounts for a higher proportion in the study area. In most cases, the b-value will stabilize at around 1. When the value of a is large, it indicates that the number of earthquakes is greater. This relation is used in the study of failures of CNC machine tools, where *M* represents the failure level and *N* represents the number of failures greater than or equal to *M* in a certain period of time.

2. Applying Gutenberg–Richter (G-R) Scaling Relations to Describe the Failure Rate of the CNC Machine Tools

We analyze the failure data of a series of CNC machine tools according to different phases to inquire into the laws followed. As the drawing of Gutenberg–Richter (G-R) scaling relations in seismic research, we divide the failures into nine grades according to the extent of criticality and put into analysis.

We draw the curves of different stages as given below:

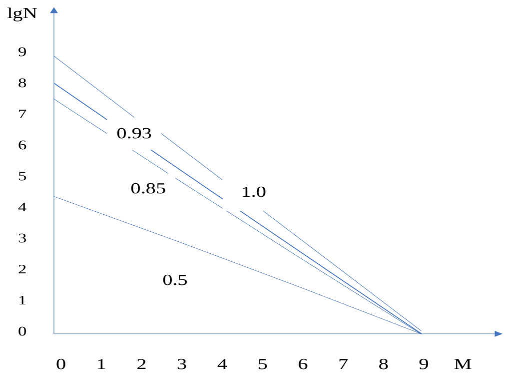

Figure 3. Gutenberg–Richter (G-R) scaling relations of a series of CNC machine tools

Notes: 0.5 shows the early research stage.
0.85 shows after the research stage.
0.93 shows after research (2001.1-2003.12) stage.
1.0 shows after research (2009.1-2015.12) stage.

The increase of the credibility of the CNC machine tools is a long-term and meticulous course of work. Through ten years' cooperation, the MTBF value of this series of machine tools has been increased greatly. It can be said that achievements in this research are still significant. For the length of the paper, we cannot list the overall measurements here. From the Gutenberg–Richter (G-R) scaling relations we can see that b-value is changed from 0.5 to 0.85 to 0.93 and the final b-value is 1.0.

2.1. Mean Time between Failures

The mean time between failures [7] (MTBF) is the mean value of the time between failures of the equipment. If the number of failures of the equipment is n and the time between failures is t_1, t_2, …, t_n, then the mean time between failures is

$$MTBF = (t_1 + t_2 + \cdots + t_n) / n \tag{1}$$

The reliability index of the CNC machine tool can be judged as MTBF, reflecting the ability of machine tools to complete the task within the specified time. The reliability index is divided into 5 grades [8-10], with "very high" about 1800 hours, "high" about 1200 hours, "intermediate" about 800 hours, "low" about 600 hours and "very low" about 400 hours. The MTBF value of early CNC machine tools in China was only over 200 hours, and the room for improvement was very large.

2.2. Collection and Division of Fault Data

CNC machine tools cannot complete the specified functions under the specified conditions and within the specified time, or the performance of one or several parameters beyond the allowable range is called failure. When studying the reliability of CNC machine tools, it is necessary to collect the failure data. Due to the timeliness and randomness of the data, it is also needed to sort the data.

The failure data of a CNC machine tool in recent years was analyzed, and the number of samples was 20, which lasted about 20 years. Due to the large amount of data, the data must first be sorted. Different ways of failure classification will lead to the difference in the number of failures corresponding to each grade. According to J.X. Ding's paper [8], the failure grade of CNC machine tools can be divided into three aspects: downtime, subsystem failure frequency and component failure frequency [11-15].

The number of failures is graded through the above three aspects, and each division method is fitted with MATLAB. As shown in Table 1, $N = (N_1+N_2+N_3)/3$, *a* and *b* are fitted by failure grade *M* and *lgN*. According to the obtained *b*-value, a_1, a_2, and a_3 corresponding to N_1, N_2, and N_3 are calculated. By comparing a_1, a_2 and a_3 with the a-value obtained by the previous fitting, the a-values obtained by the three classification methods are similar, which can be concluded that the three classification methods are feasible. From the sorted data, no reliability improvement was made from the very beginning, and after the improvement, the number of failures decreased significantly, and the production efficiency was further improved. Table 1 to Table 4 are the results of partial failure data processing

Table 1. Failure data and a-value of a CNC machine tool from January 2015 to December 2017

M	N_1	N_2	N_3	lgN	a	b	a_1	a_2	a_3
1	380	417	398	2.60	3.67	1.07	3.65	3.69	3.67
1.5	111	122	116	2.07	3.67	1.07	3.65	3.69	3.67
2	32	35	34	1.53	3.67	1.07	3.65	3.69	3.67
2.5	9	10	10	1.00	3.67	1.07	3.65	3.69	3.67
3	3	3	3	0.46	3.67	1.07	3.65	3.69	3.67
3.5	1	1	1	-0.07	3.67	1.07	3.65	3.69	3.67
4	0	0	0	-0.61	3.67	1.07	3.65	3.69	3.67

Table 2. Failure data and a-value of a CNC machine tool from January 2012 to December 2014

M	N_1	N_2	N_3	lgN	a	b	a_1	a_2	a_3
1	398	407	339	2.58	3.53	0.95	3.55	3.56	3.48
1.5	133	136	114	2.11	3.53	0.95	3.55	3.56	3.48
2	45	46	38	1.63	3.53	0.95	3.55	3.56	3.48
2.5	15	15	13	1.16	3.53	0.95	3.55	3.56	3.48
3	5	5	4	0.68	3.53	0.95	3.55	3.56	3.48
3.5	2	2	1	0.21	3.53	0.95	3.55	3.56	3.48
4	1	1	0	-0.27	3.53	0.95	3.55	3.56	3.48
4.5	0	0	0	-0.74	3.53	0.95	3.55	3.56	3.48

Table 3. Failure data and a-value of a CNC machine tool from January 2009 to December 2011

M	N_1	N_2	N_3	lgN	a	b	a_1	a_2	a_3
1	525	501	537	2.72	3.61	0.89	3.61	3.59	3.62
1.5	188	180	193	2.27	3.61	0.89	3.61	3.59	3.62
2	68	65	69	1.83	3.61	0.89	3.61	3.59	3.62
2.5	24	23	25	1.38	3.61	0.89	3.61	3.59	3.62
3	9	8	9	0.94	3.61	0.89	3.61	3.59	3.62
3.5	3	3	3	0.49	3.61	0.89	3.61	3.59	3.62
4	1	1	1	0.05	3.61	0.89	3.61	3.59	3.62
4.5	0	0	0	-0.40	3.61	0.89	3.61	3.59	3.62

Table 4. Failure data and a-value of a CNC machine tool from January 2006 to December 2008

M	N_1	N_2	N_3	lgN	a	b	a_1	a_2	a_3
1	891	832	871	2.94	3.71	0.77	3.72	3.69	3.71
1.5	367	343	359	2.55	3.71	0.77	3.72	3.69	3.71
2	151	141	148	2.17	3.71	0.77	3.72	3.69	3.71
2.5	62	58	61	1.78	3.71	0.77	3.72	3.69	3.71
3	26	24	25	1.40	3.71	0.77	3.72	3.69	3.71
3.5	11	10	10	1.01	3.71	0.77	3.72	3.69	3.71
4	4	4	4	0.63	3.71	0.77	3.72	3.69	3.71
4.5	2	2	2	0.24	3.71	0.77	3.72	3.69	3.71
5	1	1	1	-0.14	3.71	0.77	3.72	3.69	3.71
5.5	0	0	0	-0.53	3.71	0.77	3.72	3.69	3.71

Taking the failure data of Table 5 (January 2001-December 2003) as an example, the fitting is performed by MATLAB, and the fitted curve is $\lg N = 3.8001 - 0.51M$. As shown in Figure 4, the failure grade and the number of failures satisfy the relationship of Gutenberg–Richter (G-R) curve. Due to the initial reliability improvement, the failure rate is high, and the MTBF is about 400 hours. The b-value is relatively low.

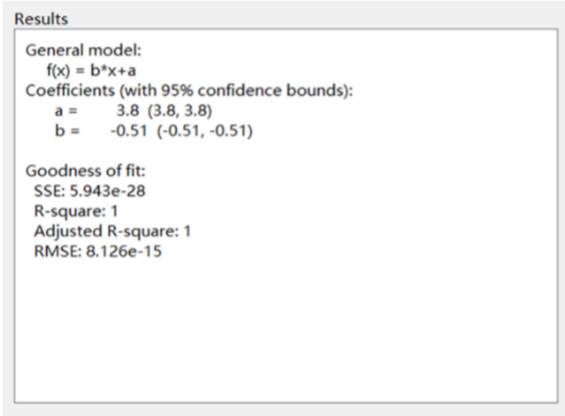

Figure 4. MATLAB fitting results Units

Table 5. First stage failure data after reliability study (January 2001 to December 2003)

M	N_1	N_2	N_3	lgN	a	b	a_1	a_2	a_3
1	1905	1995	1950	3.29	3.80	0.51	3.79	3.81	3.80
1.5	1059	1109	1084	3.04	3.80	0.51	3.79	3.81	3.80
2	589	617	603	2.78	3.80	0.51	3.79	3.81	3.80
2.5	327	343	335	2.53	3.80	0.51	3.79	3.81	3.80
3	182	191	186	2.27	3.80	0.51	3.79	3.81	3.80
3.5	101	106	104	2.02	3.80	0.51	3.79	3.81	3.80
4	56	59	58	1.76	3.80	0.51	3.79	3.81	3.80
4.5	31	33	32	1.51	3.80	0.51	3.79	3.81	3.80
5	17	18	18	1.25	3.80	0.51	3.79	3.81	3.80
5.5	10	10	10	1.00	3.80	0.51	3.79	3.81	3.80
6	5	6	5	0.74	3.80	0.51	3.79	3.81	3.80

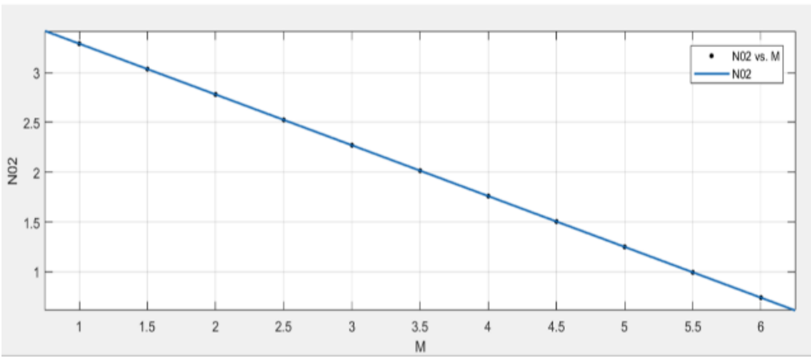

Figure 5. Initial magnitude-frequency graph

3. Analysis of Parameters

In the relationship between magnitude and frequency of earthquakes, b-value is the slope of the straight line in the logarithmic coordinate system, which is expressed as the proportional relationship between large and small earthquakes in a certain area. The larger the *b*-value is, the more the proportion of large earthquakes, so it has been studied by many scholars. In the use of the relationship between magnitude and frequency in the failure data of CNC machine tools, the b-value may be the ratio of the number of large failure grade to the number of small failure grade. We will verify this idea below; fitting the Gutenberg–Richter (G-R) curves of each year to obtain different *b*-values and plotting the *b*-value as a function of time. A failure grade greater than or equal to 4 is defined as a large failure, and a failure grade less than 4 is defined as a small failure. Draw a plot of the ratio of large failure to small failure. It can be seen from Figure 6 that the b-value curve and the curve of the ratio of the large failure to the small failure are basically opposite, that is to say, the larger the b-value, the smaller the proportion of the large failure, which shows that the b-value can reflect the ratio of large failure to small failure.

In Gutenberg–Richter (G-R) curve, a reflects the earthquake times over zero magnitude and represents the overall level. When m is zero, a represents the intercept. a values are greatly reflected by the initial data. So we should not ignore the lower level failures. In order to analyze the physical meanings of a values in the CNC machine tools faliure data, we collected a large amount of faliure data from 2003 to 2017 and drew the plot (M=1) . From Figure 7, we can see that the trend of a and lgN are similar. There is a certain connection between them . Figure 7 shows that a-values can reflect the level of integration of the CNC machine tools. We get the MTBF in 2017 of the series machine tools is more than 1000 hours. The reliability index can reach intermediate level.

4. Conclusion

the fault data of CNC machine tools have been collected and analyzed, and then the Gutenberg–Richter (G-R) curve relationship in the earthquake has been applied to CNC machine tools. Three methods are used to divide the fault levels, and the fault times of different levels are obtained. The physical meaning of the parameters is studied to describe the failure grade of the CNC machine. By comparing the b-value and the ratio of large failure to small failure with time, it is proved that b-value can reflect the ratio of large failure to small fault over a period of time. By comparing the relationship between a-value and lgN over time, it can be shown that they have a close relationship, and a-value can reflect the overall level of CNC machine tools.

The result of this paper is very close to the conclusion of seismology, which verifies that the model hypothesis is correct and feasible.

Acknowledgment

This work was sponsored by Research on the Noise Characteristics of Automobile Multi-wedge Belt and the Optimization (2018JBA01L01).

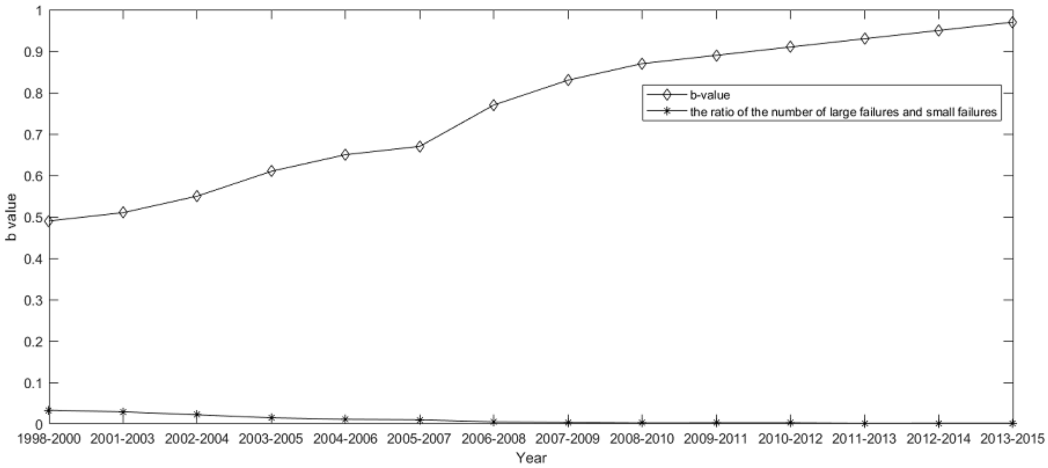

Figure 6. The trend of the b-value and the ratio of the number of large failures and small failures over time

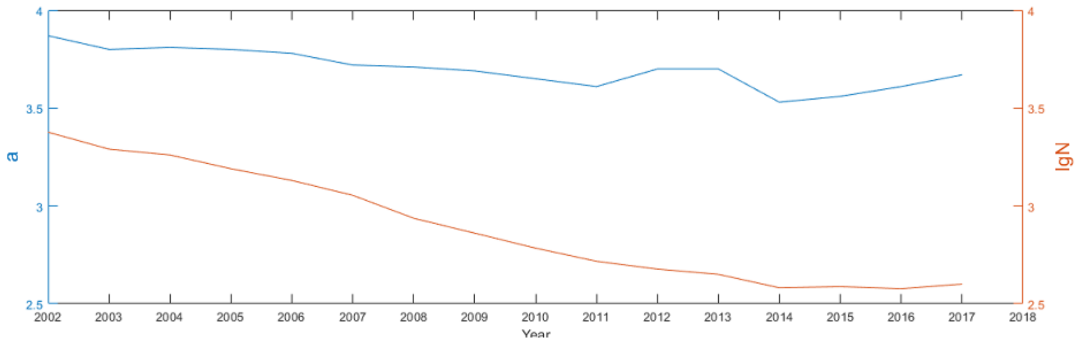

Figure 7. Comparison of a-value and lgN with time

References

[1] Lin H.B., Wei X. Research on reliability analysis and fault time distribution of CNC machine tools. Information Recording Material, 2018, 19(4), 89-90.

[2] Chen X.Z., Lv X.J., Wang, H.M. B value of the seismically active and quiescent periods and research of seismicty tendency in china. Earthquake, 2001, (1), 59-62.

[3] Wang H. Deep drainage detection system for inland vessels based on machine vision. Jordan Journal of Mechanical and Industrial Engineering, 2020, 14(1), 119-128.

[4] Dahmani N., Mukattash A. Modified grouping capability index: a new measure for evaluating of machine- component matrices. Jordan Journal of Mechanical and Industrial Engineering, 2019, 13(1), 15-20.

[5] Zhang S.F., Zhang X.T., Zhao Z.Y. Seismic hazard judgment based on seismic activity parameter b value in the middle-western of Zhangjiakou- Bohai seismic belt. Seismic Geomagnetic Observation and Research, 2018, 2(4), 51-57.

[6] Zhao J.P., Xiong J.X., Jian J.C. Equipment's operation reliability analysis and assessment based on failure data. Chinese High Technology Letters, 2017, 27(4), 359-363.

[7] Zhang Y.Z., Shen G.X., Jia Y.Z. Research on the disciplinarian and reliability of failure distribution of CNC Lathe. Transactions of the Chinese Society of Agricultural Machinery, 2006, 37(1), 156-159.

[8] Wei J.Q., Piao C.D. Reliability analysis and evaluation of foreign high-grade machining center. Machine Tool & Hydraulics, 2016, 44(1), 194-197.

[9] Ding J.X., Yu J. Analysis of fault G-R relationship of CNC Lathe. Intern Comb Eng Part, 2019, (14), 179-180.

[10] Qi X.D. Reliability Comprehensive Evaluation of Manufacturing Process for Key Components of CNC Machine Tools. Chongqing, China: Chongqing University, 2017.

[11] Zhang G.B., She L., Ran Y., Luo D.M. Study on extraction of key functional components in CNC machine tools' reliability tests. China Mechanical Engineering, 2016, 27(17), 2372-2378.

[12] Bian Q.K., Li S.Z., Mao Z.W., Li S.L., Wang Q.C. A study of the seismic activity anomaly before the ZhangBei MS 6.2 Earthquake and the characeristics of its sequence. North China Earthquake Sciences, 1999, (03), 35-42.

[13] Xue J.N., Li X., Zhang B., Wang Y.W. Statistical analysis of B-values in Shandong area. North China Earthquake.

[14] Mishra M., Abhishek, Yadav R.B.S., Sandhu M. Probabilistic assessment of earthquake hazard in the Andaman–Nicobar–Sumatra region. Natural Hazards, 2020, 105(01), 313-338.

[15] Tiwari V.M. CSIR-national geophysical research institute — 60 years of enduring scientific contributions. Journal of the Geological Society of India, 2020, 96(4), 319-324.

JJMIE

Volume 15, Number 1, March. 2021
ISSN 1995-6665
Pages 105 - 112

Jordan Journal of Mechanical and Industrial Engineering

Fault Status Information Monitoring Technology for Large Complex Electromechanical System

Baoli Wei[1*], Hongtao Jiao[2]

[1]*Department of Mechanical and Electrical Engineering, Zhengzhou Railway Vocational and Technical College, Zhengzhou 450000, China*
[2]*The College Office, Zhengzhou Railway Vocational and Technical College, Zhengzhou 450000, China*

Received July 18 2020 *Accepted March 13 2021*

Abstract

In order to improve the accuracy of fault state monitoring of electromechanical system, a fault state informatization monitoring technology for large complex electromechanical system is proposed. Based on the standard PD (Partial Discharge) signal expression derived from the traditional communication theory, the characteristic value of the fault signal is calculated, and the feature of the fault state signal is extracted by using the functions of the time and frequency of the fault state of the electromechanical system. Experimental results show that compared with the information monitoring technology based on support vector machine, the proposed fault monitoring technology has a higher monitoring accuracy.

Keywords: complex electromechanical; system fault state; informatization; monitoring technology;

1. Introduction

Large-scale complex electromechanical systems in modern engineering are gradually developing towards the direction of complicated structure, intelligent operation and process automation. Such electromechanical features make not only the components within each single device very closely interconnected, but also the different devices are very closely interconnected, and through such close structural and functional interconnections, a complete device operating system is constructed [1]. Due to the high load capacity, high transmission accuracy and the relevant characteristics of constant power transmission of large complex electromechanical systems, large complex electromechanical systems, as an indispensable component of electromechanical equipment, are widely used in modern equipment such as aviation, agricultural electromechanical equipment, factories, mines, military equipment, power systems, and metallurgical electromechanical equipment, etc. [2, 3].

If the mechanical and electrical system of a moving car breaks down, it will directly affect the life and safety of the people inside the car; for some machinery and equipment that are in a state of continuous operation for a long time, such as generating units in the electric power industry, and machine power for ore collection and transportation in the mining industry, the whole production process will be stopped due to the mechanical and electrical failure, which will cause incalculable economic losses [4]. For example, in 1988, the main axle of the power plant in Qinling Mountain area was broken, and the national economy suffered a loss of over 100 million yuan, and affected the local normal electricity use, and affected people's normal life. Our country once used a scientific survey ship to go to sea for scientific research. After a period of navigation, due to a partial breakage of the main retarder, the research ship had to slow down and move forward. As a result, the whole fleet did not arrive at the designated scientific survey area on schedule, and the scientific survey action was seriously affected [5]. In 1986, a generator unit at the Chernobyl nuclear power plant in the former Soviet Union was vibrating because of a serious mechanical and electrical failure, which led to nuclear leakage, more than 2,000 deaths, and economic losses of $3 billion. The consequences of the accident, which caused severe environmental pollution and threatened the safety of human life, were incalculable [6].

As early as one hundred years ago, people began to study the fault and fault information state of large complex electromechanical systems. However, the fault state monitoring technology for large complex electromechanical systems has become a scientific component of the equipment fault monitoring technology, which can arouse people's great attention. In 1986, the British scholar H. Optiz published some research curves of great significance in the fault monitoring of large complex electromechanical systems, and discussed that the vibration and noise generated by electromechanical systems are functions of power and error generated by electromechanical transmission [7]. There are two kinds of methods to monitor the faults of electromechanical system: one is to process the dynamic data of vibration and noise by signal processing method, the other is to detect the faults of electromechanical system by analyzing and processing the lubricating oil used in the process of working. At present, the vibration signal is widely used in electromechanical system fault monitoring, and the technology is mature, but the vibration fault

* Corresponding author e-mail: ztxyweibaoli@126.com

monitoring method has its own shortcomings. In addition, among the existing fault monitoring methods, there are many cases of using acoustic emission technology to realize fault monitoring, but the scientific research applied to the fault monitoring of electromechanical systems is not very extensive. However, due to the characteristics of high sampling accuracy and fast collection speed, the application of acoustic emission signals to the fault monitoring of electromechanical systems still has high scientific research value [8-10].

To sum up, it can be found that the fault monitoring technology of electromechanical system has a long history at home and abroad, and in some areas of electromechanical fault monitoring and technology is relatively mature [11, 12]. But from the technical level, it can be seen that the current fault monitoring technology of electromechanical system is mainly used to collect and analyze signals by means of vibration, but because vibration signals in the operation of large electromechanical equipment will produce a lot of noise, it is easy to submerge useful vibration signals in noise. Another point is that vibration sensors pick up mechanical and electrical systems only when they are in deep trouble, making them difficult to detect in the early stages of a failure [13]. With the development of science and technology, AE signal acquisition system has been developed. Because AE signal has the characteristics of high acquisition precision and high signal frequency, it is easy to collect the fault information in the early stage of signal occurrence, and because of the high frequency of AE signal, it is easy to shield the noise information generated by electromechanical equipment. So, it is found that the use of AE signal to achieve fault monitoring of electromechanical system has a little scientific research value by reference to the summarized literature. Based on the above background, the research on fault monitoring of electromechanical system can realize the fundamental transformation of electromechanical system from accident maintenance, regular maintenance to real-time maintenance according to the operation of electromechanical system, and can reduce some unnecessary economic losses, thus produce greater economic benefits and social benefits. Therefore, fault monitoring of electromechanical system is of great significance in people’s real life.

2. Design of Fault State Information Monitoring Technology for Large Complex Electromechanical System

2.1. Extracting fault state signal characteristics of electromechanical systems

The traditional fault monitoring method based on discharge current pulse is based on the IEC60270 standard. The frequency band is limited to 10-200 kHz. The measurement is the total amount of local discharge. Finally, the spectrum of Yi-Q-N (discharge phase - discharge quantity - discharge times) is drawn to identify the discharge types. This method is insufficient to obtain sufficient local discharge and noise in the information area and different types of local discharge, and the anti-noise ability is weak [14].

PD Check converts the actual time of the PD signal into the equivalent time, so that the length of the signal can be linked to other information about the signal. Formula (1) is a standardized PD signal expression based on the traditional communication theory.

$$\tilde{s}(t) = \frac{s(t)}{\sqrt{\int_0^T s(t)^2\, dt}} \tag{1}$$

In the formula, $s(t)$ represents the transformation of PD signal standardization (t is time), calculates the signal characteristics, and obtains the function of time and frequency:

$$\sigma_T = \sqrt{\int_0^T (t-t_0)^2\, \tilde{s}(t)^2\, dt} \tag{2}$$

$$\sigma_F = \sqrt{\int_0^\infty f^2 \left|\tilde{s}(f)\right|^2 df} \tag{3}$$

Formula (2) and (3) are the standard deviation of $s(t)$ in formula (1) in time domain and frequency domain. $S(f)$ is the Fourier transform of $s(t)$, t_0 is the time center of the standard signal, and t_0 expression is:

$$t_0 = \int_0^T t\tilde{s}(t)^2\, dt \tag{4}$$

The feature of a PD signal is transformed into some digital quantities, which preserve the time and frequency information of the signal. The signals generated by the same PD source are very similar, usually the collected data contains more than one signal source, and the stronger noise signal will cover the internal PD signal. In order to separate and record the source of the signal and eliminate the interference, the fuzzy logic method is applied to obtain the classification of PD pulse [15]. Different types of signals can be separated according to the characteristics of different types of impulses, which plays a vital role in the noise separation and type analysis. Then, the noise interference of fault signal is eliminated, which provides the basis for fault monitoring of electromechanical system.

2.2. Eliminating noise interference of fault signal

Through calculation and classification, the fault signals with different characteristics can be divided into different parts. This step is to remove the noise signals from different parts of the signals. For the general fault state noise signals, due to the randomness of the fault state signals, their phases are not necessarily related to the phases of the applied voltage, which is very obvious in the local spectrograph, that is, the points representing these noise pulses are scattered over all time periods without any rules, and we can easily eliminate the fault state noise signals after classification [16]. Another kind of fault state noise signal is fixed in one or several phases, they have relatively fixed phase angle, such as AC/DC rectifier. This recurrence of the periodic appearance in the same phase of the signal spectrum can also be obtained through the Fourier transform. Choose different parts, observe the discharge spectrum, we can find out the noise signal.

The aim of fault state signal type recognition is to find out the PD signal's PD source accurately and judge its harm. In principle, the more samples collected, the more accurate the analysis. However, due to a variety of noises and local sources that consistently emit fault state signals, too many signals can lead to overlap, making it difficult to separate fault state signals [17]. Therefore, the number of fault state signal acquisition can only be guaranteed to extract a complete fault state signal characteristics.

When the fault state signals are separated, the PD signals can be statistically calculated to obtain the standard parameters and the distributed parameters of the PD pulses, which can help identify the types of fault state signals [18-20].

The PDCheck system is equipped with a powerful expert identification system, in which a huge database of fault state characteristics is included. For each discharge pulse waveform analysis software, dozens of fault state characteristics are extracted according to certain steps, and then the fault state characteristics are compared with the fault state in the expert database. The fuzzy logic method is used to determine the similarity between the tested fault state type and the known fault state type, so as to reach the corresponding judgment conclusion [21]. The recognition of a signal can be divided into two levels, the first level is to judge the type of PD, which is mainly divided into internal failure state, surface failure state and corona failure state. This step is judged by the analysis of the random characteristics of the fault state signals [22]. Among the parameters that represent the signal characteristics, only the very appropriate and accurate signal characteristics can be defined as the characteristic database of the fault state signals.

2.3. Monitoring the failure state of electromechanical systems

The KELM (Kernel Extreme Learning Machine) theory is used to monitor the fault state of electromechanical system. When the KELM algorithm is used to monitor the collected health state data of electromechanical system, the test results are not stable because of the unstable performance caused by the random initialization weight. Differential evolution algorithms can be used to solve optimal input weights, but because iterative evolution takes a lot of time, there is no guarantee that the optimal network structure will be obtained [23]. In order to make the performance of the KELM algorithm more stable, the concept of kernel function is introduced according to the SVM (Support Vector Machine), and the nonlinear kernel mapping is introduced into the KELM algorithm.

Many engineering practices show that it is feasible to combine kernel functions with KELM, which improves the stability of KELM algorithm and has better nonlinear approximation ability [24]. The kernel functions commonly used in SVM are linear kernel function and polynomial kernel function. These can be applied to KELM as a kernel function.

Given any N different samples (x_i, t_i), the specific fault monitoring process is as follows:

1. Step 1: Get fault characteristic samples of electromechanical systems in different health states, and normalize the samples;
2. Step 2: Train KELM. The normalized characteristic data of electromechanical system is composed of training samples (x_i, t_i) and $i = 1, 2, \cdots, N$, and the kernel function is selected to obtain the optimal classification function:

$$f(x) = \begin{bmatrix} K(x_1, t_1) \\ K(x_2, t_2) \\ \vdots \\ K(x_N, t_N) \end{bmatrix}^T \left(\frac{I}{C} + \Omega_{ELM} \right)^{-1} \tag{5}$$

In the equation, $K(\cdot)$ represents the kernel function, I represents the fault current, C represents the fault normalized characteristic parameter, Ω_{ELM} represents the fault information entropy.

3. Step 3: Fault monitoring of mechanical and electrical systems with a constructed KELM fault monitoring model.

To sum up, according to the standardized PD signal expression derived from the traditional communication theory, the characteristic value of the fault signal is calculated, and the feature extraction of the fault state signal of the electromechanical system is completed by using the functions of the time and frequency of the fault state of the electromechanical system; on the basis of eliminating the noise interference of the fault signal, the fault state monitoring of the electromechanical system is realized through the fault monitoring algorithm design.

3. Comparative analysis of experiments

3.1. Experimental Research on Fault State Information Monitoring Technology of Electromechanical System Based on SVM

3.1.1. Sample selection

Aiming at the research object of large-scale complex electromechanical system, 590 sets of experimental data are used as training test data in the four states A_1, A_2, A_3 and A_4 of large-scale complex electromechanical system, of which 400 sets are selected as normal state A_1, A_2 50 groups of data are selected as training data for each of the three fault states A_3 and A_4, and 10 groups of data are selected as test data for each state. So, we get 550 sets of training data and 40 sets of test data.

3.1.2. Selecting kernel functions and classifiers

Compared with other kernel functions of SVM, such as linear kernel function, RBF can deal with the samples with nonlinear characteristics, and RBF needs fewer parameters than polynomial kernel function.

In addition, in the selection of classifiers, the first problem to be solved by SVM is the problem of two classifications. As we know, there are four fault modes of electromechanical system, which belong to the problem of multiple classifications.

3.1.3. Fault monitoring training and result analysis

After analysis, seven parameters are selected to represent the running state of the engine, including low-pressure rotor speed (N_1), high-pressure rotor speed (N_2), exhaust temperature after turbine (T_4), engine inlet temperature (T_2), gearbox vibration (B_1), engine inlet pressure (P_2), compressor outlet pressure (P_3), as the characteristic parameters of the mechanical and electrical system. The mechanical and electrical system failure modes are expressed as a set of four, i.e. $\{A_1, A_2, A_3, A_4\}$, in which mode A_1 refers to the operation of mechanical and electrical system in normal state; mode A_2 refers to the bearing damage failure of mechanical and electrical system;

mode A_3 refers to the regulator failure of mechanical and electrical system; mode A_4 refers to the failure of exhaust temperature and speed exceeding the limit value when the throttle lever is pushed from idle state to intermediate state.

Four failure modes $\{A_1, A_2, A_3, A_4\}$ of electromechanical system are classified and trained, in which normal state A_1 sample is represented by 1; A_2 failure is represented by 2; A_3 failure is represented by 3; A_4 failure is represented by 4. After the monitoring test, the monitoring results as shown in Figure 1 are obtained.

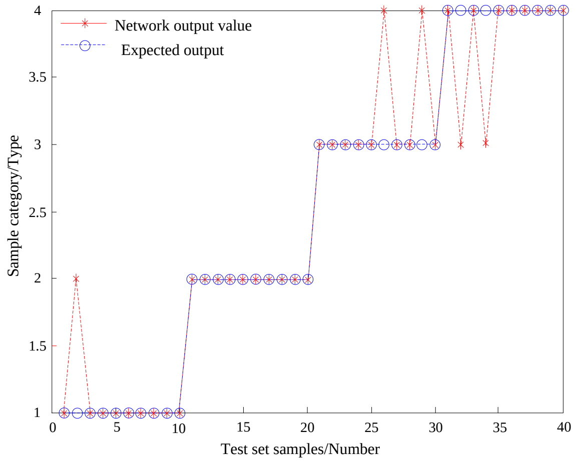

Figure 1. Support vector machine monitoring test results

From the test results of Figure 1, we can get the specific test results of 40 sets of test data in 4 states of electromechanical system, as shown in Table 1.

Table 1. Test results of four failure modes

Failure mode	Number of test samples	Number of correct monitoring	Correct monitoring rate
A_1 fault	10	9	90%
A_2 fault	10	10	100%
A_3 fault	10	8	80%
A_4 fault	10	8	80%

To sum up, the general process of fault monitoring is as follows: use SVM fault monitoring model to train 550 groups of data, then use 40 groups of data to test and monitor the trained SVM fault monitoring model, and finally correctly monitor 35 groups of data, including 1 group of A_1 status data misdiagnosed as A_2 fault, 2 groups of A_3 fault status data misdiagnosed as D fault, 2 groups of C fault status data misdiagnosed as A_4 fault The data of group A_4 is misdiagnosed as failure A_3, so it can be concluded that the final failure monitoring rate is 87.5% by testing and monitoring 40 groups of test data.

3.2. Test and Research on information monitoring technology of mechanical and electrical system fault state

Aiming at the research object of electromechanical system, 590 sets of experimental data are used as training test data under the four states of electromechanical system A_1, A_2, A_3, A_4, of which 400 sets are selected as normal state A_1, A_2 50 groups of data are selected as training data for each of the three fault states A_3 and A_4, and 10 groups of data are selected as test data for each state. So, we get 550 sets of training data and 40 sets of test data.40 groups of samples are used to test the fault monitoring model trained by the limit learning machine. Table 2 shows the output results of ELM (Extreme Learning Machine) monitor.

Table 2. Description of ELM monitor output results

Monitor output				health status
A_1 Failure mode status	A_2 Failure mode status	A_3 Failure mode status	A_4 Failure mode status	
0	0	0	1	Healthy
0	0	1	0	A_2 fault
0	1	0	0	A_3 fault
1	0	0	0	A_4 fault

In this paper, the fault monitoring of electromechanical system based on ELM is carried out on the platform of MATLAB. Because the selected characteristic parameters of electromechanical system are 7, the number of input neurons should be set to 7; the fault mode of electromechanical system is 4, that is, the number of output neurons is set to 4, and the Sigmoid function is selected as the activation function. In addition, the connection weights between input layer and hidden layer and the offset b of neurons in hidden layer are initialized randomly, and the number of neurons in hidden layer is 75. The identification results of Limit Learning Machine fault monitoring are shown in Figures 2 to 5.

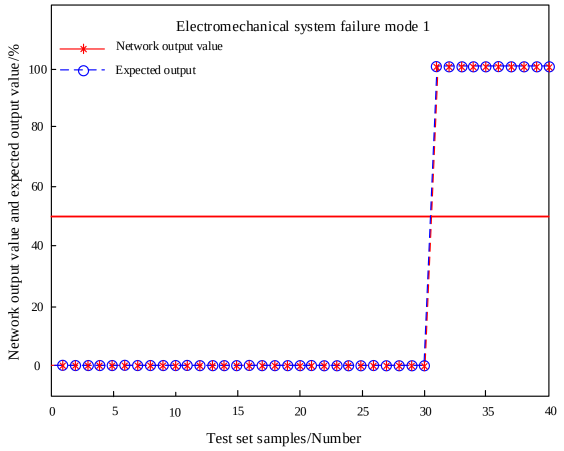

Figure 2. Output result of mode 1

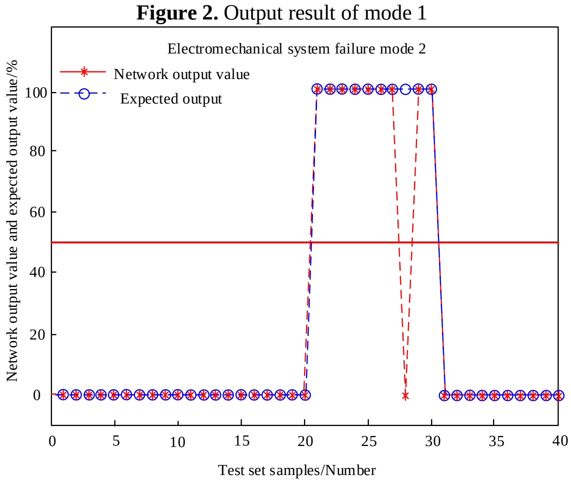

Figure 3. Output result of mode 2

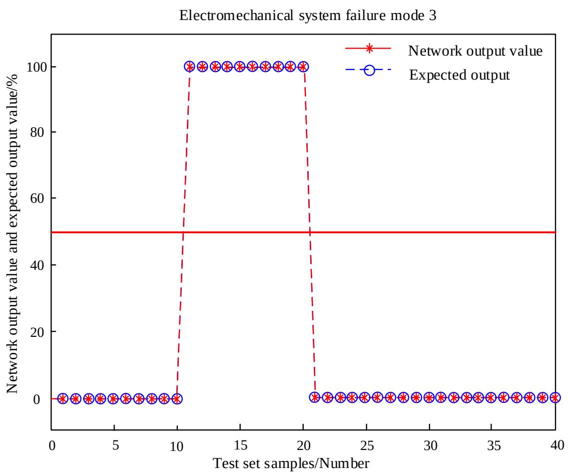

Figure 4. Output result of mode 3

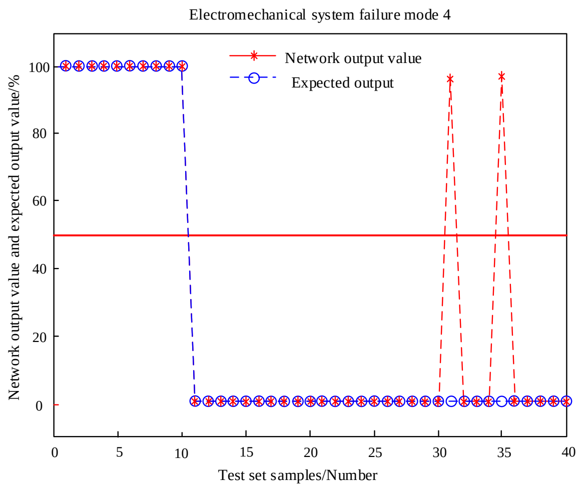

Figure 5. Output result of mode 4

It can be seen from Fig. 2 to Fig. 5 that by using the trained elm model to monitor each fault type with 10 groups of test data respectively, according to the principle that the previously set test output results are changed into binary codes, comparison and sorting are carried out, and the monitoring results of four types of large-scale complex electromechanical systems A_1, A_2, A_3, A_4 can be obtained respectively in Table 3 to Table 6.

Table 3. Monitoring results of mechanical and electrical system A_1 status

	Actual output value				Expected output			
1	0.41537	0.00005	0.00000	0.58458	0	0	0	1
2	0.40981	0.00004	0.00000	0.59015	0	0	0	1
3	0.39747	0.00003	0.00000	0.60250	0	0	0	1
4	0.37752	0.00002	0.00000	0.62246	0	0	0	1
5	0.35416	0.00001	0.00000	0.64583	0	0	0	1
6	0.34794	0.00001	0.00000	0.65205	0	0	0	1
7	0.35293	0.00001	0.00000	0.64706	0	0	0	1
8	0.35829	0.00001	0.00000	0.64169	0	0	0	1
9	0.36357	0.00001	0.00000	0.63641	0	0	0	1
10	0.36830	0.00001	0.00000	0.63168	0	0	0	1

It can be seen from Table 3 that the actual output value and expected output value of the test are compared with the output specified in the original training. The number of correct data groups monitored by these 10 groups of test data is 10, and the number of data groups monitored by the wrong fault type is 0. Therefore, the monitoring rate of A_1 state of electromechanical system is 100%.

Table 4. Monitoring results of mechanical and electrical system A_2 status

	Actual output value				Expected output			
1	0.00000	0.00000	1.00000	0.00000	0	0	1	0
2	0.00000	0.00000	1.00000	0.00000	0	0	1	0
3	0.00000	0.00000	1.00000	0.00000	0	0	1	0
4	0.00000	0.00000	1.00000	0.00000	0	0	1	0
5	0.00000	0.00000	1.00000	0.00000	0	0	1	0
6	0.00000	0.00000	1.00000	0.00000	0	0	1	0
7	0.00000	0.00000	1.00000	0.00000	0	0	1	0
8	6.4900000000000e-321	1.0436945140000e-314	1.00000	0.00000	0	0	1	0
9	0.00000	0.00000	1.00000	0.00000	0	0	1	0
10	0.00000	0.00000	1.00000	0.00000	0	0	1	0

It can be seen from Table 4 that the actual output value and expected output value of the test are compared with the output specified in the original training. The number of correct data groups monitored by these 10 groups of test data is 10, so the monitoring rate of A_2 state of electromechanical system is 100%.

Table 5. Monitoring results of mechanical and electrical system A_3 status

	Actual output value				Expected output			
1	0.00202	0.77226	0.00000	0.22571	0	1	0	0
2	0.00588	0.72855	0.00000	0.26557	0	1	0	0
3	0.00000	0.98448	0.00000	0.01552	0	1	0	0
4	0.00000	0.84964	0.00000	0.15035	0	1	0	0
5	0.00003	0.84336	0.00000	0.15661	0	1	0	0
6	0.00019	0.85666	0.00000	0.14315	0	1	0	0
7	0.00001	0.95109	0.00000	0.04890	0	1	0	0
8	0.01001	0.49985	0.00000	0.49013	0	1	0	0
9	0.00008	0.95084	0.00000	0.04908	0	1	0	0
10	0.00083	0.61570	0.00000	0.38347	0	1	0	0

It can be seen from Table 5 that the actual output value and expected output value of the test are compared with the output specified in the original training. The number of correct data groups monitored by these 10 groups of test data is 9, and the number of data groups monitored by the wrong fault type is 1. Therefore, the monitoring rate of A_3 state of electromechanical system is 90%.

Table 6. Monitoring results of mechanical and electrical system A_4 status

	Actual output value				Expected output			
1	0.48547	0.00303	0.00000	0.51150	0	0	0	1
2	0.50065	0.00330	0.00000	0.49606	1	0	0	0
3	0.53875	0.00115	0.00000	0.46010	1	0	0	0
4	0.52609	0.00223	0.00000	0.47168	1	0	0	0
5	0.47410	0.00195	0.00000	0.52395	0	0	0	1
6	0.54764	0.00134	0.00000	0.45102	1	0	0	0
7	0.50009	0.00160	0.00000	0.49831	1	0	0	0
8	0.55583	0.00195	0.00000	0.44222	1	0	0	0
9	0.50777	0.00140	0.00000	0.49083	1	0	0	0
10	0.53284	0.00216	0.00000	0.46500	1	0	0	0

It can be seen from Table 6 that the actual output value and expected output value of the test are compared with the output specified in the original training. The number of correct data groups monitored by these 10 groups of test data is 8, and the number of data groups monitored by the wrong fault type is 2. Therefore, the monitoring rate of A_4 state of electromechanical system is 80%.

To sum up, the ELM fault monitoring model is used to train 550 sets of data, and 40 sets of data are used to test and monitor the trained ELM fault monitoring model. The final result is that 37 sets of data are correctly monitored, and 3 sets of data are monitored incorrectly.

3.3. Comparison and analysis of effects of different fault monitoring technologies

The selection and comparison methods are based on the support vector machine monitoring technology. The 550 groups of data under the above-mentioned four failure states of the mechanical and electrical system are used for training, and 40 groups of data are used to test the monitoring technology based on the support vector machine. The results are as shown in Table 7.

Table 7. Monitoring results of different states of electromechanical system based on support vector machine method

Failure mode		Actual output value				Expected output			
A_1	1	0.56734	0.00001	0	0.64972	0	0	0	1
	2	0.69734	0.00002	0	0.59346	0	0	0	1
	3	0.56701	0.00003	0	0.66795	0	0	0	1
	4	0.36974	0.00003	0	0.63697	0	0	0	1
	5	0.34219	0.00001	0	0.65647	0	0	0	1
	6	0.32577	0.00001	0	0.62367	0	0	0	1
	7	0.34524	0.00002	0	0.66379	0	0	0	1
	8	0.32472	0.00003	0	0.65937	0	0	0	1
	9	0.35274	0.00001	0	0.79416	0	0	0	1
	10	0.35277	0.00001	0	0.69734	0	0	0	1
A_2	1	0	0	1	0	0	0	1	0
	2	0	0	1	0	0	0	1	0
	3	0	0	1	0	0	0	1	0
	4	1	0	0	0	0	0	1	0
	5	0	0	1	0	0	0	1	0
	6	0	0	1	0	0	0	1	0
	7	0	0	1	0	0	0	1	0
	8	1.34697	1.9465	1	0	0	0	1	0
	9	0	0	1	0	0	0	1	0
	10	0	0	1	0	0	0	1	0
A_3	1	0.04527	0.45277	0	0.25427	0	1	0	0
	2	0.00452	0.75277	0	0.27527	0	1	0	0
	3	0	0.9272	0	0.01752	0	1	0	0
	4	0	0.72752	0	0.72772	0	1	0	0
	5	0	0.452	0	0.7527	0	1	0	0
	6	0.00012	0.84527	0	0.14224	0	1	0	0
	7	1	1	0	0.04527	0	1	0	0
	8	0.01042	0.54277	0	0.40204	0	1	0	0
	9	0.0004	0.9204	0	0.02752	0	1	0	0
	10	1	0.2044	0	0.34527	0	1	0	0
A_4	1	0.25752	0.0427	0	0.5115	0	0	0	1
	2	0.45427	0.0033	0	0.49606	1	0	0	0
	3	0.54277	0.02425	0	0.4601	1	0	0	0
	4	0.54275	0.04205	0	0.47168	1	0	0	0
	5	1.357	0	0	0.57257	0	0	0	1
	6	0.42752	0.00134	0	0.45102	1	0	0	0
	7	0.500427	0.04074	0	0.49831	1	0	0	0
	8	0.57257	0.04024	0	0.44222	1	0	0	0
	9	0.51527	0.0014	0	0.49083	1	0	0	0
	10	0.5727	0.042	0	0.465	1	0	0	0

Based on the analysis of the above data, the number of monitoring errors in A_1 fault state is 2, the number of monitoring errors in A_2 fault states is 1, the number of monitoring errors in A_3 fault states is 1, and the number of monitoring errors in A_4 fault states is 1. The results of the two methods are summarized and compared as shown in Table 8.

Table 8. Comparison of results of different monitoring techniques

Monitoring technology	Total number of test samples	Correctly identify the number of samples	Number of error identification samples	Correct recogniti on rate
Monitoring technology based on SVM	40	35	5	87.5%
Proposed monitoring technology	40	37	3	92.5%

From Table 8, we can see that the proposed monitoring technology is the best, the correct recognition rate is 92.5%, while the correct recognition rate of the monitoring technology based on SVM is 87.5%. Therefore, the proposed monitoring technology has a higher monitoring accuracy.

4. Conclusions

Large complex electromechanical system is a device with complex structure in electromechanical equipment. In addition, large complex electromechanical system plays the role of transmitting power in the operation of equipment, so it carries more forces. In addition, the general large complex electromechanical system is running in the environment of poor external conditions, so it is also a component prone to failure. Once a large complex electromechanical system failure will cause the most direct impact on the reliability of the entire operation of electromechanical equipment and will lead to reduced efficiency and precision. With the development of large scale, complicated and automatic, the failure of large complex electromechanical system will make the industrial production and even the whole society run normally. Based on the feature of fault state signal, the noise interference of fault signal is eliminated, and the fault state monitoring flow is combined to realize the fault state monitoring of electromechanical system. The results show that the proposed fault monitoring technology in different modes of fault monitoring, the accuracy of fault monitoring reaches 92.5%, far higher than the failure rate of other methods, indicating that the design method can effectively improve the accuracy of fault monitoring. Although this paper has basically achieved the expected goal of graduation design, but because of the limited number of test samples, the results and conclusions can only be used as a technical guidance in practical application.

References

[1] Luo, S.; Li, S.; Tajaddodianfar, F.; et al. Adaptive synchronization of the fractional-order chaotic arch micro-electro-mechanical system via Chebyshev neural network. IEEE Sensors Journal, 2018, PP(99):1-1.

[2] Ye, H.; Kai, S. Multi-scale and frequency-dependent modeling of electric power transmission lines. IEEE Transactions on Power Delivery, 2018, 33(1):32-41.

[3] Polyakov, A.; Filimonova, E.; Chesnokov A. Upgrading automatic control of a complex electromechanical system for production of synthetic yarns and nonwoven materials. Fibre Chemistry, 2017, 48(4):1-4.

[4] Lumentut, M.; Howard, I. Intrinsic electromechanical dynamic equations for piezoelectric power harvesters. Acta Mechanica, 2017, 228(2):631–650.

[5] Jian, F.; Maré, J.; Fu, Y. Modelling and simulation of flight control electromechanical actuators with special focus on model architecting, multidisciplinary effects and power flows. Chinese Journal of Aeronautics, 2017, 30(1):47-65.

[6] Gao, C.; Yu, P.; Zhao, H. A nonlinear model and system identification of shaking table. Revista De La Facultad De Ingenieria, 2017, 32(5):107-116.

[7] Baswana, S.; Choudhary, K.; Roditty, L. Fault-tolerant subgraph for single-source reachability: General and optimal. Siam Journal on Computing, 2018, 47(1):80-95.

[8] Wei, X.; Gao, S.; Li, D.; et al. Cascading fault graph for the analysis of transmission network vulnerability under different attacks. Zhongguo Dianji Gongcheng Xuebao/Proceedings of the Chinese Society of Electrical Engineering, 2018, 38(2):465-474.

[9] Zheng, C.H.; Massimo, T. Slicing ATL model transformations for scalable deductive verification and fault localization. International Journal on Software Tools for Technology Transfer, 2018, 2018(2):1-19.

[10] Wu, T.; Guo, S.; et al. Development and trend of condition monitoring and fault diagnosis of multi-sensors information fusion for rolling bearings: a review. International Journal of Advanced Manufacturing Technology, 2018, 96(1-4):803-819.

[11] Li, L.; Chadli, M.; Ding, S.; et al. Diagnostic observer design for T–S fuzzy systems: application to real-time-weighted fault-detection approach. IEEE Transactions on Fuzzy Systems, 2018, 26(2):805-816.

[12] Almagbile A. Geometric and statistical interpretation of correlation between fault tests in integrated GPS/INS systems. Journal of Applied Geodesy, 2019, 13(3):267-278.

[13] Ende, M.; Chen, J.; Ampuero, J.; et al. A comparison between rate-and-state friction and microphysical models, based on numerical simulations of fault slip. Tectonophysics, 2018, 733:273-295.

[14] Wu, T.; Li, F.; Yang, C.; et al. Event-based fault detection filtering for complex networked jump systems. IEEE/ASME Transactions on Mechatronics, 2018, 23(2):497-505.

[15] Li, F.; Shi, P.; Lim, C.; et al. Fault detection filtering for nonhomogeneous markovian jump systems via fuzzy approach. IEEE Transactions on Fuzzy Systems, 2018, 26(1):131-141.

[16] Zane, S.; Ramsay, G.; Jimenez-Garate, M.; et al. XMM–Newton EPIC and optical monitor observations of Her X-1 over the 35-d beat period. Monthly Notices of the Royal Astronomical Society, 2018, 350(2):506-516.

[17] Gao D. Online fault prediction and simulation of micro-channel platform for network-based devices. Computer Simulation, 2017, 34(7):207-210.

[18] Wang, A.; Liang, J.; Liu, Y. Application of improved particle swarm optimization in gear fault diagnosis of automobile transmission. Jordan Journal of Mechanical and Industrial Engineering, 2020, 14(1):175-182.

[19] Tao, J.; Jia, Y.; Gao, Y. Intelligent remote monitoring system for minor faults of intelligent unmanned vehicle. Jordan Journal of Mechanical and Industrial Engineering, 2020, 14(1):61-70.

[20] Wang, H.; Li, B.; Liu, Z.; et al. HER2 copy number of circulating tumour DNA functions as a biomarker to predict and monitor trastuzumab efficacy in advanced gastric cancer. European Journal of Cancer, 2018, 88:92-100.

[21] Strauss, T.; Feher, S.; Friedsam, H.; et al. The Mu2e solenoid cold mass position monitor system. IEEE Transactions on Applied Superconductivity, 2018, PP(99):1-1.

[22] Ahuja, A.; Halperin, L. Using machine learning to monitor keratoconus progression. JAMA Ophthalmology, 2019, 137(12):1467-1468.

[23] Nykaza, E.; Blevins, M. Machine learning for spatial interpolation of noise monitor levels. Journal of the Acoustical Society of America, 2018, 143(3):1716-1716.

[24] Frelinger III, A.L. Using flow cytometry to monitor glycoprotein IIb-IIIa activation. Platelets, 2018, 29(5527):1-7.

JJMIE

Volume 15, Number 1, March. 2021
ISSN 1995-6665
Pages 113 - 121

Jordan Journal of Mechanical and Industrial Engineering

Method of Power Performance Fault Alarm of Hybrid Electric Vehicle Based on Hydraulic Technology

Wenjuan Liu

Department of Mechanical Engineering, Liaoning Mechatronics College, Dandong 118000, China

Received July 18 2020 *Accepted March 13 2021*

Abstract

Due to the lack of precision in the modeling of the vehicle power system, the fault diagnosis and alarm accuracy of the current hybrid vehicle dynamic performance fault alarm method is reduced. Therefore, a hybrid vehicle dynamic performance fault alarm method based on hydraulic technology is designed. The power system model of hybrid electric vehicle is built by hydraulic technology, which is the data base of fault diagnosis. The method of self-diagnosis and the knowledge base of fault diagnosis are used to realize the fault diagnosis of vehicle power system. The interface between mobile network and on-board information is selected to realize vehicle fault alarm by setting alarm information content. The fault diagnosis accuracy of this method is always between 88.5% and 94.5%, the fault diagnosis time is less than 0.5 s, and the highest effective failure alarm rate is 99.8%. The experimental results show that the research method has the advantages of high accuracy, short diagnosis time, high effective alarm rate, low cost, superior economic performance and good application effect.

Keywords: hydraulic technology; hybrid vehicle; fault diagnosis; fault early warning; power system modeling; mobile network;

1. Introduction

With the gradual improvement of economic and living standards, the demand for automobiles is increasing rapidly. While automobiles bring convenience, rapidity, and comfort to our life, a series of environmental and energy problems caused by automobiles are gradually prominent. Up to now, automobiles have become one of the important factors affecting the urban environmental construction and the sustainable development of national energy. Therefore, the international traditional automotive research and development, manufacturing and production field is facing great challenges, the transformation of the development of the automotive industry is imperative. With its low energy consumption and clean and pollution-free emissions, new energy vehicles have become the focus of current research in the automobile industry, and related fields, and are favored by scientific research institutions and related production fields of various countries [1, 2].

At present, there are many kinds of problems in the commonly used fuel engine vehicles. According to the relevant data, since the 1990s, due to the increasingly lack of resources and the growing voice of environmental protection in the world, various electric vehicles have emerged. Due to the large mass and volume of the battery pack of electric vehicle, the endurance and power performance of electric vehicle cannot reach the level of current internal combustion engine. In addition, the selection of electric vehicle components such as air conditioning and heating must fully consider the impact of its energy consumption on the endurance of electric vehicles. The high price and limited life of battery pack also limit the market prospect of electric vehicle. The above constraints make the development and application of electric vehicles slow down, and it is impossible to industrialize them in a short period of time. In this case, the "quasi green vehicle"-hybrid vehicle, which integrates the advantages of internal combustion engine vehicles and electric vehicles, has stepped onto the historical stage [3]. In general, hybrid electric vehicle refers to a vehicle in which the motor and engine (engine is generally called auxiliary power unit, APU) are used as the power device at the same time. Through the advanced control system, the two power devices can coordinate organically, realize the optimal distribution of energy, and achieve low energy consumption, low emissions and high automation.

As a quasi-green vehicle, hybrid electric vehicle has many products in developed countries. In order to realize market-oriented and scale-up of domestic hybrid vehicles, problems and challenges need to be solved, including: developing energy storage devices with high specific energy and high specific power, low-cost and efficient electronic communication equipment, as well as engines with high fuel economy and low emissions [4]. At present, major automobile companies are carrying out research on hybrid power unit technology, energy storage technology and vehicle integrated power electronic module. It is estimated that in the next 10 years, more than 40% of the world's newly produced vehicles will be hybrid vehicles.

The research and development of hybrid electric vehicle is of great significance to the smooth development of environmental protection engineering. Although the hybrid

* Corresponding author e-mail: ddliuwj@163.com

vehicle has been published before the 21st century, the contemporary hybrid vehicle is a brand-new machine, which is totally different from the traditional hybrid vehicle, it is not only a transport vehicle, but also a brand-new electrical equipment [5]. In the application process of hybrid electric vehicle, there are often power performance problems, which need to be diagnosed and dealt with in time to avoid unnecessary economic losses. The research of power performance fault diagnosis is the core of fault alarm. According to different signal types, fault diagnosis technology can be divided into noise diagnosis, temperature diagnosis, oil analysis, spectrum analysis, etc. In recent years, with the development of artificial intelligence technology, the automation and intelligence of fault diagnosis and early warning has gradually become a reality. For example, in literature [6], the local mean decomposition method is used to extract the feature of the fault signal of hybrid electric vehicle, determine the fault noise source, and use the discrete wavelet method to eliminate the noise and restore the fault acoustic signal of vehicle. SDP graphics technology is used to transform the acoustic signal into polar coordinates to judge whether the hybrid electric vehicle has a fault or not. The fault detection results are used to alarm the power performance of the vehicle. However, this method has the problem of long warning time, which is difficult to be widely used in practice. In literature [7], the generation mechanism, characteristics and types of DC fault arc are introduced, and three detection methods of DC fault arc in time domain, frequency domain and time frequency domain are analyzed. A simulation test system is built to obtain the normal arc and fault arc circuit signals under different loads. The time-frequency Cassie arc simulation model is established, and the current signal before and after the arc fault is reconstructed and extracted by using the 5-layer wavelet packet decomposition technology. The energy ratio is used as the characteristic parameter, and this value is taken as the basis of the fault early warning. However, the judgment of the location of the vehicle power fault by this method is not accurate, which results in the early warning results not in line with the reality.

In order to solve the problems of the above methods, this paper uses the characteristics of fault detection and analysis technology, such as long history, mature technology, early structure forming and rich data, which puts forward the fault alarm method of hybrid electric vehicle power performance based on hydraulic technology, and thus studies the structure design of fault early warning framework, fault tree knowledge and fault early warning setting, and at the same time, studies the relational database. Combined with the hydraulic technology, the fault early warning based on the hydraulic technology is realized.

2. Design of power performance fault alarm method of hybrid electric vehicle based on hydraulic technology

Due to the application of electronic technology, computer technology, information technology, automatic control technology, friction and wear technology, new technology and new materials, the hydraulic system and components have been greatly improved. In order to rationalize the design of the fault alarm method for the power performance of the hybrid electric vehicle, the composition of the power part of the hybrid electric vehicle is analyzed by using the advantages of the high power density of the hydraulic components in the hydraulic technology. The specific analysis results are as follows.

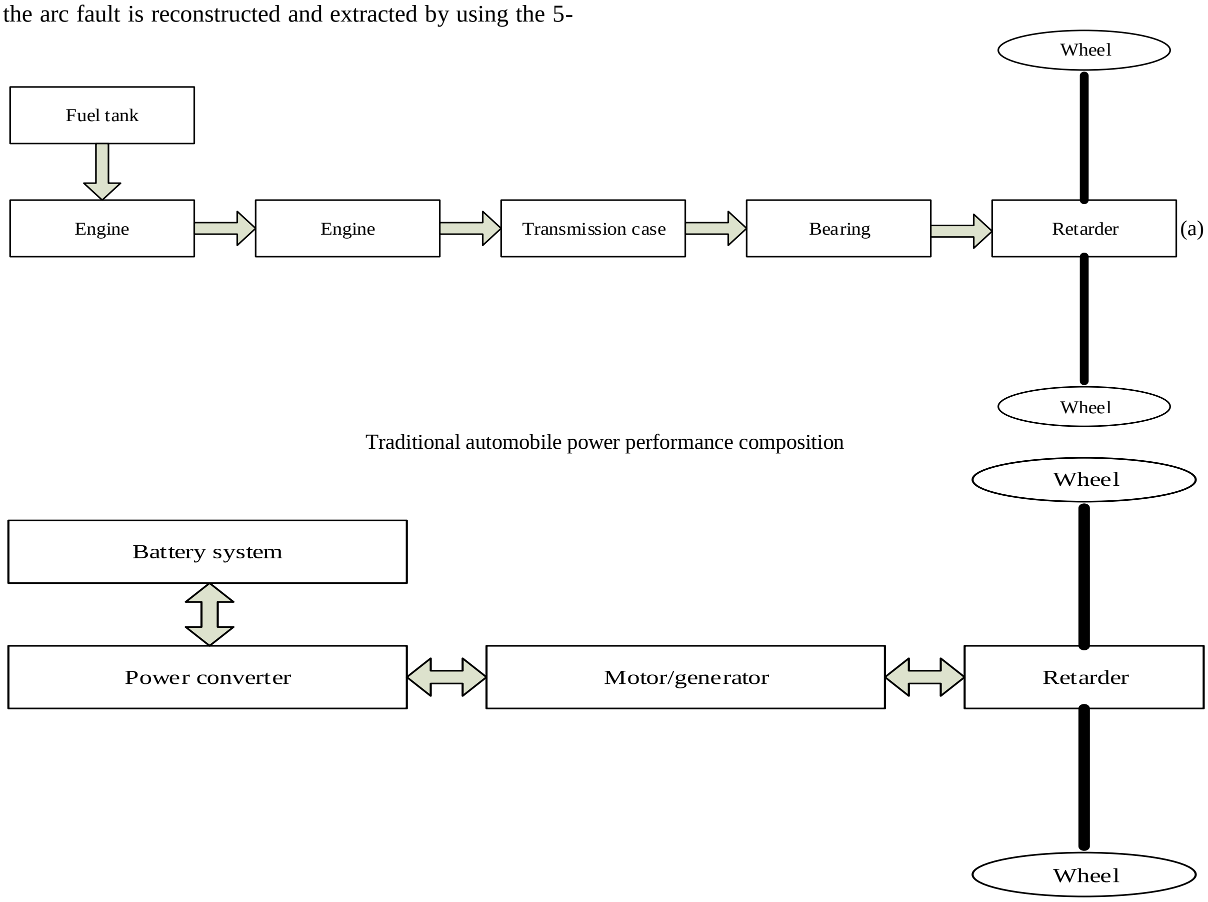

(b) Power performance composition of hybrid electric vehicle
Figure 1. Composition of vehicle power performance

Hybrid vehicle refers to a vehicle with two or more power sources, and at least one energy provides electric energy for the vehicle. According to the different types of energy, there are also many types of hybrid vehicles, such as gasoline and battery, diesel and battery, battery and fuel cell, battery and super capacitor as the power source of vehicles. Hybrid electric vehicles are considered to have both internal combustion engines and electric motors, both of which are used as driving systems.

The power system of hybrid electric vehicle is mainly composed of control system, drive system, auxiliary power system and battery pack. At the beginning of vehicle driving, the battery is in full state, its energy output can meet the requirements of vehicle, auxiliary power system does not need to work. When the battery power is less than 60%, the auxiliary power system starts: when the vehicle energy demand is large, the auxiliary power system and the battery pack provide energy for the drive system at the same time; when the vehicle energy demand is small, the auxiliary power system provides energy for the drive system and charges the battery pack at the same time.

In this paper, the vehicle driven by the mixture of internal combustion engine and electric motor is studied. As shown in Figure 1(a) is a traditional hybrid vehicle powered by diesel and fuel. Figure 1(b) is the electric drive part of the hybrid vehicle, which is the power performance part composed of generator and motor. The fault early warning method takes the above Figure 1(b) as the design basis.

2.1. Model construction of hybrid vehicle power system

According to the literature research, the hybrid vehicle uses hydraulic accumulator, hydraulic pump/motor as the power component. Taking advantage of the high-power density of the hydraulic accumulator, the hydraulic hybrid vehicle can fully recover the braking energy of the vehicle and release the energy of the amplified power in a short time [8]. The hydraulic pump/motor can work in four quadrants by changing the swashplate swing angle in the torque angle domain. It can be used to drive the vehicle under the motor condition and brake the vehicle under the pump condition. Moreover, the hydraulic pump/motor has the advantages of strong operability, high reliability and easy to change the working condition. Therefore, in this design, the hydraulic technology will be used to build the hybrid vehicle power performance model, and this model will be used as the data source of vehicle power performance fault alarm.

The displacement of hydraulic pump/motor and swashplate angle of hybrid vehicle are calculated by hydraulic technology. Because the power of the hydraulic pump/motor selected by the vehicle should be able to meet the requirement that the hydraulic power system, it can provide enough torque when the vehicle is started independently and can provide enough braking torque when the vehicle is braked. With the increase of displacement of hydraulic pump/motor, its ability to recover braking energy is greater. The driving equation of the vehicle is:

$$f(a) = f(b) + f(c) + f(d) + m_a \tag{1}$$

where: $f(a)$ is driving force of vehicle driving (N); $f(b)$ is resistance of vehicle driving slope (N); $f(c)$ is resistance of vehicle driving air (N); m_a is acceleration of vehicle driving (m/s^{-2}). The time from the start-up acceleration of the hydraulic hybrid vehicle to the uniform driving speed v is:

$$T = \frac{1}{3.6}\int_0^v \frac{m_a}{f(a) - f(c) - f(b)} dv \tag{2}$$

When the vehicle is in driving condition and the hydraulic power system is used to drive the vehicle independently, the minimum output power of the hydraulic pump/motor under the set average pressure shall be able to meet the power requirements of vehicle driving, which is expressed as:

$$Y\min = \frac{1}{3600*\beta}\left[P*f + \frac{J_d * a_m * v^2}{21.15}\right]*v_{avg} \tag{3}$$

where: $Y\min$ is the power of the hydraulic pump/motor (kW); P is the total power of the vehicle during driving; f is the kinetic energy consumption coefficient; J_d is the total mileage of the vehicle; v_{avg} is the average driving speed (km/h). When the hydraulic pump/motor operates at the maximum pressure set by the accumulator, it shall meet the power requirements of the vehicle at the maximum speed and certain climbing capacity, namely:

$$Y\max = \max(Y_1, Y_2) \tag{4}$$

$$Y1 = \frac{1}{3600*\beta}\left[P*f + \frac{J_d * a_m * v^2}{21.15}\right]*v_{\max} \tag{5}$$

$$Y2 = \frac{1}{3600*\beta}\left[P*\sin\chi + P*\cos\chi * f + \frac{J_d * a_m * v^2}{21.15}\right]*v_{slop} \tag{6}$$

where: β is the transmission efficiency from the hydraulic pump/motor to the wheel; $v_{\max}$ is the maximum speed (km/h); v_{slop} is the climbing speed (km/h); χ is the angle of climbing.

The power system model of hybrid electric vehicle consists of hydraulic pump/motor model and hydraulic accumulator model. Through the above vehicle energy calculation results, combined with hydraulic technology, the hybrid energy vehicle power system model is constructed, as follows.

After simplification, combination and linearization, the dynamic mathematical model of the electro-hydraulic servo valve can be expressed as follows [9]:

$$Q(u) = \frac{w(u)}{l(u)} = \frac{r_v}{\frac{u^2}{\delta_u^2} + \frac{2\delta u}{\delta_u^2} + 1} \tag{7}$$

where: r_v is the flow gain of servo valve; $\frac{w(u)}{l(u)}$ is the output flow of servo valve; δ_u is the natural frequency of electro-hydraulic servo valve; δ is the damping ratio of servo valve. If the frequency width of the hydraulic control system is low, the electro-hydraulic servo valve can be represented by the first order inertia link, namely:

$$\frac{w(u)}{l(u)} = r_v \tag{8}$$

The mathematical model of the motor is as follows:

$$g_i = s_i \frac{dk_i}{dt} + E_i q_i + \frac{V_i}{4\wp}\frac{dp}{dt} \tag{9}$$

where,

$$E_i = E_u + E_r \tag{10}$$

where: g_i is the flow into the high-pressure chamber of the variable cylinder; s_i is the effective working area of the variable cylinder piston; k_i is the displacement of the variable cylinder piston; E_i is the total leakage coefficient of the variable cylinder; E_u is the internal leakage coefficient of the variable cylinder; E_r is the external leakage coefficient of the variable cylinder; q_i is the pressure difference between the high-pressure chamber and the low-pressure chamber of the variable cylinder (Pa); V_i is the total volume of the two chambers of the variable cylinder; $\wp$ is the bulk elastic modulus of the oil. Through the analysis of this formula, the mathematical model of vehicle accumulator can be obtained as follows:

$$W_a = h_a - h_b = \frac{x}{S_a^2}(l_a \frac{dfa}{dt} + L_a z_a) \tag{11}$$

where: S_a is the cross-sectional area of the hydraulic accumulator oil; l_a is the mass of the liquid in the hydraulic accumulator; L_a is the viscous damping coefficient of the liquid in the hydraulic accumulator; z_a is the flow into the hydraulic accumulator; h_a is the energy generated by the power system; h_b is the energy consumed when the vehicle is braked. The flow continuity equation of accumulator is as follows:

$$q_a = -\frac{dv_j}{dt} \tag{12}$$

According to Boyle's law of thermodynamics, the power system model of hybrid electric vehicle is as follows:

$$Z = h_{a0} V_{j0}^n - h_a V_j + W(u) + g_i + W_a + q_a \tag{13}$$

where: h_{a0} and V_{j0}^n respectively represent the stable working points of the hydraulic accumulator under different constant pressure variable pump set pressure.

Through the above steps, the hybrid vehicle powertrain model is built. In the hybrid vehicle, the accumulator plays a decisive role in the power performance and braking performance of the whole vehicle. When the minimum working pressure of the accumulator is fixed, then the larger the volume is, the smaller the change range of the system pressure in the process of energy recovery is. Also, the stronger the energy recovery capacity of the system is; when the accumulator volume is fixed, the larger the inflation pressure is, the smaller the change range of the whole working pressure is when the power system provides power and recovers braking energy. In case when the volume of the accumulator is fixed, the higher the maximum working pressure of the hydraulic accumulator is, the stronger the ability of driving the vehicle independently. Also, when the maximum working pressure of the accumulator is fixed, the larger the volume is, the smaller the change range of the system pressure is, the stronger the ability of driving the vehicle independently is. Therefore, it is necessary to build the mathematical model of the accumulator accurately, so as to realize the high-precision diagnosis of the power performance fault of the hybrid electric vehicle.

2.2. Power performance fault diagnosis of hybrid electric vehicle

Using the above-mentioned mathematical model, the power composition and performance of hybrid vehicles are studied, and the self-diagnosis method is used to compare the fault diagnosis results with the rated results to complete the fault diagnosis of vehicle power performance. The self-diagnosis method uses the characteristic that the computer itself can quickly monitor the working condition of the control system and store the data. According to a certain preset program, it can automatically monitor the faults within the scope of the automobile-controlled system and store them in the form of codes in the automobile computer, so as to obtain the automobile fault information and carry out the fault diagnosis. The power performance fault diagnosis process of hybrid vehicle is shown in Figure 2.

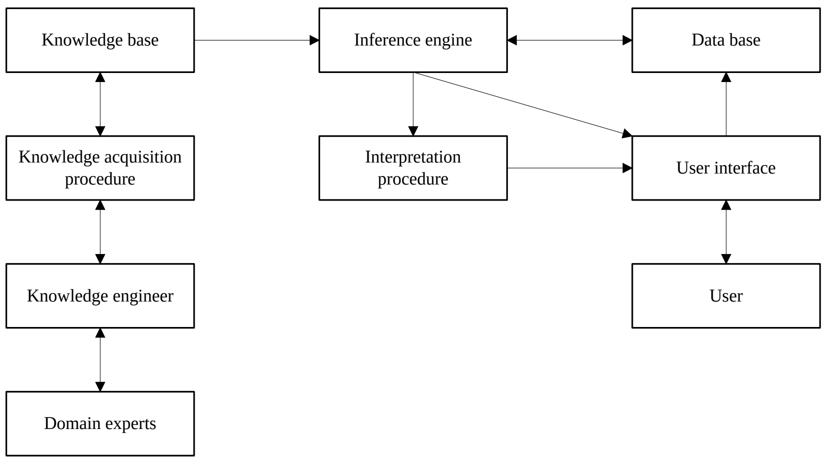

Figure 2. Diagnosis process of power performance fault of hybrid electric vehicle

Knowledge base is the core of power performance fault diagnosis of hybrid electric vehicle. Its perfection will directly affect the effect of fault diagnosis and the efficiency of fault alarm. According to prior knowledge, fault knowledge can be divided into three types: descriptive knowledge, process knowledge and control knowledge [10, 11]. Descriptive knowledge is used to describe concepts; process knowledge is used to describe the characteristics of descriptive knowledge and their relationship with each other; and control knowledge is a strategy to control and use the two types of knowledge. In the design of the fault diagnosis knowledge base, the dynamic performance faults are classified according to the causes, location, time, development of faults and possible consequences. According to the location and cause of the fault, the fault can be divided into three types: motor body fault, actuator fault and sensor fault.

Motor failure often occurs in the stator part, rotor part and bearing part of the motor body [12]. In order to monitor the fault signal, sensors are usually installed on the power components of the hybrid electric vehicle, which can collect the parameters of the power equipment during the operation of the HEV electric drive system and judge the data. In order to systematize the knowledge display of vehicle dynamic performance fault, it is set as the form of data table and stored in the diagnosis knowledge base. Among them, the classification and causes of hybrid vehicle power performance faults are shown in Table 1.

Table 1. Power performance fault table of hybrid vehicle

Fault No	Failure mode	Cause of failure
1	Damaged failure mode	Bearing wear End ring cracking Stator winding short circuit/open circuit
2	Degraded failure mode	Demagnetization of permanent magnet Aging of stator winding insulation
3	Loose fault mode	Loose stator core Loose sensor connector
4	Maladjustment failure mode	Rotor eccentricity
5	Leakage proof failure mode	Blocked/blocked cooling water Cooling water leakage
6	Other failure modes	Noise/vibration

In the research of motor fault, three kinds of faults, stator, rotor and bearing, are selected to detect and judge. Among them, stator failure includes stator core and stator winding [13, 14]. The failure of stator core may be caused by loose core or overheated temperature. The stator winding fault may be caused by turn to turn short circuit and insulation crack. There are two kinds of rotor problems: support problem and unbalance problem. Bearing fault includes vibration, high temperature and electrified. To improve the accuracy of fault diagnosis, set the fault information list of motor body as shown in Table 2.

The fault of power controller mainly occurs in the cooling process, power conversion unit and control module. The main causes of cooling failure are water pump problem and water circuit problem. The fault of the inverter includes the fault of the filter energy storage unit, the fault of the high voltage power on unit and the fault of the inverter circuit. The abnormality of control unit mainly includes additional power supply failure and sensor unit failure. The specific fault information is classified as shown in Table 3.

Table 2. List of hybrid vehicle motor fault information

Fault location	Specific failure causes	
Stator failure	Stator core	Loose core Local overheating
	stator winding	Turn to turn short circuit Insulation crack
Rotor failure	Bracket cracking out-off-balance	
Bearing failure	Vibration Over temperature Charged	

Table 3. Fault information list of hybrid vehicle power controller

Fault No	Fault type	Fault performance
1	Cooling failure	Water pump failure Waterway failure
2	Inverter unit failure	Filter energy storage unit failure High voltage power on unit failure Inverter circuit fault
3	Control unit fault	Auxiliary power failure Sensor unit failure

Through the above information list, the dynamic performance fault knowledge base is established and used to diagnose the vehicle dynamic performance fault. In addition to the above diagnosis information, the fault diagnosis problem is converted to the deviation of vehicle power state or variable characteristics within the normal range. Therefore, the failure of dynamic performance may lead to the degradation of system performance and failure. According to the time characteristics, faults can be divided into sudden faults, gradual faults and intermittent faults. The sudden fault mainly occurs suddenly and permanently (similar to step signal), which can be understood as the deviation of system signal; when the gradual fault occurs, its value starts from zero and occurs slowly at a certain speed; the intermittent fault mainly occurs when it occurs and disappears when it occurs, and its fault amplitude also changes constantly, increasing the above setting to In order to improve the reliability of vehicle power performance diagnosis, fault diagnosis knowledge base is used.

2.3. Realization of hybrid vehicle power performance fault alarm

Using the above design content, the fault diagnosis of hybrid vehicle's power performance is completed. On this basis, the fault warning of hybrid vehicle's power performance is realized.

The fault information of the vehicle is integrated into computer language, and the fault information is sent to the mobile information receiving terminal of the vehicle owner through the vehicle communication interface, and the alarm sound effect is sent out by the sound inside the vehicle. After analyzing some functions of fault alarm, the products of gntop company, the intelligent hardware supplier of vehicle network, are finally selected [15, 16]. The main control chip of the product is ELM327, which supports all communication protocols. In addition, there is a Bluetooth module, which supports Bluetooth 3.0 and has stable performance. The fault alarm implementation flow is shown in Figure 3.

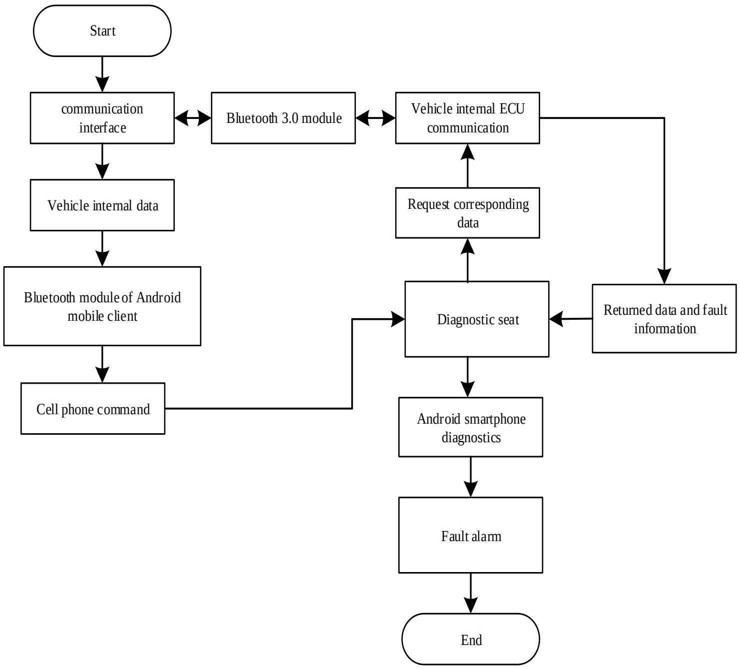

Figure 3. Realization process of fault alarm

Analysis of the above figure shows that the communication interface communicates with the vehicle internal ECU (Electronic control unit) through the Bluetooth 3.0 module and sends the acquired vehicle internal data to the Bluetooth module of the Android mobile phone client. The diagnosis seat is inserted under the dashboard on the driver's side of the cab, which is the connector for communication between the automobile ECU and the Android smartphone terminal diagnosis program. The diagnosis base receives the command from the mobile phone through the embedded Bluetooth module, sends the command to the vehicle ECU to request the corresponding data after self-analysis, then receives the data and fault information returned by the vehicle, and then sends the software to the mobile phone client through Bluetooth to realize the fault alarm.

In addition to the above design, Android client design is the most important part of the system. According to the system demand analysis, the main function modules of the client include user management, fault diagnosis, map service, intelligent early warning, value-added service, system setting, automatic upgrade, etc. In order to realize these functional modules, the client architecture is analyzed. The client can collect vehicle driving information, including vehicle speed, rotating speed, battery voltage, engine coolant temperature, power performance fault code, vehicle position, etc., and can also play the role of driving record. The diagnostic program automatically adapts and selects the communication protocol, which is saved as the default configuration after correct initialization. The program will automatically identify the power performance diagnostic base and establish the Bluetooth serial port connection. The user can choose the sensor data to be monitored by himself. After the original data is returned, it will be displayed to the user through the analysis of the diagnostic program and saved to the local storage. The program will package GPS position information, power performance fault diagnosis information, owner information, etc. and send them to the server through the network. Client architecture design is mainly to complete the purpose of layered design software modules. Firstly, the module level is designed, and then the modules are designed in detail. From the bottom up, the client app can be divided into four layers: system hardware layer, middleware layer, software function layer and software UI (user interface) layer. Set the contents of vehicle fault alarm information table as shown in Table 4.

Table 4. Alarm information

Describe	Field	Data type	Remarks
Vehicle number	carId	Bigint	Primary key
license plate number	carCode	varChar(3 0)	Not null
Vehicle color	carColor	varChar(3 0)	Not null
Vehicle type	carCype	varChar(3 0)	Not null
4S shop name	shame	varChar(3 0)	Not null
4S shop phone	sPhone	varChar(3 0)	Not null
Fault code	troubleId	Bigmt	Primary key
Fault number	troubelCode	Int	Not null
Fault type	trouble	varChar(30)	Not null
Alarm number	alarmId	Bigint	Primary key
Alarm time	alarmTime	DataTime	Not null

In the hybrid electric vehicle power performance fault alarm, Android system is introduced to complete the reading of vehicle operation parameters, vehicle location information, vehicle information, fault information, etc., and then Android Bluetooth technology is used to build a short-range wireless communication mode inside the vehicle, which is transmitted to the software platform of Android terminal, and at the same time, GPS global positioning technology is used to obtain the real-time position of the vehicle. Finally, through the communication technology, the owner information, vehicle information and vehicle fault information are sent to the remote service center, so as to realize the real-time alarm of vehicle power performance fault. So far, the design of fault alarm method of hybrid electric vehicle power performance based on hydraulic technology has been completed.

3. Method application test

In order to prove the feasibility and accuracy of the fault alarm method based on hydraulic technology, the experiment is carried out. In this test, the methods of literature [6] and literature [7] will be used to compare and test with the design methods in the paper, so as to verify the feasibility of the design methods in the paper.

3.1. Test environment

In order to ensure the authenticity and effectiveness of this test, the test object is Toyota hybrid vehicle. The specific components are as shown in Figure 4.

(a) Hybrid vehicle

(b) Test motor

(c) Test accumulator

Figure 4. Physical diagram of test hybrid vehicle powertrain

In the test process, in order to control the uniformity of its variables, the above test sample model and manufacturer are set, and the specific design results are as shown in Table 5.

Table 5. Components and parameters of test object

Component manufacturer model	Component manufacturer model	Component manufacturer model
Variable hydraulic pump/motor	Guizhou Liyuan Co., Ltd	GY-A4V40
Bladder type hydraulic accumulator	Fenghua Chaori Hydraulic Co., Ltd	NXQL16/200-A
Constant pressure variable axial piston pump	Beijing Metallurgical Hydraulic Machinery Factory	TZB63H-F-R
Oil source drive motor	Dalian electric machinery factory	JO2-82-4

Through the above parameters, the test samples in this test are composed, and the design method, literature [6] method and literature [7] method are used to compare, so as to test the application effect of the design method in the paper.

3.2. Analysis of test results

1. Accuracy rate of fault diagnosis

The accuracy rate of fault diagnosis is the basis of the power performance fault alarm of hybrid electric vehicle. Therefore, the accuracy rate of fault diagnosis of different research methods is compared, and the results are shown in Figure 5.

It can be seen from the comprehensive comparison of the three methods that the accuracy of fault diagnosis of the research method is always between 88.5% and 94.5, which is far higher than the experimental comparison method, which shows that the method can realize the accurate diagnosis of the hybrid vehicle power performance fault.

2. Troubleshooting time

The fault diagnosis time is the main factor affecting the fault alarm efficiency of the hybrid electric vehicle power performance. Therefore, the fault diagnosis time of different methods is compared, and the results are shown in Figure 6.

It can be seen from the analysis of Figure 6 that the fault diagnosis time of literature [6] method is between 0.7 s-7.0 s, and the fault diagnosis time of literature [7] method is also between 0.7 s-7.0 s. The change of the fault diagnosis time curve of the two methods is large, which shows that the performance of the two methods is not stable. Compared with the two methods, the fault diagnosis time of the proposed method is less than 0.5 s, which shows that the method can be realized for the rapid diagnosis of hybrid vehicle power performance fault.

3. Effective failure alarm rate

Effective fault alarm rate refers to the probability of early warning for these fault information after obtaining the fault location information. The comparison results are shown in Figure 7.

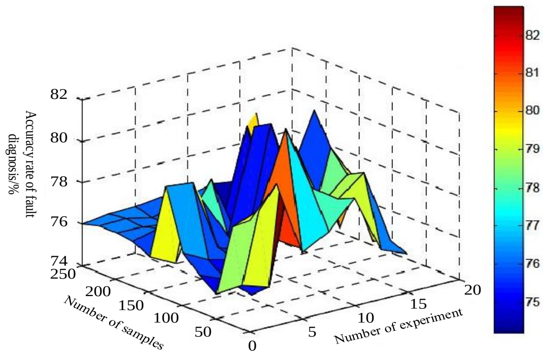

(a) Literature [6] method

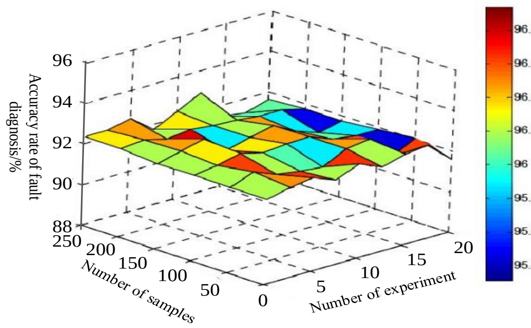

(b) Literature [7] method

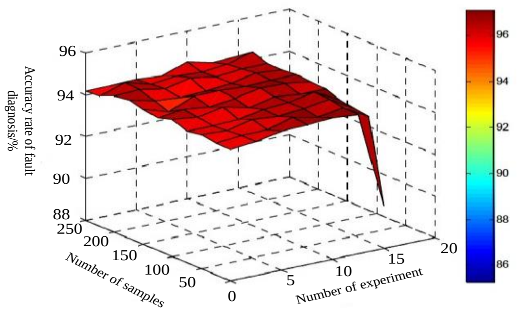

(c) Proposed method

Figure 5. Test of fault diagnosis accuracy of different methods

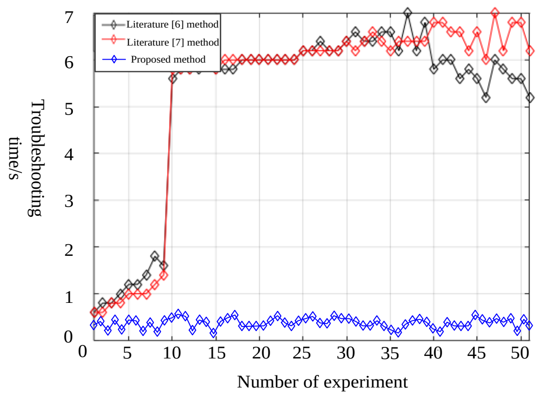

Figure 6 Fault diagnosis time test of different methods

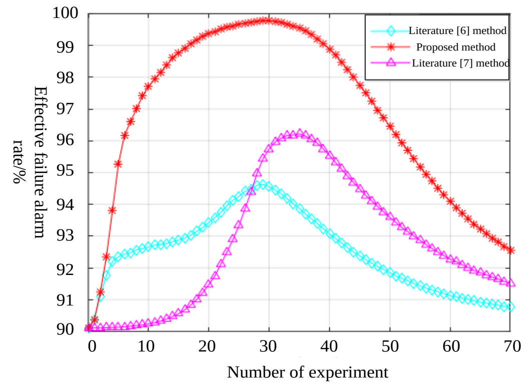

Figure 7. Effective failure alarm rate

From Figure 7, it can be seen from the test results of the above formula that there are certain differences between the proposed method and the other two methods in terms of effective fault alarm rate. The highest effective failure alarm rate of literature [6] method is 94.7%, the highest effective failure alarm rate of literature [7] method is 96.2%, the highest effective failure alarm rate of research method is 99.8%, and the effective failure alarm rate is always higher than that of literature comparison method, which shows that the performance of this method is optimal.

4. Cost comparison

Cost is a comprehensive indicator to verify the application performance of the method in this paper. Therefore, compare the cost changes of hybrid vehicles before and after the method in this paper, and the results are shown in Figure 8.

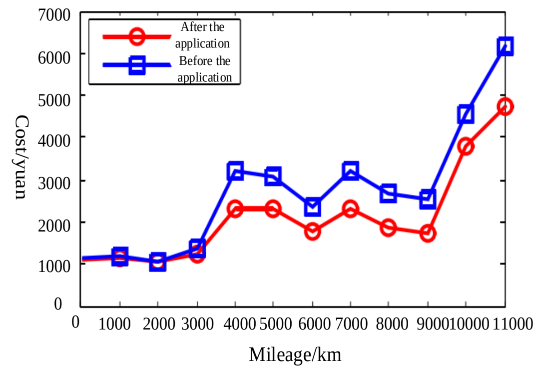

Figure 8. Cost change test

It can be seen from the analysis figure that the driving cost of hybrid electric vehicle decreases after adopting the method in this paper, which shows that the economic performance of this method is superior.

4. Conclusions

The research of fault alarm is an important part of the development process of hybrid electric vehicle. How to use more effective methods to improve the accuracy, reliability and adaptability of the fault diagnosis of hybrid electric vehicle is an important topic in the research. In this paper, the theory and method of hydraulic technology are used to deeply mine the fault diagnosis and alarm methods of vehicle. The research data at home and abroad show that there are many researches on the fault diagnosis of the drive system of the hybrid electric vehicle, but the key is to find out the fault diagnosis method suitable for the system according to the characteristics of the hybrid electric vehicle, and it is difficult to consider the practicability and feasibility of the design method. In this paper, the characteristics of the electric system of electric vehicles are studied and the advantages and disadvantages of various fault diagnosis methods are compared. A fault alarm method based on hydraulic technology for the power performance of hybrid electric vehicles is proposed. The experimental results show that compared with the traditional method, this method has the advantages of high accuracy, short diagnosis time, high effective alarm rate, low cost, superior economic performance and good application effect. Due to the limited time and level, there are still some shortcomings in this method, which should be improved in future research.

Acknowledgement

The work was funded by Liaoning province Educational science projects “Research on the effectiveness of practice teaching in higher vocational colleges based on the integration of work field and study field” (No. JG18EB087).

References

[1] Wang, Y.Q., Scott, J.M. & Suresh, G.A., et al. Power management system for a fuel cell/battery hybrid vehicle incorporating fuel cell and battery degradation. International Journal of Hydrogen Energy, 2019, 44(16), 8479-8492.

[2] Ma, H.Q. & Cao, X.X. Research on the key technologies of hydraulic new type ship lift. Water and Energy International, 2019, 61(11), 78-78.

[3] Mohamed, E.H., Ines, B.S. & Lilia, E.A. An efficient method for energy management optimization control: Minimizing fuel consumption for hybrid vehicle applications. Transactions of the Institute of Measurement and Control, 2020, 42(1), 69-80.

[4] Hüseyin, T.A. Simulation of diesel hybrid electric vehicle containing hydrogen enriched CI engine. International Journal of Hydrogen Energy, 2019, 44(20), 10139-10146.

[5] Masahiro, A., Toshihiko, N. & Yuto, M. Proposal of self-excited wound-field magnetic-modulated dual-axis motor for hybrid electric vehicle applications. IET Electric Power Applications, 2018, 12(2), 153-160.

[6] Feng, P. Fault detection simulation of left wheel brake of hybrid electric vehicle. Computer Simulation, 2018, 35(01), 121-125.

[7] Guo, L., Ke, X.B., Tang, Y.S., et al. New energy vehicle arc fault detection method and test system design. Insulating Material, 2018, 51(11), 74-79.

[8] Bae, S.H. & Park, J.W. A study on optimal operation strategy for mild hybrid electric vehicle based on hybrid energy storage system. Journal of Electrical Engineering & Technology, 2018, 13(2), 631-636.

[9] Lee, S.R., Lee, J.Y. & Jung, W.S., et al. Design and control method of ZVT interleaved bidirectional LDC for mild-hybrid electric vehicle. Journal of Electrical Engineering & Technology, 2018, 13(1), 226-239.

[10] Hahn, J.S., Lee, J.H. & Choi, K. Heterogeneous preferences of green vehicles by vehicle size: Analysis of Seoul case. International Journal of Sustainable Transportation, 2018, 12(9), 675-685.

[11] Timothy, E.L., Matthew, E. & Jeffrey, L. Hydrogen fuel cell electric vehicle performance and user-response assessment: Results of an extended driver study. International Journal of Hydrogen Energy, 2018, 43(27), 12442-12454.

[12] Zhou, X., Lu, F. & Huang, J.Q. Fault diagnosis based on measurement reconstruction of HPT exit pressure for turbofan engine. Chinese Journal of Aeronautics, 2019, 32(05), 1156-1170.

[13] Edmond, Q.W., Wang, J. & Peng, X.Y., et al. Fault diagnosis of rotating machinery using Gaussian process and EEMD-treelet. International Journal of Adaptive Control and Signal Processing, 2019, 33(1), 52-73.

[14] Liu, J.W., Li, Q. & Chen, W.R., et al. A discrete hidden Markov model fault diagnosis strategy based on K-means clustering dedicated to PEM fuel cell systems of tramways. International Journal of Hydrogen Energy, 2018, 43(27), 12428-1244.

[15] Zhang, X., Yue, S. & Zha, X.B. Method of power grid fault diagnosis using intuitionistic fuzzy Petri nets. IET Generation Transmission & Distribution, 2018, 12(2), 295-302.

[16] Ahmad, A.S., & Ahmet, K. A nonlinear torsional dynamic model of multi-mesh gear trains having flexible shafts. Jordan Journal of Mechanical and Industrial Engineering, 2007, 1(1), 31-41.

JJMIE

Volume 15, Number 1, March. 2021
ISSN 1995-6665
Pages 123 - 132

Jordan Journal of Mechanical and Industrial Engineering

Mould Pollution Control Model of Aluminum Alloy Equipment Considering Ultraviolet Radiation Intensity

Wenbo Yang[1*], Gang Li[2]

[1]General Affairs Office, Yantai Vocational College, Yantai 264670, China
[2]Department of Food and Biochemical Engineering, Yantai Vocational College, Yantai 264670, China

Received July 18 2020 Accepted March 13 2021

Abstract

Due to the particularity of the aluminum alloy equipment material, it is extremely susceptible to mold corrosion and corrosion in the case of external environmental pollution, affecting the performance of the equipment. Taking the aluminum alloy equipment contaminated by mold as the research object, the control model of mold contamination was constructed under different ultraviolet irradiation intensity. This includes separating and purifying from corrosion samples of aluminum alloy, and obtaining test culture strains, measuring the change of pH value in the corrosion medium, and then studying the growth characteristics of Aspergillus niger in pure Chagas medium. Through electrochemical testing and surface morphology analysis, the growth and corrosion behavior of mold on the surface of aluminum alloy were studied. It is essential to change the irradiation intensity and irradiation time of ultraviolet ray to study its control effect on aluminum alloy mold corrosion. The experimental results show that the sterilization effect is the most effective and economical when the UV intensity is 84000 μW/cm2 and the irradiation time is 30 min.

Keywords: Ultraviolet radiation intensity; aluminum alloy equipment; mold contamination; control model; corrosion behavior;

1. Introduction

Due to its high strength and low density, aluminum alloys are widely used in fields with strict quality and strength requirements, such as aviation, aerospace, and navigation. As a newly developed road traffic operation tool, high-speed rail often uses lightweight and high-strength 7-series aluminum alloy as the supporting material due to its high speed. As the high-speed railway technology continues to mature, the convenience of China's high-speed rail has envied the world and has developed into the first of China's “four new inventions”. Since the Industrial Revolution, the endothermic greenhouse gases and highly polluted gases such as carbon dioxide emitted by humans into the atmosphere have increased year by year, and the greenhouse effect and pollution of the atmosphere have also increased. Due to the significant differences in the global climate and environment, factors such as rain and sand during operation cause severe corrosion of key parts of the train, which seriously affects the safety and service life of high-speed trains [1]. Especially in recent years, the degree of global air pollution has been increasing, and the CO_2 content in the high-altitude atmosphere has increased significantly, which also provides sufficient favorable conditions for the growth and reproduction of mold spores, such as nitrogen and carbon sources [2]. As mold spores continue to grow and reproduce on the surface of aluminum alloy equipment, it will gradually cause different degrees of pollution and corrosion on the metal surface. For a long time, it will reduce the mechanical strength and service life of aluminum alloy equipment. Aluminum alloy equipment is inevitably exposed to the atmosphere during the operation, so the surface of the aluminum alloy equipment must be effectively protected to reduce the changes in the mechanical properties of the aluminum alloy equipment caused by mold contamination.

Ultraviolet is a general term for electromagnetic waves with a wavelength of 0.01 to 0.40 microns. According to the size of the wavelength, it can be divided into three bands: UVC also known as short-wave sterilization ultraviolet (100 to 280 nanometers), UVB also known as medium wave erythema effect ultraviolet (280 to 315 nanometers) and UVA also known as long-wave black spot effect ultraviolet (315 to 400 nanometers). Energy-saving lamps and fluorescent lamps have the same light emitting principle, and the spectrum is generated by the excitation of mercury atoms. Low-pressure mercury lamps mainly produce two kinds of ultraviolet rays with wavelengths of 254 nm and 185 nm, which can be used for air disinfection, sterilization, drinking water disinfection and photochemical reactions. The ultraviolet sterilization lamp is the same as the fluorescent lamp in construction, accessories, and wiring methods. The only difference is the construction material of the tube wall. The lamp material used in the ordinary lamp tube is ordinary glass. It is difficult for ultraviolet light to pass through. Phosphor powder emits visible light after absorption; most of the ultraviolet sterilization lamp wall uses quartz glass [3]. The principle of ultraviolet ray

* Corresponding author e-mail: yangwb163yxdz@163.com

sterilization is mainly to destroy the nucleic acid substance of the mold, causing it to fail to reproduce, destroying its protein structure, causing its functional metabolism to malfunction, and thus unable to carry out normal metabolism and causing the death of the mold. Because the effective structure of mycotoxins is protein, ultraviolet light can also cause the functional structure of mycotoxins to be destroyed, thus achieving the purpose of eliminating toxicity.

Ultraviolet rays are widely used in medicine as a new type of disinfection and sterilization method, and the results of research at home and abroad show that ultraviolet rays can be widely used in urban tap water disinfection. There are also experiments to verify that ultraviolet rays have a certain killing effect on fungi. In practical applications, the sterilization effect of ultraviolet rays mainly depends on the irradiation intensity. The irradiation intensity represents the amount of energy contained in ultraviolet rays, so the irradiation intensity can directly affect the sterilization effect of ultraviolet rays. The main reasons that affect the intensity of ultraviolet radiation are the following, such as the choice of lamp, if the quartz tube is not qualified, it is difficult to achieve a specific intensity, and the resistance of the ballast itself can also affect the intensity of irradiation [4]. Secondly, the ultraviolet sterilization effect is also affected by the irradiation distance. The irradiation effect of the ultraviolet lamp is directly related to the distance between the irradiated object and the ultraviolet lamp. The farther away from the ultraviolet lamp, the lower the irradiation intensity, and the closer the distance, the higher the irradiation intensity. And the most important point that affects the ultraviolet sterilization effect is the irradiation time. The length of the irradiation time will also have a huge impact on the irradiation effect. Finally, the influence of the irradiation environment, the temperature and environmental factors have a great impact on the irradiation effect. Generally, the lower the irradiation temperature is, the worse the sterilization effect of ultraviolet irradiation is. Increasing the irradiation temperature will improve the irradiation effect. According to the data of UV sterilization research, use UV to remove the mycotoxins from the aluminum alloy equipment, which provides a theoretical basis for the control of mold pollution in the aluminum alloy equipment.

2. Factors affecting mould contamination of aluminum alloy equipment

Environmental pollution is one of the important reasons that cause aluminum alloy equipment to be susceptible to mold corrosion. The discharge of the three wastes from industrial enterprises leads to the problems of high carbon emissions and pollution of river water bodies, which significantly increases the content of carbon dioxide and other acidic substances in the atmospheric cycle, and provides sufficient conditions for the growth and reproduction of mold [5]. Lightweight aluminum alloy equipment itself has poor corrosion resistance. The presence of microorganisms on the metal surface is usually not valued by the crew inspection personnel. Mold contamination and corrosion are subtly affecting the strength, life and mechanical properties of aluminum alloy equipment. Before conducting relevant mold pollution control experiments, it is necessary to analyze the influence of various external environmental factors on the formation of mold corrosion of aluminum alloy equipment, which helps to ensure the objectivity and authenticity of the subsequent research results. Factors such as atmospheric pollution, corrosion of aqueous solutions, various types of organic media, ambient temperature, and stress on the metal equipment itself will have an important impact on the mold contamination behavior of aluminum alloy equipment. See Figure 1 below:

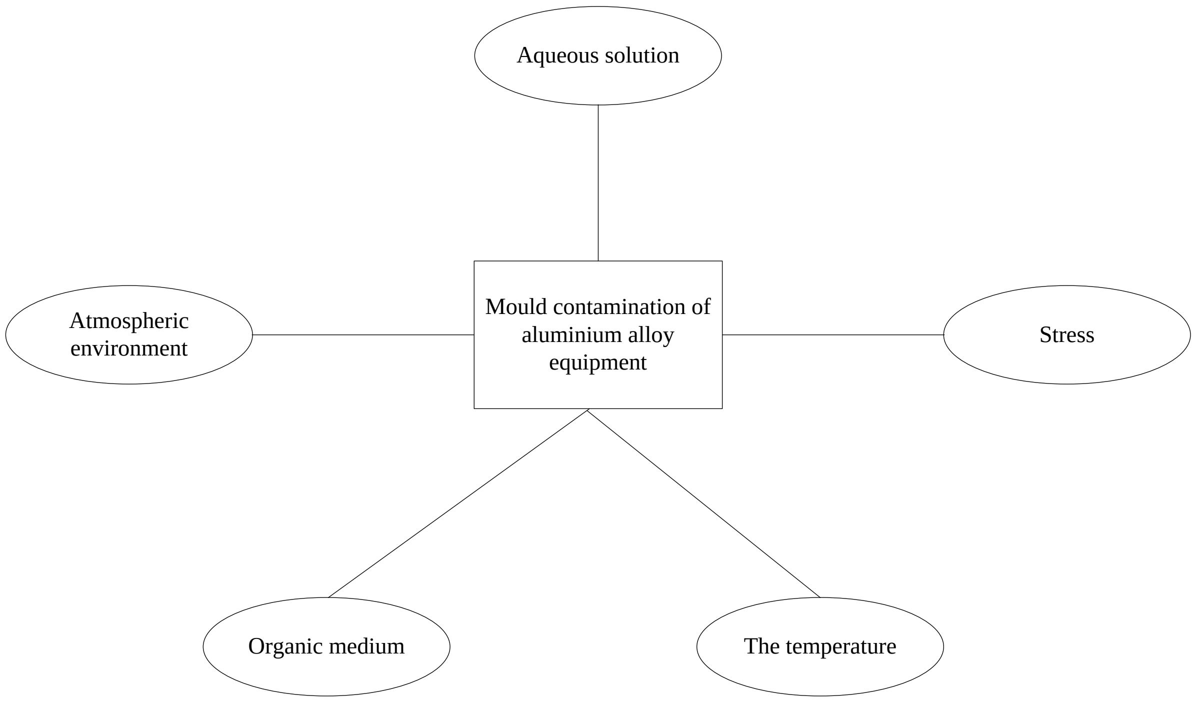

Figure 1. Various environmental factors affecting mold contamination of aluminum alloy equipment

O_2 in the atmosphere will not have a beneficial effect on the mold corrosion of aluminum alloy equipment, but with the increase of air pollution, the content of CO_2 and other acidic substances and nitrogen oxides in the air increase, which is the mold spores attached to the metal equipment providing a favorable food source and an appropriate living environment. In a relatively humid atmospheric environment, the acidic substances produced by the combination of CO_2 and nitrogen oxides with water will also cause certain corrosion effects on aluminum alloy equipment [6]. Some aluminum alloy equipment or depressions will contain some acidic substances, chlorides and fluorides, which will not only cause a certain degree of corrosion to the aluminum alloy equipment itself, but the volatilization of organic matter will also cause pollution and corrosion to other aluminum alloy equipment. Aluminum alloy equipment that has been corroded and contaminated by chemical substances is more susceptible to microbial attack, accelerating the rate of damage to the surface coating of aluminum alloy equipment. Lipid carbon oxides in the atmosphere and in the equipment are prone to form acidic hydrolysates, which are strongly polluting and corrosive. These materials provide convenient conditions for the survival and reproduction of mold spores, and constitute double pollution for aluminum alloy equipment. And destruction, long-term reduction of the mechanical strength and mechanical properties of aluminum alloy equipment [7]. The temperature change of the outside of the aluminum alloy equipment and the ambient temperature and the atmospheric stress are also one of the important causes of mold contamination and corrosion on the surface of the aluminum alloy. The temperature change of the aluminum alloy equipment before and after the work is large, and the severe temperature difference will make the surface of the aluminum alloy equipment. The organizational structure of the aluminum alloy has changed, and the mold attached to the surface of the aluminum alloy equipment will use this structural change to accelerate the pollution and erosion of the aluminum alloy equipment surface. The results of surface corrosion morphology and elemental analysis of aluminum alloy equipment are shown in Figure 2.

There are many kinds of molds, and the growth and reproduction are rapid. They can promote their own growth by degrading various organic substances. The organic acids in the metabolites can cause a certain degree of damage to metals, non-metals, and coatings. A large number of reports show that molds have been detected in the corrosion products of carbon fiber metal materials used in outer space, aircraft fuel tanks, and aluminum alloy materials for ships, and mold corrosion has become one of the major safety hazards in the engineering field [8]. In order to provide theoretical support and technical guidance to engineering safety, it is of great significance to systematically study the mold corrosion mechanism and protection technology.

3. Materials and methods

As the research methods and mechanisms of microbial corrosion have matured and formed a system, the problem of mold corrosion has gradually become more prominent. The current evaluation methods for mold corrosion mainly investigate the tolerance of aluminum alloy materials to mold in the mold environment by simulating the mold growth environment. According to the different materials and equipment use environment, the commonly used test standards in China are military equipment environment, military communication equipment environment, civil aircraft loading environment, ship electronic equipment environment and electrical and electronic product environment. The damage caused by molds to materials is divided into two situations, directly eroding the material and decomposing the material as their own nutrients, resulting in the deterioration of the physical properties of the material and direct or indirect corrosion and degradation of the bottom layer and surrounding materials through their own metabolism. For electronic devices, they can also be used in components and the formation of a biological bridge between them can cause circuit failure [9, 10]. Comprehensive mold testing standards for multiple environments, the impact of mold on materials is divided into five levels, as shown in Table 1:

Table 1. Classification of the degree of mold influence

Degree of mold	Coverage area	Level	Mold growth
Not moldy	0	1	No mold
Trace mold	1~10%	2	Scattered and rare mould on the surface
Mildly moldy	11-30%	3	Mycelium distribution on the surface, not covered with culture medium
Mildewed medium	31-70%	4	There are a lot of mould on the surface, and the properties of the material change
Serious mildew	71-100%	5	Mould grows on the surface with a certain thickness and the material deteriorates rapidly

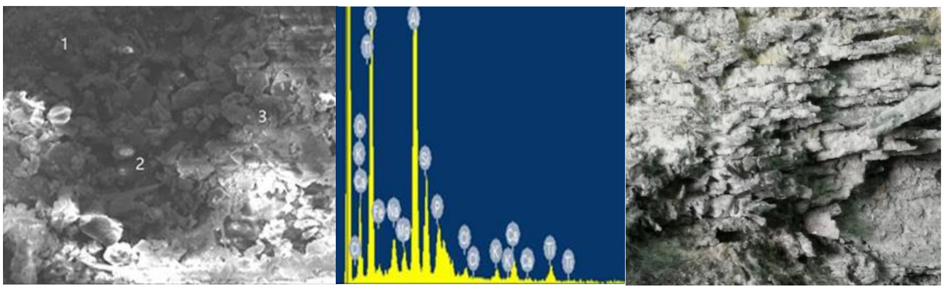

Figure 2. Corrosion morphology and element analysis of aluminum alloy equipment surface

In the mold test, in order to simulate the mold growth environment, the mold species were directly inoculated on the sample, hung in the mold experiment box, and cultivated for at least 14h to detect changes in the material structure and performance. In the determination of mold environmental test results, the naked eye and magnifying glass are often used to observe the growth of mold and the macroscopic changes of materials [11-13]. In laboratory research, the method of mold corrosion research is similar to that of bacterial corrosion. The corrosion mechanism is analyzed by surface morphology analysis and electrochemical testing technology.

3.1. Experimental materials

3.1.1. Experimental reagents and drugs

The main drugs used are shown in the Table 2:

Table 2. Experimental drugs and reagents

Drug name	Purity	Manufacturer
Sodium chloride	AR	Sino pharm Chemical Reagent Co., Ltd
Potassium chloride	AR	Sino pharm Chemical Reagent Co., Ltd
Dipotassium phosphate	AR	Sino pharm Chemical Reagent Co., Ltd
Sodium nitrate	AR	Sino pharm Chemical Reagent Co., Ltd
Magnesium sulfate	AR	Sino pharm Chemical Reagent Co., Ltd
Sucrose	AR	Sino pharm Chemical Reagent Co., Ltd
Agar	AR	Beijing aoboxing Biotechnology Co., Ltd
Epoxy resin	AR	Feicheng Deyuan Chemical Co., Ltd
Absolute ethanol	AR	Sino pharm Chemical Reagent Co., Ltd
Acetone	AR	Sino pharm Chemical Reagent Co., Ltd
Glutaraldehyde 25% solution	AR	Tianjin kemio Chemical Reagent Co., Ltd
Pickling solution	-	Wuhan huakete New Technology Co., Ltd
Caustic lotion	-	Wuhan huakete New Technology Co., Ltd

3.1.2. Laboratory equipment

The main instruments and equipment used in this experiment are shown in Table 3:

Table 3. Experimental instruments

Equipment name	Model	Manufacturer
Electrochemical workstation	CS350	Wuhan Kesite Instrument Co., Ltd
Electronic balance	BS224S	Sartorius, sartorius, Germany
Electronic analytical balance	AL 104	Mettler-Toledoinstr(shanghai)Ltd
pH meter	PHS-3C	Shanghai Precision Scientific Instrument Co., Ltd
Portable pressure steam sterilizer	CMSX-280	Beijing Yongguang medical instrument factory
Constant temperature and water-proof incubator	GH4500	Tianjin taist Instrument Co., Ltd
Ultraviolet lamp	Philips TUV 64 T5 HO 4P-SEA	-

Ultraviolet irradiation device: three 30W ultraviolet sterilization lamps are hung on the upper part of the ultraviolet sterilization chamber, the wavelength is 254 nm, and the ultraviolet irradiation intensity at 20 cm below the lamp tube is 5mW/cm^2 [14]. The inside of the sterilization chamber is covered with aluminum foil to reflect ultraviolet rays and prevent energy from leaking out of the chamber. Before UV irradiation, the UV lamp is preheated for 30 min to ensure the stability of the irradiation. When the UV illuminance meter (calibrated at 254 nm) is placed at the target position, the UV irradiation intensity can be measured there, and the UV irradiation dose can be changed by changing the irradiation time.

3.1.3. Experimental materials and experimental equipment

The material used in this experiment is made of 7075 aluminum alloy sheets. The mass fraction of each component is: Si: 0.4%, Fe: 0.5%, Cu: 1.2-2.0%, Mn: 0.3%; Mg: 2.1-2.9 %; Cr: 0.18-0.28%; Zn5.1-6.1%; Ti: 0.2%; Al: balance. Electrochemical test electrodes and morphological characterization samples are all cut with a size of 10mm×10mm×3mm. The electrode is soldered to the copper wire by soldering. The electrode and the test piece are encapsulated with black epoxy resin. The working surface size 10 mm×10 mm, all electrodes and test pieces are polished with 180, 600, and 1200 mesh sandpaper before use, washed with water and absolute ethanol and dried, then stored in a desiccator. Use absolute ethanol and acetone cotton balls when using wipe to remove oil and impurities on the surface [15, 16]. The experiment uses micro-arc oxidation test pieces for the samples with an oxide layer thickness of 20 μm and 60 μm. Similarly, the copper wire is welded, and the black epoxy package is used to retain a working surface. High temperature steam sterilization before the experiment to prevent the introduction of other bacteria Species of bacteria or fungi.

The main strain that causes mildew in aluminum alloy equipment is Aspergillus niger. According to the literature, when the irradiation intensity is 350 μW/cm^2 and the irradiation time reaches 30 minutes, the killing rate of Aspergillus niger strain can reach 97%. The irradiation distance is 1.5 m, because the device should be applied on the conveyor belt, and the conveyor speed is 0.2 m/s. According to the calculation, the irradiation time needs to be 7.5 seconds. According to the irradiation effect, the irradiation intensity is multiplied by the irradiation intensity. It is known from time that the required irradiation intensity is 84000 μW/cm^2. Ultraviolet lamps with such high irradiation intensity are relatively rare and the cost of use is high, so alternative measures are needed. According to an article published in the Chinese Journal of Disinfection [17, 18], the ultraviolet sterilization intensity has the following relationship with distance:

$$E = \frac{97.72}{L^{1.828}} \tag{1}$$

In the above formula, E is ultraviolet intensity, L is the distance from the ultraviolet lamp. This formula is derived under the irradiation condition of an ultraviolet lamp with a power of 30 W and a standard irradiation intensity of 100 μW/cm^2. If the UV lamp is hung at a distance of 10 cm from the sample, the irradiation intensity is about 6515 μW/cm^2. If the power is changed to 150 W for standard UV lamps with a radiation intensity of 440 μW/cm^2, the illumination intensity at 10 cm should be approximately 28665 μW/cm^2. At this time, if three lamps are used for simultaneous illumination, the 84000 μW/cm^2 radiation intensity required for the calculation can be met. The designed irradiation device is shown in Figure 3:

The transmission speed of a general conveyor belt is 0.2 m/s, and the distance of 7.5 seconds for a simulated conveyor belt transmission is 1.5 m. The above irradiation device is set, and cardboard is arranged around it to isolate ultraviolet rays. The main material used for the irradiation device is a thin plastic plate, and then use wide tape to make a hard box with a length of 150 cm, a width of 100 cm, and a height of 12 cm, and then install an ultraviolet lamp. The three lamps are distributed according to one lamp every 25 cm, the installation position of the lamp is at the position of 10, so that the designed purpose can be achieved.

3.2. Fabrication and identification of mold medium

3.2.1. Making medium

The mold medium used in the experiment was Cha's medium. The medium composition was: $NaNO_3$ content 3 g/L, KCl content 0.5 g/L, $MgSO_4 \cdot 7H_2O$ content 0.5 g/L, K_2HPO_4 content 1 g/L, $FeSO_4$ content It is 0.01 g/L, sucrose content is 30 g/L, and agar content is 20 g/L. The medium used in each experiment is now used. The prepared culture medium, culture dish, ten 10 mL colorimetric tubes and 150 mL distilled water are sterilized under high temperature and high pressure. The process is as follows: open the sterilization pot, adjust the voltage to 225 V, wait for the water in the pot to boil and close the air valve until the pressure in the pot reaches 1.5 MPa, the temperature is 120°C, adjust the voltage to 115 V, keep the temperature in the pot between 121°C-126°C for 15 to 20 min, then cut off the power supply and wait for the pot to boil When the internal pressure drops to 0 MPa, open the air valve, wait until the temperature drops to room temperature, and then place the reagent on the sterilization test bench. Take 30 mL of sterilized culture medium and pour it into the culture dish respectively, place it under the ultraviolet lamp for cooling, dilute the spore content of the bacteria with distilled water to 10^6/mL, inoculate it into the culture dish with agar culture medium, place it in the 28°C incubator for culture, and use it after 2 h.

There are two kinds of test media used in this experiment, one is pure agar-free medium without adding bacteria, and the other is agar-free medium inoculated with bacteria at a volume ratio of 2%. Take a small piece of bacteria on the petri dish after dilution, dilute it with distilled water to a spore content of 10^6/mL and inoculate it into the test medium. All glassware used is sterilized by the above method. The electrodes and salt bridges used are sterilized under an ultraviolet lamp for 30 minutes before use, and the laboratory operation room is sterilized with an ultraviolet sterilization lamp for 30 minutes before use.

3.2.2. Mold identification

The Aspergillus niger used in this experiment was taken from moldy food, and the corrosion samples of aluminum alloy were continuously separated and purified in the medium until a single mold colony appeared in the medium, as shown in Figure 4.

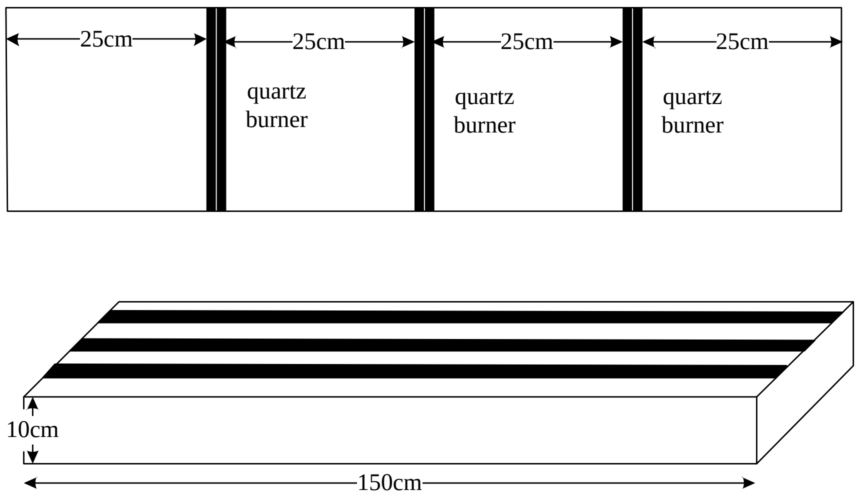

Figure 3. UV irradiation device.

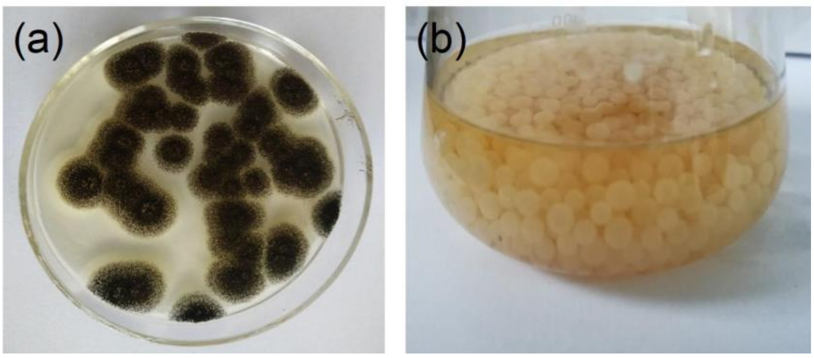

Figure 4. The isolated and purified mold colonies.

Fig. 4 (a) is the mold colony on the solid medium, and Fig. 4 (b) is the mold pellet formed by shaking culture in the liquid medium, and the PCR method was used to identify Aspergillus niger. Inoculate a single colony of Aspergillus niger onto the liquid culture medium and place it on a shaker for shaking culture. The temperature in the shaker is 30°C and the rotation speed is 150-180 r/min. After shaking culture for 2 h, due to the uniform winding of Aspergillus niger, the shape of the colony of Aspergillus niger in the liquid culture medium is crystal clear and spherical. Filter with double-layer filter paper. After the pellets of Aspergillus niger are slightly dry, store them in -20°C in the refrigerator. The pre-processing steps before doing PCR are as follows:

1. Grind the pellets of Aspergillus niger frozen at -20°C in liquid nitrogen to a fine powder, divide the powdered Aspergillus niger into 1.5 m1 centrifuge tubes, 100 mg per tube, add 0.6 mL DNA extract Draw buffer, water bath at 65°C for 30-35 min.
2. Place the centrifuge tube in a centrifuge at 12000 r/min at 4°C for 10 minutes, take the supernatant and transfer to a new 1.5 m1 centrifuge tube.
3. Add an equal volume of extract (phenol: chloroform: isoamyl alcohol=25: 24: 1) to the supernatant in the centrifuge tube and invert gently 5-7 times.
4. Add 1/10 volume of 3 mol/L sodium acetate solution and 0.6 times volume of isopropanol, gently invert 5-7 times, and let stand at -20°C for 30 min.
5. Centrifuge at 12000 r/min for 5 min at 4°C. Discard the supernatant and add 200 gL of TE buffer to dissolve the precipitate. TE buffer is mainly used to dissolve nucleic acids and store DNA and RNA stably.
6. Add 1 μL of ribonuclease (RNase A), RNase A can hydrolyze RNA, but it has no effect on DNA. Able to get DNA sequence. Compared with the standard gene library, the mold used in this experiment was Aspergillus niger.

3.3. Electrochemical test

The electrochemical test was carried out in pure agar medium. In this experiment, a three-electrode system was used, with 7075 aluminum alloy as the working electrode, a saturated calomel electrode as the reference electrode, and a platinum electrode as the counter electrode. The CS350 electrochemical workstation was used for open circuit potential. Electrochemical impedance and polarization curve test.

Because mold is an oxygen-consuming microorganism, in the liquid environment, it will grow on the surface of the liquid. When assembling the test device, place the electrode working surface close to the liquid surface. The open circuit potential (Open Circuit Potential, OCP) each test time is 15min, record the relationship between the potential of the working electrode and the reference electrode with time.

Electrochemical impedance (Electrochemical impedance spectroscopy, EIS) is a very important method in corrosion testing. During the detection, a small amplitude sinusoidal potential current is applied, which is basically non-destructive to the corrosion product film and the surface of the material. According to the impedance diagram, some dynamics of corrosion can be obtained Parameters, and be able to reason about corrosion dynamics and establish a reasonable equivalent circuit diagram. In this experiment, a 10 mV AC disturbance voltage was applied to the working electrode, the scan frequency range was 10^4 Hz-10^{-2} Hz, and the test was performed at room temperature. The physical picture is shown in Figure 5:

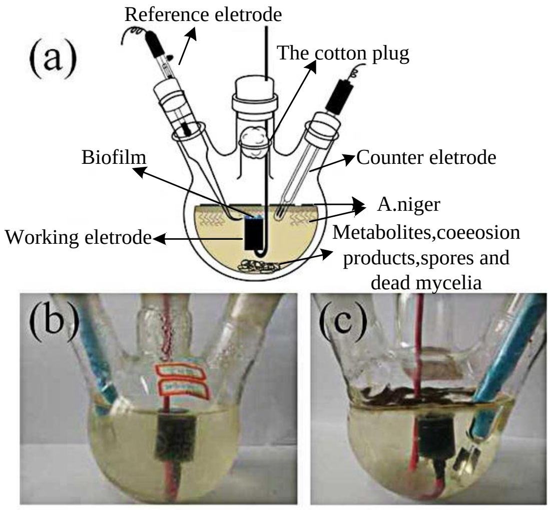

Figure 5. Electrochemical device diagram.

In the above figure, Fig. 5 (a) is a simulation figure, Fig. 5 (b) is a device without mold, and Fig. 5 (c) is a device with mold added. All the electrochemical tests in this experiment were carried out at Coster Electrochemical Workstation (CS350). The open circuit potential is the self-corrosion potential, which can reflect the change of the corrosion state of the material surface. In the study of microbial corrosion, the formation, destruction or shedding of biofilms can be preliminarily judged based on the change in open circuit potential. However, the strength of the material corrosion cannot be judged solely by the change in open circuit potential. It can only be used as an auxiliary information. It should be combined with other analytical methods to analyze the electrochemical process of microbial corrosion. Electrochemical impedance (Electrochemical impedance spectroscopy, EIS) is a conventional electrochemical test method for corrosion research. Applying a small amplitude AC signal (10 mv) to the system during the test will not change the surface state of the working electrode. The same working electrode can be continuously monitored, and the corrosion can be judged according to the change in the size and shape of the impedance arc. Time trends. EIS is measured at a stable open circuit potential with a frequency range of 10^5 Hz to 10^{-2} Hz. The electrochemical impedance data was fitted using Zview2 software (Scribner Inc). Polarization curves (Potential dynamic polarization curves) are also measured at a stable open circuit potential. The scanning range set in this experiment is one 200 mv to 300 mv, and the scanning speed is 0.5 mv/s. The polarization curve was fitted by Cview2 software (Scribner Inc).

4. Results and discussion

4.1. Mold growth test

In order to improve the mechanical properties of 7075 aluminum alloy metal materials, other added metal components, such as Cu, Zn, Mg, Si, etc. combine with A1 to form an intergranular phase. During the corrosion process, as the metal elements are eluted, the physical and chemical properties of the material surface change the unevenness to make the material prone to corrosion. A large number of studies have shown that metal oxides such as nano-ZnO, CuO and AgaO can affect the growth state of microorganisms, and are widely used in biomedical biomimetic materials, daily skin care products and antibacterial materials. Trace elements such as iron, silicon, zinc, copper, iodine, selenium, and manganese can affect the growth of microorganisms. The 7075 aluminum alloy selected for the experiment contains three metal ions, Cu^{2+}, Zu^{2+}, and Mg^{2+}. Aspergillus niger is a fungal microorganism that metabolizes a large amount of organic substances containing hydroxyl, carboxyl, and amine groups during life cycle activities. Organic acids are dissolved into the medium, resulting in changes in the pH value of the environment. By recording the changes in the pH value of the medium during the test, the growth of Aspergillus niger in pure Cha's medium for 7 h can be investigated. As shown in Figure 6:

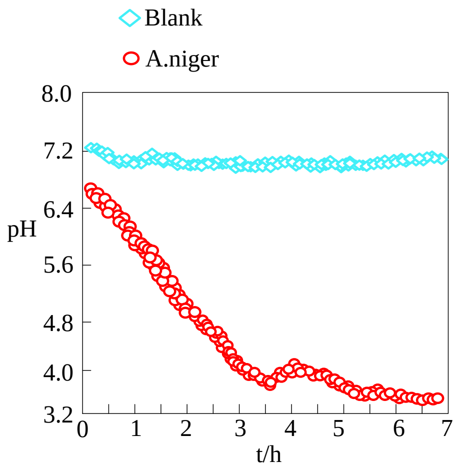

Figure 6. PH value of the test system in 7 h.

In the blank group, the pH value of the medium is basically unchanged, and is maintained at about 7.2. In the culture medium added with bacteria, the pH value decreased significantly, the rate of decrease increased after 1 h, the pH value was only 3.8 on the 3 h, and remained stable after a slight decrease on the 3.5 h, indicating that the fungus was in the medium and 28°C after the 1 h. It grows rapidly and secretes a large amount of organic acids. On the 3 h, it reaches a stable growth period. The growth and mortality of molds reach a balance, and the number of molds in the medium reaches the maximum. According to the change trend of pH value, Aspergillus niger grew in pure medium for 3 h and reached a stable growth period. Therefore, the growth morphology of the 7075 aluminum alloy surface after inoculated with mold for 1, 2, and 3 h is recorded in the form of a picture, as follows in Figure 7:

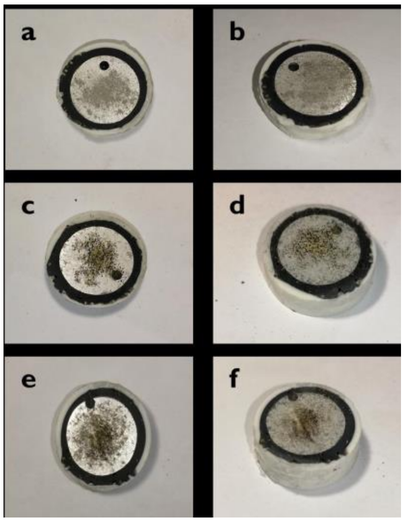

Figure 7. The growth of mold on the surface of aluminum alloy.

In the above figure, figures a and b show the growth of mold on the aluminum alloy surface for 1 h, figures c and d show the growth of mold on the aluminum alloy surface for 2 h, and figures e and f show the growth of mold on the aluminum alloy surface for 3 h. As can be seen from the above figure, on the 1 h, the mold can be evenly distributed on the surface of the aluminum alloy, and there are only a small number of conidia on the mycelium. On the 2 h, the conidia of the mycelia increase significantly, and the spores start to multiply, and they continue to conid mycelium to achieve a period of rapid growth, and by the 3 h the spores are also basically evenly distributed on the surface of the aluminum alloy. The results in the figure intuitively prove that Aspergillus niger can grow and reproduce rapidly under the conditions allowed by environmental nutrition, thereby affecting the surface structure of the aluminum alloy through life activities. The microscopic appearance of molds growing on different hours is shown in Figure 8:

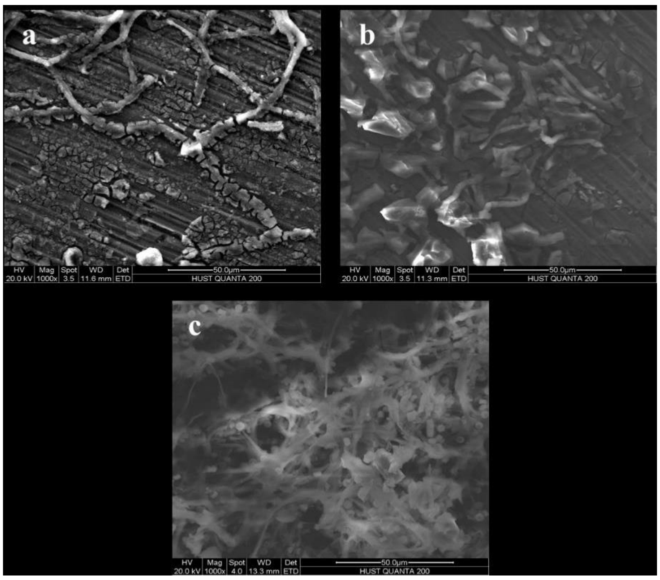

Figure 8. SEM image of mold on aluminum alloy surface.

In the above figure, a is the microscopic morphology of Aspergillus niger attached to the surface of the aluminum alloy for 1 h. There are accumulations of corrosion products on the surface of the aluminum alloy, which are distributed along the direction of mycelial growth and present a branched structure. Picture b is the surface microscopic morphology of the fungus growing for 2 h. The distribution of corrosion products is similar to the distribution in picture a, but scattered spores are distributed around the corrosion products. The results are the same as in the macro picture. To increase the growth rate. The mold grows on the surface of the aluminum alloy for 3 h. As shown in Figure c, the mycelium contains many spores distributed in it, and the mycelia and corrosion products intersect and accumulate on the surface of the aluminum alloy.

4.2. Study on the control law of ultraviolet radiation intensity on mold

Ultraviolet radiation is an effective method to control the corrosion of microorganisms. It can destroy the life activities of microorganisms or prevent the microorganisms from contacting with the matrix material by ultraviolet rays to inhibit the damage caused by the microorganisms to the matrix material. Ultraviolet rays can effectively inhibit the growth of fungi. In this section, three effective ultraviolet irradiation intensities will be selected for comparison. After 30 minutes of irradiation, the application effect of ultraviolet rays in mold corrosion will be studied. The open circuit potential of aluminum alloy in the mold medium with three different ultraviolet irradiation intensities is shown in Figure 9.

Except for the blank group that has not been irradiated with ultraviolet rays, the open circuit potential of other ultraviolet irradiation systems is relatively stable. The open circuit potential of the lowest ultraviolet intensity of 40,000 μW/cm^2 showed a negative trend shift with little tendency on the 1 h and 1.5 h, and a stable positive shift in the later period. It remained stable afterwards; the open circuit potential of 60,000 μW/cm^2 did not change, and remained basically stable; the open circuit potential of 84000 μW/cm^2 intensity continued to rise and remained stable, indicating that the stability of the oxide film on the aluminum alloy surface after UV irradiation can be improved. Which can effectively protect the aluminum alloy from corrosion caused by mold.

In addition, to further verify the effectiveness of using ultraviolet rays to remove mycotoxins in aluminum alloy equipment, the method in this paper and the method in literature [1] were used to carry out the inactivation test of mold spores under the same length of time. The comparison results are shown in Figure 10.

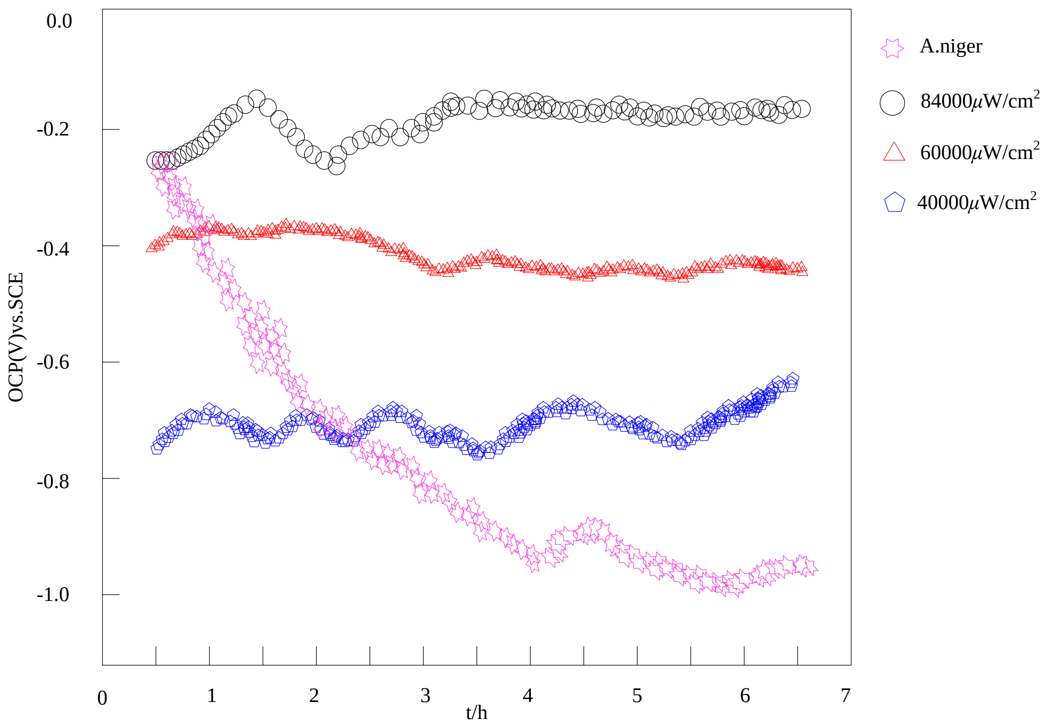

Figure 9. Open circuit potential of aluminum alloy under different ultraviolet irradiation intensity.

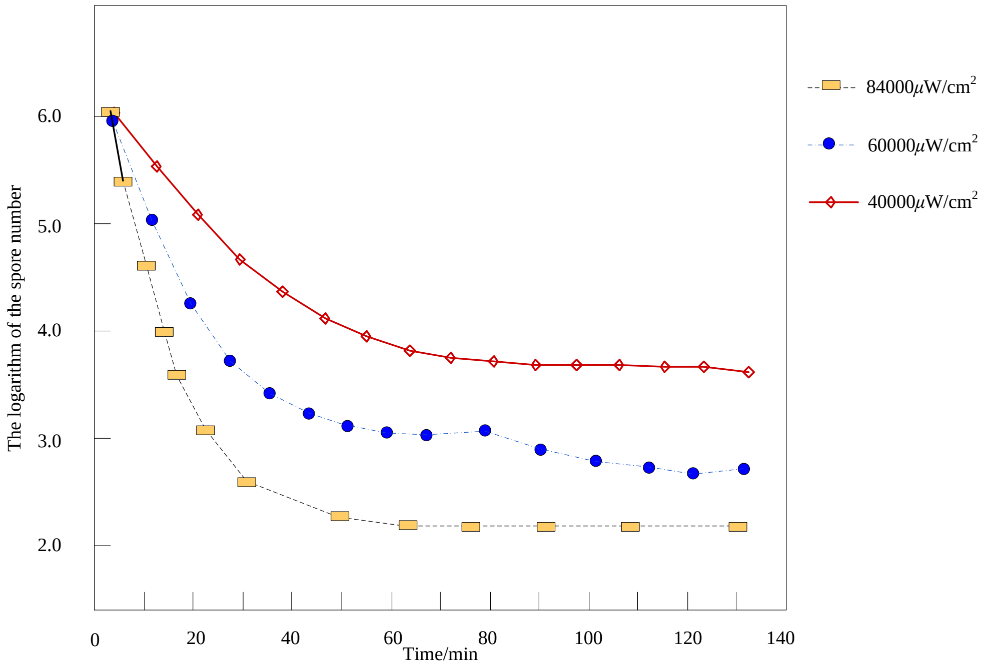

(a)The results of inactivation of mold spores in this method

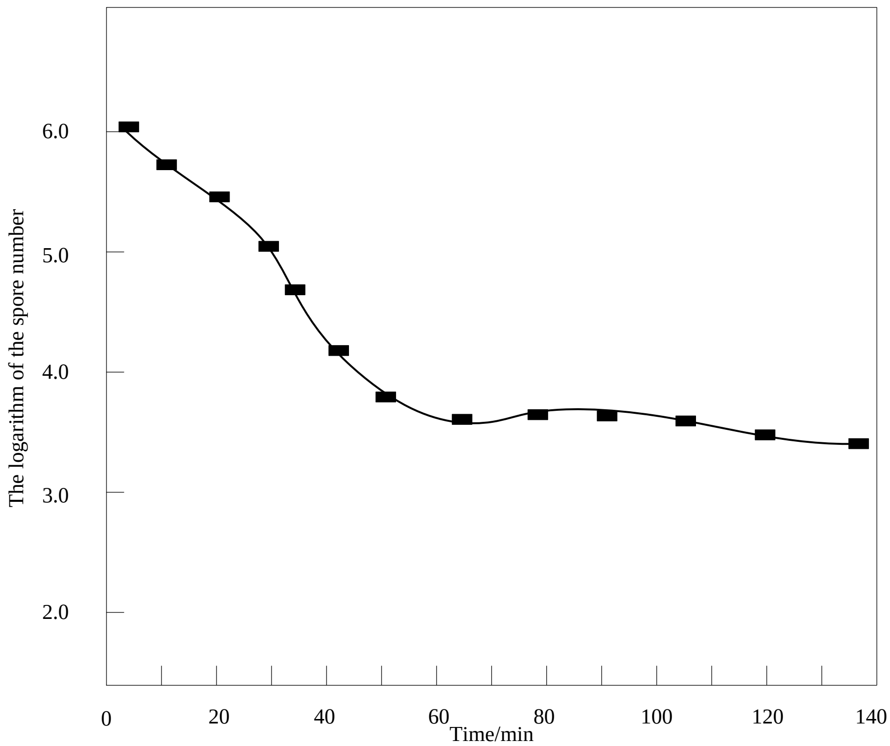

(b)The results of inactivation of mold spores under the method of literature [1]

Figure 10. Comparison results of inactivation of mold spores

Analyzing Figure 10(a), we can see that in the case where the ultraviolet irradiation intensity is 84000 μW/cm^2, the logarithm of the spore number tends to be stable after about 30 minutes of irradiation. Considering energy saving and other aspects, it is concluded that when sterilizing aluminum alloy equipment under ultraviolet irradiation, the irradiation intensity can be selected to be 84000 μW/cm^2 and the irradiation time is 30min. The sterilization effect is the most effective and economical. Analysis of Figure 10(b) shows that the method in literature [1] has a poor bactericidal effect on mold spores. The logarithm of the number of spores stabilizes when the experimental time reaches 50 minutes, and its bactericidal effect is significantly lower than that of the method in this paper.

5. Conclusion

In this paper, combined with electrochemical testing, surface morphology and composition analysis, the corrosion behavior of Aspergillus niger on the surface of aluminum alloy was studied, and the corrosion protection performance of mold on the surface of aluminum alloy under different ultraviolet irradiation intensity was explored. It is concluded that considering energy saving and other aspects, when sterilizing aluminum alloy equipment by ultraviolet irradiation, the irradiation intensity is $84000\mu W/cm^2$ and the irradiation time is 30min. The sterilization effect is the most effective and economical.

References

[1] Zhou W., Zhang Z.G. (2019). Analysis on Corrosion Effect of Mold Pollution on Aviation Aluminum Alloy Equipment. Environmental Science and Management, 44(1):87-92.

[2] Chen G.J., Wang H.Q., Chen Y.M., et al. (2019). Contrastive Study on Indoor Temperature-humidity Threshold Value for Mould Germination Risk on the Hygroscopic Wall. Journal of University of Souht China (Science & Technology), 33(2):1-7.

[3] Jin Z.Q, Wang S.X. (2018). Synergistic Effects of Microwave, Ultraviolet and Ozone Combination on Mold Spores and Aflatoxin. Journal of Northwest A&F University (Natural Science Edition), 46(4):147-154.

[4] Yue X.Y., Zhang H., Chen W.F., et al. (2018). Temporal and Spatial Distribution Characteristics of Mold Communities during Storage of Corn as Studied by Denaturing Gradient Gel Electrophoresis. Food Science, 39(4):307-311.

[5] Yadong L., Jae H.K., Gu X.H. (2018) Developing Methodology for Service Life Prediction of PV Materials: Quantitative Effects of Light Intensity and Wavelength on Discoloration of A Glass/EVA/PPE Laminate. Solar Energy, 174(1): 1726-1733.

[6] Yang S. (2019). Simulation of Absorbing Frequency Dynamic Regulation of Metal Material Absorber. Computer Simulation, 36(6): 251-254.

[7] Xu Z.X., Hua W.Y., Xiong L.J., et al. (2020). Novel Design of Volume of Detention Tanks Assisted by a Multi-Source Pollution Overflow Model towards Pollution Control in Urban Drainage Basins. Environmental Science and Pollution Research, 27(11):12781-12791.

[8] Tian C.M., Zhang Y.F., Yang H., et al. (2018). To Analysis of the Irrandiance and Monitoring Results of The Same Ultraviolet Lamp with Different Ultraviolet Lamp. Henan Journal of Preventive Medicine, 29(5):321-323.

[9] Zhang W.W., Sun Y.H., Wei H.Y., et al. (2019). Germicidal effects of ultraviolet on condensed milk barrel and its dynamic. Food & Machinery, 35(4):108-112.

[10] Jin Z.Q., Wang S.X. (2018). Synergistic Effects of Microwave, Ultraviolet and Ozone Combination on Mold Spores and Aflatoxin. Journal of Northwest A&F University (Natural Science Edition), 46(4): 147-154.

[11] Mahmoud I.A., Fahmyaly M., Mohib A., et al. (2019). Integration of Benchmarking with Overall Equipment Cost Loss for Industrial Process Improvement. Jordan Journal of Mechanical and Industrial Engineering, 13(1):49-59.

[12] Kumar A., Ram M. (2018). Mathematical Modelling for Reliability Measures to Sugar Mill Plant Industry. Jordan Journal of Mechanical and Industrial Engineering, 12(4):269-279.

[13] Zgeye S M. (2019). A Comparative Study on Beam Divergence Angle and Wave Length between Semiconductor Laser and Helium-Neon Laser. American Journal of Mechanical and Industrial Engineering, 4(5):69.

[14] Ning N., Zhang J.K., Yang S. (2018). Effect of Photo Reactivating Light Intensity on the Photo Reactivation of Escherichia Coli. Liaoning Chemical Industry, 47(9):866-868.

[15] Hao K.Y., Chen X.Y., Li Y.W., et al. (2018). Correlative Analysis of Ultraviolet Radiation and Air Quality in Linzhi. Environmental Science & Technology, 41(7):103-106.

[16] Chen Y. (2018). Measurement and Analysis of Measurement Error of Ultraviolet Radiation Illuminance Caused by Ambient Reflection. Inner Mongolia Environmental Sciences, 30(2):163+165.

[17] Li L.W., Chen Y.Y., Li K.L., et al. (2018). Experimental Measurement and Analysis of the Irradiance of Different Types of Ultraviolet Germicidal Lamps. China Light & Lighting, (11):18-22.

[18] Umarov A.V., Khamzaev H.E., Mirsalikhov B.A. (2020). Temperature Dependence of the Heat Capacity of Polymeric Compositions Based on Polyethylene (LDPE) with a Metal Oxide Filler. American Journal of Mechanical and Industrial Engineering, 5(1):1.

JJMIE

Volume 15, Number 1, March. 2021
ISSN 1995-6665
Pages 133 - 142

Jordan Journal of Mechanical and Industrial Engineering

Fault Tolerant Control Method of Power System of Tram Based on PLC

Zhenzhen You

School of Electronics and Information Engineering, Hunan University of Science and Engineering, Yongzhou 425199, China

Received July 18 2020 *Accepted March 18 2021*

Abstract

Due to the large fault classification granularity of tram power system, there is still a problem that the gain coefficient is not reasonable in different control links, so a fault-tolerant control method of tram power system based on PLC is designed. First, the fault classification of the tram power system is carried out, then the fault diagnosis of the tram power system is carried out. Finally, the fault-tolerant control of the tram power system is carried out through the angle fault-tolerant control unit, PID control algorithm model and brake pull fault-tolerant control unit, as to complete the fault-tolerant control of the tram power system based on PLC. The experimental results show that the reasonable value of proportional gain coefficient, integral gain coefficient and differential gain coefficient are 30.00, 15.00 and 29.98 respectively.

Keywords: PLC; tram; Power system; Fault-tolerant control; Fault diagnosis;

1. Introduction

The power system of the tram is composed of power battery, the first and second contactor groups, bidirectional DC / DC converter and motor controller. The power battery is isolated from the high-voltage line network through the controller to avoid the impact of the high-voltage line network current on the power battery and protect the safety of the power system. As for the power system of tram, in case of an accident, it may cause huge losses to people, property, etc. The safety performance of tram power system determines the safety of operators and the economic benefits of tram. In the above background, the research of fault-tolerant control technology has been pushed to the forefront and there has been a rapid development. Fault tolerant control opens a new way to improve the reliability and safety of tram power system.

Fault tolerant control refers to the way that the system can automatically compensate the fault when it occurs, and recover the performance of the system as soon as possible, and as to ensure the stability, safety and reliability of the system operation. Fault tolerant control is of great significance for practical systems, especially for systems with high reliability and safety requirements, such as all kinds of aircrafts, underwater robots, etc. “Fault tolerance” is originally a concept in computer system design technology, which is the abbreviation of fault tolerance. The basic idea of fault tolerance is that a control system will fail sooner or later, so when designing the control system, we should consider how to compensate the failure once the control system fails, to ensure the stability and safety of the system. Fault tolerant control consists of two parts: fault diagnosis and fault compensation. Fault diagnosis refers to the process of using existing knowledge to comprehensively process and analyze the collected information according to the collected various state information of the diagnosed system, so as to obtain the comprehensive evaluation of the system operation and fault condition; fault compensation refers to the process of readjusting the parameters of the controller, namely software compensation or changing the structure of the controller, namely hardware compensation, after the fault occurs, so as to achieve the purpose of fault tolerance.

In recent years, many researchers have put forward many different definitions for fault-tolerant control. Although the expressions are different, the essence of fault-tolerant control is clear, that is, “when the control system fails, the system can still maintain its own operation in a safe state and meet certain performance index requirements as far as possible”. At present, fault-tolerant control is mainly aimed at the aircraft, and the reconfiguration design theory of control law is the main one. The fault-tolerant control of the power system has become mature, but due to the large fault classification granularity of the power system, there is still a problem that the gain coefficient is not reasonable in different control links. Therefore, this paper puts forward the research on the fault-tolerant control method of the power system of the tram based on PLC. PLC is a programmable logic controller, which uses a kind of programmable memory for its internal storage program. It performs logic operation, sequence control, timing, counting and arithmetic operation for the user's instructions, and controls various types of machinery or production processes through digital or analog inpu\t / output.

* Corresponding author e-mail: youzhenzhen198307@163.com

2. Fault classification of tram power system

Before fault-tolerant control of tram power system, fault classification of tram power system is required. At present, there are many methods for the fault classification of hybrid electric vehicle power system, most of which are from the fault analysis of a certain part of the tram. However, in order to better pave the way for the fault tolerance of the vehicle control system [1], according to the clue of the functional structure of the tram vehicle control system, the fault can be divided into three levels as shown in the following figure according to the concept of hierarchical system: organization level, coordination level and execution level. The top layer of the hybrid electric vehicle control system is the organization layer, which is the core of the vehicle control system. The fault-tolerant control strategy and fault-tolerant module strategy of the tram system are embedded in the vehicle controller program at this level. The organization layer analyzes driver input signals, accelerator pedal signals, brake pedal signals, vehicle speed signals, gearbox and clutch signals, and outputs command signals of corresponding power sources. The coordination layer is the second layer of the control layer. It is a secondary control system composed of control units of each sub module, including engine, motor, battery management unit, etc. The bottom layer is the executive unit of the control system, which consists of engine, motor, clutch, reducer and other components. The direct fault of the vehicle comes from these devices. The main stratification diagram is as follows:

According to the hierarchical structure of the above tram power system [2], the following layer by layer analysis summarizes the control system faults, mainly including eight aspects, as follows:

1. First, the power box of tram power system is composed of power battery group and super capacitor group. When the power battery or super capacitor fails, the power supply system will fail, causing the power system of the tram to reduce power or stop, thus affecting the normal operation of the tram;
2. Second, the failure of power battery pack, battery failure refers to the loss of charge and discharge capacity. The failure modes include too fast capacity attenuation, shorter service life, premature failure of one or more battery cells in the battery pack, falling off of active substances in the battery plate or partition, etc. in the actual work, the main performance is capacity reduction, internal resistance is too large, charging and discharging temperature is too high. The failure reasons include the poor conductivity of active substance [3] in the battery, the short circuit or open circuit in the battery, and the rapid temperature rise during the operation of the battery. In case when a large number of cells are combined into a battery pack, if one or more cells fail, the failure of the whole battery pack will be accelerated;
3. Third, the inconsistent failure of the power battery pack; the inconsistency of power battery pack is reflected in the difference of voltage and resistance capacity of each cell, which is mainly caused by the difference of battery manufacturing process and the inconsistency of battery voltage caused by long-term charge and discharge of battery. When the capacity of the battery pack is inconsistent, with the frequent charging and discharging of the battery, the small capacity battery will not keep up with the pace of the large capacity battery, resulting in the premature damage of the small capacity battery, and the discharge performance and heat dissipation of the whole battery pack will also be reduced. Usually, the terminal voltage of lithium battery is measured as the basis of diagnosis. When inconsistent single battery is found, the single battery can be repaired and reused; when it cannot be repaired, it shall be isolated and replaced in time. The state changes and phenomena of battery performance parameters are shown in the table below.

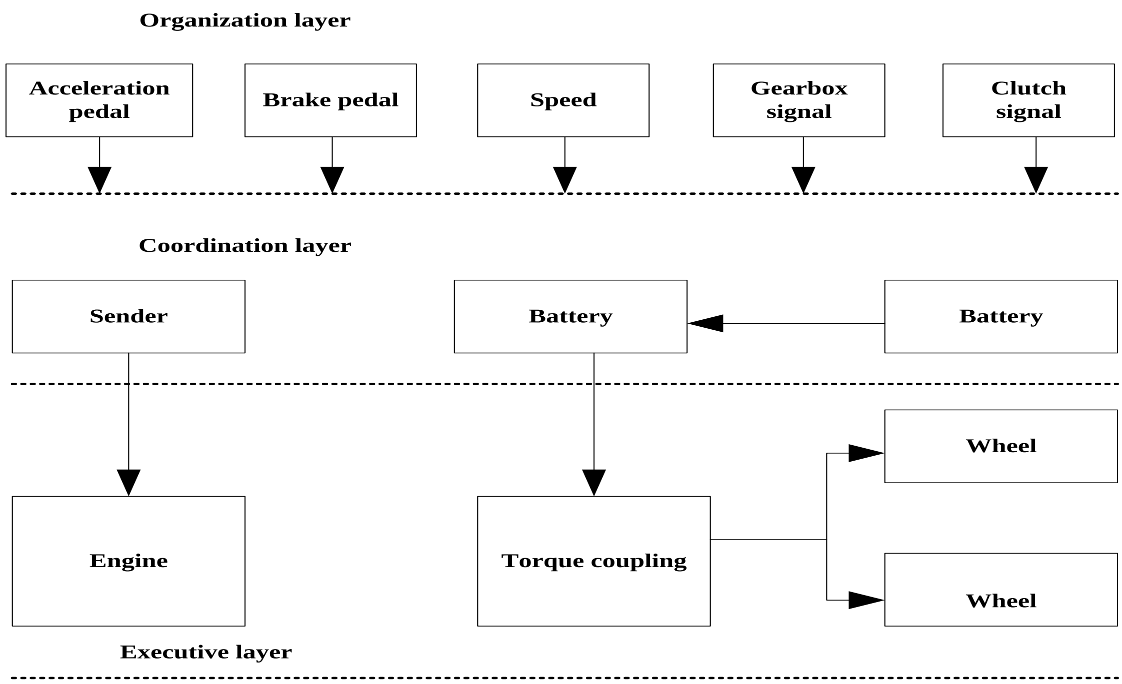

Figure 1. Hierarchical diagram of tram power system control system

Table 1. Parameter change phenomenon and diagnosis method of battery damage

Physical parameter	Phenomenon	Diagnosis method
Temperature change	Short-term temperature rises quickly and then stabilizes	Measure battery temperature
Capacity change	Reduced battery capacity	Detect changes in battery voltage and current
Voltage change	Abnormal closed-circuit voltage	Detection of battery cell voltage under high current charge and discharge
Internal resistance change	Increased internal resistance	Measuring battery internal resistance

4. Fourth, the damage of lithium battery. When the battery is overcharged and discharged for many times, the small damage gradually accumulates and develops into battery failure, and finally the battery will not be repairable;
5. Fifth, power battery voltage and current fault [4]. The power battery control unit is responsible for receiving the current value and voltage value uploaded by the battery sensor in real time and judging whether the power battery fails through the fluctuation of these two values. Taking the power battery voltage as an example, the power battery voltage detection fault includes circuit break and voltage detection accuracy. In order to improve the accuracy of voltage detection, the power battery is divided into several groups. The detection system detects the voltage of each power battery branch and the total voltage of the battery. In case of voltage failure, the power battery will transmit the failure information to the control center and ask for an alarm;
6. Sixth, the power battery temperature fault, including different parts of the temperature is uneven or a part of the temperature is too high and so on. In general, multiple temperature sensors are set in the power battery box. The control unit is responsible for collecting sensor signals and controlling the cooling system. If a temperature fault is detected, the control unit will upload the fault information [5] to the hybrid system control center to decide either power reduction or shutdown;
7. Seventh, the power battery in the power system of the tram has leakage fault. When the insulation between the power supply electrode and the insulation resistance is lower than the specified standard, the information will be fed back to the control center [6], and the sensor will judge the leakage of the power battery and make a decision of shutdown.
8. Eighth, network control system failure. The network control system, including many sensors, actuators and other components, is an important part of the information transmission in the hybrid system, which plays an important role in the stable operation of the tram, especially if the state information feedback of the power box fails, it can lead to overcharge or over discharge of the battery [7] and super capacitor, and damage the power box. The main faults of the sensor are as follows:

Table 2. Sensor failure

Serial number	Classification	Details
1	Classification according to the degree of failure	Hard fault, which means that the sensor structure is damaged, the fault amplitude is large and the change is sudden, this type of fault is easier to identify
		Soft fault refers to the variation of sensor characteristics, the fault amplitude is small and the change is slow, this kind of fault is difficult to identify
2	Classification by fault performance	Intermittent failures, manifested as good or bad sensors
		Permanent failure, manifested as failure to return to normal after failure
3	Classification by failure process	Abrupt fault, large signal change rate
		Slowly changing faults, small signal change rate
4	Classification by fault modeling	Multiplicative failure
		Additive failure
5	According to the breakdown reason	Deviation failure
		Impact failure
		Open fault
		Drift fault
		Short circuit fault
		Periodic failure
		Non-linear dead zone fault

3. Fault diagnosis of tram power system

According to the above classification results of tram power system fault, diagnose the tram power system fault to improve the accuracy of fault diagnosis [8], and provide basis for fault-tolerant control of tram power system. In order to diagnose the fault of the power system of the tram, it is necessary to establish the tram model, use CRUISE to model and simulate the hybrid tram, simulate multiple performance indicators of the vehicle to be controlled, and provide the basis for optimizing fault-tolerant control. CRUISE software is to build the vehicle control system in a modular way, and the driver model can truly reflect the behavior of people operating the car. CRUISE has an interface with Matlab / Simulink, which can embed user designed modules and control algorithms into the vehicle simulation model. This study was conducted through CRUISE. The modules used for building the tram model mainly include: vehicle module, which contains the basic information of the vehicle, the most important information is the equipment quality and full load mass of the tram; FC module, which contains the characteristic curve of the engine, which is designed according to the actual tram parameters; motor module The motor module mainly includes the characteristic curve (MAP) and the efficiency distribution diagram of the motor. From the selection of two main power sources, the tram power in this simulation enjoys a low fuel consumption of 1.2 L; the battery module includes some basic characteristics of the battery. For example, the battery voltage value, SOC of the battery, the maximum charge and discharge current and voltage allowed by the battery, internal resistance of the battery, etc. In this study, the battery pack is matched with the Prius; the driver module, the driver module, is an important information hub connecting the human and vehicle components, and transmits the status of the motor, engine and gearbox to cockpit through the bus bus bus connection unique to the CRUISE software. In the module, the driver module also sends the load signal of accelerator pedal to the vehicle controller module, as well as the output of brake pressure and temperature signals; the vehicle controller is embedded in the module, and the vehicle controller is introduced into the CRUISEsimulation model through the MATLAB API module, in which the MATLAB model is the logic threshold control strategy module designed in this study The bus bus connects the input and output of the API embedded module; the display module contains some commonly used data, such as vehicle speed, acceleration, driving distance, motor torque speed signal, engine torque speed signal, and temperature signal.

According to the built tram model, the fault diagnosis of the tram power system is carried out. The fault diagnosis module in the design strategy uses the generalized observer to get the estimated value of the sensor fault signal, and transmits it to the decision-making body for analysis. In the case of no fault in the original system, without considering the influence of interference, noise [9] or unmodeled part of the system, the initial error of the detection filter will be gradually eliminated, the filter can fully track the response of the original system, and the output error will remain zero. If there is a fault in the original system at a certain time, the output of the filter will not be able to fully track the output of the system after the fault, so there is a residual. The expression formula of this state is as follows:

$$q = a(b) + d / o \tag{1}$$

In formula (1), q represents dimensional state variable, a represents dimensional control vector, b represents dimensional measurement vector, d and o represent constant respectively.

For the actual control system, the premise of fault diagnosis is that the fault can be detected. Only when it is clear that the fault can be detected, the fault diagnosis process can be completed [10]. For the failure of discrete system, the following equation is used to describe:

$$c(t) = x + e / \frac{f}{q} \tag{2}$$

In formula (2), $c(t)$ represents the sudden change of input quantity at t time, x represents the initial value of fault state, and f represents the expandable state variable.

For the unknown fault in the power system of the tram [11], the fault detection observer [12] is used to detect whether the power positioning tram power system has actuator fault:

$$B = k + \frac{c}{y} \tag{3}$$

In formula (3), B represents the state variable of the detection observer, k represents the parameter of the dynamic positioning controller when no fault occurs, y is the output of the system, and c represents the state variable estimation parameter.

Based on the above calculation, it is detected whether the actuator of the tram power system has failed, but it is impossible to know which actuator has failed [13]. Next, separate the failed actuator:

$$W = F / Q + e \tag{4}$$

In formula (4), W represents the initial value of observation error, F represents the actuator fault judgment parameter, and Q represents the function of time.

According to the above diagnosis results, the actuator with failure [14] can be separated. When the thrust is distributed, the actuator with failure [15] will not be distributed with force and torque, while the controller's force and torque will be distributed to the actuator without failure, which provides the basis for fault-tolerant control. The decision-making mechanism can isolate the system output affected by the fault through the control selector [16], and select the controller based on the health system output to form a feedback control loop, to maintain the stability of the system.

4. Fault tolerant control of tram power system

The fault-tolerant control method in this design is generally divided into three parts, namely, angle fault-tolerant control unit [17], PID control algorithm model [18] and brake pull fault-tolerant control unit [19]. The overall framework is shown in the figure below.

It can be seen from the above figure that in the angle fault-tolerant control unit, the tram power system collects the angle sensor and acceleration sensor signals in real time, inputs the detected value of the acceleration sensor into the estimation model to calculate the estimated value of the angle, and then inputs the estimated value of the angle and the detected value of the angle sensor into the fault-tolerant control model for fault diagnosis and fault compensation respectively, Thus, the expected braking force is calculated by the corresponding formula. In the fault-tolerant control unit of braking force, the tram power system collects the signal values of braking force sensor, motor speed sensor and current sensor in real time [20], inputs the detection values of motor speed sensor and current sensor into their respective estimation models to calculate the corresponding angle estimation values, and then inputs the estimated values of braking force and braking force sensor. The detection value of the controller is input into the fault-tolerant control model, and fault diagnosis and fault compensation are carried out respectively, so as to output the actual braking force value. Compare the expected braking force value with the actual braking force value, input the difference into the PID control algorithm model to control the actuator, thus forming a closed-loop control [21-23].

PID control algorithm design. PID control algorithm is the most widely used control algorithm in industrial production. The core of its control algorithm is to calculate the difference between the ideal value of the controlled object and the feedback value according to the three links of proportion, integration and differentiation, and adjust the parameter values of the three modes through its linear combination to achieve the control of the output value of the controlled object. As a classical numerical control method [24], PID control has the following advantages: first, the principle is simple, easy to operate and master; second, it can be widely used in various industrial process control fields; third, it has good control effect and strong robustness. The conventional PID controller is a kind of linear controller composed of Pro controller [25] and controlled object. Its control system schematic diagram is as follows:

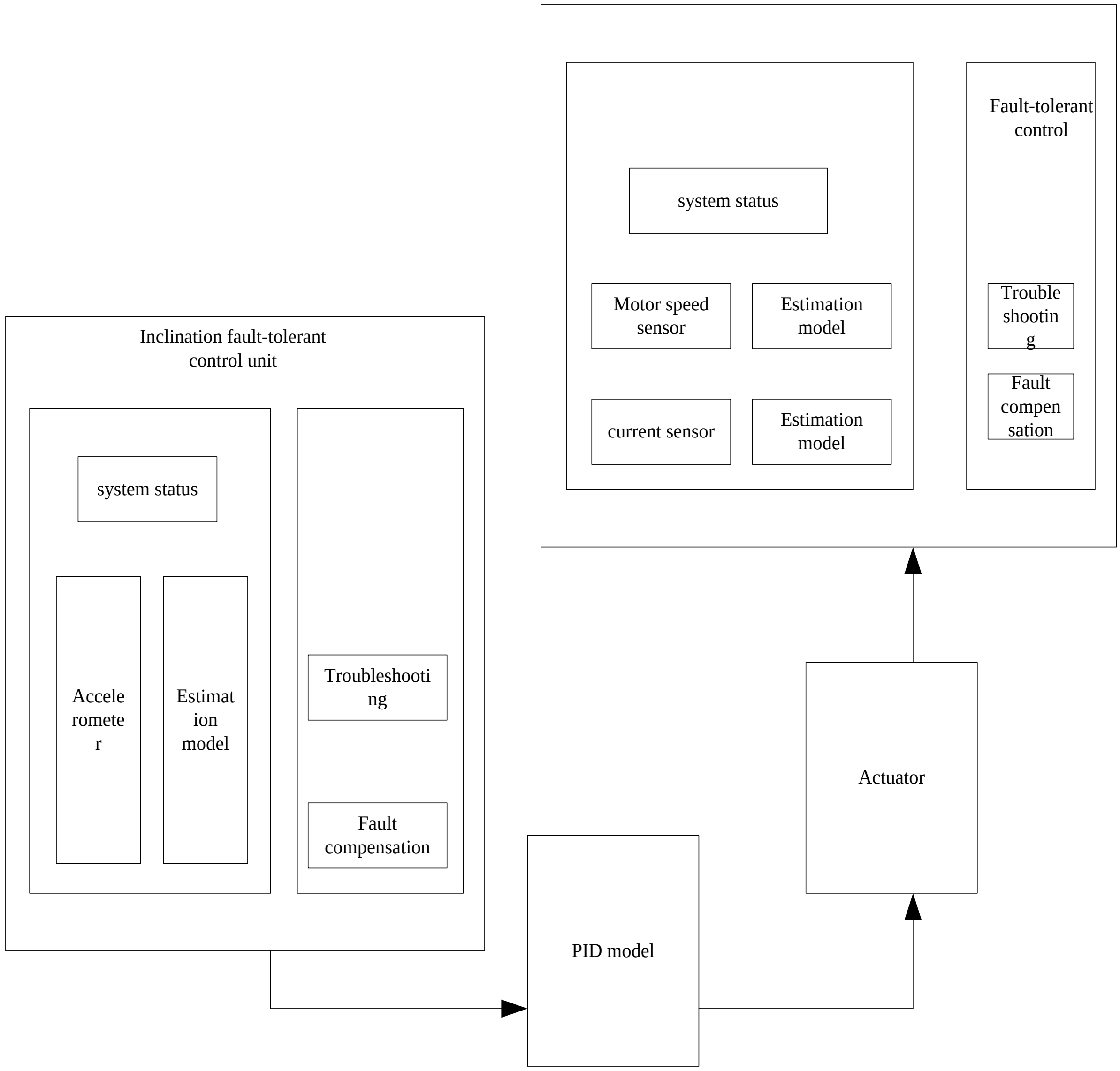

Figure 2. General framework of fault tolerant control method

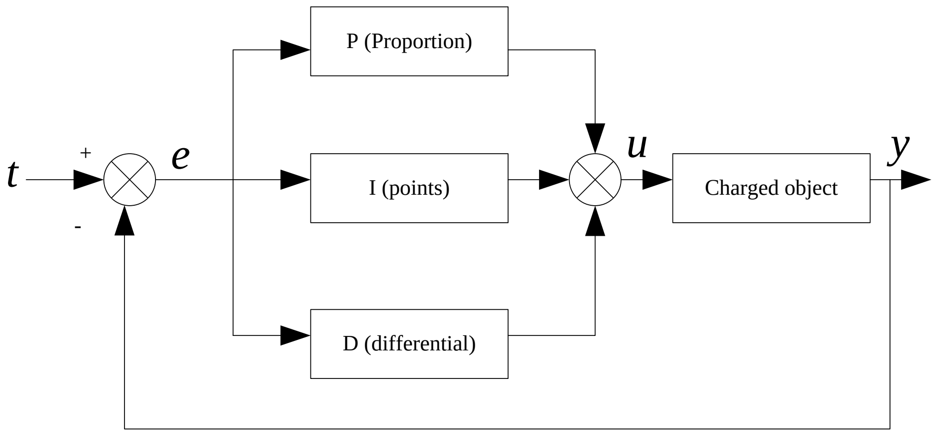

Figure 3. Schematic diagram of PID control system

It can be seen from the above figure that the PID control system compares the output value y of the controlled object with the ideal value t, and then inputs the deviation value g into the controller to generate a regulating factor to control the output of the controlled object. The mathematical model of the algorithm in the continuous time domain is as follows:

$$u = h\left(e + \frac{1}{T} + \frac{t}{g}\right) \tag{5}$$

In formula (5), u represents the output control quantity of the controller, h is the proportional gain coefficient of the controller, T is the integral time constant of the controller, t is the differential time constant of the controller, and g represents the relative deviation between the output value of the controlled object and the ideal value.

In the pro control algorithm, there are great differences in the debugging functions of proportion, integral and differential, which are described in detail as follows:

First, in the proportional control, the proportional gain coefficient makes the adjustment factor proportional to the relative deviation g, which can directly affect the control effect. Increasing the proportional gain coefficient can improve the response speed of the system and reduce the steady-state error of the system, but the excessive proportional gain coefficient will lead to system oscillation and destroy the stability of the system. Therefore, a single proportional link cannot meet the control requirements of complex system, so an integral link is needed.

Second, in the integral control link [26], the integral gain coefficient can be used to eliminate the steady-state error (or static error) of the system. In the control process, as long as the system deviation exists, the integral control will continue to operate until the steady-state error is eliminated, and the integral control will stop. The length of the controller integral time is related to the strength of the integral control function. The integral control function weakens with the increase of the integral time. The longer the time to eliminate the steady-state error is, the less the overshoot of the control system and improve its stability. On the contrary, the shorter the integral time is, the stronger the integral control function is. However, if the integral control function is too strong, the overshoot of the system will be caused, and its stability will be destroyed Qualitative.

Thirdly, in the differential control, the differential gain coefficient can be used to reflect the change rate of relative deviation. Differential control has the function of predicting the trend of deviation and makes corresponding advance adjustment to eliminate it before the deviation signal disappears, so as to reduce the adjustment time of the system, prevent the occurrence of system oscillation, and improve its dynamic characteristics. However, differential control is very sensitive to noise interference and has amplification effect on it, so if the differential control time is too long, the anti-interference ability of the system will be weakened.

Therefore, according to the PID control algorithm, this paper determines that the closed-loop control process of the mechanical electronic parking brake system is to input the expected value of power. The actual braking force is obtained by the servo motor, lead screw nut, cable and brake, and finally controlled by the PID controller.

According to the above process, the starting control of the tram power system ramp is based on personal experience to determine the time to release the handbrake as to achieve a smooth start. If the driver is inexperienced and the timing is improper, it is easy to cause the car to slip or the engine to be forced to fire. The simulation model of starting on ramp is designed to simulate the situation of the driver when starting on ramp. It includes the conversion model of engine torque transmission ratio and the control strategy model of auxiliary starting on ramp. When starting on the ramp, the driver will generally put the gear in first gear forward or reverse according to the site conditions, so the transmission ratio coefficient of the engine output torque through the final drive, transmission gear, etc. is converted into the driving force acting on the tire and the desired ideal braking force for comparison. Then the mathematical model of moment transfer of mechanical part can be obtained as follows:

$$r = i \otimes j \otimes \frac{a}{s} \tag{6}$$

In formula (6), r represents the output torque of automobile engine, i represents the maximum torque ratio of torque converter, j represents the gear transmission ratio, and s represents the reduction ratio of final drive.

The calculation formula of braking force required for parking is as follows:

$$L = \frac{m + C_g}{r \times u \times C_f} \tag{7}$$

In formula (7), L is the braking force required for parking, m is the slope angle of the tram, C_g is the mass of the tram, and C_f is the friction coefficient of the tram. According to the above calculation, the starting control strategy is designed as follows: the mechanical electric parking brake system detects the engine output torque in real time, and compares it with the required braking force converted from the mathematical model of ramp angle. Then, according to the difference between the force converted from the engine output torque and the required ideal braking force and the driver's intention, the servo motor is driven reversely at the right time Turn to release the parking brake tension, and ensure the smooth start of the vehicle to avoid the phenomenon of sudden rush and sliding.

Because most tram vehicles are powered by on-board battery [27], and DC motor has the advantages of strong aerodynamic performance, good speed regulation performance, easy control, etc. DC motor can convert DC electric energy into mechanical energy, so it is the main power of mechanical electric parking brake system. According to the electromagnetic characteristics of DC motor, the mathematical model can be obtained as follows:

$$v = r + l + \frac{w}{e} \tag{8}$$

In formula (8), v is the input voltage of servo motor, l is the armature current of servo motor, w is the back EMF of servo motor.

According to the torque equivalence of DC motor, the torque balance mathematical model of servo motor can be obtained as follows:

$$J = \frac{C}{V} + F \tag{9}$$

In formula (9), J represents the electromagnetic torque generated by the servo motor, V is the total moment of inertia of all rotating parts (including transmission mechanism, reducer and load machinery) driven by the servo motor, C is the rotation speed of the servo motor, F is the sum of all kinds of friction torque and load torque on the rotation axis of the servo motor.

On this basis, the voltage output calculated by PID controller is used as the control voltage input of servo motor, and the output of the whole servo motor is the rotation angle of servo motor. There is a saturation module in the servo motor, which is used to set the upper and lower limits of the output. The first saturation module is used to limit the upper and lower limits of the servo motor control voltage. The second saturation module is used to limit the upper and lower limits of the servo motor output rotation angle. The rotation angle of the servo motor output is used as the input of the following transmission mechanism model, so the limit value is to prevent the excessive output angle from affecting the operation of the screw nut mechanism, so as to avoid excessive wear of the mechanism. Then the model control of the transmission mechanism of the power system of the tram is carried out. In the mechanical electric parking brake system, the transmission mechanism is an important part of the executive module. The driving mechanism is mainly composed of lead screw nut and cable. The input of the lead screw nut mechanism is the rotation angle of the output of the previous servo motor, while the output of the lead screw nut mechanism is the feed of the lead screw nut mechanism. According to the previous experimental data, the relationship between the feed rate and the pull force of the screw nut meets the following empirical formula:

$$N = 6.817z^2 - 11z = 7.64 \tag{10}$$

In formula (10), z is the feed of the screw nut.

In the overall model of the lead screw nut mechanism, the servo motor overcomes the total moment of inertia, friction and load torque of the lead screw nut drive mechanism to drive the lead screw nut to rotate. In this process, through fixing the lead screw, it affects the nut to make a linear horizontal movement, and applies the braking force to the brake through the cable.

Because the observation value of the generalized observer to the system state is not affected by the sensor fault basically, this strategy directly uses the observation value of the tram power system to construct the robust state feedback controller to stabilize the system, and does not need to consider the similarity between the generalized fuzzy system and the common linear system, so the state observer and the controller of the system can be designed separately, so that the closed-loop The control system satisfies the sufficient condition of asymptotic stability. The state feedback controller of fuzzy system is established as follows:

$$M = X * I * Z(t) \tag{11}$$

In formula (11), M represents the observation value of the tram system state, X represents the generalized observation error, I represents the vehicle operation performance parameter, Z represents the observation noise, and t represents the observation time.

According to the above process, the fault-tolerant control of the tram power system based on PLC is completed.

5. Experiment

Build an experimental platform to verify the effectiveness of PLC based fault-tolerant control method of tram power system. For fault-tolerant control of tram power system, the rationality of gain coefficient in different control links determines the effect of fault-tolerant control, so the experiment verifies the rationality of gain coefficient in different control links.

5.1. Establishment of experimental platform

In this paper, the hardware of the mechanical electric parking brake system is built in the ring simulation by using the Autobox developed by DSpace company, and the power module circuit, sensor circuit, motor drive circuit, system input and output interface and system control strategy are designed respectively. The hardware structure used in the experiment is as follows.

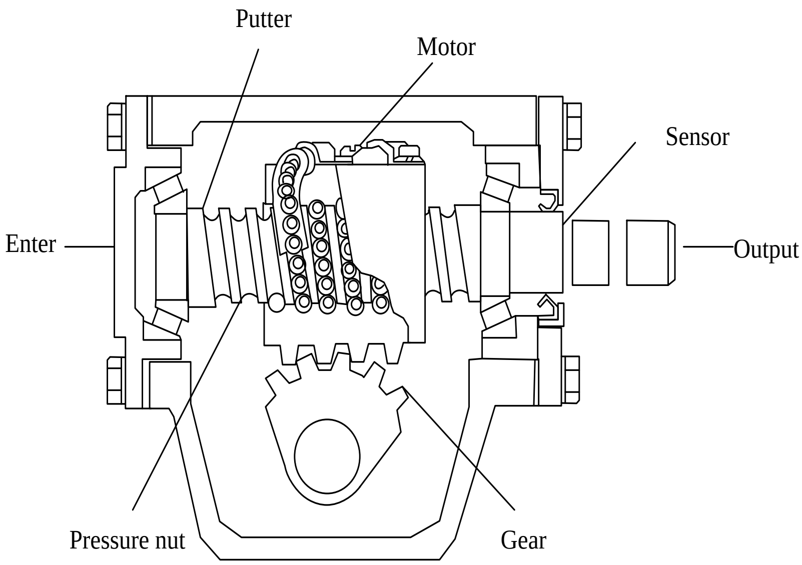

Figure 4. Experimental hardware structure

DSpace is a set of real-time simulation system, which consists of two parts: hardware system and software environment. Among them, the hardware system mainly includes processors with high-speed computing ability and various rich I / O interfaces, allowing users to combine according to their own needs; the software environment mainly includes RTI software, software for testing and debugging, such as software with the function of generating and downloading program code, software for testing and debugging, etc. The code in the hardware system is automatically generated by RTI software and downloaded to the control program to realize the real-time simulation experiment of the system, and then the variables are accessed by controldesk software to realize the experiment and debugging of the simulation system. The output table of the controller control signal applied in the experiment is as follows:

Table 3. Control signal output summary

Signal	Signal type	Signal connection
App indicator	Switch	Indicator hard wire
Mode indicator	Switch	Indicator hard wire
System fault indicator	Switch	Indicator hard wire
System failure warning tone	Switch	Buzzer hard wire

The input circuit needs to ensure that the analog and digital signals of each sensor can be collected by the control unit; the output circuit needs to ensure that the control signals output by the controlled unit can be accurately transmitted to the actuator and warning lights, etc., without interference from other external factors. The summary table of system controller signal acquisition is as follows:

Table 4. Summary of signal acquisition of experimental controller

Signal name	Signal form	Signal source connection
EPB operation button	Switch	Button hardwire
Operation button	Switch	Button hardwire
Engine speed	Digital quantity	Car electronic network
Engine torque	Digital quantity	Car electronic network
Accelerator	Digital quantity	Car electronic network
Speed	Frequency	Magnetoelectric sensor
Servo motor speed	Frequency	Motor speed sensor
Vehicle inclination	Analog	Tilt sensor
Gear information	Switch	Switch hard wire
Ignition key	Switch	Switch hard wire

At the same time, the hardware in the loop simulation uses the XP operating system installed in the notebook, on which the modeling and simulation software MATLAB r2007b and the test monitoring software control desk are installed. The main construction steps of the experimental platform are as follows:

Firstly, the simulation model block diagram of the mechanical electronic parking brake system is established in Matlab / Simulink software, and the experimental parameters are set according to the simulation results to ensure that the simulation system can output the correct simulation curve; secondly, the input and output interfaces in the simulation system are connected with the I / O interfaces provided by rt11005 module in DSpace to form a closed-loop control system; then the algorithm is defined The option is fixed step, the setting step time is 0.001 s, the build button in Matlab / Simulink of the motor converts the simulation model block diagram of the mechanical electric parking brake system into C language code; finally, the compiler code provided by DSpace is compiled and loaded into the ds2211 control board card in the Autobox, so as to realize the overall system simulation using the Autobox as the electronic control unit. At the same time, control desk is used to monitor the simulation process in real time. The overall structure of the experimental platform is as follows:

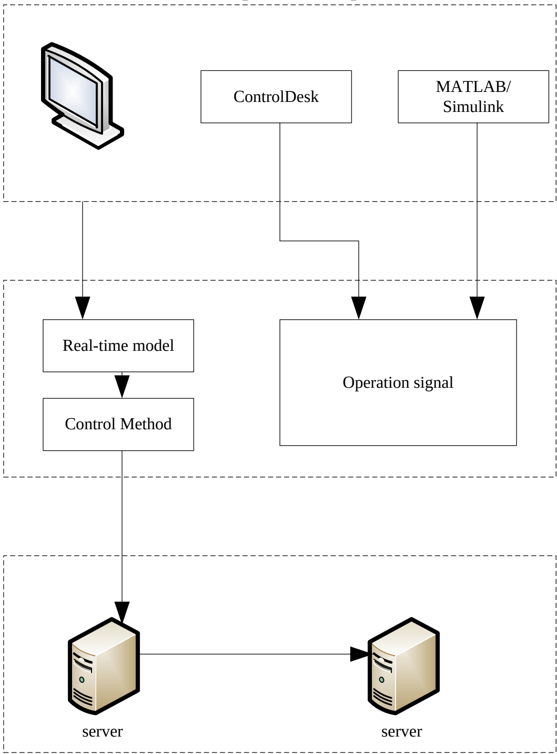

Figure 5. Experimental test platform

5.2. Rationality analysis of gain coefficient of proportional control link

In the proportional control, the proportional gain coefficient is determined by the adjustment factor and the relative deviation, which affects the strength of the fault-tolerant control. Among them, the regulation factor refers to the regulation parameter of the proportional control; the relative deviation value refers to the difference between the output value of the controlled object and the ideal value; a reasonable proportional gain coefficient can improve the response time of the fault-tolerant control, reduce the steady-state error of the power system, and ensure the safe operation of the power system of the tram. The initial value of the adjustment factor is set to 0.5, and the initial value of the relative deviation is set to 1.0. In each case, experiment 10 times, and take the average value. The results of the proportional gain coefficient are shown in the table below.

Table 5. Proportional gain coefficient

Regulatory factors	Relative deviation value	Proportional gain coefficient	Response time (ms)
0.5	1.0	20.13	12.03
1.0	1.1	21.16	11.10
1.5	1.2	22.62	10.00
2.0	1.3	23.94	9.99
2.5	1.4	24.16	9.12
3.0	1.5	30.00	10.03
...	...	...	...
5.0	1.9	35.46	11.23
5.5	2.0	39.56	12.56

As shown in Table 5, when the adjustment factor is 3.0 and the relative deviation value is 1.5, the response time of fault-tolerant control is the shortest, indicating that the rationality of proportional gain coefficient is the strongest at this time, which is 30.00.

5.3. Rationality analysis of gain coefficient of integral control link

Fault tolerant control in the integral control link, the integral gain coefficient is determined by the integral time and overshoot, and its function is to eliminate the steady-state error of the tram power system. Among them, integration time refers to the number of integrations; Overshoot refers to the maximum limit value of fault tolerance. A reasonable integral gain coefficient can eliminate the steady-state error of the power system and ensure the safe operation of the power system of the tram. The integration time is set to 1 time, and the overshoot is set to 0.5. In each case, experiment 10 times, and take the average value. The integral gain coefficient results are shown in the table below.

Table 6. Integral gain coefficient

Integral time (Times)	Overshoot	Integral gain coefficient	Steady-state error
1	0.5	12.03	+2.30
2	0.6	12.11	+2.20
3	0.7	12.23	+2.03
4	0.8	12.56	+1.92
5	0.9	12.48	+1.82
6	1.0	12.94	+1.24
...	...	...	...
19	2.4	14.26	+0.51
20	2.5	15.00	0

As shown in Table 6, when the integration time is 20 times and the overshoot is 2.5, the steady-state error of fault-tolerant control is 0, indicating that the integration gain coefficient is the most reasonable at this time, which is 15.00.

5.4. Rationality analysis of gain coefficient of differential control link

In the differential control, the differential gain coefficient is determined by noise and prediction deviation, which reflects the change rate of relative error. Among them, noise refers to the interference factors in the process of fault-tolerant control; prediction deviation refers to the difference between the output value and prediction value of the controlled object. Reasonable differential gain coefficient can improve the rate of fault-tolerant control and ensure the safe operation of the tram power system. The initial noise value is set to 30, and the initial prediction deviation value is set to 3.5. In each case, 10 experiments are conducted, and the average value is taken. The differential gain coefficient results are shown in the table below.

Table 7. Differential gain coefficient

Noise (dB)	Forecast deviation	Differential gain coefficient	Control rate (Number of faults / MS)
30	3.5	10.12	34.64
40	3.6	15.12	39.45
50	3.7	20.13	40.15
60	3.8	26.48	46.15
70	3.9	26.79	49.51
80	4.0	29.45	53.16
...	...	...	...
150	4.8	29.98	59.78
160	4.9	35.46	45.12

As shown in Table 7, when the noise is 150 and the prediction deviation is 4.8, the fault-tolerant control rate is the largest, indicating that the differential gain coefficient is the most reasonable at this time, which is 29.98.

6. Conclusion

In conclusion, in order to meet the fault-tolerant requirements of the tram power system, the PLC based fault-tolerant control method of the tram power system designed in this study can improve the rationality of the gain coefficient of the fault-tolerant control link, improve the fault-tolerant performance of the power system, and provide a more effective guarantee for the operation safety of the tram. At present, the research on fault-tolerant control of tram power system is still in its infancy, and further experimental research and demonstration are needed as an industrial product. Therefore, the following aspects need to be studied and tested:

1. First, there is no emergency braking control strategy in the fault-tolerant control simulation model, that is, when the service brake fails, the parking brake system can replace the service brake to apply the braking force to the driving vehicle, so that it can stop driving smoothly and reliably;
2. Second, although the fault-tolerant control strategy has been designed in this experiment, due to the time and cost problems, there is no specific single-chip microcomputer as the control unit, so only the dual core redundancy method is used to realize the possibility of fault compensation of electronic control system;

3. Third, because no suitable single-chip microcomputer is selected as the electronic control unit, no real vehicle test is carried out. It is hoped that there will be a chance to burn the fault-tolerant control program into the single-chip microcomputer and carry out real vehicle verification;
4. Fourthly, for the parameter uncertainty, this paper mainly considers the case that the unknown parameter enters the system state equation linearly, and there is not enough research on the adaptive control of the more general nonlinear parameter uncertainty system. In addition, this paper assumes that the unknown quantity is constant or slowly changing. How to further study the uncertain parameters of time-varying based on this paper is also an important problem.

Acknowledgement

The study was funded by the Research Foundation of Scientific Research Project of Hunan Provincial Department of Education - Research on the key technology of intelligent transplanting system based on PLC (No.19C0797); The Research Foundation of Guiding science and technology plan project of Yongzhou City - Design of control system of stereo garage based on PLC (No.2019-yzkj-01); The construct program of applied characteristic discipline in Hunan Province.

References

[1] Wei G, Qiao YH. (2018). Design and development of vehicle reversing brake assist system. Auto Sci-Tech, 4(12):1-12.

[2] Chen GH, Liu D, Weng JM. (2019) Cyber-physical fusion modeling of power frequency modulation system and its application in fault-tolerant control. Power System Technology, 43(07):2376-2383.

[3] Wang J, Zhang J. (2021) Active Fault-tolerant Control Research of Multi-Agent System. Journal of Physics: Conference Series, 1754(1):012088.

[4] Zhang CY, Wang LZ, Bu Y, & Shen LG. (2019). Multi-rotor aircraft flight performance estimation based on propulsion system model. Computer Simulation, 36(5): 83-87

[5] Raphael, Zhang P. (2018) Fault-tolerant tracking control of petri nets. Automatisierungstechnik: Methoden und Anwendungen der Steuerungs-, Regelungs- und Informationstechnik, 66(1):30-40.

[6] Han RK. (2019) Analysis of tram positioning based on GPS and IMU combined sensor data fusion. Automation Technology and Application, 38(08):65-68.

[7] Wang S, Xiong GS, Cao DH. (2018) A fault-tolerant brushless DC motor drive control method.Navigation Positioning and Timing, 5(03):93-98.

[8] Tang QD, Ge XL, Liu YC, & Hou MJ. (2018). Improved switching-table-based dtc strategy for the post-fault three-level npc inverter-fed induction motor drives. Iet Electric Power Applications, 12(1), 71-80.

[9] Wang HB, Zhao RX, Tang SQ, Yang H. (2018) Simplified fault-tolerant control strategy for dual three-phase permanent magnet synchronous motors when one phase is open. Electric Power Automation Equipment, 38(01):74-79.

[10] Zhang XB. (2018) Fault-tolerant control system in fault diagnosis of electronic special test equipment. Electronic Design Engineering, 26(03):24-27+31.

[11] Jiang W, Zhu C, Xue S, Ren K, Yang C. (2020) DC-Side-Fault-Tolerant Control of a Battery-Supercapacitor Hybrid Energy Storage System Based on Cascaded Multilevel Converter and Auxiliary Power Loop. IEEE Transactions on Industrial Electronics, 67(9):7451-7460.

[12] Roshan, Emitis, Funt, Brian. (2018). Computational color prediction versus least-dissimilar matching. J Opt Soc Am A Opt Image Sci Vis, 35(4):292-298.

[13] Jia Q, Zhang XC, Yuan YW, Fu T, Wei LG, Zhao B. (2018) Fault-tolerant adaptive sliding mode control method for tractor automatic steering system. Transactions of the Chinese Society of Agricultural Engineering, 34(10):76-84.

[14] Pan YW, Zhang CH, Du LY, Chen AL, He JW. (2018) Compound fault-tolerant control method of SRDAB interface converter in DC distribution system. Automation of Electric Power Systems, 42(20):130-137.

[15] Du SC, Quan L, Zhu XY, Zhang L, Zuo YF. (2019) Position sensor failure fault tolerance control of permanent magnet synchronous motor at zero and low speed based on high frequency injection. Proceedings of the Chinese Society of Electrical Engineering, 39(10):3038-3047 .

[16] Tao L, Leila Parsa. (2018) Design, Control, and Analysis of a Fault-Tolerant Soft-Switching DC–DC Converter for High-Power High-Voltage Applications. IEEE Transactions on Power Electronics, 33(2):1094-1104

[17] Han N, Zhou B, Qin XH, Lei JX, Shi BP. (2018) Study on fault tolerance strategy for rectifier stage power switch fault of two-stage matrix converter. Proceedings of the CSEE, 38(10):3049-3058+3156 .

[18] Chai WJ, Dong SY, Chen JY, Zhang C, Chen TY. (2019) Research on a method of fault-tolerant control of remote sensing satellite momentum wheel. Computer Measurement and Control, 27(02):79-83+88.

[19] Christoph B, Gross H. (2018). Double freeform illumination design for prescribed wavefronts and irradiances. Journal of the Optical Society of America A, 8, 35(2):236-236.

[20] Han Y, Fan W, Cao T. (2019) Spacecraft Attitude Backstep Fault Tolerant Control Based on Error Space. Flight Control and Detection, 2(04):46-54.

[21] Li J, Sheng P, Shao K. (2020) Optimization of clutchless amt shift control strategy for electric vehicles. Jordan Journal of Mechanical and Industrial Engineering, 14(1):109-117.

[22] Tao J, Jia Y, Gao Y. (2020) Intelligent remote monitoring system for minor faults of intelligent unmanned vehicle. Jordan Journal of Mechanical and Industrial Engineering, 14(1):61-70.

[23] Yan Y, Wu LB, Zhao NN, Zhang RY. (2021) Adaptive Asymptotic Tracking Fault-tolerant Control of Uncertain Nonlinear Systems with Actuator Failures and Event-triggered Inputs. International Journal of Control, Automation and Systems, 19(3).

[24] Hu G, Zheng ZT, Li YH. (2018) Fault-tolerant control when the nine-switch converter is short-circuited in the aviation power system. Aircraft Design, 38(04):47-51.

[25] Hu SY, Li J, Jin N, Liu GR. (2019) Model predictive direct power control of bidirectional AC/DC fault-tolerant converters. Electrical Measurement and Instrumentation, 56(22):89-94.

[26] Zhao WJ, Jiang LJ. (2019) Fault-tolerant control method of magnetic bearing winding circuit. Journal of Zhejiang Sci-Tech University (Natural Science Edition), 41(02):187-195.

[27] Gunasekaran, Joo Y H. (2020) Nie–Tan fuzzy method of fault-tolerant wind energy conversion systems via sampled-data control. IET Control Theory & Applications, 14(11):1516-1523.

JJMIE

Volume 15, Number 1, March. 2021
ISSN 1995-6665
Pages 143 - 152

Jordan Journal of Mechanical and Industrial Engineering

Design of Mechanical and Electrical Control System of Mixed Liquid Gas Pressure Energy Storage Based on Maximum Power Point Tracking

Jia Zhang

Fundamental Experiment Training Center, Tianjin Sino-German University of Applied Sciences, Tianjin 300350, China

Received July 18 2020 *Accepted March 18 2021*

Abstract

In order to solve the problem that the accuracy of the controller of the traditional mechanical control system is not high and the efficiency of the control system is too low, a mechanical control system based on maximum power point tracking is designed. Through the controller platform, the embedded microprocessor with arm architecture is used to design the basic peripheral circuit, and to improve the control accuracy of the controller, and to complete the hardware design of the system. According to the characteristics of the compression efficiency of the liquid pump, the energy storage device is modeled, the maximum power point tracking algorithm is used to control the speed of the motor, and the software design of the system is completed. Regarding the hardware and software design of the system, the mechanical and electrical control system design of the mixed liquid gas pressure energy storage device is realized. The experimental results show that the design system is basically consistent with the standard control value, the system efficiency is the largest, and the mechanical and electrical control accuracy of the mixed oil and gas energy storage is improved, and the active power can reach a stable state.

Keywords: Maximum power point tracking; Mixed liquid gas pressure energy storage machine; Control system; Efficiency value;

1. Introduction

With the wide application of new energy generation, energy storage technology has been developed rapidly. Because of the location of Micro Capacity compressed air energy storage system, and its cost which is relatively low, it has been widely used. Micro capacity compressed air energy storage has become a new technology of renewable energy generation and energy storage system. In the air energy storage technology, in order to improve the efficiency, we can start from the thermodynamic principle. At the same time, the energy conversion efficiency in electromechanical conversion has a great influence on the energy storage system. In the traditional air compression energy storage system, asynchronous motor is mainly used, and the traditional motor control mode is used to compress the air to obtain energy. But the disadvantage of this technology is its low efficiency [1]. The system is a hybrid energy storage system, which includes liquid gas hybrid pressure energy storage system, high energy density air compression energy storage device and high-power density super capacitor energy storage device. Because the conversion of mechanical and electrical energy has a great influence on the efficiency of the system, in the system of liquid gas mixed energy storage and compression, the research on the compressed air energy storage system has made some progress in recent years.

A combined automatic generation control system of thermal power unit and energy storage system is proposed and designed in document [2]. The basic principle, typical scheme, control process and practical engineering effect of the technology are introduced. The influence of the connection mode of the energy storage system on the electrical system of thermal power unit and the selection of the storage battery are discussed. The investment and income of the technology in engineering application are analyzed. The analysis results show that the combination of AGC frequency modulation technology with thermal power unit and energy storage system has remarkable effect and good economic benefit. The access of energy storage system has no influence on the control system and electrical system of thermal power unit. As the battery of energy storage system, lithium iron phosphate battery has many advantages, which provides reference for the practical engineering application of AGC frequency modulation technology combined with thermal power unit and energy storage system. However, the accuracy of the system is low, which leads to the instability of the active power. A multi-port power generation control system based on energy storage is proposed and designed in document [3]. According to the system requirements, the structure and function of each part are designed. The energy management scheme and configuration strategy of the energy storage unit

* Corresponding author e-mail: zhangjiatianjin@126.com.

are analyzed. The fuel cell adopts one-way dc/dc converter, voltage and current double closed-loop control. Through the energy storage unit and bidirectional dc/dc converter, the load and super capacitor energy storage unit are provided with energy when the dynamic change is in progress. The sliding mode control and the segment PI control strategy are adopted to realize the fast transfer control of energy and improve the output stability of the system. The simulation model of the system is established to verify the effectiveness of the multi-port power system control strategy. But the efficiency of the liquid pump in this system is low, and there are some hidden dangers.

In view of the problems in the above system, a new type of mechanical and electrical control system for liquid gas mixed energy storage is designed by using the maximum power point tracking strategy. The invention combines the high energy density air compression energy storage device and the super capacitor energy storage device with high power density into a hybrid energy storage system. The hybrid liquid compression energy storage system is controlled by permanent magnet synchronous motor. For the system, the maximum efficiency point tracking algorithm is used to control the motor of the system, so that the motor load liquid pump works at the maximum efficiency point, thus improving the mechanical and electrical conversion efficiency of the system. The experimental results show that the method can be used for reference, improve the conversion efficiency of electromechanical energy, and provide the basis for the construction and work of hybrid energy storage system.

2. Hardware design of mechanical and electrical control system of mixed liquid gas pressure energy storage

2.1. Controller platform

The controller platform adopts ARM embedded microprocessor and embedded controller of µ C / OS - II real-time operating system in series. The hardware platform design of the controller is shown in Figure 1.

Figure 1 shows the structure, the CPU of the controller adopts Samsung’s 32-bit RISC microprocessor S3C44BOX based on ARM7TDMI core, with the main frequency of 66 MHz. The chip integrates external memory controller, LCD controller, 4 DMA controllers and 2 darts, IIC and IIS bus controller, A / D, I / O and other interfaces, embedded controller system resources based on S3 c44box include: 8 MB SDRAM as system memory, 4MB flash as electronic disk, standard RS-232 serial communication interface. The embedded controller uses LCD and keyboard as human-computer interface, which has powerful human-computer interaction function [4].

In order to reduce the cost of the whole system, through 16 / 32-bit RISC processor S3C44B0X by using its own on-chip peripherals, a LMD18200 driver chip is connected outside the processor. The H-bridge and its control logic circuit composed of four DMOS are included in an 11 pin t-220 package. The rated current is 3 A, the peak current is 6 A, the voltage power is 55 V, and the on resistance of the power transistor is 0.3 Ω, TTL and CMOS compatible control signal input, including bridge arm single side through circuit; chip overheat alarm output and automatic shutdown. Settings LMD18200 Logical Menu Table 1.

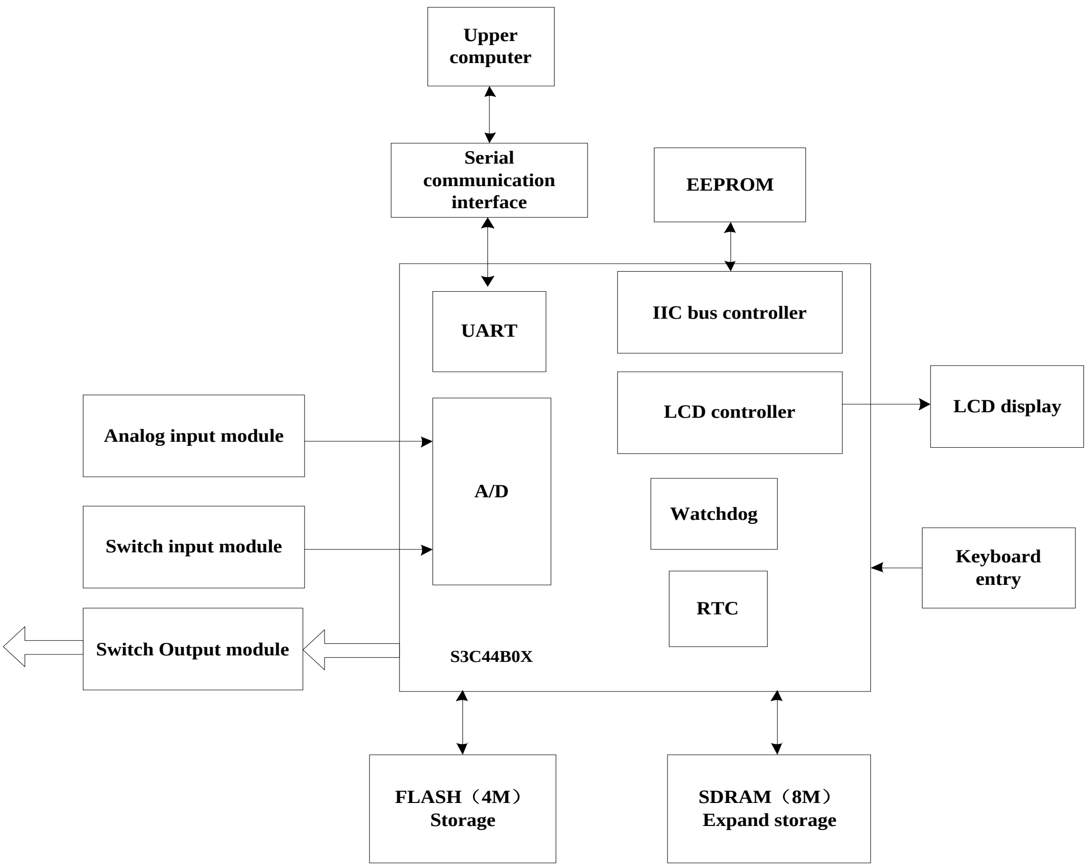

Figure 1. Hardware structure of controller

Table 1. LMD18200 logic menu

PWM	Turn	Enable	Actual output drive current	Motor working state
H	H	L	Outflow 1, inflow 2	Forward rotation
H	L	L	Inflow 1, outflow 2	Reversal
L	/	L	Outflow 1, outflow 2	Stop it
H	H	H	Outflow 1, outflow 2	Stop it
H	L	H	Inflow 1, inflow 2	Stop it
L	X	H	NONE	

Driven by the functions in Table 1, since the control signal of the motor is directly generated by the DSP, and the drive circuit of the DC motor is directly connected with a voltage of up to 26.2 V, if there is a problem in the circuit, the current will flow directly into the DSP, causing damage to the DSP and its peripheral circuits, so all the control signals and feedback signals must be isolated by the photoelectric isolation device to make the motor drive electricity The circuit is completely separated from the DSP [5]. Even if there is a problem in the circuit, it will not cause great damage to the whole system. At the same time, the frequency of PWM signal in the control is relatively high for the photoelectric isolation device, and the common photoelectric isolation device such as til113 cannot be used. When the rectangular wave of PWM signal is input from the photoelectric isolation device, when the frequency is high, only trapezoidal wave can be obtained at the output end of the photoelectric isolation device, which cannot achieve accurate PWM control. Therefore, 6n137 high-speed optocoupler isolator is selected in this paper, which can fully adapt to high signal frequency. A schematic diagram of the connection to the DSP is shown in Figure 2.

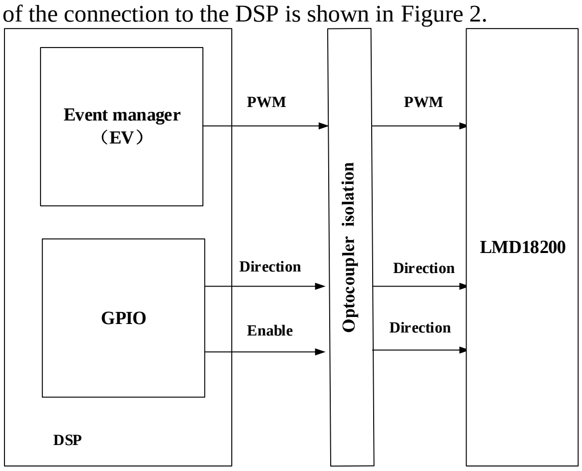

Figure 2. Connection diagram

As shown in Figure 2, the PWM pulse signal is generated by the F2812 event manager, while the direction signal and enable signal are programmed and controlled by the F2812 general input output (GPIO) bus. After the controller is designed, the peripheral circuit is designed and the hardware part of the system is designed [6].

2.2. Basic peripheral circuit

When designing the basic peripheral circuit, first design the clock circuit. Because of the particularity of the control system, in this system, the S3C44BOX processor chip uses the passive crystal oscillator, and the connection method of crystal oscillator is shown in Figure 3.

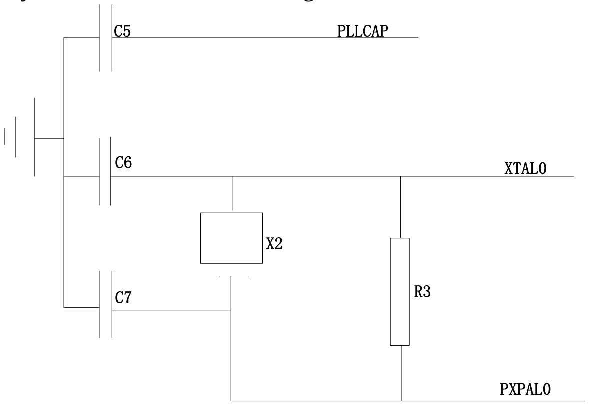

Figure 3. Clock circuit

The clock circuit connection diagram shown in Figure 3, according to the highest working frequency of S3C44BOX and the working mode of PLL circuit, 10 MHz passive crystal oscillator is selected. After 10 MHz crystal oscillator frequency is doubled by PLL circuit in S3C44BOX, the maximum can reach 66 MHz. The on-chip PLL circuit has the function of frequency amplification and signal purification. Therefore, the system can obtain a higher working frequency with a lower external clock signal to reduce the high-frequency noise caused by the high-speed switch clock [7].

The reset circuit mainly completes the power on reset of the system and the key reset function of the user when the system is running, and adopts a simple RC reset circuit. The designed reset circuit is shown in Figure 4.

From the reset circuit shown in Figure 4, when the system is powered on, charge the capacitor C1 through the resistance R1. When the voltage at both ends of C1 does not reach the threshold voltage of high level, the output of reset terminal is low level, and the system is in the reset state; when the voltage at both ends of C1 reaches the threshold voltage of high level, the output of reset terminal is high level, and the system enters the normal working state. When the user presses the button S1, the charge at both ends of C1 is discharged, the output of reset end is low level, the system enters the reset state, and then repeats the above charging process, the system enters the normal working state. Based on the above operations, the hardware design of the mechanical and electrical control system of mixed liquid gas pressure storage is completed, and the software part of the control system is designed according to the properties of mixed liquid gas pressure storage [8].

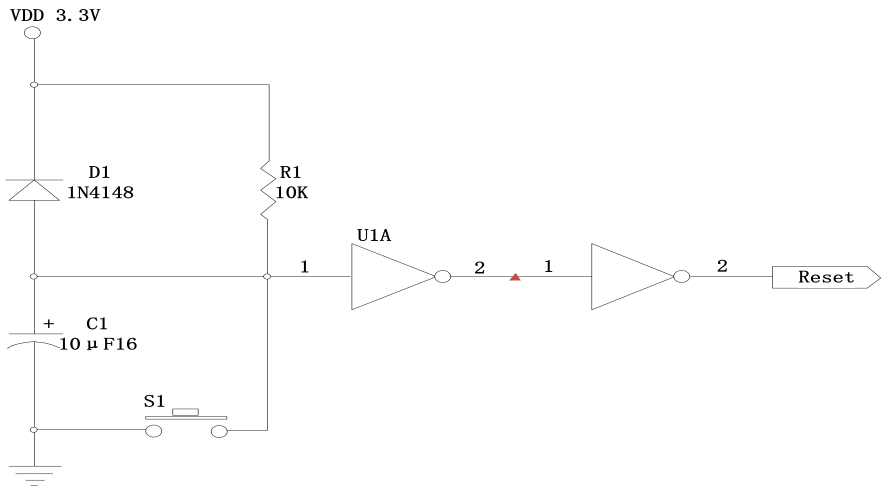

Figure 4. Reset circuit

3. Software design of mechanical and electrical control system of mixed liquid gas pressure energy storage

3.1. Characteristics of liquid pump

In the process of energy storage, the motor first converts energy from electrical energy to mechanical energy, and then the liquid pump, driven by mechanical energy, provides energy for the liquid in the liquid tank to be delivered to the gas tank. The liquid delivered to the gas tank by medium pressure, just like the liquid piston, compresses the gas in the gas tank, and then reserves the energy in this process. In the process of energy release, the high-pressure gas in the gas tank will send the liquid in the gas tank back to the liquid tank, at the same time, it also provides energy for the rotation of the hydraulic motor. The rotation of the motor drives the rotation of the motor, thus generating electric energy. The mechanical and electrical conversion link of the mixed liquid gas compression energy reserve system is mainly composed of the liquid pump and the motor. The liquid pump is the load of the motor, and the control of the motor will determine the working state of the liquid pump. Therefore, it is necessary to study the working characteristics of the liquid pump and optimize the control strategy of the motor based on this. The motor converts electrical energy into mechanical energy and outputs torque T_{sm} to the hydraulic pump. The rotational speed N of the motor can be calculated as follows:

$$N = \frac{1}{J}\int (T_{sm} - T_{hm})dt \tag{1}$$

In the above formula, T_{hm} is the load torque of the liquid pump as the motor load, T_{sm} is the motor control torque, J is the inertia coefficient of the shaft, and the friction loss of the shaft is ignored. The liquid flow from the liquid tank to the liquid pump Q is:

$$Q = DN \tag{2}$$

where D is the displacement of the liquid pump, according to the standard gas equation:

$$\rho V = nRT \tag{3}$$

Among them, ρ, V, n, R and T are respectively expressed as the pressure, volume, quantity, temperature and constant of ideal gas. The product of pressure and volume before and after gas compression is constant in the isothermal process, so we can get:

$$\rho_{am} V_s = \rho\left(V_s - \int_0^t Qdt\right) \tag{4}$$

where ρ_{am} is the standard atmospheric pressure and V_s is the volume of the air tank. According to the above formula, the pressure ρ of compressed gas can be calculated, and the torque expression of liquid pump can be calculated as follows:

$$\begin{cases} T_{hm} = \dfrac{\Delta PD}{2\pi} \\ \Delta P = P - \rho_{am} \end{cases} \tag{5}$$

According to the above formula (4) and formula (5), the efficiency of liquid pump is equal to the product of volume efficiency η_v and mechanical efficiency η_m, that is:

$$\eta_{pump} = \eta_v \times \eta_m \tag{6}$$

In the above formula, volume efficiency and mechanical efficiency have the following quantitative relationship:

$$\begin{cases} \eta_v = \dfrac{Q_{out}}{DN} \\ \eta_m = \dfrac{D\Delta p}{T_{sm} 2\pi} \end{cases} \tag{7}$$

where Q_{out} is the flow of liquid from the liquid pump. During the whole compression process, set the work efficiency of compressed gas as η_y, the motor efficiency as η_d, and the converter efficiency as η_{bv}. the total efficiency of the whole compression and energy storage process can be expressed as follows:

$$\eta_W = \eta_{bv}\frac{\eta_d}{\eta_y} \tag{8}$$

It can be seen from the above formula that according to the principle of thermodynamics, multiple compression and reduction of compression ratio can improve the work efficiency of compressed gas. The efficiency of permanent magnet synchronous motor is higher and less affected by load. Assuming that the motor efficiency and converter efficiency are fixed, the efficiency of liquid pump can be improved, which can effectively improve the total efficiency of the system [9].

According to the data provided by the liquid pump manufacturer, the compression efficiency characteristics of the liquid pump are shown in Figure 5.

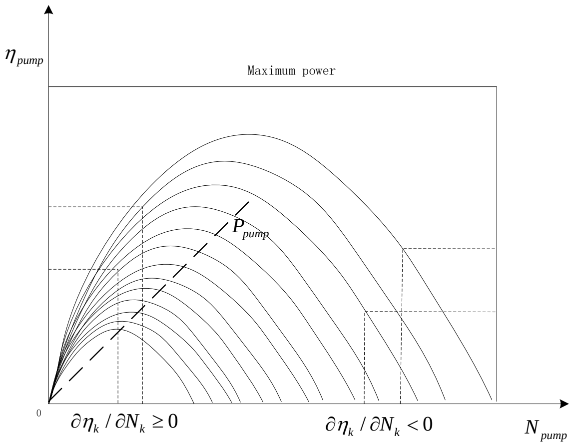

Figure 5. Working efficiency characteristics of liquid pump

As can be seen from Figure 5 that the sampling speed has the following quantitative relationship with the efficiency of the liquid pump:

$$\frac{\partial\eta_k}{\partial N_k} = \frac{\eta_k - \eta_{k-1}}{N_k - N_{k-1}} \tag{9}$$

where, N_k and η_k represent the rotational speed of k-sampling and the corresponding efficiency calculation value respectively. The rotational speed and pressure of the liquid pump determine the working efficiency of the liquid pump [10]. Therefore, in order to make the liquid pump work with higher efficiency, we should consider the pressure change and control the motor speed, so that the liquid pump works at the most reasonable speed [11].

3.2. Motor speed control based on maximum power point tracking

The liquid pump realizes the conversion from the kinetic energy of liquid to the mechanical energy of rotating shaft, which is represented by the mechanical conversion module. Combined with the above analysis of the working characteristics of the liquid pump, the energy storage device is modeled by using the characteristics of the input quantity as the speed and pressure difference, and the output quantity as the flow and the load torque of the motor. Based on the gas state equation, the calculation can be obtained:

$$\left(V_{air} - \int_0^t Q dt\right) p_a = p_{am} V_{air} \tag{10}$$

where V_{air} is the volume of the air tank. Since the inverter is connected with three-phase symmetrical load, only two variables need to be considered in modeling (the third variable can represent the three-phase voltage of the stator with the first two variables linearly). The three-phase voltage of the stator in the three-phase static coordinate system can be expressed as:

$$U = \frac{1}{3}\begin{bmatrix} 2 & -1 \\ -1 & 2 \\ -1 & -1 \end{bmatrix} U_{inv} \tag{11}$$

The stator voltage in the two-phase rotating coordinate system is calculated by the above formula. The calculation formula is as follows:

$$\begin{bmatrix} x_{sd} \\ x_{sq} \end{bmatrix} = \sqrt{\frac{2}{3}} \begin{bmatrix} \cos\theta & \cos(\theta - \frac{2\pi}{3}) & \cos(\theta + \frac{2\pi}{3}) \\ -\sin\theta & -\sin(\theta - \frac{2\pi}{3}) & -\sin(\theta + \frac{2\pi}{3}) \end{bmatrix} \begin{bmatrix} x_{s1} \\ x_{s2} \\ x_{s3} \end{bmatrix} \tag{12}$$

In the above formula, θ represents the angle difference between the rotor and the stator position, which can be obtained by rotating speed. The calculation formula is $\frac{d\theta}{dt} = N_p\omega$, N_p represents the pole pairs of the motor, and ω represents the shaft angular speed of the hydraulic pump. In this model, the motor consists of an energy accumulation module and an electromechanical conversion module. The motor current in the energy accumulation module can be obtained from the stator voltage and the motor electromotive force e:

$$L_s \frac{di}{dt} = (U - e) - ri_{line} \tag{13}$$

where, L_s and r are the stator inductance and winding resistance of the motor respectively. When the output voltage value is a specific value, the output power reaches the maximum value. Then the power consumed on the load internal resistance R_0 is:

$$P_{R_0} = I^2 R_0 = \left(\frac{V_p}{R_r + R_0}\right)^2 R_0 \tag{14}$$

where V_p is a constant. When the output power of the inverter is set as P_{R_0}, it can be seen that there is only one maximum point, that is, the maximum power point, and the derivation of load internal resistance R_0 can be obtained:

$$\frac{dP_{R_0}}{dR_0} = \frac{(R_r - R_0)V_p^2}{(R_r - R_0)^3} \tag{15}$$

where V is the voltage source voltage and R_r is the internal resistance of the voltage source. According to the two ends of the above formula, and then the derivation of R_0, we can get:

$$\frac{d^2 P_{R_0}}{dR_0^{\ 2}} = \frac{2R_0 - 4R_r}{(R_r + R_0)^4} \tag{16}$$

Let $\frac{dP_{R_0}}{dR_0} = 0$, get $R_r = R_0$, substitute it into formula (16), get $\frac{d^2 P_{R_0}}{dR_0^{\ 2}} = \frac{-2R_r}{(R_r + R_0)^2} < 0$. Therefore, when the output power P_{R_0} is the maximum value, $R_r = R_0$. That is, when the internal resistance of the load and the internal resistance of the power supply are equal, the output power reaches the maximum value. For a linear circuit with constant internal resistance, the external resistance of the load can be adjusted to make its resistance equal to the internal resistance value, so as to obtain the maximum power point, that is, the optimal working point [12].

The torque of motor and liquid pump is added to the shaft to generate the motor speed. The maximum power point obtained from the above formula is used to control the motor speed. The expression is:

$$J\frac{d\omega}{dt} = T_{sm} - T_{hm} - fw \tag{17}$$

where f is the coefficient of friction.

3.3. Implementation control

Based on the maximum power point control and maximum efficiency point control algorithm, the inversion control module of the control system is realized by programming and PI control. The calculation formula is as follows:

$$\mathrm{T_{sm\_ref}} = \mathrm{Cont}[w_{\mathrm{ref}} - w_{\mathrm{mes}}] + T_{sm} \tag{18}$$

In the above formula, $\mathrm{Cont}[w_{\mathrm{ref}} - w_{\mathrm{mes}}]$ represents the controller of variable, which is generally implemented by PI controller. $\mathrm{T_{sm\_ref}}$ is the reference value of motor torque. The motor module is inverted, and the motor winding module is used as the energy accumulation module. The controller is used to realize the inversion operation, and the reference value and measurement value of the stator current are obtained [13-15]. Under the measured value, the park transform is inverted as follows, and the voltage reference value of the inverter is calculated. Using the voltage reference value, the reference value of the regulating amount is calculated, and the calculation formula is as follows:

$$\mathrm{m_{ref}} = \frac{u_{ref}}{u_{cap}} \tag{19}$$

where, $\mathrm{u_{rect\_ref}}$ is the reference value of inverter voltage and u_{cap} is the measured value of inverter voltage. Starting from the calculated maximum reference value of the inverter, the tracking control flow of the maximum efficiency point of the energy storage system is shown in Figure 6.

Process according to the process shown in Figure 6, in the initial stage, the reference speed is given by using the quadratic interpolation method to make the liquid pump start quickly; after the start-up, the working point of the liquid pump is judged to be on the left or right side of the maximum efficiency point by using the working efficiency characteristic diagram of the liquid pump, so as to correct the speed and complete the tracking control of the maximum efficiency point of the liquid pump; the maximum power point tracking is calculated by using the power of the liquid pump to get the control strategy, when the motor power is less than the design power of the system, gives a higher reference speed, so that the system power increases rapidly, so as to quickly store energy; when the motor power reaches the design power of the system, calculate the reference speed of the system at the maximum power, so as to control the system at the maximum power point. Finally, the software design of the control system is completed.

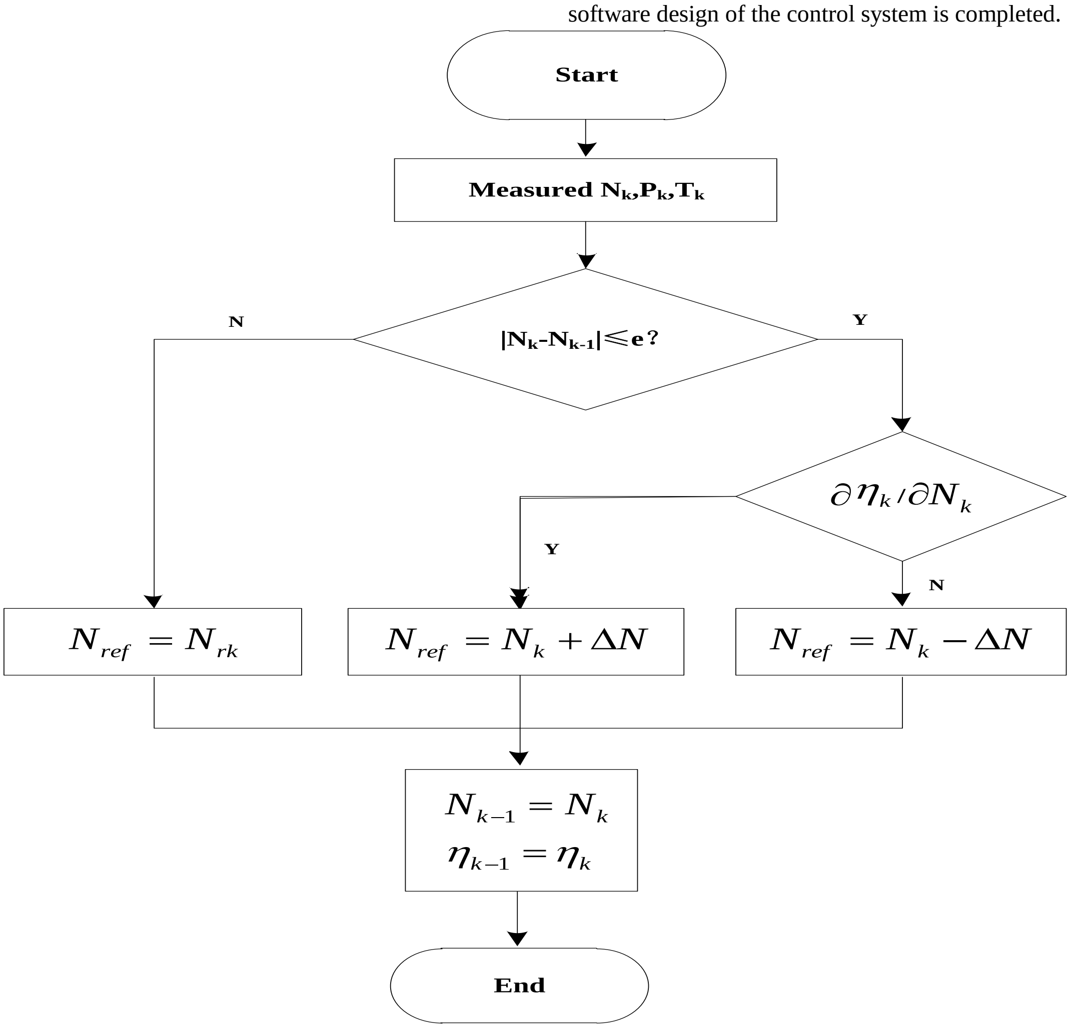

Figure 6. Maximum efficiency point tracking control process

4. Experimental results and analysis

In order to prove the application performance of the designed mechanical and electrical control system based on the tracking of maximum power point in the actual power work, the combined automatic generation control system of thermal power unit and energy storage system [2] in literature and the multi-port power generation control system based on energy storage [3] are set up as the experimental comparison system. In the same working environment, the mixed liquid gas is treated by three systems compressed energy storage is controlled by mechanical and electrical equipment.

4.1. Experimental platform and parameter setting

Based on the MATLAB/Simulink, the compression process of the system is taken as an example to simulate different control systems. Set up the experimental platform, as shown in Figure 7.

On the experimental platform shown in Figure 7, the inverter unit is controlled by the upper computer in the mixed liquid gas compressor and the permanent magnet synchronous motor is driven to drive the liquid pump to work, and the air is compressed to the air tank to realize energy conversion and storage. Figure 8 shows the mixed liquid gas compressor and accumulator.

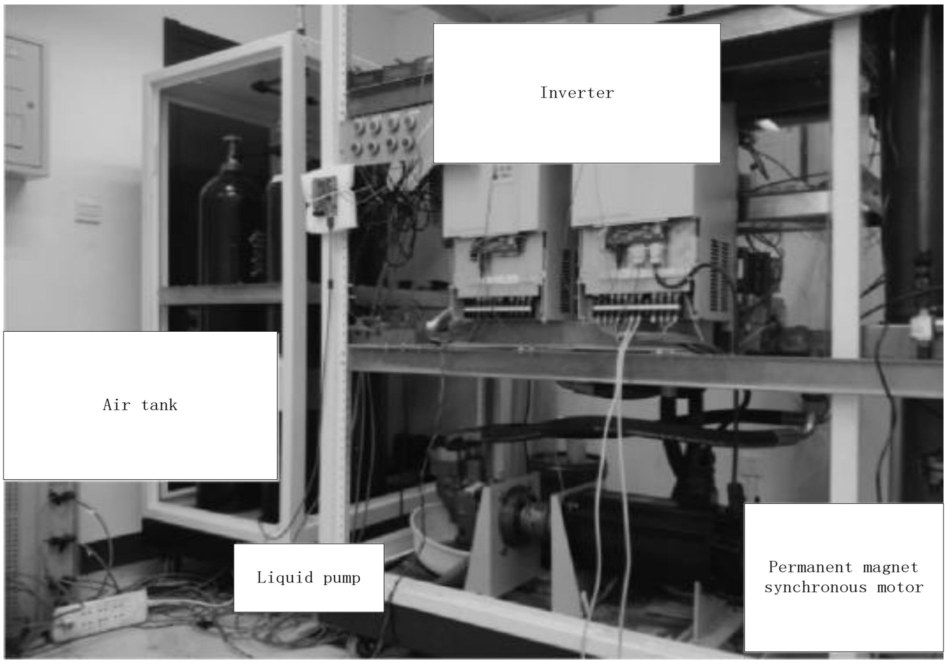

Figure 7. Experimental platform

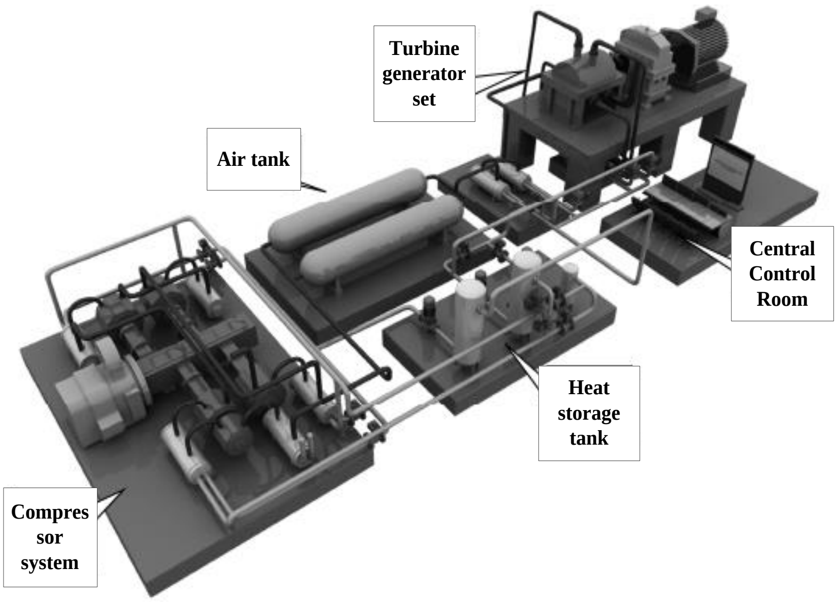

Figure 8. Mixed liquid gas compressor

Figure 8 comes from http://www.njeiri.com/front/article/506.htm. Through the experimental platform, the main parameters of the mixed liquid gas compressor and energy storage machine are set: the power is 15 kW; the rated power of the motor is 11 kw, the rated speed is 2000 r / min; the model of the liquid pump is Parker f12-125; the capacity of the air storage tank is 500 L; the maximum air storage pressure is 150bar (1bar = 1 × 105 Pa); the winding resistance (line line) of the motor is 0.3 Ω; the winding inductance (line line) is 6.54 mh; the rotational inertia of the motor is 162.6 kg·cm^2. According to the above experimental platform and experimental parameter settings, two traditional control systems and the control system designed in this paper are used to carry out experiments, and the performance of the three control systems is compared.

4.2. Liquid pump efficiency

Based on the above experimental preparation, the efficiency of the liquid pump can be observed in real time in the upper computer interface by using the sensor signal and the upper computer using the above formula (6). The experimental waveform is shown in Figure 9.

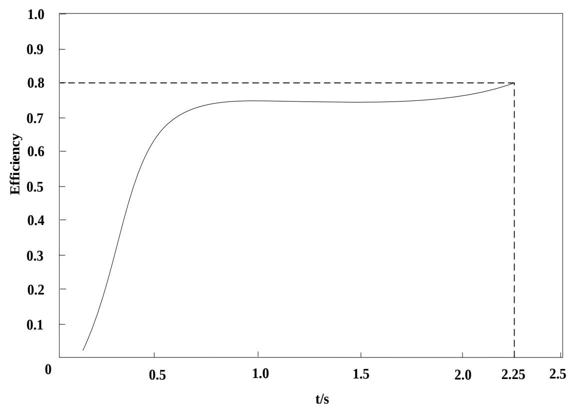

Figure 9. Efficiency of liquid pump

The input electric energy is measured by the electric energy meter at the interface between the experimental platform and the external power grid, and the following formula is used:

$$E = p_f V \ln\left(\frac{p_f}{p_0}\right) - p_0 V\left(\frac{p_f}{p_0} - 1\right) \tag{20}$$

In the above formula, p_f is the final gas pressure, p_0 is the initial gas pressure, and V is the gas volume. The results show that the efficiency of liquid pump is 0.52. Taking the efficiency of the liquid pump as the experimental index, the mechanical and electrical control system based on the tracking of the maximum power point, the automatic generation control system based on the combination of the thermal power unit and the energy storage system and the multi-port power generation control system based on the energy storage are compared and analyzed. The experimental results of the three control systems are shown in Table 2.

Table 2. Experimental results of three control systems

Control index of control system	Experimental result			
	Combined automatic generation control system of thermal power unit and energy storage system	Multi-port power generation control system based on energy storage	Mechanical and electrical control system of mixed liquid compressed energy storage based on maximum power point tracking	Contrast value
Input electric energy / (kW / h)	10.16	12.38	15.86	16.02
Storage energy / (kW / h)	5.42	7.31	8.30	8.33
Liquid pump efficiency	0.32	0.42	0.50	0.52

From the data shown in Table 2, it can be seen that under the same experimental platform, when the mechanical and electrical control system based on maximum power point tracking designed in this paper is used to control the mixed gas compressor, the efficiency of the system's liquid pump is the highest, and the system's liquid pump efficiency is the highest when the combined automatic generation control system of thermal power unit and energy storage system is used to control the mixed gas compressor The efficiency of the system is slightly lower than that of the combined automatic generation control system of thermal power unit and energy storage system. Considering the waveform analysis of other parameters of the above system, the control system designed in this paper has high efficiency. However, there are some security risks in the joint automatic generation control system of thermal power unit and energy storage system and the multi-port power generation control system based on energy storage. Therefore, the mechanical and electrical control system based on maximum power point tracking designed in this paper is more efficient Suitable for energy storage system. Due to the loss of gas and liquid flow in the experiment, the experimental results of the mechanical and electrical control system based on maximum power point tracking are slightly lower than the given comparison value. Through simulation and experimental verification, it can be clearly seen that the control system designed in this paper improves the shortcomings of traditional control system based on the algorithm of maximum power point or maximum efficiency point.

4.3. Control accuracy

In order to verify the effectiveness of the system in this paper, the mechanical and electrical control accuracy of the hybrid liquid gas compression energy storage system based on maximum power point tracking, the joint automatic power generation control system of thermal power unit and energy storage system and the hybrid liquid gas compression energy storage mechanical and electrical control accuracy of the multi-port power generation control system based on energy storage are compared and analyzed, and the comparison results are shown in Figure 10. The control accuracy = the working power of the system × 100% under ideal conditions.

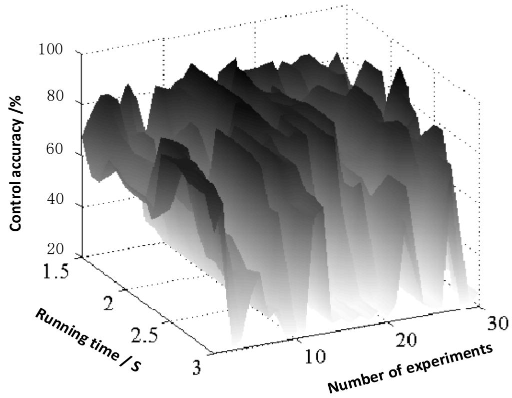

(a) The control accuracy of this system

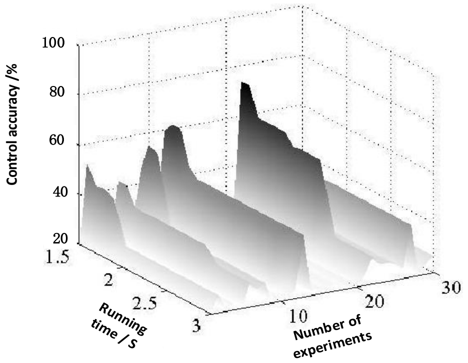

(b) Control accuracy of combined thermal power unit and energy storage system

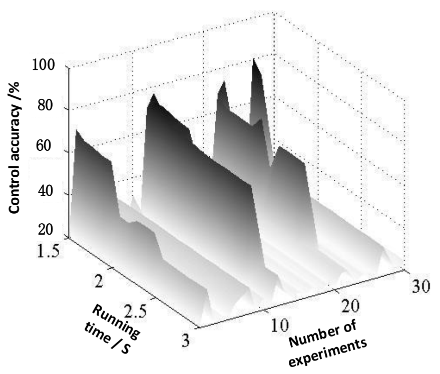

(c) Control accuracy based on energy storage system

Figure 10. Comparison of control accuracy of different **systems**

According to Figure 10, the mechanical and electrical control accuracy of the designed mechanical and electrical control system based on maximum power point tracking is up to 90%, while the mechanical and electrical control accuracy of the combined automatic generation control system of thermal power unit and energy storage system and the multi-port power generation control system based on energy storage is up to 75% And 80%, which shows that the control accuracy of the system is higher than that of the traditional control system.

4.4. Active power

In order to further verify the effectiveness of the system designed in this paper, the mechanical and electrical control system based on maximum power point tracking, the combined automatic power generation control system of thermal power unit and energy storage system and the active power of the mixed liquid compressed energy storage system based on the multi-port power generation control system of energy storage are compared and analyzed. The comparison results are shown in Figure 11.

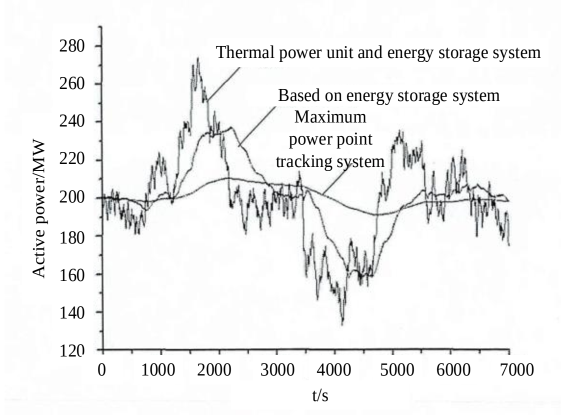

Figure 11. Comparison of active power of mixed liquid compressed energy storage

According to Figure 11, with the increase of operation time, the active power of the mechanical and electrical control system based on maximum power point tracking is between 190 mw and 210 MW, with a small change range; the active power of the system is between 130 MW and 280 MW; the active power of the hybrid liquid gas pressure storage system of the multi-port power generation control system based on energy storage is between 160 MW and 240 MW. The active power of the hybrid liquid gas pressure storage system of the combined automatic power generation control system of the thermal power unit and the energy storage system and the multi port power generation control system based on energy storage changes greatly. This shows that the active power of the hybrid liquid gas pressure storage system designed in this paper. The power is more stable than that of the traditional system.

5. Conclusion

With the development of energy storage system, the technological innovation of various energy storage methods is also in-depth. Compressed air energy storage technology as a relatively new way of energy storage, due to its unique advantages, has been widely concerned and actively studied by scholars all over the world. In this paper, a new type of compressed air energy storage system is designed. In the cycle of the compressed air energy storage system with liquid gas circulation, according to the different pressure range, the segmented compression ratio is determined, and the influence of this control mode on the efficiency is further analyzed. This refinement can keep the system in a quasi-constant temperature process and improve the efficiency of the system. The maximum efficiency point tracking control strategy of the hydraulic system is optimized. By setting the effective range of maximum efficiency point, the real-time performance of speed control is reduced. In the future, we need to complete the experiment on the experimental platform to solve the problems in the experiment. The correctness of the simulation analysis and the feasibility of the system are verified by experiments.

Acknowledgement

The research is supported by: Tianjin Education Commission Scientific Research Program (Program NO. 2020KJ083).

References

[1] Voznenko TI, Chepin EV, Urvanov GA. The control system based on extended BCI for a robotic wheelchair. Procedia Computer Science, 2018, 123:522-527.

[2] Mu CH, Wu PY, Sun GH, et al. Frequency modulation technology and application of automatic generation control combined with thermal power unit and energy storage system. Thermal Power Generation, 2018, 47, 378(05):35-40.

[3] Feng XT, Tao YY, Sun TT. Energy management and control strategy of multi port power system based on energy storage. Electrical automation, 2018, 40, 238(04):70-73.

[4] Wang Y, Yang X, Liang H, et al. A review of the self-adaptive traffic signal control system based on future traffic environment. Journal of Advanced Transportation, 2018, 2018(PT.3):1096123.1-1096123.12.

[5] Cuenca N, Antunes DJ, Castillo A, et al. Periodic event-triggered sampling and dual-rate control for a wireless networked control system with applications to UAVs. Industrial Electronics, IEEE Transactions on, 2019, 66(4):3157-3166.

[6] Jeong SY, Park JH, Hong GP, et al. Autotuning control system by variation of self-inductance for dynamic wireless EV charging with small air gap. IEEE Transactions on Power Electronics, 2019, 34(6):5165-5174.

[7] Kobayashi H, Kawagoe N, Kondo K, et al. Method to design control system of traction inverter of DC-electrified railway vehicle for an increase in regenerative brake power. IEEJ Transactions on Industry Applications, 2019, 139(1):30-39.

[8] Gil JD, Roca L, Zaragoza G, et al. A feedback control system with reference governor for a solar membrane distillation pilot facility. Renewable energy, 2018, 120(MAY):536-549.

[9] Xiao MZ, Pan W, Fei L, et al. Segmented power distribution control system based on hybrid cascaded multilevel converter with parts of energy storage. Iet Power Electronics, 2018, 10(15):2076-2084.

[10] Chang Z, Hu JK, Tao SR, et al. Simulation research on pressure stability optimization control of hydraulic cylinder of scraper. Computer Simulation, 2018, 35(06):248-251+466.

[11] Antonolpoulos F, Petrakis EGM, Sotiriadis S, et al. A physical access control system on the cloud. Procedia Computer Science, 2018, 130:318-325.

[12] Yue G, Pan YT, Zhang HJ, et al. A multi-neuron neural network algorithm for DSP servo control system of unmanned reconnaissance vehicle. Beijing Ligong Daxue Xuebao/Transaction of Beijing Institute of Technology, 2019, 39(2):203-208.

[13] Venkatachalam V, Prabhakaran D, Thirumarimurugan M, et al. LMI based stability analysis of non-linearly perturbed DC motor speed control system with constant and time-varying delays. International Journal of Power Electronics, 2019, 10(1-2):1-17.

[14] Wang WW, Liang X, Zhang MZ, et al. A new method for voidage correlation of gas-liquid mixture based on differential pressure fluctuation. Chemical Engineering Science, 2019, 193:15-26.

[15] Xu H, Fan Y, Tong X, et al. Designing control system of hypersonic vehicle with dynamic pressure constraints considered. Xibei Gongye Daxue Xuebao/Journal of Northwestern Polytechnical University, 2019, 37(1):41-47.

المملكة الأردنية الهاشمية

الجامعة الهاشمية

المجلة الأردنية
للهندسة الميكانيكية والصناعية

JJMIE

مجلة علمية عالمية محكمة

تصدر بدعم من صندوق البحث العلمي

http://jjmie.hu.edu.jo/

ISSN 1995-6665

المجلة الأردنية للهندسة الميكانيكية والصناعية

المجلة الأردنية للهندسة الميكانيكية والصناعية: مجلة علمية عالمية محكمة تصدرعن الجامعة الهاشمية بالتعاون مع صندوق دعم البحث العلمي والابتكار- وزارة التعليم العالي والبحث العلمي في الأردن.

ترسل البحوث إلى العنوان التالي

رئيس تحرير المجلة الأردنية للهندسة الميكانيكية و الصناعية

الجامعة الهاشمية
كلية الهندسة
قسم الهندسة الميكانيكية
الزرقاء - الأردن

هاتف : 3903333 5 00962 فرعي 4147

Email: jjmie@hu.edu.jo

Website: www.jjmie.hu.edu.jo